Measurement of beauty production from dimuon events at HERA/ZEUS

Dissertation
zur Erlangung des Doktorgrades
des Fachbereichs Physik
der Universität Hamburg

vorgelegt von Ingo Bloch
aus Hamburg

Hamburg, 2005

Gutachter der Dissertation:	Prof. Dr. R. Klanner Dr. A. Geiser
Gutachter der Disputation:	Prof. Dr. E. Lohrmann Prof. Dr. R.-D. Heuer
Datum der Disputation:	02.11.2005
Vorsitzender des Prüfungsausschusses:	Prof. Dr. G. Heinzelmann
Vorsitzender des Promotionsausschusses:	Prof. Dr. G. Huber
Dekan des Fachbereichs Physik:	Prof. Dr. G. Huber

Meiner lieben Familie gewidmet

Abstract

This thesis presents a measurement of beauty production from dimuon events in ep collisions at HERA, using an integrated luminosity of 114 pb^{-1} collected with the ZEUS detector. The beauty quark mass provides a large scale that should allow quantum chromo dynamic (QCD) calculations using perturbative methods. Measurements of beauty production thus offer the opportunity to test the predictions. The redundancy of the ZEUS muon-detection system was exploited to improve the reconstruction of muons with low transverse momenta from semileptonic beauty decays. This yielded sensitivity to $b\bar{b}$ events produced near the kinematic threshold. Dimuon charge correlations as well as hadronic isolation and mass of the dimuon system were used to separate the beauty signal from backgrounds. A beauty cross section in a region of phase space with large muon acceptance (visible cross section) was determined for the process $ep \to b\bar{b}X \to \mu\mu X'$ for muons with transverse momenta of $p_{\mathrm{T}}^{\mu} > 0.75$ GeV or $p_{\mathrm{T}}^{\mu} > 1.5$ GeV (depending on the clarity of the muon signature). Based on this measurement, the total cross section of beauty production in ep collisions at a centre-of-mass energy of $\sqrt{s} = 318$ GeV was determined for the first time:

$$\sigma_{\mathrm{tot}}(ep \to b\bar{b}X) = 16.1 \pm 1.8(\mathrm{stat.})^{+5.3}_{-4.8}(\mathrm{syst.})\ \mathrm{nb}.$$

The measured cross section is larger than the corresponding next-to-leading-order QCD prediction of $\sigma_{\mathrm{tot}}^{\mathrm{NLO}}(ep \to b\bar{b}X) = 6.8^{+3.0}_{-1.7}$ nb. Differential cross sections were measured in p_{T}^{μ} and η^{μ}. For a subset of dimuon events with muons from different b quarks, angular correlations in $\Delta\phi^{\mu\mu}$ of the dimuon system were also measured. The results were found to be in good agreement in shape though not in normalisation with leading-order plus parton-shower Monte Carlo simulations. The next-to-leading-order QCD prediction describes the shape of the cross section in $\Delta\phi^{\mu\mu}$, while still slightly underestimating the normalisation.

As the technical part of this thesis, simulations were performed with the aim to reduce initially large synchrotron-radiation induced backgrounds strongly interfering with the operation of the H1 and ZEUS detectors after the HERA luminosity upgrade in 2000/2001. By an optimisation of the synchrotron-radiation collimation system, these backgrounds could be reduced by more than an order of magnitude.

Kurzfassung

In dieser Arbeit wird eine Messung von Beauty-Produktion in ep Kollisionen bei HERA unter Verwendung des Zwei-Myon Zerfallskanals beschrieben. Die Messung verwendet einen vom ZEUS Detektor aufgezeichneten Datensatz mit einer integrierten Luminosität von 114 pb^{-1}. Die Beauty-Quarkmasse stellt eine hohe Skala zu Verfügung, die Quantenchromodynamik-Rechnungen (QCD) unter Verwendung pertubativer Methoden zulassen sollte. Beauty-Messungen eröffnen somit die Möglichkeit die Vorhersagen zu testen. Die im ZEUS Myondetektions-System vorhandene Redundanz wurde ausgenutzt um die Rekonstruktion von Myonen mit niedrigen Transversalimpulsen zu verbessern. Diese Verbesserung ermöglichte die Rekonstruktion von semi-myonisch zerfallenden $b\bar{b}$ Ereignissen nahe der kinematischen Schwelle. Ladungskorrelationen im Zwei-Myon-System, sowie hadronische Isolation und Masse der Myonenpaare wurden verwendet um das Beauty-Signal von Untergründen zu separieren. Für den Prozess $ep \to b\bar{b}X \to \mu\mu X'$ wurde ein Wirkungsquerschnitt in einem Bereich des Phasenraums mit grosser Myonen-Akzeptanz (sichtbarer Wirkungsquerschnitt) für Myonen mit Transversal-Impulsen von $p_{\mathrm{T}}^{\mu} > 0.75$ GeV oder $p_{\mathrm{T}}^{\mu} > 1.5$ GeV (in Abhängigkeit der Deutlichkeit der Myon-Signatur) bestimmt. Basierend auf dieser Messung wurde zum ersten Mal der totale Wirkungsquerschnitt für Beauty-Produktion in ep Kollisionen bei $\sqrt{s} = 318$ GeV bestimmt:

$$\sigma_{\mathrm{tot}}(ep \to b\bar{b}X) = 16.1 \pm 1.8(\mathrm{stat.})^{+5.3}_{-4.8}(\mathrm{syst.})\ \mathrm{nb}.$$

Der gemessene Wirkungsquerschnitt ist größer als die entsprechende QCD Vorhersage in nächstführender Ordnung von $\sigma_{\mathrm{tot}}^{\mathrm{NLO}}(ep \to b\bar{b}X) = 6.8^{+3.0}_{-1.7}$ nb. Es wurden weiterhin differentielle Wirkungsquerschnitte in p_{T}^{μ} und η^{μ} gemessen. Für einen Unterdatensatz bestehend aus Zwei-Myon-Ereignissen mit Myonen von verschiedenen Beauty-Quarks wurden Winkelkorrelationen $\Delta\phi^{\mu\mu}$ im Zwei-Myon-System gemessen. Die Messungen wurden in der Form, nicht aber in der Normierung von Monte-Carlo-Simulationen beschrieben. Die QCD Vorhersage in nächstführender Ordnung beschreibt die Form des Wirkungsquerschnittes in $\Delta\phi^{\mu\mu}$, bleibt aber in der Normierung leicht unter den Messungen.

Als technischer Teil dieser Arbeit wurden Simulationen durchgeführt, mit dem Ziel der Reduktion von Synchrotronstrahlungs-Untergründen die nach dem HERA Luminositäts-Upgrade (2000/2001) die Datennahme in den H1 und ZEUS Detektoren stark behinderten. Durch die Optimierung des Synchrotronstrahlungs-Kollimatorsystems konnte dieser Untergrund um mehr als eine Größenordnung reduziert werden.

Contents

1 Introduction **1**

2 Beauty production - theoretical context **3**

2.1 The standard model . . . 3

2.1.1 Quantum Chromodynamics . . . 5

2.2 Electron proton scattering at HERA . . . 7

2.2.1 Electron proton cross sections . . . 9

2.2.2 Factorisation and parton densities . . . 9

2.2.3 Photoproduction events and photon structure . . . 11

2.3 Parton hadronisation . . . 13

2.4 Beauty production and decay . . . 15

2.4.1 Beauty production . . . 15

2.4.2 Beauty fragmentation and hadrons . . . 17

2.4.3 Semi muonic beauty decay . . . 17

2.5 Beauty production models and predictions . . . 18

2.5.1 Monte Carlo event generators . . . 19

2.5.2 NLO QCD calculations . . . 21

2.6 Sources of muon pairs in *ep* collisions . . . 22

2.6.1 Muons from open HFL decays . . . 22

2.6.2 Quarkonium decays (hidden beauty and charm) . . . 24

2.6.3 Bethe-Heitler and Drell-Yan events . . . 25

3 Beauty production - experimental context **27**

3.1 Beauty at the Sp$\bar{\text{p}}$S . . . 27

3.2 Beauty at LEP . . . 30

3.3 Beauty at the Tevatron . . . 31

3.4 Beauty at H1 and ZEUS . . . 32
3.4.1 Measurements in μ+jet(s) . . . 32
3.4.2 Inclusive measurements using impact parameters . . . 34
3.4.3 Beauty and charm from $D^* + \mu$ events . . . 35
3.5 Conclusion . . . 36

4 HERA & reduction of backgrounds at HERA II **39**
4.1 HERA luminosity upgrade (HERA II) . . . 41
4.2 Suppression of backgrounds at HERA II . . . 43
4.2.1 Disentangling the background components . . . 45
4.2.2 Synchrotron radiation backgrounds . . . 50
4.2.3 Electron induced particle backgrounds . . . 65
4.2.4 Proton induced particle backgrounds . . . 66
4.2.5 Resulting collimator modifications at ZEUS . . . 66

5 The ZEUS detector **69**
5.1 Central Tracking Detector . . . 72
5.2 The Micro Vertex Detector . . . 73
5.3 Uranium-Scintillator Calorimeter . . . 74
5.4 Muon Chambers . . . 76
5.4.1 Forward Muon Spectrometer . . . 76
5.4.2 Barrel and Rear Muon Chambers . . . 78
5.5 Backing Calorimeter . . . 79
5.6 Luminosity measurement . . . 80
5.7 Trigger and data acquisition . . . 80

6 Dataset and event reconstruction **85**
6.1 The ZEUS HERA I data sample . . . 85
6.2 Monte Carlo samples . . . 86
6.3 Event reconstruction . . . 88
6.3.1 CTD track reconstruction . . . 88
6.3.2 CAL energy reconstruction . . . 89
6.3.3 CAL island and energy flow object reconstruction . . . 90
6.3.4 Jet reconstruction . . . 93

6.3.5 Pseudo thrust . . . 94
6.3.6 Electron reconstruction . . . 96
6.3.7 Muon reconstruction . . . 97
6.3.8 Muon and dimuon isolation . . . 103

7 Event selection and MC corrections **105**
7.1 Principle of the measurement . . . 105
7.2 Event selection . . . 106
7.2.1 Trigger selection . . . 106
7.2.2 Calorimeter based selection . . . 108
7.2.3 Dimuon Selection . . . 108
7.2.4 Background and cleaning cuts . . . 114
7.3 Muon corrections applied to MC samples . . . 114
7.3.1 Muon MC efficiency correction . . . 115
7.3.2 Muon trigger correction . . . 116
7.3.3 J/ψ and ψ' MC reweighting in $p_{\mathrm{T}}^{\mu\mu}$ . . . 117
7.3.4 Υ MC reweighting in Q^2 . . . 117

8 Signal determination **121**
8.1 Normalisation of backgrounds . . . 121
8.1.1 Normalisation of quarkonium and BH backgrounds . . . 121
8.1.2 Normalisation of the charm background . . . 121
8.1.3 Determination of the light-flavour background . . . 122
8.2 Signal normalisation . . . 123
8.2.1 Control distributions . . . 125

9 Cross sections **129**
9.1 Signal extraction . . . 129
9.1.1 Corrections for background charge correlations . . . 129
9.2 Visible and total beauty cross section . . . 130
9.2.1 Systematic error of the visible and total beauty cross section . . . 134
9.3 Differential muon cross sections . . . 136
9.3.1 Differential muon cross section in p_{T}^{μ} and η^{μ} . . . 136
9.3.2 Angular muon-correlation cross section . . . 139

9.3.3 Systematic errors of the differential muon cross sections 140
9.4 Comparison with NLO calculations and other measurements 140
9.4.1 NLO prediction for the total cross section 140
9.4.2 Comparison with the $D^* + \mu$ results 140
9.4.3 NLO prediction for the differential cross sections 143

10 Conclusion and Outlook **147**

A Coordinate systems **151**

B Design changes from positrons to electrons **153**

C MC samples - detailed list **155**

D Definition of the std. $\mathcal{G}$MUON quality **157**

E *Tight* and *loose* matching for the efficiency correction application **159**

F Trigger definition **161**
F.1 Muon plus Dijets for Running Periods 1999-2000: TLT HFL 1 161
F.2 Generic Charm: TLT HFL 10/11 161
F.3 Low E_T Dijet: TLT HPP 14 162
F.4 Medium Q^2 DIS Electron: TLT DIS 3 162
F.5 DIS Electron plus Muon: TLT DIS 27 162
F.6 Barrel/Rear Muon Trigger: TLT EXO 11/12 162
F.7 Semi-Isolated Muon with the Barrel/Rear Muon Chambers: TLT MUO 3 163
F.8 Forward Muon Trigger: TLT MUO 1, 2, 4 163

Bibliography **179**

Chapter 1

Introduction

The elementary structure of matter is described successfully by the standard model (SM) where forces between 12 fundamental fermions (quarks and leptons) are mediated by the exchange of gauge bosons. While the leptons, e.g. the electron or the muon, exist as free particles, the quarks are confined within bound states, the hadrons (e.g. protons). The strong force, binding the quarks in hadrons, is described in the theory of quantum chromo dynamics (QCD) by the exchange of massless gluons. For processes at high energy (higher than about 1 GeV) the coupling strength of the gluons becomes small and perturbative QCD methods can be applied. Thus perturbative calculations should be reliable in all processes where a high enough energy scale is present. The masses of heavy quarks (c, b and t) are sufficiently large to be chosen as this scale. Thus processes involving heavy quarks provide a rich testing ground for QCD, though the presence of more than one hard scale (e.g. additional large transverse momenta) can complicate calculations.

Perturbative methods in QCD have improved over the last years and many beauty production measurements have been performed in high-energy particle collisions - at CERN (in $p\bar{p}$ and e^+e^- collisions), at the Tevatron (in $p\bar{p}$ collisions) and at DESY (in ep collisions). Though in general agreement of the QCD predictions with the experimental data was found, a trend was observed for the data to exceed the predictions. These differences have so far not been fully solved, though some of the larger excesses (especially at the Tevatron) could recently be resolved.

The goal of this thesis is to extend the phase space of beauty measurements at HERA to previously unmeasured regions, especially to low transverse momenta and thus to contribute to the understanding of beauty production. To reach this aim, a measurement of beauty production in ep collisions was performed, using the beauty decay into two muons, $ep \rightarrow b\bar{b}X \rightarrow \mu\mu X'$.

The dimuon double tag is sensitive to correlations in the $b\bar{b}$ system. This is an advantage compared to single tag measurements, as it allows to test the $b\bar{b}$ correlations. Measurements of angular correlations in the $b\bar{b}$ system are of interest as they allow to estimate the influence of higher orders of the perturbative calculations.

Muons were found using a new combined muon reconstruction package. The combination of several parts of the ZEUS muon detection system, including previously unused detector components, yielded a great increase in muon detection efficiency. The redundancy of the muon signature in the ZEUS muon detectors was used to improve the signal to noise ratio thus

allowing to lower the transverse momentum threshold for the muons as compared to earlier analyses.

The simulation of light flavour background for a dimuon selection is challenging, as no generator based cuts can be applied. The response of the detector to hadrons needs to be simulated for a vast amount of particles, essentially impossible to simulate within reasonable time. In this thesis, dimuon charge correlations as well hadronic isolation and mass of the dimuon system were exploited to estimate the background from the data themselves and thus to separate the beauty signal from backgrounds.

The B hadrons from low p_{T}^b events frequently lead to very broad sprays of particles, that cannot reliably be reconstructed as jets. It is thus not possible to have a high acceptance at low p_{T}^b *and* require jets. Still the b-quark mass guarantees a higher transverse energy than present in usual light flavour events. Thus only a lower limit on the total transverse energy was set in this thesis to enhance beauty events. A large, highly enriched beauty sample with a purity of about 50% was obtained.

The low muon momentum cuts and the "jet-less" selection resulted in a large coverage of the beauty production phase space. For the first time at HERA this allowed for a measurement of the total beauty cross section in ep collisions at $\sqrt{s} = 318$ GeV without any cuts. Only very small regions of phase space were extrapolated in the measurement of the total cross section.

The muon direction of flight is correlated with the original b-quark direction. To have a more detailed look at single muon and thus also b-quark properties, differential cross sections in p_{T}^{μ} and η^{μ} were measured. The correlations of the muons with the b quarks can also be used to measure angular correlations in the $b\bar{b}$ system by measuring a cross section in $\Delta\phi^{\mu\mu}$. Leading order calculations produce $b\bar{b}$ pairs with $\Delta\phi^{b\bar{b}} = \pi$. Contributions at lower values of $\Delta\phi^{b\bar{b}}$ are present only in higher order calculations. As the cross section in $\Delta\phi^{\mu\mu}$ is correlated with the cross section in $\Delta\phi^{b\bar{b}}$, it can be used to estimate contributions from higher orders.

The document is organised as follows: **Chapter two** gives an overview of the theoretical framework of high energy electron proton scattering with special emphasis on the description of beauty production, hadronisation and decay into muons. In **chapter three**, a set of measurements of beauty production in high energy collisions is presented and compared to QCD predictions. **Chapter four** takes a small detour describing the HERA collider and the methods developed to suppress beam-induced backgrounds after the HERA upgrade in 2000/2001. The main focus lies on synchrotron-radiation induced backgrounds, the technical task of this thesis. **Chapter five** gives an introduction to the ZEUS detector. In **Chapter six**, the data and Monte Carlo simulation (MC) sets used in this analysis are summarised and the reconstructed variables are defined. **Chapter seven** explains how the beauty event candidates were selected. Corrections that were applied to the reconstructed MC information are also summarised here. In **chapter eight**, the normalisation of the signal and backgrounds are described. In **chapter nine**, the determination of the total and differential beauty cross sections and the determination of the corresponding systematic errors is described. Comparisons to predictions from leading order + parton showers (LO+PS) and next–to–leading order (NLO) calculations are shown. A summary and discussion of the results and an outlook on possible improvements concludes the thesis in **chapter ten**.

Chapter 2

Beauty production - theoretical context

This section summarises the theoretical and phenomenological methods used to describe beauty quark production in HERA electron proton collisions and the subsequent decay into muons. First the present theoretical framework of particle physics, the standard model with emphasis on the strong interactions is sketched. This is followed by a summary of the description of *ep* scattering. Issues specific to beauty production and decay are discussed and finally a summary of the sources of dimuon events in *ep* collisions is given.

2.1 The standard model

The current knowledge about the fundamental particles and their interactions, being the matter of study in particle physics, is encompassed in the Standard Model of elementary particles (SM).

In the SM, matter is made up from 12 fundamental constituents which are spin-1/2 fermions (leptons, quarks) and their anti particles, grouped into three generations, as summarised in tab. 2.1. The names of the quarks provide an additional quantum number called flavour. So far

Generation	leptons	c_{em} $[e]$	mass [MeV]	quarks	c_{em} $[e]$	mass [GeV]
1	e^-, e^+	∓ 1	0.511	u, $\bar{u}$	$\pm 2/3$	$1.5 - 4{\cdot}10^{-3}$
	ν_e, $\bar{\nu}_e$	0	$< 3{\cdot}10^{-6}$	d, $\bar{d}$	$\mp 1/3$	$4 - 8{\cdot}10^{-3}$
2	μ^-, μ^+	∓ 1	105.7	c, $\bar{c}$	$\pm 2/3$	$1.15 - 1.35$
	ν_μ, $\bar{\nu}_\mu$	0	< 0.19	s, $\bar{s}$	$\mp 1/3$	$0.08 - 0.13{\cdot}10^{-3}$
3	τ^-, τ^+	∓ 1	1777	t, $\bar{t}$	$\pm 2/3$	174.3 ± 5.1
	ν_τ, $\bar{\nu}_\tau$	0	< 18.2	b, $\bar{b}$	$\mp 1/3$	$4.1 - 4.4$

Table 2.1: Fundamental fermions. c_{em} denotes the electromagnetic charge in units of the electron charge. The definitions of the neutrino and quark masses are given in [1].

no substructure of the fundamental particles could be found down to resolutions of 10^{-18} m.

Stable matter consists only of fermions from the first generation; the other particles are observed in short lived states, decaying again into particles consisting of members of the first generation. The production of the second most heavy quark, the beauty quark, in electron proton (*ep*) collisions at the collider HERA is the subject of this thesis.

The fermions decay and interact via the exchange of gauge bosons leading to only four forces. These fundamental forces of nature are summarised in tab. 2.2. The electromagnetic, weak and

force	mediating gauge boson			typical coupling strength
	name	spin	mass [GeV]	
gravity	graviton	2	0	$\sim 10^{-38}$ (*)
electro-magnetic	photon (γ)	1	0	1/137
weak	intermediate bosons ($W^{\pm}$, Z^0) (H) (**)	1	M_W: 80 M_W: 91	1/30 at scale of M_W
strong	8 gluons (g)	1	0	0.1 - 1

Table 2.2: The four known forces of nature. Three of these, the electro-magnetic, the weak and the strong force are embedded into the SM. It has not yet been achieved to also include the gravitation. Remarks: (*) Measured at the scale of cm, not part of the SM. (**) The weak gauge bosons couple to the Higgs field (H, not yet observed directly).

strong force can be described in terms of quantum field theories. In this formalism, particles are described by functions of space-time coordinates, called fields, that can be considered as generalised coordinates of a Lagrange formalism. Interactions between particles are represented by gauge transformations under which the corresponding Lagrangian density function is invariant. The gauge transformation fixes the interaction between two particles or fields, though not the strength. For the gravitation, no experimentally confirmed quantum theory could be found up to now. The SM is thus incomplete and a description encompassing also gravitation might be necessary for a more complete picture of matter and forces of our universe. Other open questions within the SM, for example the missing explanations for the SM parameters (e.g. the coupling strengths), also support the assumption that the SM is still incomplete.

While pure electromagnetic interactions (pure γ exchange) can be described in an Abelian theory called Quantum Electro Dynamics (QED), the combination of the electromagnetic and the weak force (γ and W/Z exchange) in the electroweak theory by Glashow, Salam and Weinberg (GSW) as well as the theory of strong interactions, Quantum Chromo Dynamics (QCD) are based on a non-Abelian formalism. This formalism results in interactions not only between the fermions, but also between the exchanged bosons. The combination of the electroweak theory and QCD is called the SM. A detailed introduction to the SM can be found in standard textbooks (e.g. [2]), here a short overview is given.

The discovery of the last un-detected particle within the SM, the Higgs, is expected soon after the start of the new pp accelerator LHC at CERN. The Higgs particle is a scalar field with a non-vanishing vacuum expectation value. The coupling of the Higgs field with the W and Z bosons generates the masses of the weak bosons.

2.1.1 Quantum Chromodynamics

Quantum chromodynamics is a non-Abelian gauge theory that describes the strong interaction. Here a brief sketch of the basic principles of QCD is given. Further details relevant for the description of heavy-quark production and decay will be given in sec. 2.4.

Within QCD, the gauge bosons called *gluons* interact with quarks carrying *colour charges*. Being not colour neutral themselves, the gluons can also interact with other gluons. For each given quark flavour there are 3 possible colour charges and the corresponding anti-charges (R, G, B and $\bar{\text{R}}$, $\bar{\text{G}}$, $\bar{\text{B}}$). The 8 gluons are linearly independent colour-anticolour combinations.

Colour singlet states of 2 or more bound quarks (e.g. mesons: $q\bar{q}$ or baryons: qqq or $\bar{q}\bar{q}\bar{q}$) are referred to as *hadrons*. In scattering processes quarks or gluons within bound states are generally called *partons*. It should be noted that no bare colour charge has so far been observed. In high energy interactions, no free quarks thus exit the hard scattering process, but the partons

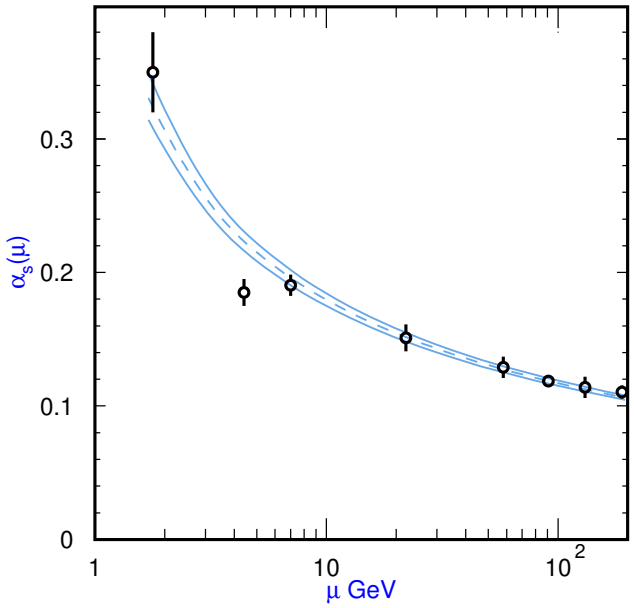

Figure 2.1: The dependence of the strong coupling α_s on the renormalisation scale μ [1]. The data are, in increasing order of μ, τ width, Υ decays, deep inelastic scattering, e^+e^-event shapes at 22 GeV from the JADE data, shapes at TRISTAN at 58 GeV, Z width, and e^+e^-event shapes at 135 and 189 GeV.

'fragment' (split or recombine with other partons) into several hadrons (see sec. 2.3), which are, at high enough energy, measurable as collimated bundles of particles (called *jets*) in the final state. The absence of free quarks is called *confinement* and can be explained by the self coupling of the gluons, leading to an anti-screening effect of the colour charge. The force between two colour charges grows with rising distance yielding enough energy to produce new quark pairs, before the original quarks are separated. The gluon self coupling also leads to much smaller colour coupling at small distances, called *asymptotic freedom*.

Both features are demonstrated in the dependence of the strong coupling constant α_s on the dominant energy scale μ, as shown in fig. 2.1. For large values of the energy scale, corresponding

to short distances, the coupling is small and the quarks can move freely. For lower energy scales, thus larger distances, the coupling and thus also the binding force becomes large.

The parameter μ is called renormalisation scale, and will very briefly be introduced in the following. For low energy scales perturbative calculations are not possible as the strong coupling becomes large. Here one has to rely on non-perturbative QCD models. In the high-energy regime however the strong coupling becomes small and rather precise calculations using perturbative methods (pQCD) can be used (see e.g. [3]). The QCD calculations beyond leading order (LO), called next-to-leading order (NLO), contain e.g. gluon and quark loops, of which basic example Feynman diagrams are given in fig. 2.2. When integrating over the phase space, these loops

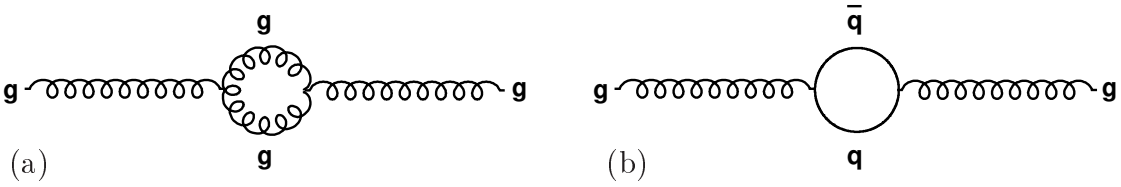

Figure 2.2: One-loop corrections to the gluon propagator. (a) gluon and (b) quark loop.

lead to so called *ultraviolet divergencies*, associated with infinite momenta of the virtual loop partons. Additional *collinear or infrared divergencies* are introduced by soft collinear emissions of gluons. Both these divergencies can be removed by first changing the space-time integration dimensions from 4 to $4-\varepsilon$ ($\int d^4 \rightarrow \lim_{\varepsilon\rightarrow 0} \int d^{4-\varepsilon}$) (*dimensional regularisation*) and, in a second step, using a *renormalisation scheme* to reparametrise the amplitudes in terms of physical finite quantities (for both regularisation and renormalisation see e.g. [4]). A commonly used renormalisation scheme is the modified minimal subtraction scheme ($\overline{\text{MS}}$) [5]. In this context an arbitrary renormalisation scale μ is introduced. The requirement, that measurable quantities should not depend on the chosen renormalisation scale leads to an effective coupling constant $\alpha_s(\mu)$ which is expressed in the renormalisation group equation:

$$\mu^2 \frac{\partial \alpha_s(\mu)}{\partial \mu^2} = \beta(\alpha_s(\mu)) \tag{2.1}$$

where the *β-function* can be written as a perturbative expansion in α_s describing the dependence of α_s on the renormalisation scale (running coupling). The $\mathcal{O}(\alpha_s)$ (LO) solution of eq. 2.1 is given by:

$$\alpha_s(\mu) = \frac{12\pi}{(33-2n_f)\cdot \ln(\mu^2/\Lambda^2_{\text{QCD}})} \tag{2.2}$$

where Λ_{QCD}[1] is a free parameter determined experimentally and n_f the number of active quark flavours (flavours with a mass below μ). If α_s is known at a defined scale, and taking into account the flavour dependence of Λ_{QCD}, α_s can thus be calculated perturbatively at all scales.

The coupling is small for the region $\mu \gg \Lambda_{\text{QCD}}$. As it needs to be small for perturbative methods to converge, the requirement $\mu \gg \Lambda_{\text{QCD}}$ separates the hard, perturbatively calculable regime

[1] The value of Λ_{QCD} depends both on the number of flavours for which it is expressed and also and the chosen regularisation/renormalisation scheme.

from the soft regime of large distances for which only phenomenological solutions exist. In the $\overline{\text{MS}}$ scheme and for 5 active flavours Λ_{QCD} has a measured value of [1]:

$$\Lambda^{(5)} = 217^{+25}_{-23}\ \text{MeV}. \tag{2.3}$$

As seen from eq. 2.2, α_s approaches zero for very large values of μ, which gives the asymptotic freedom for very small distances allowing quarks to be treated as free particles. On the other hand α_s gets much larger than one for $\mu \to \Lambda_{\text{QCD}}$, thus confining quarks within bound states at low energies and large distances.

2.2 Electron proton scattering at HERA

Electron nucleon scattering provides a rich source of information on the electroweak and the strong force. At HERA, distances down to 10^{-18} m are probed. Here the basics of ep scattering and the main results of proton and photon structures are given. The precise knowledge of the photon and proton structures are essential for studies of beauty production, as they provide the initial state particles for heavy flavour (referring to partons with larger masses than the that of the s quark, HFL, see sec. 2.4) production.

The basic electron proton scattering process

$$ep \to lX \tag{2.4}$$

can be described as the exchange of an electroweak boson, as depicted in fig. 2.3. In neutral

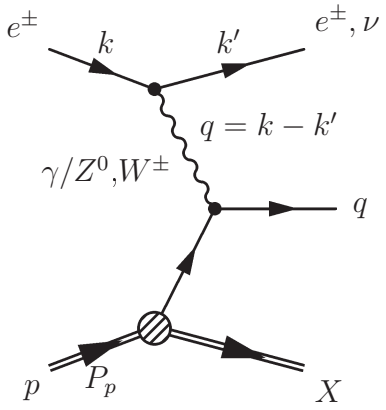

Figure 2.3: Basic ep scattering process at HERA. The quark from the proton scatters on the electroweak boson from the electron.

current (NC) events, the exchanged boson is a photon or a Z^0. In charged current events (CC), a $W^{\pm}$ is exchanged, changing the scattered electron into a neutrino.

Four variables Q^2, s, x and y provide a set of Lorentz-invariant variables that are used to describe the kinematics of unpolarised ep collisions: The transfered momentum squared or boson virtuality Q^2 is given by

$$Q^2 = -q^2 = k - k' \quad 0 < Q^2. \tag{2.5}$$

The centre-of-mass energy $\sqrt{s}$ of the ep system is given by

$$s = (P_p + k)^2. \tag{2.6}$$

The so called inelasticity y is defined as

$$y = \frac{P_p \cdot q}{P_p \cdot k} \quad 0 < y < 1. \tag{2.7}$$

Furthermore, a variable, called the *Bjorken scaling variable* x, is defined by

$$x = \frac{Q^2}{2P_p \cdot q} \quad 0 < x < 1. \tag{2.8}$$

In events where the momentum transfer Q^2 is much larger than the masses of the interacting particles, so that the masses can be neglected, the following relation holds:

$$Q^2 = xys \tag{2.9}$$

and, in the laboratory coordinate system defined by

$$\begin{aligned} k &= (E_e, 0, 0, -E_e) \\ k' &= (E'_e, E'_e \sin\theta_e \cos\varphi_e, E'_e \sin\theta_e \sin\varphi_e, -E_e \cos\theta_e) \quad \text{and} \\ P_p &= (E_p, 0, 0, E_p), \end{aligned} \tag{2.10}$$

the kinematic variables can be calculated as [6]

$$\begin{aligned} Q^2 = 2E_e E'_e(1 + \cos\theta_e) \quad &, \quad s = 4E_e E_p, \\ y = (E'_e/2E_e)(1 - \cos\theta_e) \quad &, \quad x = Q^2/(4yE_e E_p). \end{aligned} \tag{2.11}$$

Two regimes are defined depending on Q^2. Events with a high photon[2] virtuality of $Q^2 \gtrsim 1\ \mathrm{GeV}^2$ and large hadronic centre-of-mass energy ($W^2 = (P_p+q)^2 > m_p^2$) are referred to as *Deep Inelastic Scattering* (DIS) events, whereas those where the exchanged photon is only weakly virtual (with $Q^2 \ll 1\ \mathrm{GeV}^2$) are called *photoproduction* (γp).

In the DIS regime and for $E_p \gg m_p$ (infinite momentum frame), ep scattering can be described as the incoherent sum of elastic scattering processes of the lepton off a set of (non-interacting) partons which are interpreted as quarks and gluons. This picture is called the *quark parton model* (QPM) [7, 8]. In this picture, the variable x can be interpreted as the fraction of the proton momentum carried by the struck (massless) quark. The quarks that have not been struck are not influenced by the photon quark scatter and are called *spectator quarks*. The inelasticity y can be interpreted as the fraction of the lepton energy transferred to the hadronic system in the proton rest frame.

[2]The boson in the ep scatter will generally be referred to as photon. The W or Z exchange is strongly suppressed by the W/Z masses for values of $Q^2 < m^2_{Z/W}$.

2.2.1 Electron proton cross sections

Electron proton scattering as depicted in fig. 2.3 can be approximated at lowest order QED in terms of two unintegrated form factors called *structure functions* $F_1(x,Q^2)$ and $F_2(x,Q^2)$. These functions describe the charge-density distribution of the proton. When also including the $\gamma - Z^0$ interference (at values of $Q^2 \sim m_{W/Z}$), the additional structure function F_3 enters.

The double differential DIS cross section in x and Q^2 for photon (NC) and W exchange (CC) can be expressed as [1]

$$\frac{d^2\sigma_{NC}}{dxdy} = \frac{4\pi\alpha^2}{xyQ^4}\left[\left(1-y-\frac{x^2y^2M^2}{Q^2}\right)F_2^{NC}+y^2xF_1^{NC}\mp\left(y-\frac{y^2}{2}\right)xF_3^{NC}\right] \quad (2.12)$$

$$\frac{d^2\sigma_{CC}}{dxdy} = \frac{4\pi\alpha^2}{xyQ^4}(1\pm\lambda^2)\frac{1}{2}\left(\frac{G_FM_W^2}{4\pi\alpha}\frac{Q^2}{Q^2+M_W^2}\right)^2 \left[\left(1-y-\frac{x^2y^2M^2}{Q^2}\right)F_2^{CC}+y^2xF_1^{CC}\mp\left(y-\frac{y^2}{2}\right)xF_3^{CC}\right] \quad (2.13)$$

where α and G_F denote the fine structure constant and the Fermi constant, respectively. In the QPM F_1 and F_2 can be expressed as sums over quark and anti-quark densities and are connected via the Callan-Gross relation [9]

$$F_2 = 2xF_1. \quad (2.14)$$

QCD corrections can be described by including the longitudinal structure function called F_L (see e.g. [10]).

At values of $Q^2 \ll M_{Z/W}^2$ photon exchange dominates over the mass suppressed $W^\pm$ and Z^0 contribution:

$$\frac{\sigma(Z,W^\pm)}{\sigma(\gamma)} \sim \left(\frac{Q^2}{Q^2+M_{Z,W^\pm}^2}\right)^2. \quad (2.15)$$

Measurements of this behaviour are shown in fig. 2.4. Up to Q^2 of $\mathcal{O}(10^4\ \mathrm{GeV}^2)$ the W exchange expressed by the CC cross section is suppressed. When the momentum transfer is surpassing this value, the $\gamma - Z^0$ interference becomes more relevant and the pure QED picture as expressed by eq. 2.14 does not hold. The smaller CC cross section for positrons compared to electrons can be explained by the smaller d than u quark content of the proton as positrons interact with the d and electrons with the u quark in CC interactions.

2.2.2 Factorisation and parton densities

QCD calculations describe lepton-hadron (and hadron-hadron) collisions as the incoherent sum of the partonic interactions (of quarks and gluons). At present the calculation of the distribution of partons within the hadrons is not possible, due to the absence of a hard scale necessary for applying perturbation methods. Still it is possible to separate the hard (short range) scattering processes from the soft (long range) processes - a method that is called *factorisation* [12]. In this approach, the structure function F_2 can be expressed as the convolution of the perturbatively

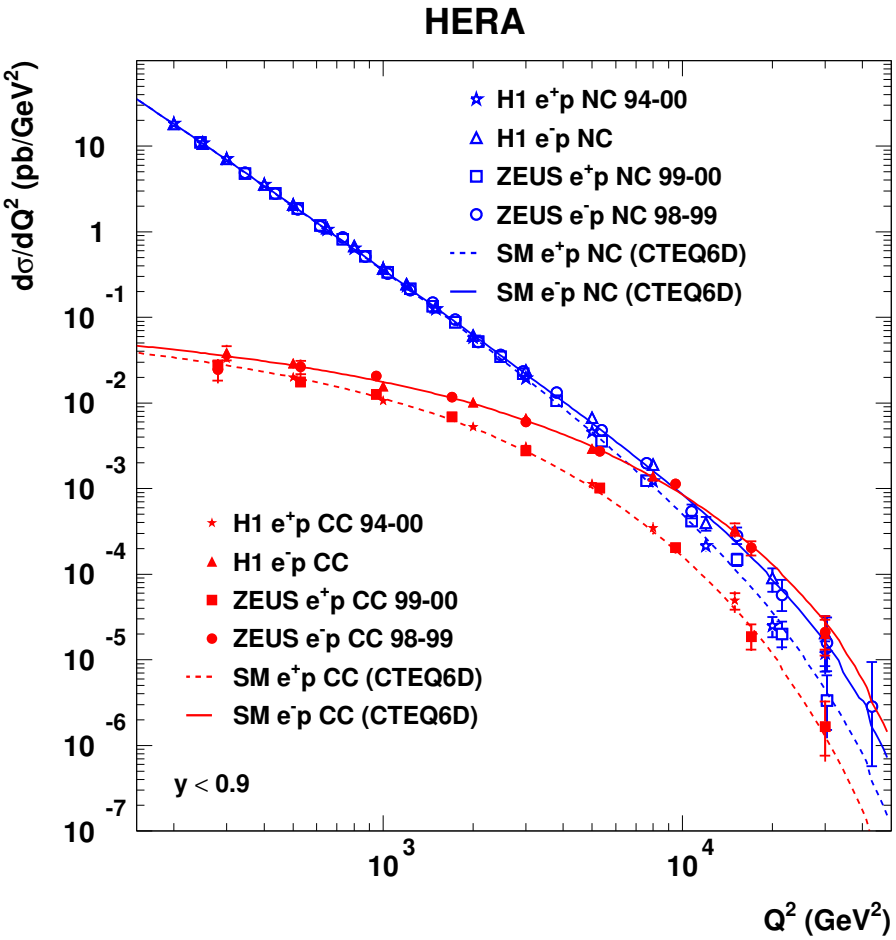

Figure 2.4: Inclusive differential charged current (CC) and neutral current (NC) cross sections as a function of Q^2 from the ZEUS and H1 collaborations [11]. The SM predictions for NC and CC DIS are shown in solid and dashed lines respectively. The suppression of the CC cross section with respect to the NC cross section is seen clearly in the region $Q^2 < M^2_{Z/W}$.

calculable scattering process and so called *parton density functions* (PDF) which are determined experimentally:

$$F_2(x,Q^2) = \sum_i \int_x^1 d\xi \; C_2^i\left(\frac{x}{\xi}, \frac{Q^2}{\mu^2}, \frac{\mu_f^2}{\mu^2}, \alpha_s(\mu^2)\right) f_i(\xi, \mu_f^2, \mu), \tag{2.16}$$

where the measured *parton density functions* $f_i(\xi, \mu_f, \mu)$ give the probability to find a parton i with momentum fraction ξ in the proton and the *coefficient functions* (or Wilson coefficients) C_2^i are perturbatively determined parton scattering cross sections. The scale μ is the renormalisation scale. The additional scale μ_f gives the value below which softly radiated gluons from the partons are included in the parton density functions rather than determined in the calculation and depends on the chosen *factorisation scheme*. The evolution in Q^2 of the parton densities can be calculated using *parton evolution schemes* like DGLAP [13], CCFM [14] or BFKL [15], which make use of different ordering of the radiated gluons along the line connecting the parton and the hard scatter.

Knowing the evolution with Q^2, which is perturbatively calculable, the experimental extraction of the PDFs is possible by measuring the cross section at given scales and for given processes.

According to the *factorisation theorem* of QCD the PDFs are process independent. Thus, based on the processes used for the determination of the PDFs, predictions can be made for other processes.

In fig. 2.5 the PDFs as determined at HERA from analyses using next–to–leading order (NLO) techniques on DIS data are shown. The u and d valence quarks carrying only about 50% of the

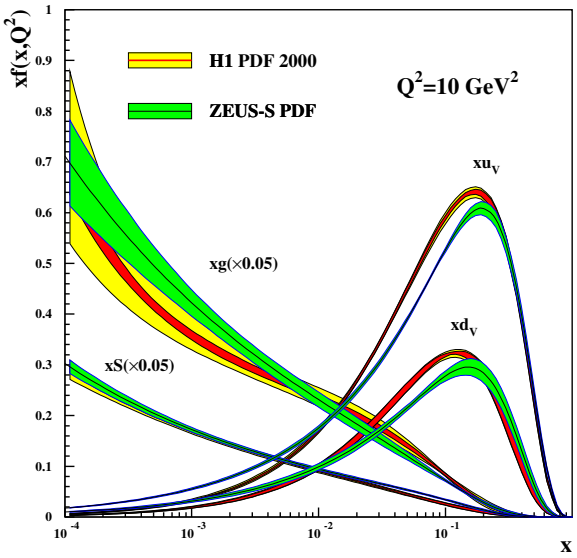

Figure 2.5: Proton density functions for u, d and s quarks as well as gluons as extracted from NLO QCD analyses on DIS data by the ZEUS and H1 collaborations [16] at $Q^2 = 10\ \mathrm{GeV}^2$.

proton momentum dominate at values of $x \sim 1/6$, whereas the gluons as well as the s quarks (coming from the gluon sea) are most prominent at lower values of x.

2.2.3 Photoproduction events and photon structure

The inclusive ep cross section is dominated by γp events ($Q^2 \ll 1\ \mathrm{GeV}^2$), as the photon propagator enters with a term $1/Q^4$, see eq. 2.12. Events of this type result most of the time in very low transverse momenta of the produced particles and thus escape detection, as does the electron. Those events however that have a final state with sizable transverse momenta are detected and can also be calculated in pQCD. The previously explained interpretation of x as the momentum fraction of the struck parton is not valid here.

2.2.3.1 Weizsäcker Williams approximation

The photoproduction process can be described as the interaction of a (quasi-) real photon with the proton using the Weizsäcker-Williams approximation [17]. When neglecting the small

contribution from longitudinally polarised photons, the differential cross section can be split into two contributions:

$$\frac{d^2\sigma^{PhPr}(y,Q^2)}{dydQ^2} = P_{\gamma/e}(y,Q^2)\cdot\sigma_{\gamma p\to eX}(y) \tag{2.17}$$

where $\sigma_{\gamma p\to eX}$ is the cross section for a real photon scattering on a proton and the *Weizsäcker Williams function*

$$P_{\gamma/e}(y,Q^2) = \frac{\alpha}{2\pi yQ^2}\left(1+(1-y)^2-\frac{2m_e^2y^2}{Q^2}\right) \tag{2.18}$$

gives the probability that an electron (with the mass m_e) emits a photon with the energy fraction y and the virtuality Q^2.

2.2.3.2 Photon structure

Quasi-real photons 'live' long enough to have a sizable probability of fluctuating into a $q\bar{q}$ pair before interacting. Additionally to interactions in which the photon enters directly into the hard scatter, *ep* scattering processes exist where one can think of the photon as being a virtual hadronic cloud. In analogy to the proton structure functions, the factorisation principle also holds for the photon, and *photon structure functions* can be determined.

The main input to photon structure functions is derived from $\gamma\gamma$ processes in e^+e^-scattering. For events with a large asymmetry in photon virtuality, that is for one quasi-real and one highly virtual photon, the process can be treated as deep inelastic $e\gamma$ scattering. The highly virtual photon then probes the hadronic structure of the quasi-real photon.

Structure functions are defined in analogy to *ep* DIS (see sec. 2.2.1), relating the $e\gamma$ cross section with the parton content of the photon. Like in the proton case, parton density functions f_i^γ can be extracted from experimental data using parton evolution equations.

2.2.3.3 Resolved processes

Events where only a part of the hadronic cloud of the photon enters into the hard scatter are referred to as *resolved* processes. Those events where the photon does not fluctuate and the full energy of the photon is involved in the hard scatter are called *direct* processes.

Examples for direct and resolved processes at LO are shown in fig. 2.6. Fig. 2.6a shows the LO direct process, also referred to as *boson gluon fusion* (BGF). This is also the dominant process for beauty production at HERA. Fig. 2.6b and c give LO resolved examples. In fig. 2.6b a quark from the hadronic cloud of the photon enters the hard scatter, whereas in fig. 2.6c a radiated gluon enters, giving rise to a gluon-gluon fusion process.

The interpretation and terminology of these processes is strongly connected with the technical implementation and the perturbative order of the models and calculations. A strict separation of direct and resolved is possible only in LO QCD.

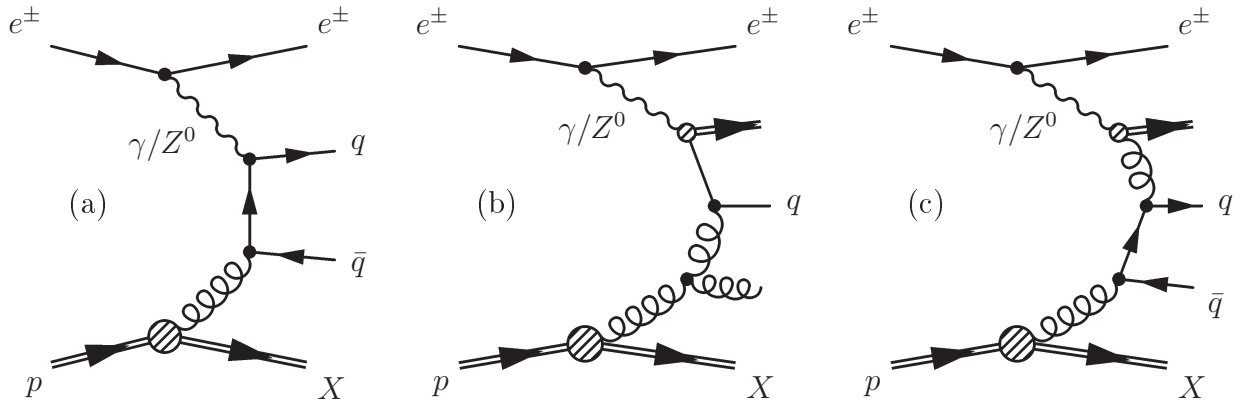

Figure 2.6: Leading order Feynman diagrams for the direct and and resolved components of photoproduction processes : (a) direct boson–gluon–fusion (b) resolved process with interaction of a quark from the hadronic structure of the photon with a gluon from the hadronic structure of the proton also referred to as excitation from the photon and (c) resolved process where a gluon from the hadronic structure of the photon interacts with a gluon from the hadronic structure of the proton.

2.3 Parton hadronisation

As a consequence of QCD colour confinement, free quarks do not exist. Thus directly after the production of quark pairs in a scattering process, colour neutral bound states with two or more quarks need to be formed from the two initial quarks. This process is generally referred to as *hadronisation* or *fragmentation*.

Methods as applied in MC models or event generators (see sec. 2.5.1), explicitly simulate the transition from partons to an observable final state. These models include perturbative and non-perturbative components. In a first perturbative step additional partons are emitted from the initial parton (*parton cascade*). A second non-perturbative step using phenomenological *hadronisation (or fragmentation) models* is used to form hadrons from these partons.

Parton cascades The MC simulations used in this analysis model parton cascades as *parton showers* (PS) approximating multiple parton emissions by a series of successive parton splittings. The probability that a parton is emitted from a parent parton with a given virtuality is taken from corresponding *splitting functions* [13] that are also part of the parton evolution equations mentioned in sec. 2.2.2. Initial- and final-state parton showers are treated differently. The initial-state parton shower starts from a parton coming from the proton which continues to emit partons with increasing virtuality until it enters the hard scatter[3]. Outgoing partons with positive virtuality are the source of time-like final state parton showers. The emissions are stopped when the outgoing partons reach a minimal virtuality for which perturbative methods are not applicable, usually chosen to be about 1 GeV.

[3]Technically this is generally implemented as a backward evolution starting at the hard scatter and evolving towards the parton.

Hadronisation The transformation of final state partons into bound hadrons can not be understood in terms of perturbative calculations, so phenomenological methods are used. These models produce a hadronic final state from a given parton configuration.

The model applied in the MC generators put to use in this thesis is called *string fragmentation*, as depicted in fig. 2.7. In this model $q\bar{q}$ pairs are connected by colour field lines, called strings.

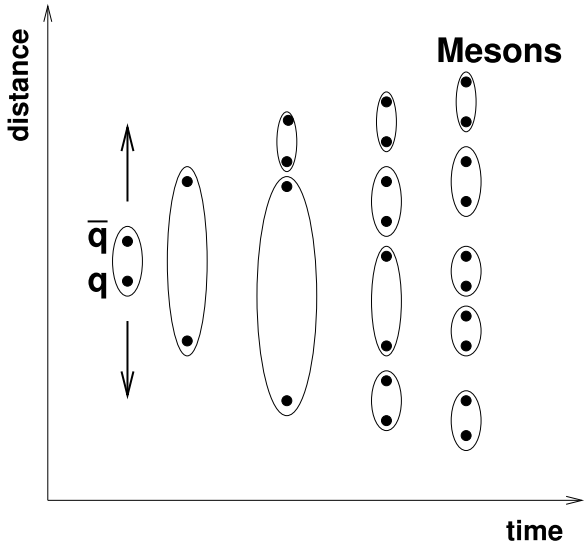

Figure 2.7: Visualisation of the string fragmentation model. From [18].

The potential is assumed to rise with the distance r between the quarks. If the stored potential energy is sufficient to produce a new $q\bar{q}$ pair, the string is broken up into two. This process continues until the available energy is used up. To form hadrons, *fragmentation functions* $f(z)$ are used. These describe the probability, that a hadron H originates from a parton P with the fragment of the parton longitudinal energy $z = (E+p_{\parallel})_h/(E+p)_P$. The transverse momentum spectrum of the hadrons is assumed to be Gaussian. A commonly used fragmentation function for heavy-flavour production is the so called *Peterson fragmentation function* $D(z)$ [19]:

$$D(z) = \frac{1}{z\left[1 - 1/z - \varepsilon/(1-z)\right]^2} \tag{2.19}$$

where the free parameter ε is expected to scale with the quark mass:

$$\varepsilon \propto \frac{1}{m_q^2} \tag{2.20}$$

For beauty quark production is has been determined from a fit to a measurement of semileptonic B-meson decays in e^+e^- collisions [20], yielding:

$$\varepsilon_b \approx 0.003. \tag{2.21}$$

The exact value of ε_b depends on the chosen parton showering scheme.

2.4 Beauty production and decay

Beauty as well as charm and top quarks are generally referred to as *heavy quarks* as their mass (see tab. 2.1) is both considerably larger than that of the *light quarks* (u, d and s) and than the value of Λ_{QCD}. As the heavy-quark masses provide a hard scale so that α_{s} is sufficiently low to apply pQCD, one would expect that theoretical predictions for processes involving heavy quarks should be rather reliable. This has made heavy-flavour processes an interesting testing ground for pQCD. Still after many years of study some small riddles remain. Especially the data from beauty events sometimes tends to lie above predictions from NLO QCD. This may be due to the fact that these processes generally provide more than one scale (additionally to the large quark mass e.g. in ep collisions the parton's transverse momentum p_{T} or the virtuality of the exchanged photon Q^2) complicating the calculations. Also the fragmentation and hadronisation processes used to extrapolate experimental data to the heavy-quark calculations have to be reliable to gain good compatibility of predictions with the data. Here the methods relevant for the production and decay of beauty quarks are described.

The theoretical description of heavy-quark production and decay is usually split into several parts. In a first step, the heavy-quark production cross section is calculated at the parton level using a scale corresponding approximately to the heavy-quark mass as well as higher order corrections if possible. Then, the quark becomes an on–mass–shell meson or baryon by binding with a quark from the fragmentation process. In a following step the decay of the heavy hadron is modelled according to experimentally determined branching ratios. The decay also involves electro–weak decay of a heavy quark to a light quark. Strong corrections for the last process can in most cases be determined perturbatively.

2.4.1 Beauty production

The dominant contribution to the ep beauty quark production cross section in LO ($\mathcal{O}(\alpha\alpha_{\mathrm{s}})$) is the BGF process, as depicted in fig. 2.6a. The BGF cross section can be calculated as

$$\hat{\sigma}_{\mathrm{BGF}} = \frac{\pi e_b^2 \alpha \alpha_{\mathrm{s}}}{\hat{s}} \left\{ (2 + 2\omega - \omega^2) \ln \frac{1+\chi}{1-\chi} - 2\chi(1+\chi) \right\} \tag{2.22}$$

with $\hat{s} = (p_b + p_{\bar{b}})^2$ the squared centre-of-mass energy of the $b\bar{b}$ pair and e_b the electromagnetic beauty quark charge [21, 18]. The variables ω and χ are given by $\omega = 4m_b^2/\hat{s}$ and $\chi = \sqrt{1-\omega}$. The charm BGF cross section is obtained by exchanging the charm and beauty electromagnetic charge. Due to the lower charge of the beauty quark and the higher mass, the factor $e_q^2/\hat{s}$ is smaller for beauty than for charm BGF processes, leading to a strong suppression of the beauty cross section relative to the charm cross section. Along the same argument, beauty quarks are produced predominantly close to threshold, leading to small transverse momenta ($p_{\mathrm{T}}^b \leq m^b$) of the beauty quarks relative to the incoming particles. These general features are observed also for resolved processes, shown in fig. 2.6b and c, as well as for higher order contributions.

Calculations have also been performed at NLO as higher order contributions to the beauty cross section have been found to be significant (see e.g. [22]). Some Feynman graphs entering these calculations are shown in fig 2.8 and 2.9. Comparing with LO graphs, the main difference is the additional radiation of hard gluons and the interference with virtual corrections. When

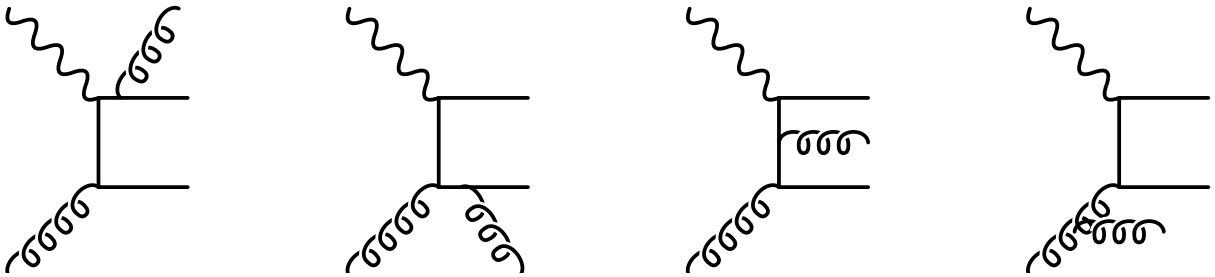

Figure 2.8: Examples of NLO Feynman diagrams for gluon radiation.

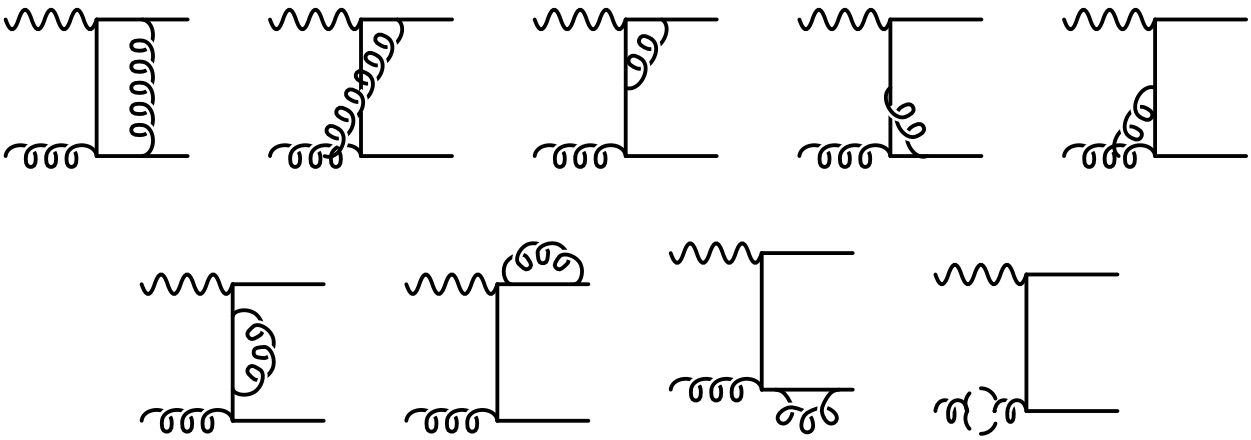

Figure 2.9: Examples of NLO Feynman diagrams for virtual corrections.

going from LO to NLO one needs to keep in mind that the pictures and separations used in the context of LO+PS calculations are not fully valid in the context of NLO calculations. In a simplified example, fig. 2.10 shows that a part of the parton shower applied in MC techniques is included in the hard scatter in NLO calculations.

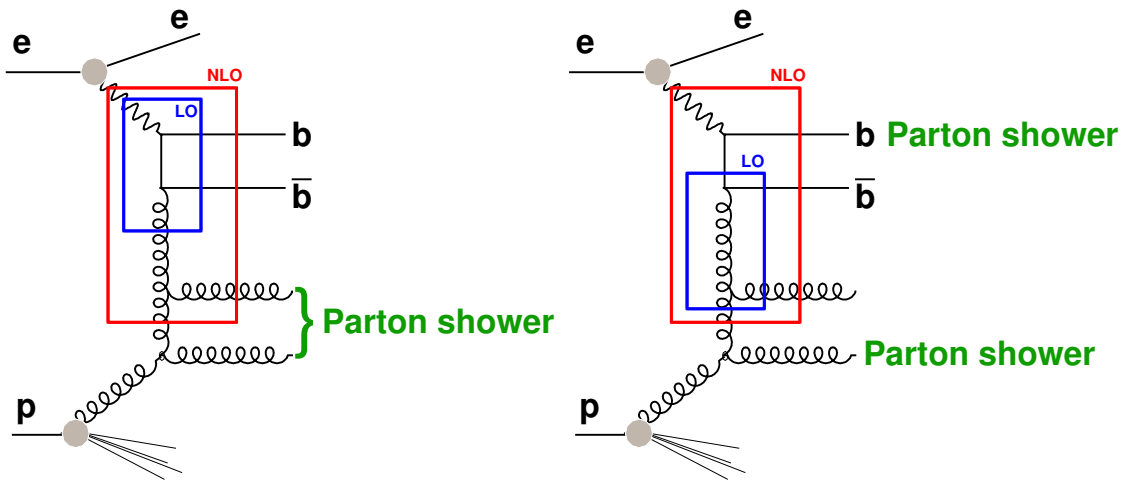

Figure 2.10: LO, NLO and PS in $b\bar{b}$ production. A part of the parton shower applied to initial and final state partons in LO is part of the hard scatter in NLO.

2.4.2 Beauty fragmentation and hadrons

The beauty quarks are transformed into heavy hadrons according to the Peterson fragmentation function (see eq. 2.19). Typical values for the experimentally determined parameter ε_q of this function are $\varepsilon_c = 0.035$ for charm production and $\varepsilon_b = 0.0035$ for beauty production (values taken from [23]). The shape of the fragmentation function for these values in arbitrary normalisation are compared in fig. 2.11. The B-hadrons (hadrons containing beauty quarks)

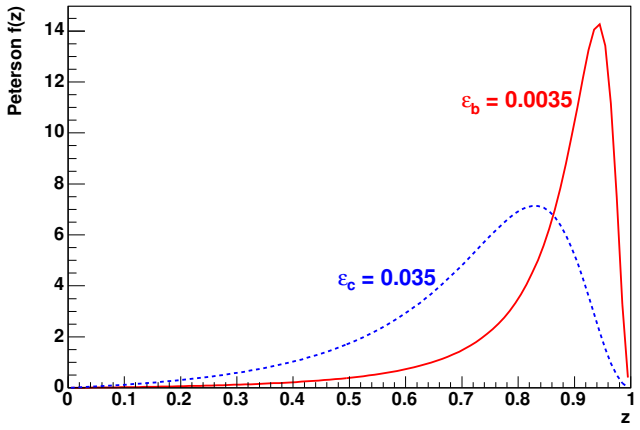

Figure 2.11: Comparison of the shape of the Peterson fragmentation function for typical charm and beauty values of ε_q. The values for ε_q have been chosen according to [23].

are generated with a harder spectrum than the C-hadrons (hadrons containing charm quarks). A list of the most frequently produced B- and C-hadrons is given in tab. 2.3. B-hadrons

Hadron	quark content	mass [MeV]	decay length $c\tau$[μm]	$I(J^P)$
$B^{\pm}$	bu	5279.0 ± 0.5	501	$\frac{1}{2}(0^-)$
B^0	bd	5279.4 ± 0.5	460	$\frac{1}{2}(0^-)$
B_s^0	bs	5369.6 ± 2.4	438	$0(0^-)$
Λ_b	udb	5624 ± 9	368	$0(\frac{1}{2}^+)$
$D^{\pm}$	cd	1869.4 ± 0.5	311.8	$\frac{1}{2}(0^-)$
D^0	cu	1864.6 ± 0.5	123.0	$\frac{1}{2}(0^-)$
$D_s^{\pm}$	cs	1968.3 ± 0.5	147.0	$0(0^-)$
Λ_c^+	cud	2284.9 ± 0.6	59.9	$0(\frac{1}{2}^+)$

Table 2.3: Examples of B- and C-hadrons [1].

have both a higher mass and a longer lifetime than C-hadrons. The higher mass is given by the higher mass of the contained b-quark, whereas the longer lifetime is driven mainly by the smaller transition probability $b \to c$ as compared to $c \to s$ given by the Cabibbo-Kobayashi-Maskawa (CKM) matrix elements $|V_{cb}| \approx 0.04$ and $|V_{cs}| \approx 0.97$ [1] respectively.

2.4.3 Semi muonic beauty decay

B-hadrons can not be detected directly as only their decay particles reach the detectors. A simple picture for hadron decay is given by the *spectator model*, depicted in fig. 2.12. Here

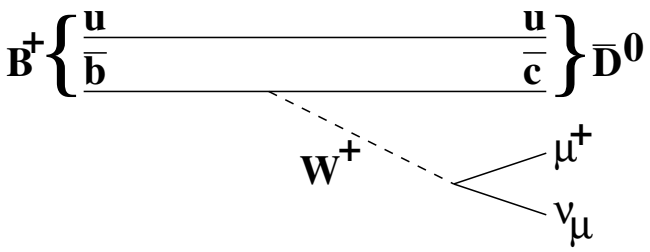

Figure 2.12: Hadron decay $B^+ \to \mu^+ \nu_\mu \bar{D}^0$ in the spectator model.

the beauty quark decays weakly without being influenced by the accompanying up quark, thus QCD effects (e.g. binding effects and gluon radiation) are neglected. The high mass of the b quark leads to a suppression of QCD effects (asymptotic freedom), justifying these model assumptions.

The subsequent muonic decay of the W provides a clear experimental signature among the possible final states of B-hadron decays. Beauty quarks decay predominantly via an intermediate charm quark rather than directly to an up quark, as the weak transition probability $b \to c$ given by $|V_{cb}|$ is an order of magnitude larger than $b \to u$ given by $|V_{ub}|$. The emitted W boson yields a muon and a muon neutrino with a probability of [1]

$$10.68 \pm 0.12\%. \tag{2.23}$$

Additionally to this direct muon production, *cascade decays* provide a source of muons from beauty decay, see fig. 2.13. The requirement of two muons in the final state provides an even

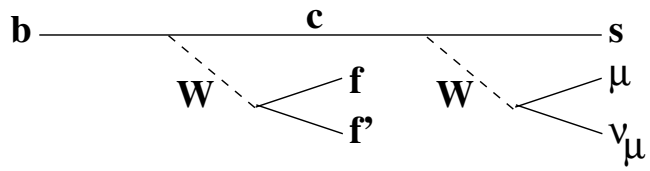

Figure 2.13: Weak *cascade* decay of a beauty quark.

clearer experimental signature, as there are only a few physics processes that lead to such a signature (see sec. 2.6). The dimuon signature has been chosen for the analysis presented herein.

2.5 Beauty production models and predictions

In this thesis, data were compared to distributions from LO+PS event generators and measured cross sections were partially compared to NLO calculations. In the following the event generator methods and the NLO calculations that were used are described.

2.5.1 Monte Carlo event generators

Leading order plus parton shower event generators make use of Monte Carlo techniques (a general introduction is given in [24]). The leading order plus parton shower generators PYTHIA [25] and RAPGAP [26] have been used to describe signal distributions in this thesis and the methods used within these generators are summarised here.

To generate final state hadrons, all generators use the same basic scheme as shown exemplarily in a direct BGF event in fig. 2.14. Perturbative matrix elements are calculated for the hard

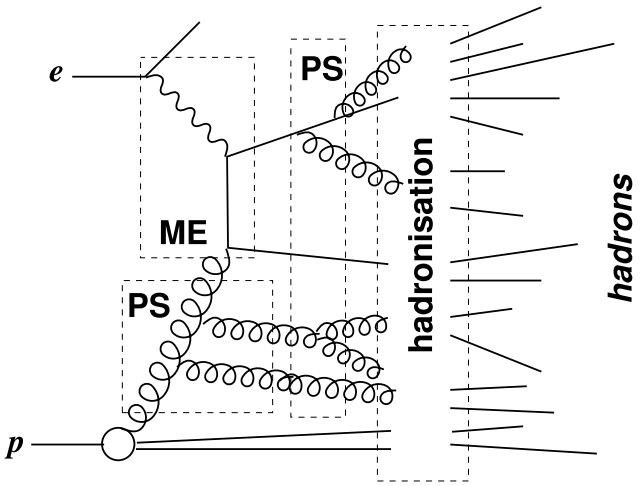

Figure 2.14: Methods of *ep* event generators in a BGF event. The box labelled ME is calculated perturbatively at LO. Parton showers are applied in the boxes labelled PS and finally the outgoing partons are transformed into hadrons in the hadronisation step after which they are decayed according to experimentally determined decay probabilities and spectra. From [18].

scatter at leading order (marked ME in fig. 2.14). For BGF events, the heavy-quark mass is taken into account, so that at $p_{\mathrm{T}}^{b} \to 0$ the cross sections stay finite and no additional cuts are required. Additional partons are produced in parton showers applied to the input and output particles (parton showers, marked PS in fig. 2.14). The parton showers effectively approximate higher order effects. These MC generators are therefore referred to as LO+PS generators.

All resulting outgoing particles are hadronised using phenomenological methods as explained in sec. 2.3. The subsequent decay of the unstable heavy hadrons is applied according to experimentally determined decay probabilities and spectra. The decay spectra and branching ratios are taken from measurements of other experiments. These measurements reflect general properties of B-hadrons not restricted to the special production environment. B-hadron momentum spectra as implemented e.g. in the generator PYTHIA are compared to Belle and BaBar data [27] in fig 2.15a. Good agreement is found. Momentum spectra of electrons and muons from decays of B mesons from different production environments are compared in fig 2.15b and found to be very similar. The B-hadron and muon spectra are thus largely independent of both the centre-of-mass energy and the final state hadron mixture. It is therefore reasonable to assume that also the B-hadron and muon distributions at HERA are described well by the spectra implemented in the MC models.

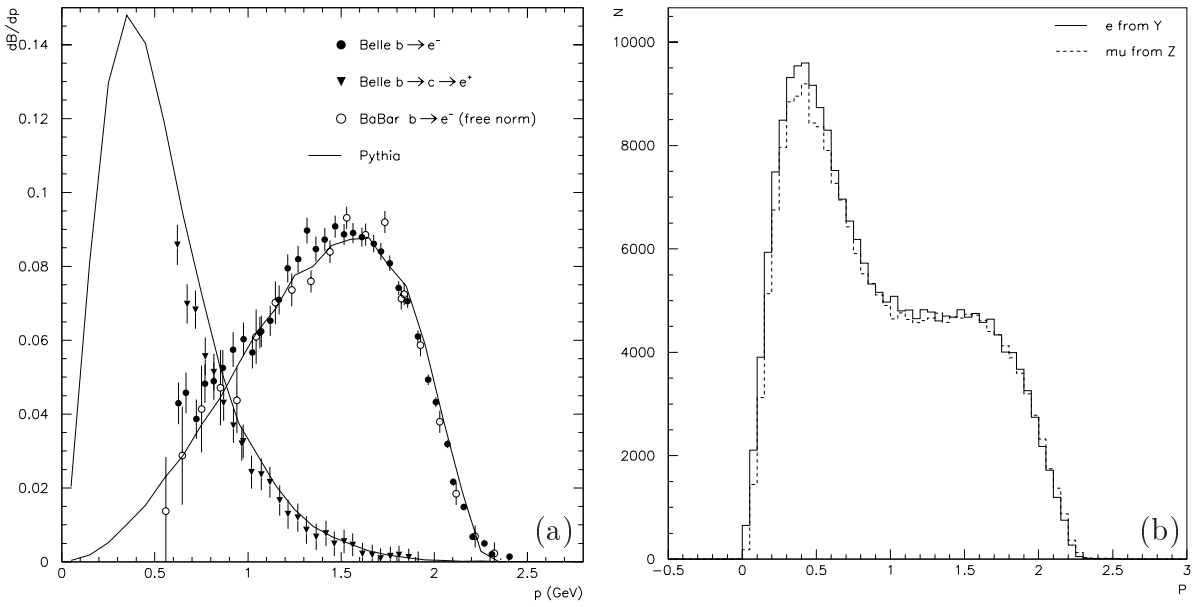

Figure 2.15: B-hadron momentum spectra. (a) Differential branching ratio dB/dp for the electron momentum in the B-hadron centre-of-mass system as measured by Belle for direct (circles) and indirect (triangles) B-meson decays compared to the PYTHIA prediction (line). The momentum distribution measured by BaBar is shown with arbitrary normalisation (empty circles). (b) PYTHIA prediction for the electron momentum distribution of the B-hadron mixture at the $\Upsilon(4s)$ resonance (BaBar/Belle centre-of-mass energies) with the muon spectrum of the B-hadron mixture at LEP centre-of-mass energies (from [28]).

The final state hadrons are subsequently filtered through a detailed ZEUS detector simulation (Mozart[4]) based on GEANT [29] to describe the detector response. After these steps, the generated events can directly be compared to experimental data.

In the following the main production processes of the PYTHIA generator are summarised. Technically, four main processes are generated. They are called direct, resolved and excitation from the proton and the photon and are generated with different tradeoffs between the perturbatively calculated hard scatter and the partonic structure functions:

- **direct**: Stands for pure boson gluon fusion where the photon from the electron interacts directly with a gluon from the proton producing a quark anti-quark pair. See fig. 2.6a.
- **resolved**: Stands for all processes where a gluon from the hadronic substructure of the photon (described via the photon structure function) enters into the process calculated in the LO matrix element. See fig. 2.6c.
- **resolved excitation from the proton/photon**: Resolved processes in which a heavy quark from the proton/photon partonic structure enters the hard scatter. See fig. 2.6b.

[4]MOnte Carlo for ZEUS Analysis Reconstruction and Tracking

The contribution from final or initial state gluons splitting into $q\bar{q}$ pairs (so called gluon splitting) was found to be negligible for the description of the data selected in this analysis.

The events for the DIS regime have been modelled with RAPGAP using only direct events. Here the photon structure is suppressed due the high virtuality or, in other words, the short "lifetime" of the photon.

2.5.2 NLO QCD calculations

The optimal scheme for NLO QCD predictions depends on the dominant scale. If the virtuality, Q^2, and the transverse momentum of the b quark squared, $(p_T^b)^2$, are of the order of m_b^2, threshold effects due to the b mass need to be considered and the so called massive scheme (used e.g. in the programs FMNR [30] and HVQDIS [31, 32]) is used. Once Q^2 or $(p_T^b)^2$ are much larger than m_b^2, massless schemes can be used. Here the b-quark is treated as a massless parton in the hard scatter. There are also methods in which the massive and massless approaches are combined [33]. The NLO calculations for this analysis were performed in the massive scheme, as most of the selected events have low Q^2 and beauty quarks transverse momenta of the order of the quark mass.

The programs HVQDIS and FMNR were used to calculate the NLO predictions for the cross sections to be measured. Here HVQDIS was used for the DIS regime and FMNR for photoproduction. For differential cross sections, only FMNR was used relying on the Weizsäcker-Williams approximation (see sec. 2.2.3.1) for the DIS part.

The parameters set within HVQDIS and FMNR are given in tab. 2.4. For both predictions the

Parameter	**HVQDIS**	**FMNR**
beauty mass	4.75 GeV	4.75 GeV
Q^2 range	1 to 10^4 GeV^2	< 1 GeV
Proton struc.	CTEQ5F4	CTEQ5M
Photon struc.	-	GRV-G HO

Table 2.4: Parameters used for the NLO predictions.

factorisation scale μ_f was set equal to the renormalisation scale μ. For FMNR the scale was set to:

$$\mu_f = \mu = \sqrt{{p_{\mathrm{T}}^b}^2 + m_b^2} \tag{2.24}$$

with p_{T}^b being the transverse momentum of the higher p_{T} beauty quark in the laboratory system. For HVQDIS μ was chosen as:

$$\mu_f = \mu = \sqrt{Q^2 + m_b^2} \tag{2.25}$$

To produce final state muons from the b quarks the following scheme was used. First the b quarks are fragmented collinearly into B hadrons. These are then decayed into muons applying muon momentum decay spectra as used within PYTHIA. The muons are emitted isotropically in the B hadron rest frame. To estimate the theoretical uncertainty of the NLO calculations the mass as well as the renormalisation and fragmentation scale were varied by a factor 2, and the b-quark mass was varied between 4.5 and 5 GeV.

2.6 Sources of muon pairs in *ep* collisions

In this analysis a dimuon tag was chosen as the experimental signature for beauty events. In the following all processes leading to muons close to the primary event vertex (prompt muons) in the final state are summarised. Only muons originating from the decay of beauty quarks or beauty-cascade decays are considered as signal, all other processes are treated as background. Technical backgrounds with fake muons or real muons not produced at the primary vertex (e.g. Kaon- or pion-decay muons) are discussed in sec. 6.3.7.

2.6.1 Muons from open HFL decays

2.6.1.1 Muons from open beauty decays

Muons are considered as beauty-signal muons if they originate from the direct decay of a beauty quark, or if they come from a cascade decay, that is the decay of a charm quark that originated from the decay of a b-quark. In fig. 2.16 the production of signal muons from beauty decay is

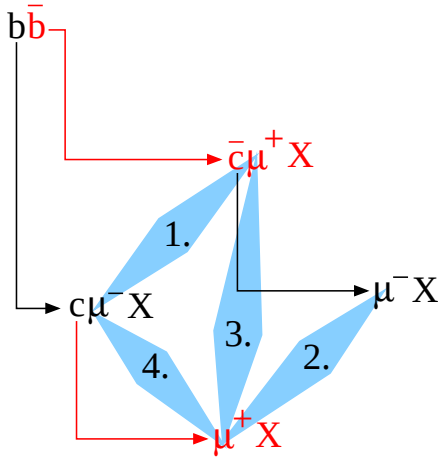

Figure 2.16: Origin of muons from beauty decay. Here the maximal yield of 4 signal muons from two cascade decays is shown.

shown. Muon signal pairs can be produced in four different ways:

1. the direct decay of both beauty quarks into muons, yielding unlike sign dimuons ($\mu^+\mu^-$),
2. the indirect decay of both charm quarks from beauty quarks into muons, yielding unlike sign dimuons ($\mu^+\mu^-$),
3. the direct decay of one beauty quark into one muon and the indirect (cascade) decay of the second beauty quark via a charm quark into a muon yielding like sign dimuons ($\mu^+\mu^+/\mu^-\mu^-$) and
4. the cascade decay of one of the beauty quarks into a muon and of the beauty-decay charm also into a muon, again yielding unlike sign dimuons ($\mu^+\mu^-$).

Generally all processes with prompt muons from B-hadron decays are counted as signal. These include e.g. a small fraction of muons originating from indirect b or cascade c decays and decays via intermediate tau leptons.

The weak force can change the strong flavour of quarks. This can change the type of a neutral meson "in flight", making it oscillate or mix, e.g. from a B^0 to a $\overline{B}^0$. This process also changes the charge of the final state muons, thus muons from process 1.) can lead to like sign muon pairs if one of the two B-mesons has oscillated. Two example oscillation diagrams are shown in figure 2.17. The time integrated probability $\overline{\chi} = f'_d\chi_d + f'_s\chi_s$ of a neutral B^0_d or B^0_s meson

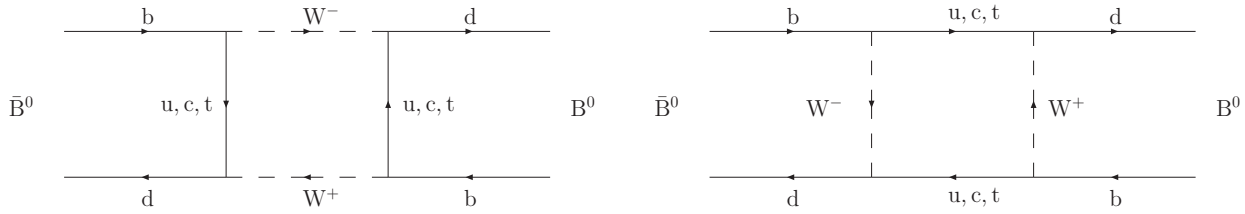

Figure 2.17: Example diagrams for $B^0_d\overline{B^0_d}$ mixing. Mediated by the weak CKM flavour transition the quarks change their flavour sign. The top quark dominates the "u,c,t" line in these diagrams as, due to their lower mass, the up and charm quarks are stronger helicity suppressed.

to oscillate into its anti meson is measured to $\overline{\chi} = 0.1257 \pm 0.0042$ [1].

2.6.1.2 Muons from open charm decays

The decays from charm quark events can produce only unlike sign prompt dimuon events, corresponding to process 2. in fig. 2.16. Cascade-like decays of charmed mesons, yielding like-sign muon pairs contain non-prompt muons only. These are not considered signal muons.

To separate beauty from charm one can exploit the mass and lifetime differences of the hadrons. Both these features are however not exploited to separate charm in this analysis.

2.6.1.3 Differences and common features

All muonic HFL decay processes have in common, that the muons are accompanied by hadrons, i.e. they are *nonisolated*.

The mass reconstruction of the beauty or charm quark mass is not possible, as the muon neutrinos from the weak decay escape detection. Still the beauty mass sets an upper limit on the invariant dimuon mass for muons coming from the same beauty quark (process 4.). The dimuon invariant mass from the processes 1. to 3. is not limited by the beauty quark mass. The charm quark mass sets no upper limit on the invariant dimuon mass.

2.6.2 Quarkonium decays (hidden beauty and charm)

Muonic decays of quarkonia (bound $q\bar{q}$ states of equal type quarks) as shown in fig. 2.18 are a

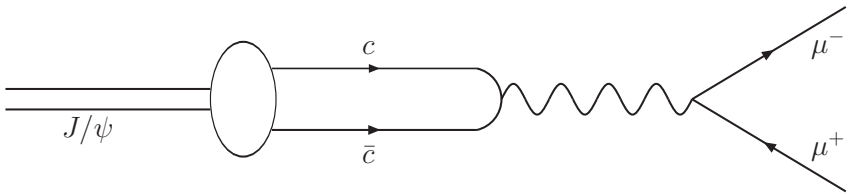

Figure 2.18: Diagram for the charmonium decay (J/ψ or ψ') to a muon pair. $b\bar{b}$ and lighter $q\bar{q}$ bound states decay similarly.

source of unlike sign muon pairs. The invariant mass of the muon pair gives the mass of the original bound state. These dimuons can thus be identified by peaks in the dimuon invariant mass distributions. In this section $b\bar{b}$, $c\bar{c}$ and light $q\bar{q}$ states are considered.

The contributions from these processes were described using the event generators PYTHIA (Υ) and HERWIG [34] (J/ψ and ψ').

2.6.2.1 Upsilon decays

Bound states of two b quarks are called Υ. There exist several excited states of the ground state $\Upsilon(1S)$, referred to as $\Upsilon(2S)$, $\Upsilon(3S)$ etc. The elastic cross section for $\Upsilon(1S)$ production at HERA has been measured by the ZEUS collaboration [35]. A cross section of

$$\sigma(\gamma p \to \Upsilon(1S)p) = 375 \pm 170(\text{stat.})^{+75}_{-64}(\text{syst.}) \text{ nb}$$

was determined at an average γp centre-of-mass energy of $W_{\gamma p} = 120$ GeV. A similar measurement was carried out by H1 [36] with compatible results.

The $\Upsilon(1S)$ mass and muon branching ratio is given by:

$$m_{\Upsilon(1S)} = 9460.30 \pm 0.26 \text{ MeV} \qquad Br(\Upsilon(1S) \to \mu^+\mu^-) = 2.48 \pm 0.06\%.$$

These unlike sign muons are not accompanied by hadronic activity and thus isolated.

The muonic final states of the heavier excited $b\bar{b}$ states $\Upsilon(2S)$ and $\Upsilon(3S)$ are also isolated. They have masses and muon branching ratios of:

$$m_{\Upsilon(2S)} = 10.02326 \pm 0.00031 \text{ MeV} \qquad Br(\Upsilon(2S) \to \mu^+\mu^-) = 1.31 \pm 0.21\%$$

and

$$m_{\Upsilon(3S)} = 10.3552 \pm 0.0005 \text{ MeV} \qquad Br(\Upsilon(3S) \to \mu^+\mu^-) = 1.81 \pm 0.17\%,$$

respectively. All masses and branching ratios are taken from [1].

The Υ is considered background for this analysis, but can be reduced to a negligible level using appropriate selection cuts, as described in sec. 7.2.

2.6.2.2 J/ψ, ψ' decays

Like $b\bar{b}$ states, corresponding $c\bar{c}$ states exist, called J/ψ and ψ'. Additionally to the direct $c\bar{c} \rightarrow J/\psi X$ production, J/ψs are decay products of $b\bar{b}$ events. Muons from charmonia are thus considered background, when they are the product of a direct process, or as part of the signal when the charmonium states are produced as decay products of a $b\bar{b}$ event. These two classes can be separated by a muon isolation requirement, as the muons from beauty-induced charmonia are again accompanied by hadrons, whereas the direct background is a source of isolated muons.

The charmonium masses and decay ratios of the J/ψ and the ψ' into muons are:

$$m_{J/\psi} = 3096.916 \pm 0.011 \text{ MeV} \qquad Br(J/\psi \rightarrow \mu^+\mu^-) = 5.88 \pm 0.10\%$$

and

$$m_{\psi'} = 3686.093 \pm 0.034 \text{ MeV} \qquad Br(\psi' \rightarrow \mu^+\mu^-) = (7.3 \pm 0.8)\cdot 10^{-3}$$

respectively [1].

2.6.2.3 Light meson decays

A final source of muons from quarkonia is given by the decay of light $q\bar{q}$ states (ϕ, ρ^0, ω, η and η' mesons) into muons. All these mesons have masses around or below 1 GeV. This background can thus be easily removed by setting a lower limit on the dimuon mass.

2.6.3 Bethe-Heitler and Drell-Yan events

A source of isolated muon pairs with no restriction on the dimuon invariant mass is given by muon pair production in Bethe-Heitler ($\gamma\gamma$ process, BH) and Drell-Yan ($q\bar{q}$ annihilation, DY) like events. LO Feynman graphs in HERA ep collisions are given in fig. 2.19. The muon Drell-

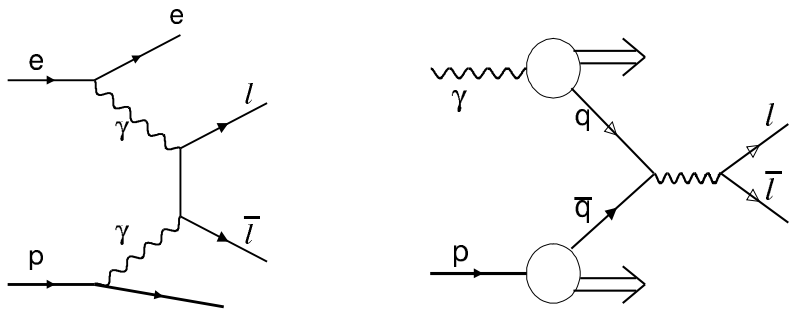

Figure 2.19: Diagrams for Bethe-Heitler and Drell-Yan like muon pair production. *left:* Bethe-Heitler, *right:* Drell-Yan.

Yan process is the electroweak production of a muon pair in the s-channel, where the boson originates from the annihilation of a $q\bar{q}$ pair. This process, having a small cross section in the first place, is strongly suppressed due to the necessity of a resolved photon in the initial state as a source for quarks.

The Bethe-Heitler process, which is a boson-boson fusion in the t-channel, dominates the dimuon production at HERA and was simulated using the generator LPAIR [37, 38].

Again this background contribution can be separated by a muon isolation requirement.

Chapter 3

Beauty production - experimental context

Since the discovery of the beauty quark via the Υ in 1977 [39] beauty production has been studied and a wealth of information was derived in the interplay of theory and experiments. In this section a selection of beauty measurements from the CERN Sp$\bar{\text{p}}$S and LEP, the Tevatron and DESY HERA I are presented and compared to predictions. The conclusions from these measurements set the framework for the work of this thesis. The discussion of the results from a ZEUS beauty analysis using a $D^* + \mu$ tag is of special importance for this analysis. The charm MC normalisation determined in the $D^* + \mu$ measurement was used as an external constraint in this thesis.

3.1 Beauty at the Sp$\bar{\text{p}}$S

The UA1 collaboration presented measurements of inclusive single b quark cross sections as well as of correlations in the $b\bar{b}$ system in $p\bar{p}$ collisions at the CERN Sp$\bar{\text{p}}$S at a centre-of-mass energy of 630 GeV (see [22, 40] and references therein). These results have also been an inspiration for the analysis presented herein. To allow some comparison between the two analyses, the UA1 analysis is presented in more (also technical) detail.

Using a data sample of 4.7 pb^{-1}, reconstructed muons were selected by requiring $p_{\text{T}}^{\mu} > 3$ GeV. This yielded 3846 dimuon events. To separate muons from the same or different parent particles, a cut at $m^{\mu\mu} = 4$ GeV was introduced where required. An isolation criterion depending on event topology was used to separate isolated and nonisolated muon pairs.

Distributions obtained from MC simulations and background calculations were fitted simultaneously to three dimuon distributions:

- the dimuon mass distribution for $2\text{m}^{\mu} < m^{\mu\mu} < 35$ GeV separately for like- and unlike-sign, isolated and nonisolated events,
- the azimuthal distance $\Delta\phi^{\mu\mu}$ between the two muons for $m^{\mu\mu} = 4$ GeV, shown in fig. 3.1 and
- the distance in pseudorapidity-azimuth[1] space between the two muons $\Delta R = \sqrt{\Delta\eta^2 + \Delta\phi^2}$ for the same events as for the $\Delta\phi^{\mu\mu}$ fit, with the additional requirement of $\Delta\phi^{\mu\mu} < 2/3\pi$,

[1] The pseudorapidity η is defined as $\eta = -\ln(\tan\frac{\theta}{2})$.

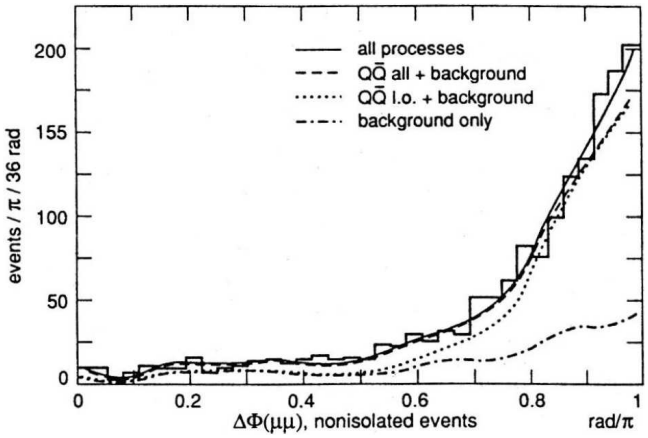

Figure 3.1: UA1: Dimuon azimuthal distance for nonisolated muon pairs ($p_{\mathrm{T}}^{\mu} > 3$ GeV, $m^{\mu\mu} > 4$ GeV) as part of the overall mass and angle fit. The curve 'all processes' includes contributions from Υ, J/ψ, ψ' and low mass mesons as well as Drell-Yan, heavy flavour ($Q\bar{Q} = b\bar{b} + c\bar{c}$, where 'l.o.' refers to the direct only and 'all' to the direct plus resolved contribution) and background contributions [22].

to obtain the following parameters:

- the normalisation of the total heavy flavour ($b\bar{b}$+$c\bar{c}$) and b cascade-decay contributions,
- the fractions of direct gluon-gluon fusion to initial- or final-state gluon splitting in $b\bar{b}$ + $c\bar{c}$ events,
- the $B^0\overline{B^0}$ mixing parameter χ and
- the normalisation of the Drell-Yan, Υ, J/ψ, ψ' and contributions from light mesons.

The $c\bar{c}$ fraction as well as the fractions of $b\bar{b}$ cascade decays were constrained using external measurements where the muon momentum relative to the associated jet, $p_{\mathrm{T}}^{\mathrm{rel}}$, was used to obtain these normalisations. The K, π and other background normalisations were also taken from $p_{\mathrm{T}}^{\mathrm{rel}}$ measurements. The fraction of isolated events was also taken from external constraints.

The resulting single inclusive b quark cross sections are compared to an $\mathcal{O}(\alpha_{\mathrm{s}}^3)$ QCD calculation [41] (similar to FMNR) in figure 3.2. Previous measurements of beauty from J/ψ events are also included. Good agreement is found. From these measurements a total cross section for b quarks was determined in the rapidity range of $|y_{\mathrm{rap}}^b| < 1.5$

$$\sigma_{\mathrm{tot}}(p\bar{p} \to bX,\ |y_{\mathrm{rap}}^b| < 1.5) = 13.0 \pm 2.8_{\mathrm{norm.}}\ {}^{+6.9}_{-4.3}{}_{\mathrm{shape}}\ \mu\mathrm{b} \tag{3.1}$$

which has been extrapolated to the full phase space yielding a total cross section for $b\bar{b}$ pair production at the Sp$\bar{\mathrm{p}}$S of

$$\sigma_{\mathrm{tot}}(p\bar{p} \to b\bar{b}X) = 19.7 \pm 4.3_{\mathrm{norm.}}\ {}^{+10.4}_{-\ 6.5}{}_{\mathrm{shape}}\ \mu\mathrm{b}. \tag{3.2}$$

This was found to be in good agreement with massive NLO QCD predictions of 19^{+10}_{-8} μb using $m_b = 4.5$ GeV.

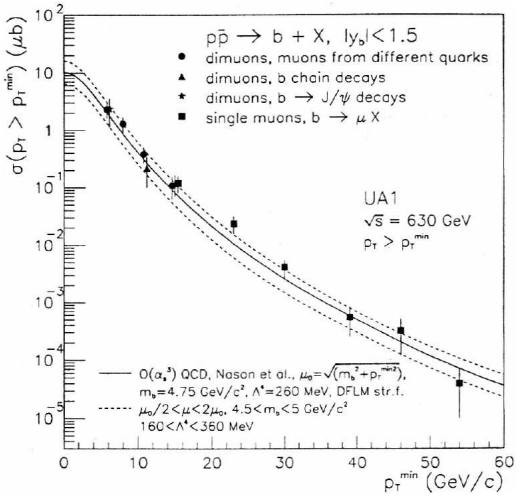

Figure 3.2: Inclusive single beauty quark cross section for $|\eta| < 1.5$ and $p_{\mathrm{T}} > p_{\mathrm{T}}^{\mathrm{min}}$ from UA1 [22]. Presented are the cross section measurements extracted from single muon events and dimuon events originating from different beauty quarks and from beauty chain decays as well as measurements extracted from single muon events originating from J/ψ from beauty quarks and the comparison to a next–to–leading order calculation [41].

Using nonisolated muon pairs only and reducing the data sample by requiring $m^{\mu\mu} > 4$ GeV to eliminate the contributions from quarkonia, $b\bar{b}$ correlation measurements were performed. Here higher order effects (of $30 - 40\%$) could be found with a significance of about seven standard deviations. By making use of the correlation of the highest-p_{T} muon with the highest-p_{T} b quark, angular-correlation cross sections were obtained, as shown in fig. 3.3. Good agreement

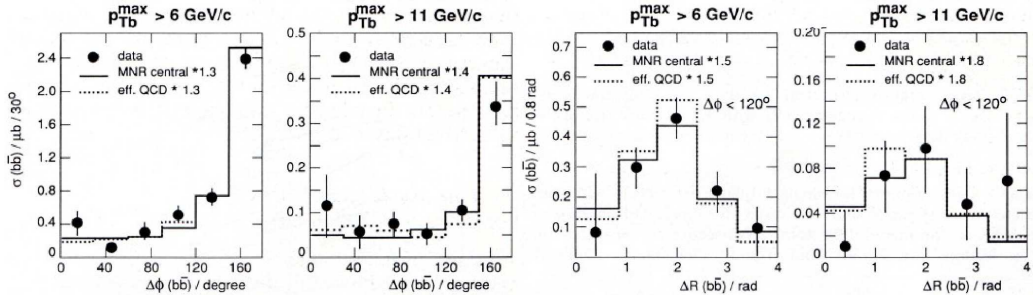

Figure 3.3: Beauty quark correlations from dimuon events in $\Delta \mathrm{R}^{b\bar{b}}$ and $\Delta\phi^{b\bar{b}}$ in two different ranges of transverse momentum of the beauty quarks $p_{Tb}^{max} > 6(11)$GeV [22] compared to a NLO calculation.

in shape and also, within the (large) errors, in normalisation was found in comparison with NLO predictions. This can be interpreted as a successful test of the corresponding QCD matrix elements.

3.2 Beauty at LEP

Measurements of the open beauty production in photon-photon collisions at LEP were carried out by the OPAL, DELPHI and L3 collaborations with compatible results [42]. As an example, a recent measurement by L3 [42] is shown here. In photon-photon collisions the direct and resolved contributions are expected to contribute with comparable rates. The resolved contribution is of special interest as it depends on the gluon distribution in the photon.

The measurement was based on an integrated luminosity of 627 pb^{-1} recorded at e^+e^- centre-of-mass energies from 189 to 209 GeV. Events were selected from a sample of events with low photon virtuality of $\langle Q^2 \rangle \simeq 0.015$ GeV^2 by first selecting a sample of hadronic events. This sample was then enriched in beauty events by the requirement of reconstructed semileptonic electrons or muons. Hadronic events were selected by requiring at least five tracks, a visible energy of $E_{\rm vis} < \frac{1}{3}\sqrt{s}$ and a visible mass of $W_{\rm vis} > 3$ GeV. Electrons or muons were required to have momenta larger than 2 GeV and to lie in the the polar range of $|\cos\theta^e| < 0.725$ and $|\cos\theta^\mu| < 0.8$ respectively. The distribution of the lepton momentum with respect to the closest jet, $p_{\rm T}^{\rm rel}$, was used to extract the beauty contribution. Combining the electron and muon visible cross sections, the total cross section for open-beauty production in photon-photon collisions at a luminosity weighted average centre-of-mass energy of $\langle s \rangle = 198$ GeV was determined to

$$\sigma(e^+e^- \to e^+e^- b\bar{b}X)^{\rm total} = 12.8 \pm 1.7 \pm 2.3 \text{ pb}.$$

In fig. 3.4 this cross section is compared to a NLO QCD prediction. Measurements by L3 of

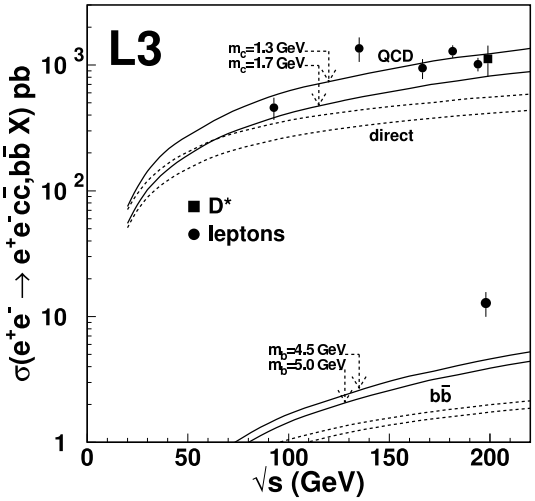

Figure 3.4: The open-charm, upper, and open-beauty, lower, production cross section in photon-photon collisions measured with the L3 detector. The dashed lines correspond to the direct-process contribution and the solid lines represent the NLO QCD prediction for the sum of the direct and single-resolved (only one of the two photons is resolved) processes.

charm production are also shown. The beauty measurement was found to be a factor of three, and three standard deviations, higher than expected.

3.3 Beauty at the Tevatron

The CDF and D0 collaborations presented several comparisons of beauty data in $p\bar{p}$ collisions at a centre-of-mass energy of 1.8 to 1.96 TeV with NLO predictions. As a general trend, the measurements lay above the NLO predictions. An example measurement of beauty from muon events [43] is shown in fig. 3.5. Over the last years this long standing difference has been

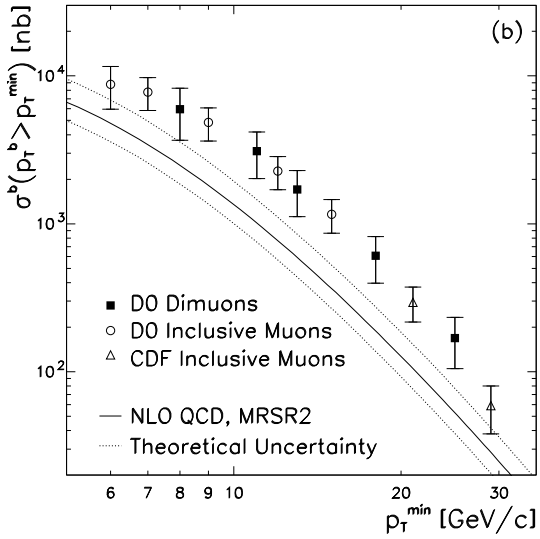

Figure 3.5: Beauty quark cross section from D0 and CDF as a function of p_{T}^b compared to a NLO QCD calculation [43].

reduced [44] by both more refined theoretical and experimental methods.

Improvements on the experimental side include the use of b-jets and B-hadrons rather than extrapolating to b-quarks. The theoretical description was improved by e.g. the introduction of the so called *fixed order and next to leading log* (FONLL) scheme [45] resumming higher terms of $\log(p_{\mathrm{T}}/m)$ of the heavy open quarks and the use of improved fragmentation and parton distributions functions.

A recent measurement by CDF based on 39.7 pb^{-1} using J/ψ's from b-quarks as a tag for beauty events is shown here [46]. The J/ψ was reconstructed in the muonic decay channel using central muons with $|y^{\mu}_{\mathrm{rap}}| < 0.6$ and with transverse momenta of $p^{\mu}_{\mathrm{T}} > 1.5$ GeV. To separate prompt J/ψs from beauty-induced events, a lifetime criterion was used, as shown in fig. 3.6a for muons in the dimuon p_{T} range of 1.25 GeV $< p^{\mu\mu}_{\mathrm{T}} <$ 1.5 GeV. This variable is called *pseudo proper decay time, x* and is defined as:

$$x = L_{xy} \times (M^{J/\psi}/p_{\mathrm{T}}^{J/\psi}) \tag{3.3}$$

where L_{xy} is projection of the vector connecting the event vertex with the displaced J/ψ decay vertex in the tranverse plane onto the transverse momentum direction of the J/ψ. This definition reduces the momentum dependence of the lifetime measurement. Using an unbinned maximum likelihood fit, the beauty fraction was extracted as a function of $p_{\mathrm{T}}^{J/\psi}$. It varies from 10% in the low $p_{\mathrm{T}}^{J/\psi}$ region up to 45% at high $p_{\mathrm{T}}^{J/\psi}$.

The resulting single beauty-hadron ($\mathrm{H_b}$) cross section is shown in fig. 3.6b. Very good agreement in both shape and normalisation with the FONLL prediction is found over a large range of $p_{\mathrm{T}}^{\mathrm{H_b}}$.

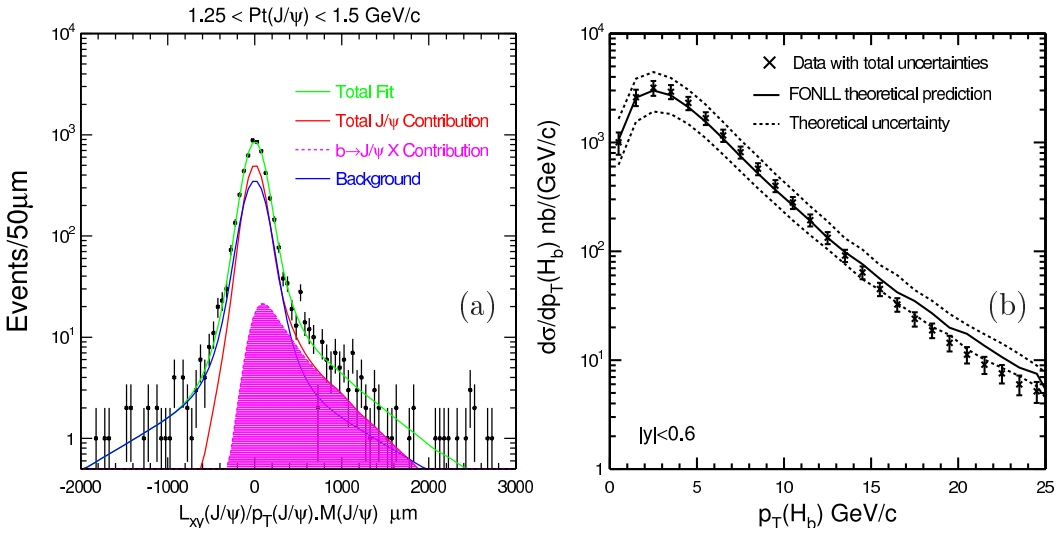

Figure 3.6: Determination of the differential beauty hadron cross section in $p_{\mathrm{T}}^{\mathrm{H_b}}$ in $p\bar{p}$ collisions at 1.96 TeV. (a) The pseudo proper lifetime distribution for the dimuon p_{T} range of 1.25 GeV $< p_{\mathrm{T}}^{\mu\mu} <$ 1.5 GeV. The breakdown in the contributing processes is fitted to the data. (b) The resulting B-hadron cross section. The FONLL prediction is also shown.

By the use of improved methods on both the experimental and the theoretical side, better agreement of the QCD calculations with the data was achieved.

3.4 Beauty at H1 and ZEUS

Recent measurements of beauty production in electron proton collisions at HERA are presented. The results are obtained using data from the collider experiments H1 and ZEUS from the years 1996 to 2000 (HERA I). The following measurements are shown and compared to QCD predictions:

- differential measurements using muons and jets,
- the beauty contribution to the proton structure function F_2 for large Q^2 ($Q^2 > 150$ GeV^2) and
- differential measurements using a $D^* + \mu$ tag.

3.4.1 Measurements in μ+jet(s)

In events with a jet and a muon, two properties of the b hadrons were exploited to tag beauty events: the large b mass and the lifetime. The b mass leads to a relatively large transverse momentum of the muon relative to the closest jet, p_T^{rel}. The long lifetime of the b was used by measuring the distance of closest approach in the transverse plane, δ, of the muon track to the beam spot or main vertex. A sign was added to δ, which is positive if the muon track crosses the jet axis downstream of the beam spot, else it is negative.

3.4.1.1 Beauty in γp in μ+jets

H1 has measured differential cross sections in events with a muon and 2 jets in the photoproduction regime for $Q^2 < 1$ GeV^2 using an integrated luminosity of 50 pb^{-1} [47]. To tag beauty events a simultaneous fit to both the p_T^{rel} and the signed δ distribution was performed. The cross sections obtained are given in fig. 3.7. ZEUS performed a similar measurement [48, 49] relying on p_T^{rel}, but in a wider muon eta range of $|\eta^\mu| < 2.5$.
Differential cross sections in p_T^μ and η^μ are shown in fig. 3.7 together with the massive NLO QCD prediction (FMNR), which has been corrected, using LO+PS MC simulations, to describe the measured hadron-level properties. Reasonable agreement of the NLO prediction with data is observed. The data are a bit steeper in p_T^μ in the H1 measurement, see fig. 3.7a. H1 and ZEUS agree within errors, as shown in fig. 3.7a and b. It would thus be interesting to extend

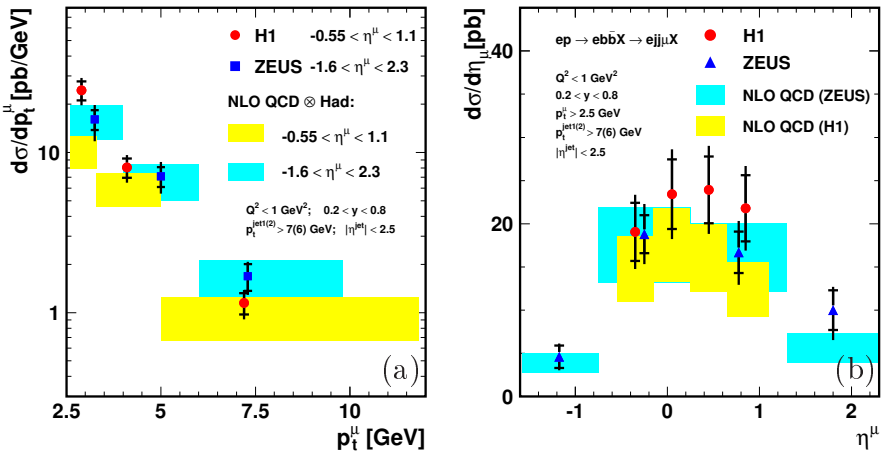

Figure 3.7: Differential cross sections in (a) p_T^μ and (b) η^μ of muons from beauty events in γp with NLO predictions as measured by H1 [47] and ZEUS [48, 49].

beauty measurements to the difficult low p_{T}^μ regime. To access this region of phase space is one of the aims of this thesis.

3.4.1.2 Beauty in DIS in μ+jet

Beauty cross sections were also measured for $Q^2 > 1$ GeV^2 using the same techniques as described above. H1 has used a Q^2 range of $2 < Q^2 < 100$ GeV^2 [47]. The H1 cross sections were obtained for events with

- $p_T^\mu > 2.5$ GeV, $\quad -0.75 < \eta^\mu < 1.15$,
- $0.1 < y < 0.7$,
- $p_{T\ \mathrm{jet}}^{\mathrm{Breit}} > 6$ GeV and $|\eta_{\mathrm{jet}}^{\mathrm{lab}}| < 2.5$

where the index 'Breit' refers to the Breit frame. The η^μ cross section is shown in fig. 3.8a. ZEUS has performed a similar measurement in DIS [50] (fig. 3.8b) using data in the Q^2 range of $1 < Q^2 < 1000$ GeV^2 and defining the kinematic range as

- $p_T^\mu > 2.0$ GeV, $\quad -1.6 < \eta^\mu < 1.3$,
- $0.05 < y < 0.7$,
- $E_{T\ \mathrm{jet}}^{\mathrm{Breit}} > 6$ GeV $\quad$ and $\quad -2.0 < \eta_{\mathrm{jet}}^{\mathrm{lab}} < 2.5$

The p_T^μ spectrum from both H1 and ZEUS is slightly steeper than the prediction (not shown). An interesting feature is seen in the η^μ distribution in fig. 3.8: for both H1 and ZEUS (kinematic ranges differ) the cross section rises towards higher η^μ, a trend that is not well reproduced by the NLO predictions. Also here an extension of the muon phase space to more forward direction

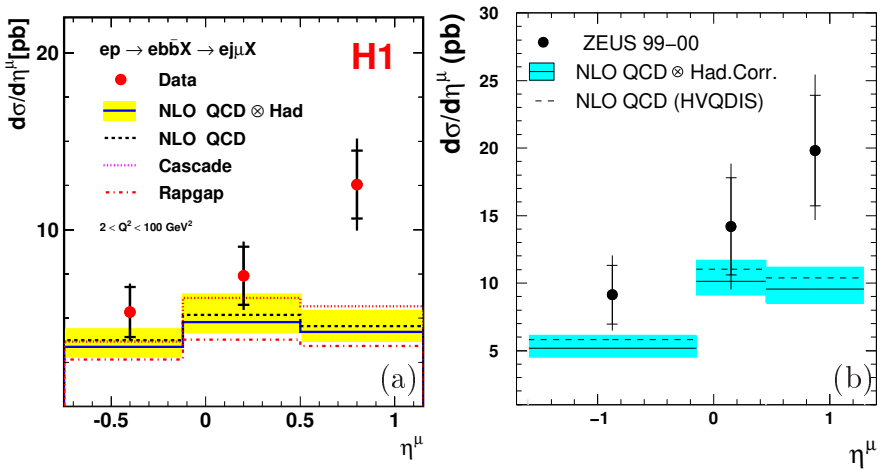

Figure 3.8: The η^μ cross section of muons from beauty events in DIS as measured by (a) H1 and (b) ZEUS [50].

might help to clarify the differences that were found. This is also a goal of this thesis.

3.4.2 Inclusive measurements using impact parameters

Events with heavy-flavour mesons can contain several tracks with large impact parameters. To inclusively determine the beauty contribution, events were selected in an H1 analysis by inclusive lifetime tagging, using all $p_T > 0.5$ GeV tracks with reasonable precision vertex tracker information [51]. For these tracks the impact parameter significance $S_{1(2)} = \delta_{1(2)}/\sigma_{\delta_{1(2)}}$ was calculated for the track with the largest (second largest) impact parameter δ (with $|\delta| < 0.1$ cm). The sign of the impact parameter was chosen relative to the direction of the closest jet if present or from the hadronic final state, also requiring $sign(S_1) = sign(S_2)$. This method yields high statistics and a good separation of beauty from charm and light-flavour processes.

3.4.2.1 Beauty contribution to F_2

To determine the beauty contribution to the proton structure function, double differential beauty cross sections in bins of x and Q^2 were measured using inclusive lifetime tagging. The resulting $F_2^{b\bar{b}}$ is shown in fig. 3.9. Good agreement with both the H1 PDF 2000 fit [52] and MRST03 [53] was found. The integrated beauty cross section for $Q^2 > 150$ GeV^2 and $0.1 <$

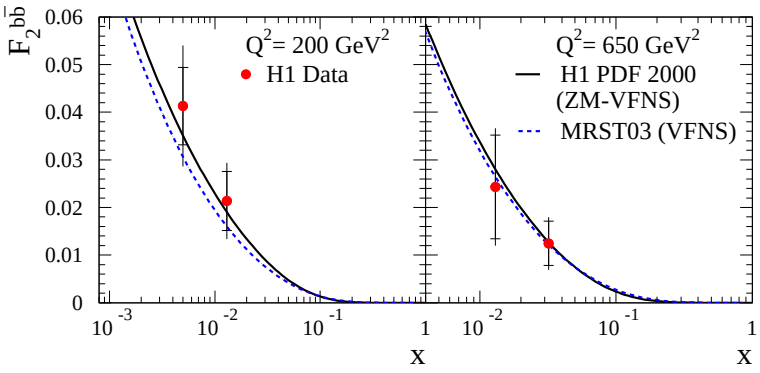

Figure 3.9: The beauty contribution to the proton structure function F_2 in bins of x and Q^2 as measured by the H1 collaboration [51]. The H1 PDF 2000 fit and the MRST03 fit are compared with the measurement.

$y < 0.7$ has been determined to be $\sigma^{b\bar{b}} = 55.4 \pm 8.7 \pm 12$ pb. This is compatible with several predictions: H1 PDF 2000 (massless, ZM-VFNS) $\sigma^{b\bar{b}} = 52$ pb, NLO (massive⊗massless, VFNS) $\sigma^{b\bar{b}} = 47$ pb, and NLO (massive, FFNS) $\sigma^{b\bar{b}} = 37$ pb.

This measurement was recently extended to the lower Q^2 range of $12 \leq Q^2 \leq 60$ GeV^2 and $0.0002 \leq x \leq 0.005$ [54]. Also here agreement with QCD predictions was found.

Comparing the data with the different theoretical approaches, no clear distinction of the methods can be made as agreement within the errors is found with all predictions.

3.4.3 Beauty and charm from $D^* + \mu$ events

Events with a muon and a D^* meson provide another clear signature for heavy-quark production. This signature was exploited in an analysis performed by ZEUS based on 1996 to 2000 HERA I data of 114 ± 2 pb^{-1} [55]. H1 has performed a similar measurement [56]. As this signature provides very low background, one can reduce the transverse momentum cuts on the muons yielding sensitivity to b-quark production near the kinematic threshold reaching down to $p_{\mathrm{T}}^b = 0$ GeV. The $D^* + \mu$ analysis is particularly interesting in the context of the dimuon analysis presented in this thesis as the kinematic ranges covered by the two analyses are very similar.

To separate beauty from charm induced events, charge, mass and angular correlations are exploited. There are several classes of events:

- Muon and D^* from the same B meson: results in unlike sign $D^* + \mu$ pair in the same detector hemisphere, with the additional constraint that the invariant mass of the pair must be below the B meson mass.
- Muon and D^* from direct charm production: leads again to an unlike sign pair, but now the muon and the D^* are predominantly in different hemispheres.
- Muons and D^* from different B-mesons: leads to both unlike and like sign pairs, depending on whether the muon comes from the prompt B decay or from a cascade charm quark

or whether $B^0\overline{B^0}$ mixing has occurred. Beauty production is the only source of genuine like-sign $D^* + \mu$ pairs.

- Combinatorial background: no sizable charge correlations or mass restrictions.

Muons with a p_T cut of $p_T^\mu > 1.4$ GeV in an η range of $-1.75 < \eta^\mu < 1.3$ were selected. The D^* was reconstructed in the 'golden decay channel' with $p_T^{D^*} > 1.9$ GeV and $|\eta^{D^*}| < 1.5$.

Figure 3.10 shows the D^* candidate-mass distributions separated by sign, mass and angle restrictions. Beauty-induced events dominate the region restricted to $\Delta R < 2$ and $3 < M(D^* + \mu) < 5$ (see fig. 3.10a), whereas charm events are concentrated in the region $\Delta R > 2$ with no $M(D^* + \mu)$ cut (see fig. 3.10b).

Beauty dominates the sample where both the muon and the D^* come from the same beauty quark. Thus a cross section for single b or $\bar{b}$ production in photoproduction was extracted using PYTHIA to extrapolate to the unmeasured phase space. The result is given for a beauty rapidity of $y^b_{\text{rap}} < 1$ and $Q^2 < 1$ GeV^2 as well as an inelasticity of $0.05 < y < 0.85$ using a b-quark mass of 4.75 GeV:

$$\sigma(ep \to b(\bar{b})X) = 15.1 \pm 3.9 \text{ stat.}^{+3.8}_{-4.7} \text{ syst. nb} \tag{3.4}$$

This was compared to the FMNR prediction in the same kinematic range of

$$\sigma_{\text{NLO}}(ep \to b(\bar{b})X) = 5.0^{+1.7}_{-1.1} \text{ nb} \tag{3.5}$$

with $\mu = \mu_f = \mu_0 = \sqrt{m_b^2 + p_T^{b2}}$ and $m_b = 4.75$ GeV, where the theoretical error was obtained by simultaneously varying the above parameters in the range $\mu_0/2 < \mu < 2\mu_0$ and 4.5 GeV $< m_b <$ 5 GeV. The NLO calculation is thus lower than the measured cross section. As the $D^* + \mu$ cross section is dominated by the low and medium p_T regime, this result is in agreement with the slight excess observed at lower p_T in the jet+μ measurements.

3.5 Conclusion

NLO QCD predictions are found to generally agree with the data. At the Tevatron the good agreement was obtained only after making use of both improved theoretical and experimental methods. LEP measurements show the largest excess of about 3σ with respect to the NLO QCD predictions. In measurements performed at HERA, the predictions are somewhat below the data in some kinematic regions, especially at low p_T and higher η. It is thus interesting to extend HERA measurements further into these regions of phase space.

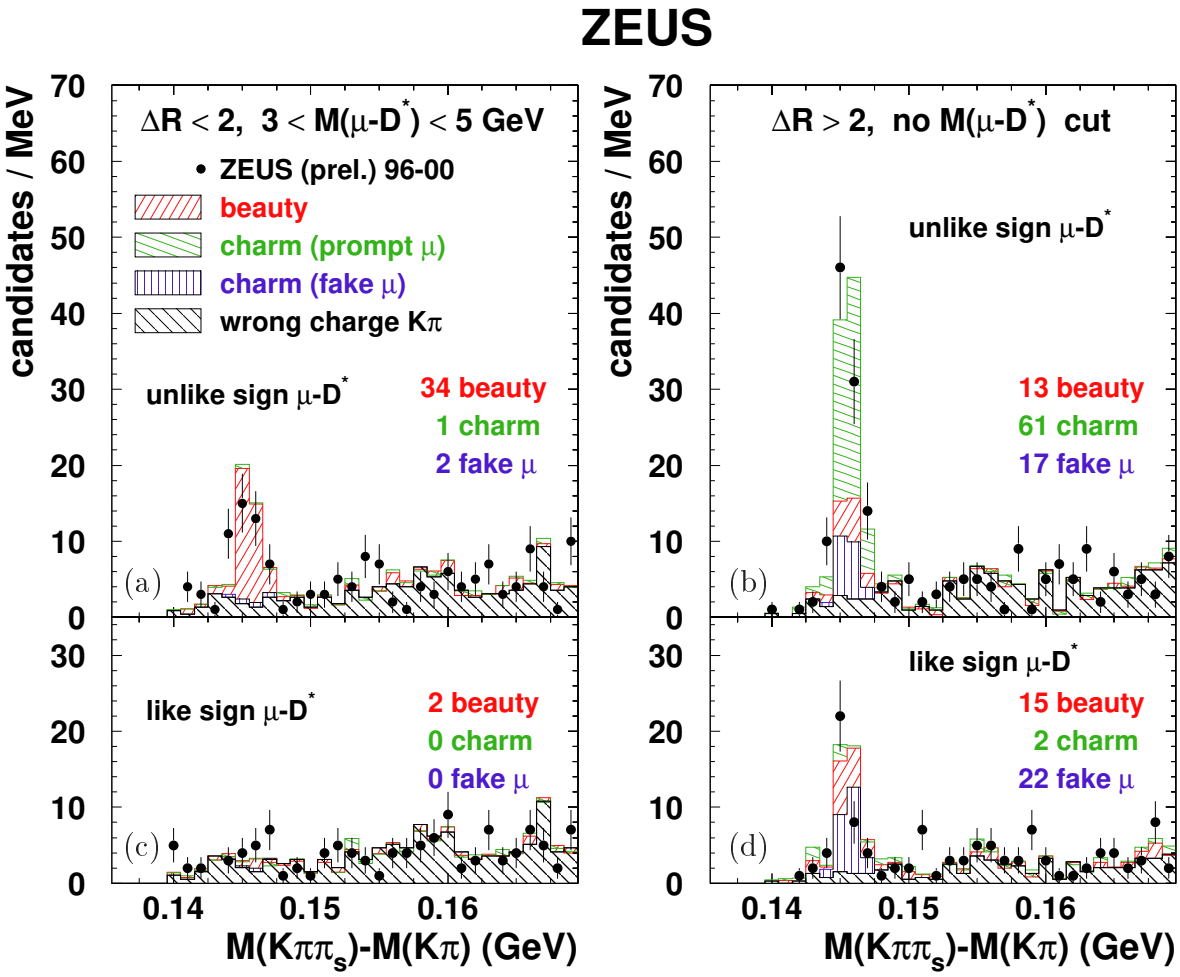

Figure 3.10: D^* candidate mass distributions for selected $D^* + \mu$ events in bins of charge combinations of the muon and the D^* as measured by the ZEUS collaboration [55]. The distributions have also been separated depending on the event topology, i.e. depending on the angular distance of the muon to the D^* candidate. Events in which the muon is within a cone of $\Delta R^{\mu - D^*} < 2$ of the D^* and an additional kinematic restriction of $3 < M(\mu - D^*) < 5$ GeV to select decays of beauty quarks are shown in (a) and (c). The histograms (b) and (d) show events with a large angular distance of $\Delta R^{\mu - D^*} > 2$ between the muon and the D^*. In (a) and (b) events containing a D^* and muon of opposite charge are shown, in (c) and (d) events with the same charges. The breakdown into the expected contributions from different processes is also shown.

Chapter 4

HERA & reduction of backgrounds at HERA II

The HERA (Hadron Elektron Ring Anlage) [57] electron (positron[1]) proton collider with a circumference of 6.3 km about 20 meters below the ground is part of the DESY laboratory in Hamburg, Germany (fig. 4.1 and 4.2). Electrons at an energy of 27.5 GeV are brought into

Figure 4.1: Aerial photo of the DESY laboratory. The HERA collider and the pre-accelerator PETRA are marked by dashed lines.

collision with protons at 920 GeV yielding a centre of mass energy of 318 GeV. Collisions are recorded by 4 (3 since 2003) detectors, shown in fig. 4.2. In the north hall at H1 and in the south hall at ZEUS, the electron and proton beam are brought into collision. HERA-B (up to

[1]The leptons will always be referred to as electrons, except for places where distinction is needed.

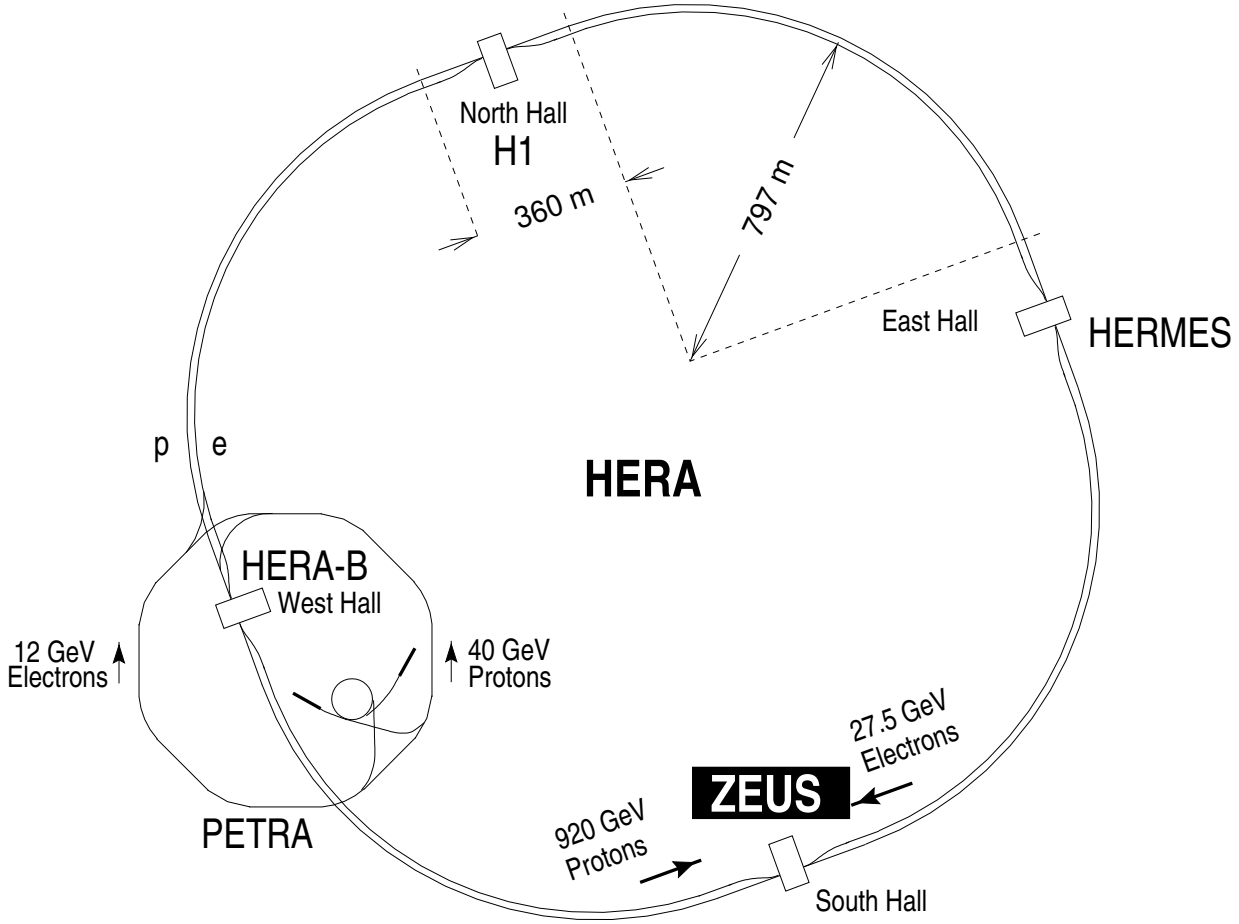

Figure 4.2: The electron proton storage ring HERA. Experiments are situated at each straight section. While the H1 and ZEUS detectors make use of both particle beams, the HERMES and HERA-B detectors use only the electron and the proton beam respectively. The pre-accelerators are sketched in the lower left corner.

2003, West Hall) and HERMES (since 1995, East Hall) are fixed target experiments and make use of only one beam. HERA-B measured collisions of the protons with a wire target and was designed to study $\mathcal{CP}$ violation in the $B^0\overline{B^0}$ system. At HERMES the electron beam, being longitudinally polarised here (see below), is sent onto a polarised or unpolarised gas jet target. The study of the spin structure of the proton is HERMES' main aim.

The electron and proton beams are accelerated and stored in separate accelerator rings. The electron beam is injected at an energy of 12 GeV from the last segment of the pre-accelerator chain PETRA. It is then accelerated inside HERA to the full energy of 27.5 GeV by a system of both normal and superconducting cavities. The protons are injected similarly and accelerated from the injection energy of 40 GeV to 920 GeV by two normal conducting acceleration systems.

Typical magnetic fields of electron bending dipoles are 0.3 T, whereas the protons are bent by fields of $\sim$5 T. The bending radius in the long arcs between the interaction points (IPs) is 797 m, which is exceeded only close to the IPs when the beams are bent stronger to collide head on.

If the electron beam is not disturbed it becomes transversally polarised by the emission of

synchrotron radiation. Special arrangements of several long dipole magnets (so called *spin rotators*) are used to turn the electron polarisation vector yielding local longitudinal polarisation. The polarisation is used at the HERMES IP (and from 2001 onwards also at H1 and ZEUS).

From 1992 to 1998 the machine was operated at beam energies of $E_e = 27.5$ GeV and $E_p = 820$ GeV giving an *ep* centre-of-mass energy of 300 GeV. From 1998 to 2000 an *ep* centre-of-mass energy of 318 GeV was realised by rising the proton energy to 920 GeV. Electrons were used during the years 1997 and 98 as well as in the year 2005, positrons in the remaining periods. The delivered luminosity in these configurations is shown in fig. 4.3.

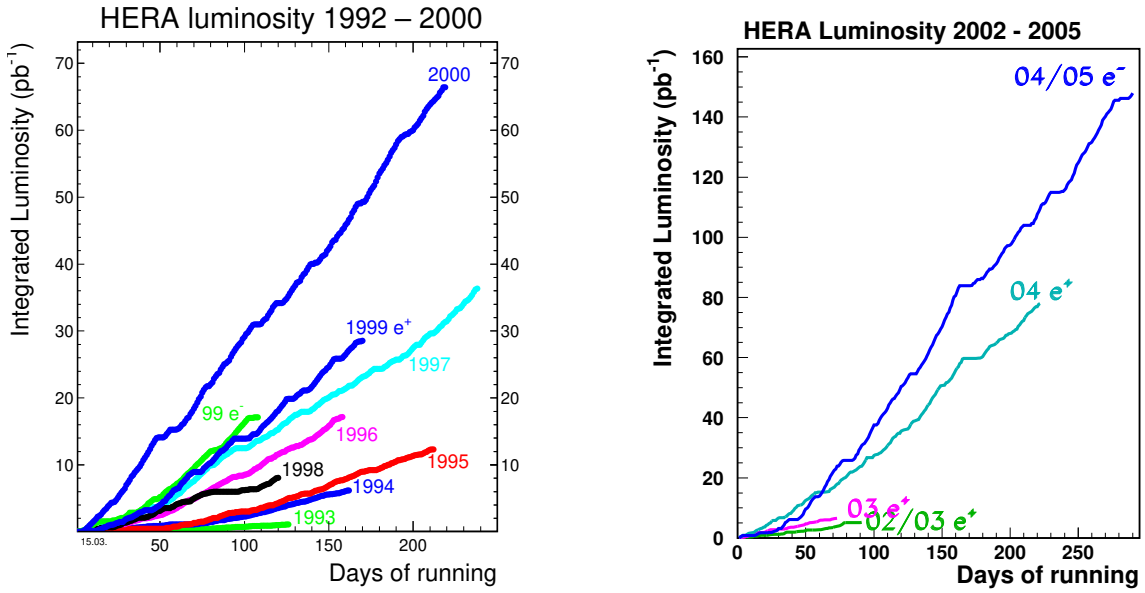

Figure 4.3: Integrated luminosity delivered by HERA for the running periods 1993-2000 (left) and 2002-2005 (right).

4.1 HERA luminosity upgrade (HERA II)

Having succeeded to measure many essential physical properties of *ep* collisions it was decided to upgrade the HERA collider with the aim to widen the reach for research at HERA especially in the context of heavy flavour physics, high Q^2 events and exotic phenomena. In 2000/2001 the collider and also the experiments were thus upgraded to achieve roughly a factor five higher specific luminosity and by the increased data sample and new detector components also higher precision measurements. The HERA upgrade is described in detail in HERA upgrade reports [58, 59]. The main machine parameters before and after the upgrade are summarised in tab. 4.1.

The HERA magnet lattice was mainly modified at a length of about 100 meters left and right of the experiments H1 and ZEUS. The changes yielded a separation of the two beams closer to the IPs yielding the possibility of a stronger focus at the IPs. At the same time spin rotators were

HERA parameters

Type	HERA I design [60]		typical in 2000 [61]		HERA II design [58, 61]	
Luminosity	$1.5{\cdot}10^{31}$ cm^{-1}s^{-1}		$1.7{\cdot}10^{31}$ cm^{-1}s^{-1}		$7.0{\cdot}10^{31}$ cm^{-1}s^{-1}	
Centre-of-mass energy	300 GeV		318 GeV		318 GeV	
	Lepton	Proton	Lepton	Proton	Lepton	Proton
Energy	30.0 GeV	820 GeV	27.5 GeV	920 GeV	27.5 GeV	920 GeV
Nr. colliding Bunches	210	210	180	180	180	180
Beam current	58	160	45	100	58	140
Particles per bunch	$3.6{\cdot}10^{10}$	10^{11}	$3.5{\cdot}10^{10}$	$7.3{\cdot}10^{10}$	$4.0{\cdot}10^{10}$	10^{11}
Beam width (σ_x)	247 μm	247 mm	190 μm	190 μm	118 μm	118 μm
Beam height(σ_y)	78 μm	78 mm	50 μm	50 μm	32 μm	32 μm

Table 4.1: HERA parameters.

installed also for H1 and ZEUS. About ±60 meters were completely rebuilt. To gain a very small beam size at the IP and thus higher luminosity, the beams are now focused much closer to the IP. The start of the proton beam focus quadrupoles has been moved from 27 m from the IP to 11 m. For this purpose, two new types of magnets had to be developed: A special mirror-plate proton quadrupole and a very thin superconducting multipurpose electron magnet. The special mirror plate quadrupole is shown in fig. 4.4. Note the triangular hole in the centre of

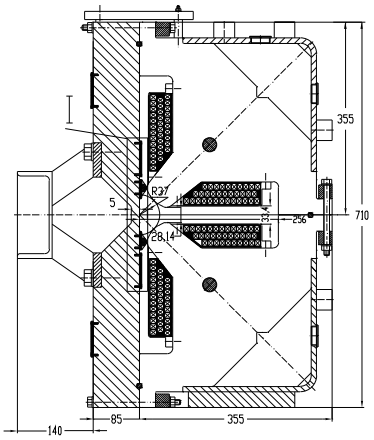

Figure 4.4: *xy* cut through a mirror quadrupole. The electron beam pipe passes through the triangular shaped hole on the left, while the protons are focused by the quadrupole on the right side [59]. The thickness of the remaining mirror plate at the triangular hole defined the width of a synchrotron radiation absorber (Absorber 4, shown in fig. 4.16).

the mirror plate. This hole was necessary, as at the magnet position, the electrons are already so close to the protons, that a usual quadrupole would not fit. The electron beam-pipe passes in the triangular hole on the outer side of the mirror plate. At this place the quadrupole field is already weak enough not to disturb the electron orbit.

The multipurpose superconducting electron magnets GG and GO are used to both strongly focus and bend the electron beam only 1.5 m away from the IPs, thus already in the strongly restricted space inside the detectors.

A sketch of the horizontal electron magnet lattice in the vicinity of H1 and ZEUS with the resulting electron and proton beam orbit of the machine after the upgrade is shown in fig. 4.5[2]. Electrons pass from the left to the right through the detector. At -92 m (see also fig. 4.10) the

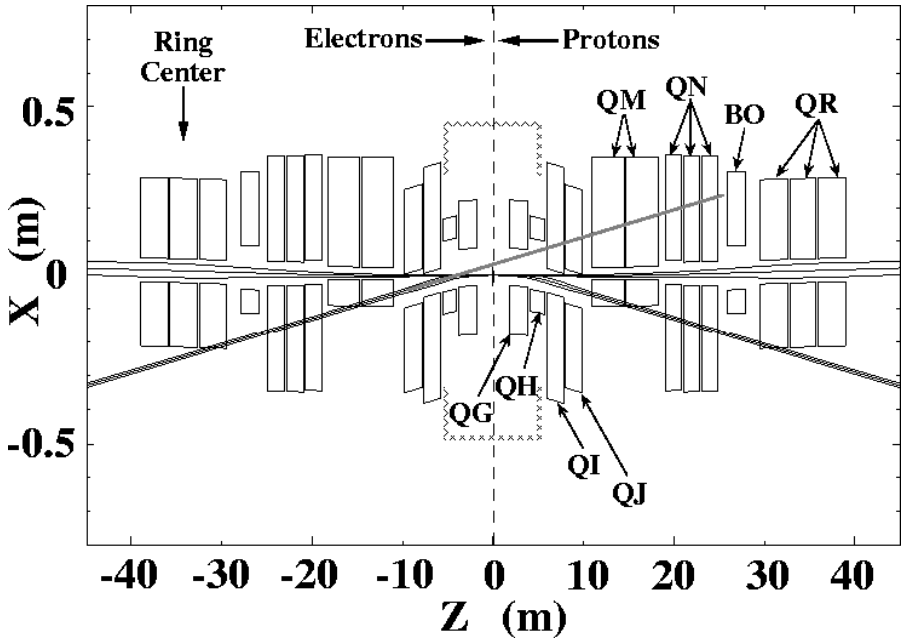

Figure 4.5: The HERA II interaction region at H1 and ZEUS. The proton beam passes straight through the centre of the image, while the electron beam is bent from $x_{\text{HERA}} \approx -30$ cm at $z_{\text{HERA}} \approx -40$ m towards the proton beam at $x_{\text{HERA}} \approx 0$ cm at $z_{\text{HERA}} \approx 0$ m. All magnets, depicted by the boxes in this figure, were newly build for the HERA upgrade (from [59]).

electron beam is bent towards the IP, passes two chicanes to reduce off-momentum electrons and collimate synchrotron radiation and is finally bent at about -3 m to collide head on with the protons.

4.2 Suppression of backgrounds at HERA II

Higher beam induced backgrounds after the upgrade initially delayed the data taking - how they were overcome is described in this section. Here special emphasis was put on the synchrotron radiation induced backgrounds, as the reduction of these was part of this work.

The design of the upgraded interaction zones proved to be challenging concerning the suppression of synchrotron radiation backgrounds. Before the upgrade already 50% of the radiation power could be collimated before it reached the detector. After the upgrade though, the sources of synchrotron radiation where both closer to the detector and due to the stronger focusing also much more powerful. As collimation in front of the detectors was not feasible, the radiation fan had to be led through the detectors and absorbed after the passage. Many new collimators

[2]By default, coordinates are given in the ZEUS coordinate system defined in fig. A.1 (appendix). If labelled x_{HERA}, they are given in a HERA coordinate system, also defined in fig. A.1.

and a specially shaped beam pipe were constructed for this purpose. The synchrotron-radiation collimation system inside the ZEUS detector after the upgrade is shown in fig. 4.6.

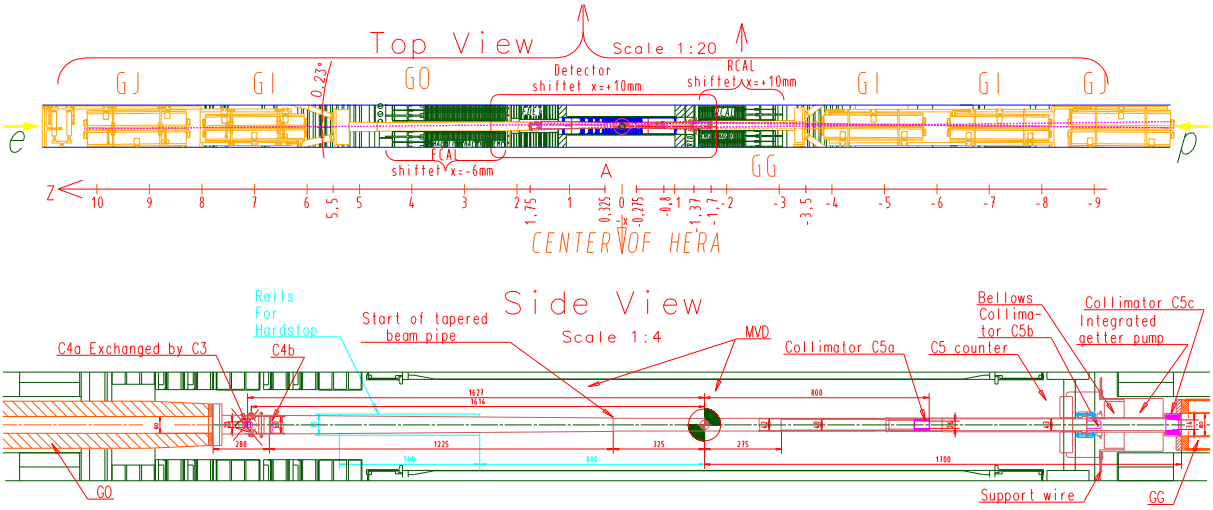

Figure 4.6: The central synchrotron-radiation collimation system after the upgrade. The collimator C5A at $z = -0.8$ m, the C5B at $z = -1.4$ m and the C5C at $z = -1.7$ m are designed to shield the central detector components from back scattered synchrotron radiation. Additional collimators placed at $z = -3.6$ m (Abs1), $z = -5.7$ m (Abs2) and $z = -8.3$ m (Abs3) shield the beam pipes against direct synchrotron radiation. The central beam pipe splits into 3 separate beam pipes (proton, electron and photon pipe) at the position of the final absorber at $z = -11$ m (Abs4).

Still, the startup of HERA II after the upgrade construction phase was accompanied by unexpected high backgrounds at the experiments essentially disabling data taking. In a joined effort of HERA, H1, HERMES and ZEUS these backgrounds were studied and measures to reduce them established.

Several early machine experiments clarified that, at low beam-currents (below 50% of the design currents), the background in the experiments was dominated by synchrotron radiation. The dominant source, a direct line of sight from a bending magnet 92 meters away from the interaction regions (BI92) was quickly removed by inserting an additional collimator at $z_{\text{HERA}} = -66$ m which absorbed that part of the BI92 synchrotron radiation fan, which hit the collimators directly inside the tracking chambers and led to very high standing currents. The synchrotron-radiation fan from the pre-upgrade magnet BI92 could not reach the experiments before the upgrade - only the upgraded beam line permitted parts of the fan to propagate up to the detectors.

This section summarises findings and solutions concerning the influence of electron beam synchrotron radiation as well as shortly summarises findings concerning further electron and proton beam related backgrounds. The vast amount of studies performed by the HERA background task forces is summarised in reports on backgrounds by HERA [62], H1 [63, 64] and ZEUS [65, 66, 67].

4.2.1 Disentangling the background components

To determine the contribution of the different background production mechanisms to the main limiting factor - the tracking chamber currents, numerous relations of the synchrotron radiation and particle backgrounds with beam currents, timing as well as tagger and trigger rates were exploited.

The backgrounds depend on a very large parameter space, including the HERA beam quality and beam steering influenced not only by the quality of the pre accelerators but also by possible minimal movements of magnets and other changes of the accelerator like the vacuum quality, the level of experience of the shift crews involved and many more. Thus the determination of the separate contributions was a long and difficult task relying on a large set of indications, which cannot be described fully here. Here only the main input gained from the dependence of the backgrounds on the beam currents will be described, some other methods will only briefly be mentioned.

The knowledge about the separate contributions on the beam currents was essential, to be able to extrapolate from low test particle currents to the full design currents of HERA II and determine, whether the backgrounds could be suppressed sufficiently to be able to run the detectors at full beam currents.

The background induced large drift chamber currents were found to be due to three main components:

- Doubly scattered synchrotron radiation
- electron beam gas scattering and
- proton beam gas scattering.

Synchrotron radiation preamble Throughout these chapters basic knowledge is assumed concerning synchrotron radiation properties. Some very brief definitions are given here. Further explanations can be found in [68, 69].

- **Origin of synchrotron radiation**: Accelerated charged particles are the source of electro-magnetic dipole fields. When an electron beam is bent by a dipole magnet, it is accelerated to pass along a circular path, thus emitting a dipole field in its rest frame. The Lorentz boost of the electron rest system relative to the laboratory system then leads to the typical shape of the the synchrotron radiation light, being emitted in a strongly collimated cone in the electron direction of movement with an opening angle of approximately $\Delta\theta^{SR-fan} = 1/\gamma$, with γ being the Lorentz factor of the electron beam.
- **Critical energy**: The critical energy E_{crit} of synchrotron radiation energy spectra is used to characterise the spectra. It splits the synchrotron-radiation spectrum into two parts of equal radiation power.
- **Bending radius dependence of E_{crit}**:

$$E_{\text{crit}} = \frac{3\hbar c\gamma^3}{2R} \tag{4.1}$$

- **Beam energy dependence of the synchrotron radiation power P_s:**

$$P_s = \frac{e^2 c}{6\pi\epsilon_0} \frac{1}{(m_0 c^2)^4} \frac{E^4}{R^2} \tag{4.2}$$

with E the beam energy and $v_e = c$

4.2.1.1 Synchrotron radiation contribution

To determine the synchrotron radiation contribution to the total central tracking detector (CTD, see sec. 5.1) background current, an electron beam with isolated bunches (to be able to study the timing of synchrotron radiation from single bunches) was accelerated and the CTD current as well as hit patterns and hit timing were recorded. Also beams with different currents were compared.

Following eq. 4.2, the synchrotron radiation power emitted by an electron beam with the energy E in a circular accelerator rises proportionally to E^4. The synchrotron-radiation intensity at a fixed beam energy rises linear with the current I_e. If some fraction of the synchrotron radiation is backscattered from a surface downstream of the detector before it enters the tracking chambers, it leads to hits that arrive delayed relative to the passage of the beam. Example measurements of the beam energy dependence are shown in fig. 4.7 and of the single bunch timing in fig. 4.8. The study of the energy dependence was however partially compromised by changes in the electron orbit at different energies, leading to additional backgrounds. Still, the spacial distribution of hits clearly indicates the development of a bump in the rear part of the CTD. This hints towards photons entering the CTD after scattering from the C5A collimator located in this vicinity. The main part of this background led to delayed hits in the CTD, as is shown in fig. 4.8. The only background type that can lead to delayed hits is backscattered synchrotron radiation. From this data, a lower limit on the synchrotron-radiation contribution to the CTD current of 80 % at low electron beam currents (around 3 mA) was estimated.

Additionally the beam current dependence can be used to estimate the synchrotron-radiation contribution. The synchrotron-radiation power rises linearly with the electron current, as does the photon-induced CTD current:

$$I^{\text{CTD}}_{\text{synchrotron radiation}} \propto I_e \tag{4.3}$$

4.2.1.2 Electron particle contribution

The beam-gas background from the electron beam at a given energy should be roughly proportional to the squared electron-beam current. This is due to the production mechanism: the synchrotron photons release residual gas molecules from the beam-pipe walls (higher desorption rate), which in turn collide with the electron beam. These electrons lose some part of their momenta (off-momentum electrons) and are bent into the beam-pipe and central collimation system inside the tracking chambers where they shower and lead to high chamber currents. The synchrotron-radiation power goes up linearly with the electron current. The increased power proportionally leads to gas release from vacuum chamber walls, the so called dynamic vacuum. Additionally a higher beam current is available to collide with the released gas:

$$I_e^{\text{CTD}} \propto I_e^2 \tag{4.4}$$

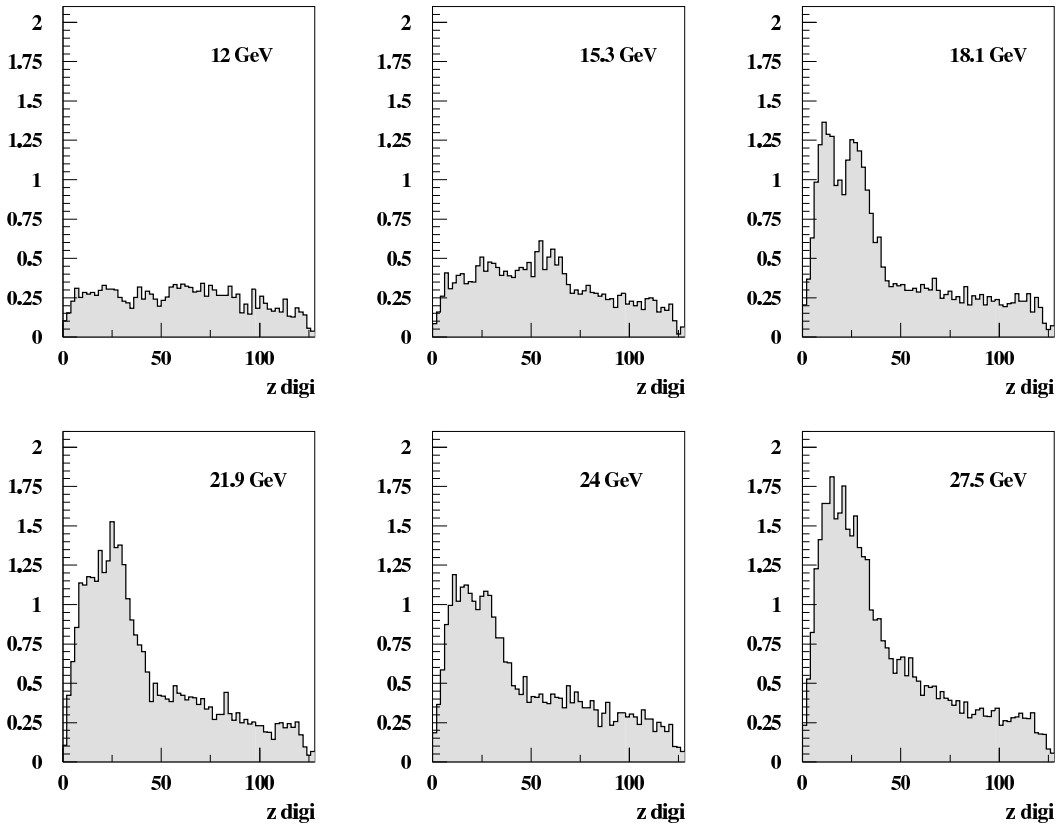

Figure 4.7: Hits recorded by the CTD z-by-timing system in SL1 during an electron beam energy scan. $z\ digi = 0$ is at the rear end of the CTD at $z = -105$ cm, $z\ digi = 128$ in the forward at $z = +105$ cm. The electron beam energy is shown at the upper right corner of every plot.

It is also possible to estimate the electron particle contribution from rates of detector components (counters), that are shielded against synchrotron radiation.

4.2.1.3 Proton particle contribution

The proton beam-gas background is due to proton collisions with particles released by the synchrotron radiation, so it is proportional to the product of both beam currents:

$$I_e^{\mathrm{CTD}} \propto I_e \cdot I_p \tag{4.5}$$

Again, counter rates can be used to estimate the proton background. It was found, that the major sensitivity to proton background arose from interactions close to the IP. More than 70% of the proton induced CTD current came from background events up to 3.6 m away from the IP.

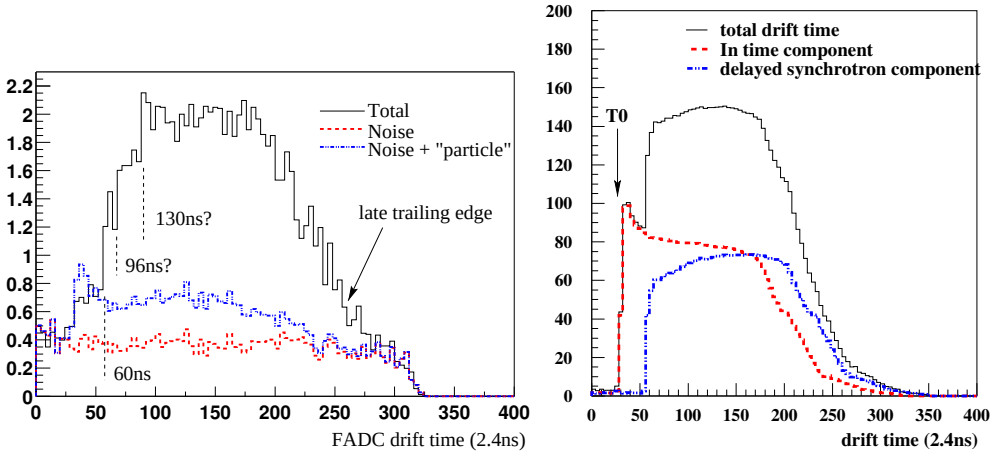

Figure 4.8: Unfolding direct and delayed hits in the CTD. The in-time component was estimated from track-triggered hits.

4.2.1.4 Total contribution

The total CTD current estimated from beam currents for constant energy and beam steering should therefore be given by

$$I_{\text{tot}}^{\text{CTD}}(I_e, I_p) = I_0 + b{\cdot}I_e + c{\cdot}I_e^2 + d{\cdot}I_e{\cdot}I_p \tag{4.6}$$

with I_0 being the standing CTD current due to the surrounding uranium calorimeter (see sec. 5.3). By fitting the CTD current dependence on the electron current for fixed proton currents, one can determine the constants of eq. 4.6 and by this also the relative contribution. Actually a modified version of eq. 4.6 is currently in use at ZEUS [70]:

$$I_{\text{mod, tot}}^{\text{CTD}}(I_e, I_p) = 15 + 0.35{\cdot}I_e + \left[0.011{\cdot}(50{\cdot}I_e + 2.0{\cdot}I_e^2)\right] + \left[0.28{\cdot}(1 + 0.095{\cdot}I_e){\cdot}I_p\right] \tag{4.7}$$

where I_e and I_p are given in mA and $I_{\text{mod, tot}}^{\text{CTD}}$ gives the sum of the signal wire currents in one quadrant of the first CTD superlayer in units of 0.1 μA. The first term corresponds to the CTD pedestal current, the second is the contribution from synchrotron radiation, the third the electron beam and the forth the proton beam contribution. Changes in the composition of the background contributions are then reflected by changes in the above fit parameters. As the base pressure was not included in this parametrisation, the parameters change when the base pressure improves with time. Extrapolations to full HERA II design currents are shown in fig. 4.9. Here both the situation before the improvements described hereafter and the situation after the improvements have been implemented is shown.

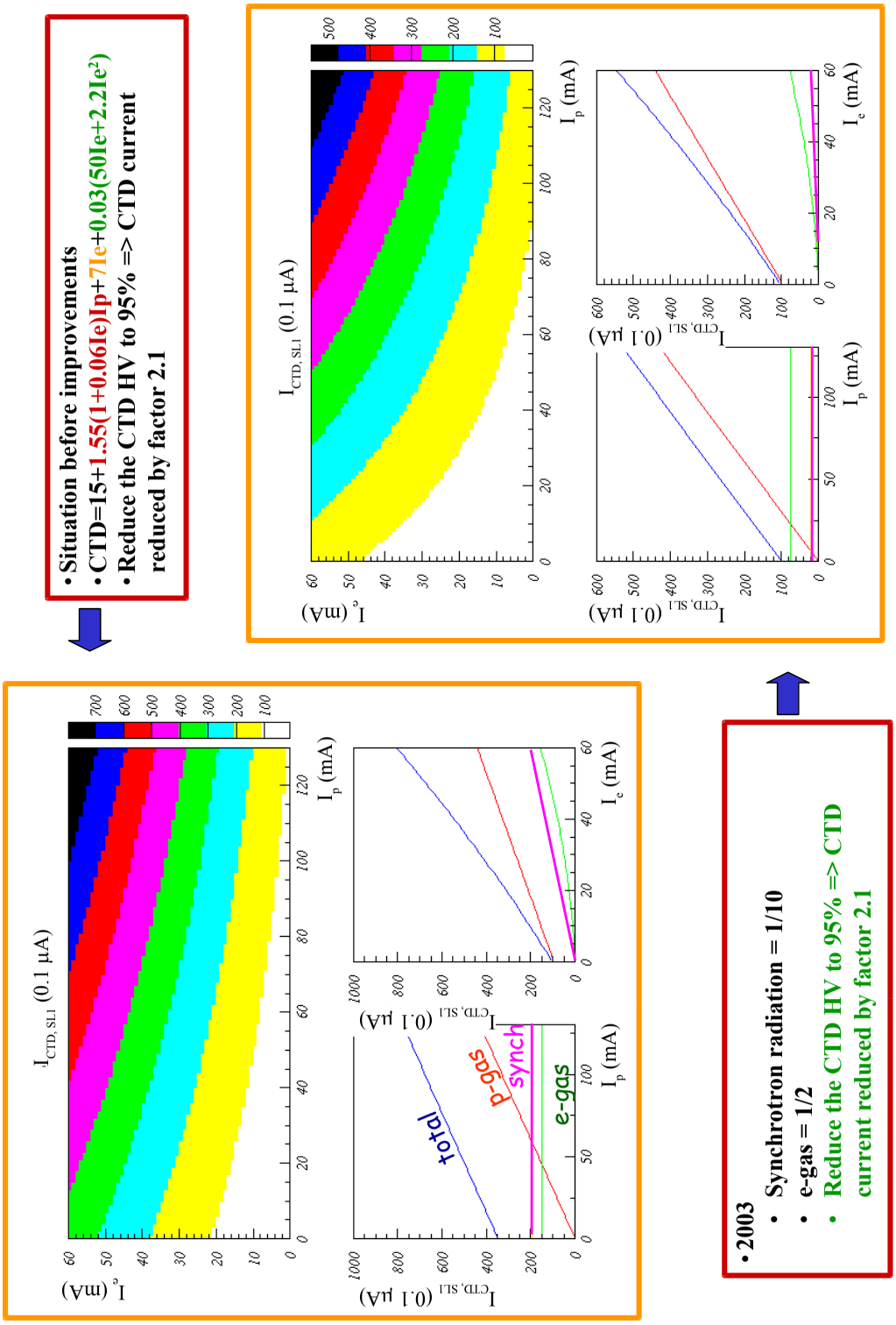

Figure 4.9: Fits to the $I_{\mathrm{CTD}}(I_e,\ I_p)$ distribution [70]. The total current broken down into the subcomponents determined using the phenomenological eq. 4.7. The fit parameters given at the top right corner reflect both the less good vacuum conditions in 2002 than in mid 2003 and also the fact, that the improvements had not been implemented.

4.2.2 Synchrotron radiation backgrounds

The synchrotron-radiation simulation as well as its verification and comparison to data are described here. Resulting modifications to the synchrotron radiation collimation system are summarised in sec. 4.2.5.

4.2.2.1 Simulations of synchrotron radiation backgrounds

To understand the precise origin of the synchrotron-radiation background and, based on that knowledge, develop minimally interfering shielding measures, a dedicated simulation environment was set up. This included the simulation of synchrotron-radiation emission from the electron beam ±100 m around the IPs as well as the subsequent scattering of the photons into the tracking chambers. The simulation code used for this main simulation was based on a package built by D. Pitzl [68] and A. Meseck [71].

Many modifications were performed to arrive at a more realistic description of the upgraded ZEUS and H1 interaction regions. These changes included e.g. the extension of the simulation range from $z_{\mathrm{HERA}} \pm \sim 20$ m around the IP to $-100 < z_{\mathrm{HERA}} < 20$ m, the inclusion of vertical and horizontal corrector coils, many new electron magnets as well as major upgrades to the photon tracking geometry package to describe elliptical rather than cylindrical pipes.

A sketch of the horizontal plane of the simulation environment is shown in fig. 4.10, an example 3D display of scattered photons inside the simulated ZEUS detector is shown in fig. 4.11.

The principle of the simulation can be summarised as follows:

- **Step 1: Direct photons**
  - track N electrons through HERA magnet lattice
  - produce / simulate primary photons from tracked electrons (tangentially)
  - track photons through HERA beam-line and collimators / absorbers
  - 'predict' the number and critical energy of the primary photons at collimators;
- **Step 2: Backscattered spectra**
  - simulate interaction of primary photons with energies from a spectrum of a given critical energy in a given material (sandwich structure of materials, inclined relative to incoming photons)
  - calculate backscattered spectra / angular distributions and total number of backscattered photons (processes implemented: Compton and Rayleigh scattering as well as photo effect energy deposit);
- **Step 3: Tracking backscattered photons**
  - track backscattered photons with given energy spectrum through beam-pipe, collimators, magnets, detector and iterate
  - 'predict' the number and energy of scattered photons in central detectors.

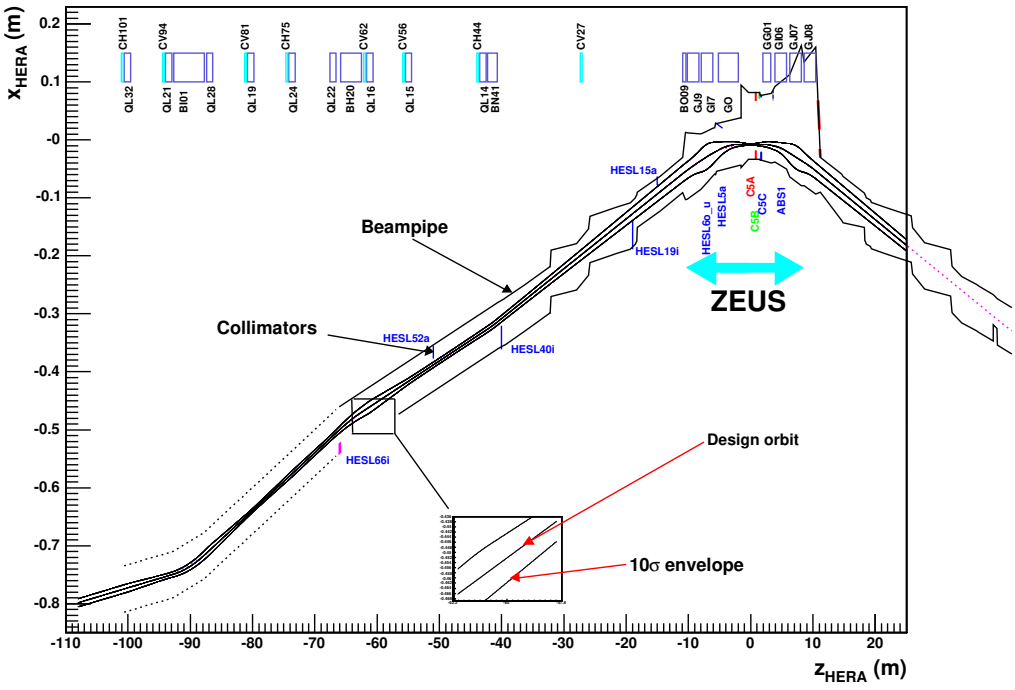

Figure 4.10: The horizontal plane of the simulation environment. Shown are the design electron orbit and its 10σ envelope, the beam-pipe and the collimators. At the top the z positions of the (lepton-) magnets are shown. Note the highly distorted scale ($x : z \approx$ 1:100).

Internal photon energy cutoffs were applied for direct photons at $E_{\text{crit}} > 10$ keV in step 1 and for scattered photons at $E_\gamma > 10$ keV. This summarises the main simulation. Using all three steps together, it is possible to predict, for a chosen scenario, the number and energy of photons per second arriving at e.g. the CTD. As the HERA upgrade foresaw both electron and positron running, simulations were performed for both the HERA electron and positron configuration. In order to simulate electrons, the position and strength of several magnets was modified using the current electron orbit and optic parameters as summarised in table B.1. Additionally, the x-position electron orbit at the IP was shifted by 0.75 cm to the ring outside relative to the positron orbit.

Other more specialised approaches (using e.g. GEANT) were chosen for specific cross checks of the main simulation and detailed optimisations. Some of the results of these approaches will be summarised later. When the simulation strategy was defined, the other obvious approach, to use the standard ZEUS detector simulation (MOZART), was considered but not pursued. This decision was based on doubts concerning the proper simulation of $\mathcal{O}(10)$ keV photons in MOZART as well as the much higher time consumption for simulations using the much more complex full detector description.

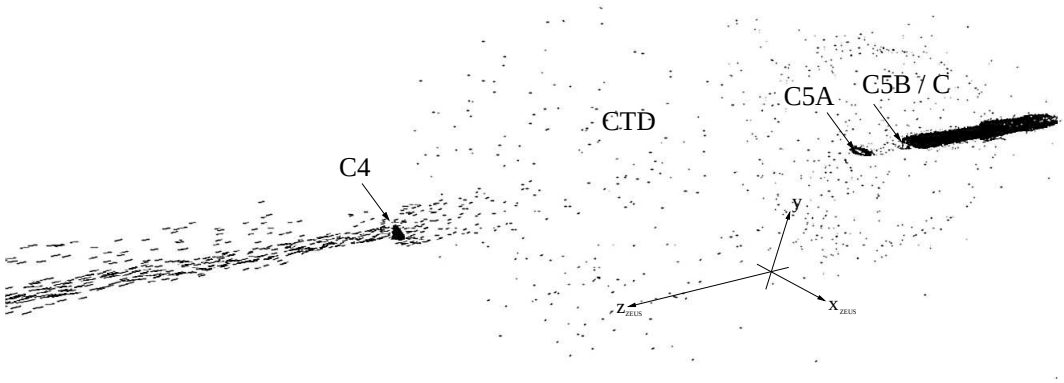

Figure 4.11: Representation of backscattered synchrotron radiation photons scattering inside the simulated ZEUS detector. Each dot corresponds to an energy loss of more than 20 keV.

4.2.2.2 Verification of the simulation

Dedicated scenarios were set up to check the results of the simulations.

The basic primary photon simulation (step 1) had not been modified in terms of synchrotron radiation properties, which had previously been cross checked by the original authors using e.g. the results of an analytical approach [58]. The modifications performed in the optics and tracking sector of step 1 were checked mainly by measuring the response of the CTD currents to movements of chosen collimators. As an example, the xy distribution of the photons at the movable collimator at $z_{\mathrm{HERA}} = -15$ m is shown in fig. 4.12. This distribution could be verified by several beam studies. In these studies, the radiation fan from the BI was directed into the experiment by very careful opening the collimator at $z_{\mathrm{HERA}} = -15$ m. The CTD current started to go up when the collimator was moved out to a position greater than about 14 mm distance to the e-beam, not absorbing the broad fan from the BI magnet any longer, agreeing nicely with the simulation.

The backscattered spectra (step 2) were cross-checked against GEANT. In this comparison, the same input spectra and a very similar geometry setup were used for both simulations. This yielded a very good agreement with differences well below 3%.

The backscattered tracking and hit distributions in the central detectors (step 3) were checked with CTD data and the ZEUS simulation MOZART as well as additional stand alone GEANT setups. Comparisons to CTD data were done e.g. by implementing an approximate description of the MVD cables and comparing angular and spacial distributions. The ϕ dependence of the hits in the CTD could be modelled very well, as seen in fig. 4.13 left. The z distribution of simulated photons entering the CTD is compared to CTD z-hits in fig. 4.13 right. The worse agreement in the z distribution can be explained by the missing simulation of the CTD z-hit response (photon passage through SL1 of the simulated CTD is compared to z-hits measured by the CTD). The alternative GEANT-based simulation modelled the central-detector region including the beam-pipe, the C5A and some parts of the MVD. This model was intended to be used especially for redesigning details of the C5A front surfaces. For this reason, the z-shape was modelled quite precisely, but the xy-shape was implemented box-like rather than

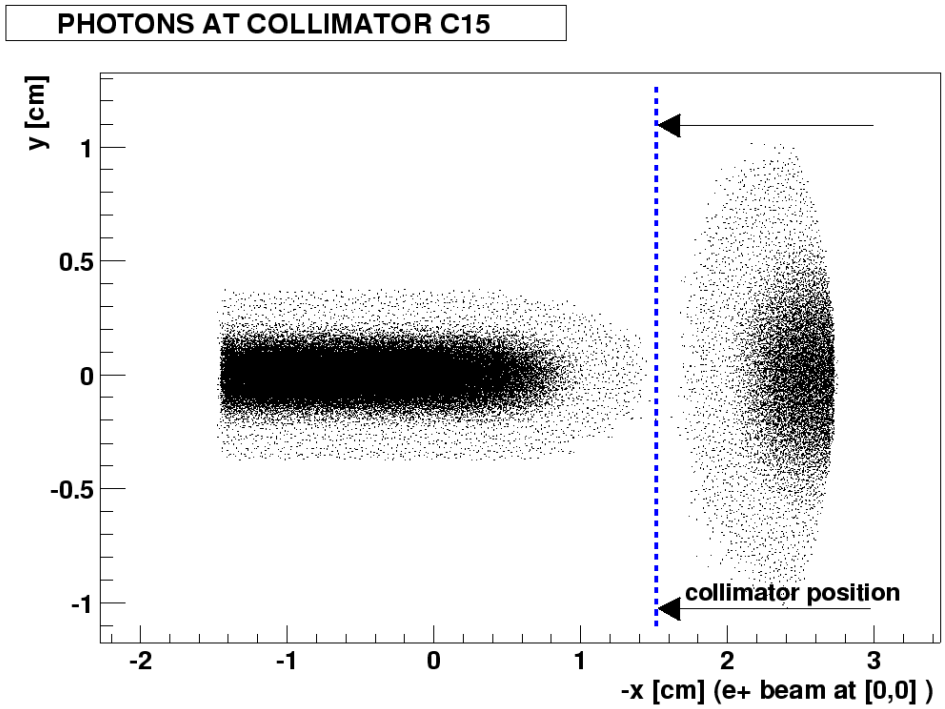

Figure 4.12: The direct photon xy distribution at the movable collimator 15 ($z_{\text{HERA}} = -15$ m). Photon coordinates are given relative to the electron beam position at $z_{\text{HERA}} = -15$ m. The broad spot on the right side is generated by the BI magnet at $z \approx 90$ m. The slim synchrotron fan on the left is produced by a collection of magnets in front of the 15 m collimator. The sharp cut on the left side is due to a collimator at $z_{\text{HERA}} = -19$ m, and the round shape on the right is introduced by the beam-pipe.

elliptically. In the GEANT simulation, fixed-energy photons were sent parallel to the electron beam onto the C5A rear face. These hits were located in four spots at the left, right, up and down side of the C5A. To compare this set-up with step 3, photons from the main simulation were sent similarly onto the elliptical C5A. The results are compared in fig. 4.14. Reasonable agreement was found, considering differences in geometry description.
Finally the main simulation was cross checked against the full ZEUS detector simulation package, MOZART. In order to study photons with such low energies, it was necessary to make some modifications to the standard MOZART configuration cards. The following changes were made:

- Rayleigh scattering was switched on;
- The GEANT cuts (cut-off values below which different particle types are ignored by GEANT) were reduced for electrons and photons from 0.001 GeV to 0.00001 GeV. All other cut values were kept at the standard values used in physics analyses.

Comparisons were made of hits in super-layer 1 of the CTD, where for the main simulation, 'hits' means photons which actually reached super-layer 1, while for the MOZART distributions it means the energy deposited by the photons in super-layer 1. The MOZART distributions were made from a sample of 400,000 photons with energies ranging from 10 to 300 keV. Also here good agreement was found when comparing arrival points of photons in SL1 from the main simulation to energy deposits from MOZART.

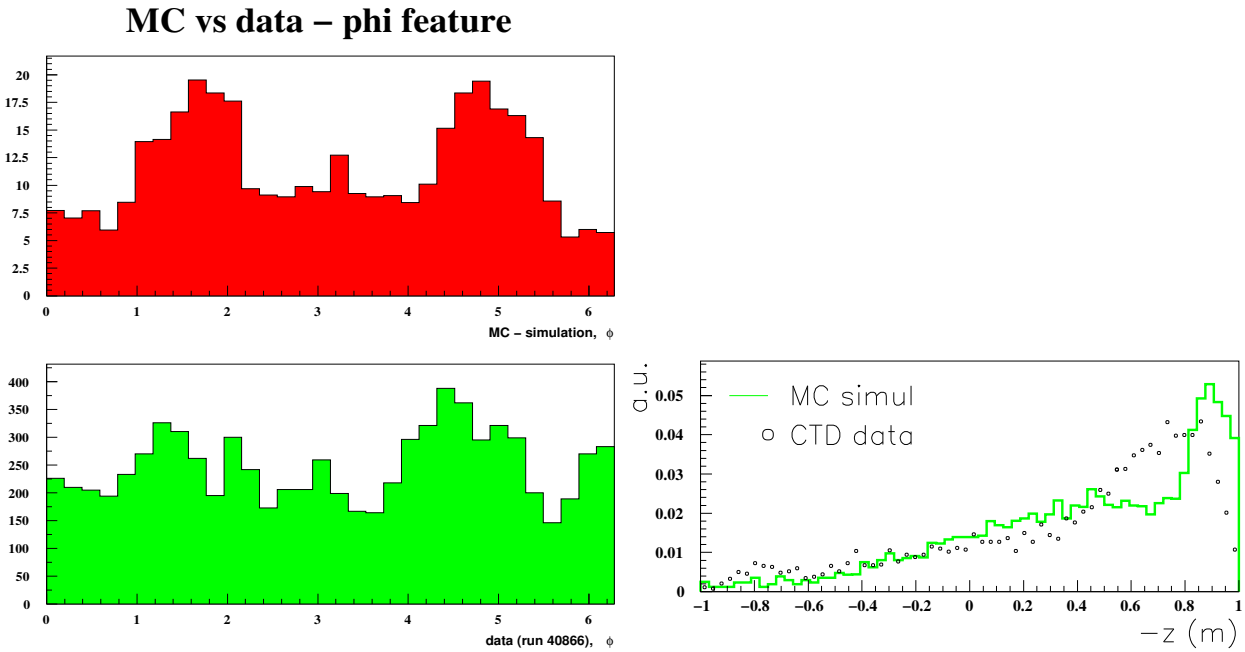

Figure 4.13: Comparison of the synchrotron radiation simulation (SL1 passage) to CTD data (random trigger hits). On the left the ϕ shape of hits in the rear 50 cm of the CTD is shown - upper plot: MC, lower plot: data. On the right the simulation SL1 passage (smeared by 4 cm) is compared to CTD z-hits.

The agreement with the independent GEANT checks and the good description of the ϕ-dependence proved that the main simulation gave a good description of the interactions of low-energy photons.

4.2.2.3 Results

In the following chapters the main synchrotron radiation simulation results will be presented. Very many simulations were performed to achieve maximal reduction of synchrotron-radiation backgrounds while at the same time minimising both vacuum deterioration by higher-order mode (HOM) heating[3] and particle showering in the additional material installed to absorb the synchrotron radiation. Only a small subset of these studies is shown here.

4.2.2.4 Direct photons (step 1)

Photon distributions and critical energies at selected positions along the beam-line $z = \pm 110$ m from the ZEUS and H1 IP were determined with step 1 using the design layout of HERA II. The simulation results were compared to several HERA II electron only runs using vertical and horizontal corrector bumps to move the synchrotron-radiation fan. These comparisons, however, will not be shown here as none of the tests revealed major contributions to direct hits in the ZEUS detector.

[3]This heating effect is due to induced currents and respective ohmic losses in the beam pipe and absorber metal by the passage of the charged beam.

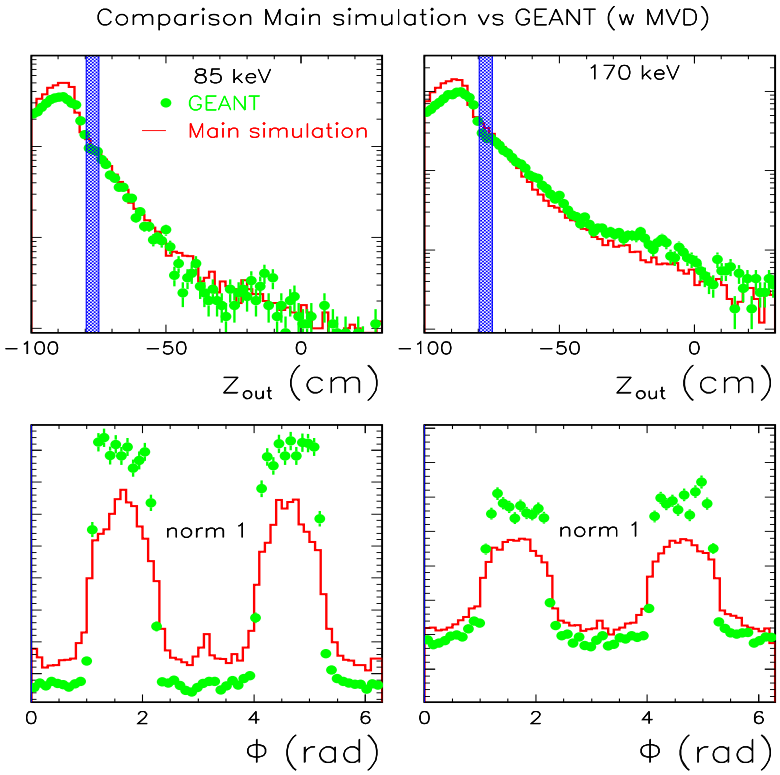

Figure 4.14: Comparison in shape and normalisation of step 3 (see sec. 4.2.2.6) to a GEANT simulation. Compared are the z and ϕ-distributions of photons entering the CTD SL1. The dots show the result from GEANT, the solid line shows the step 3 result. In step 3 only an approximation of the MVD cables was implemented, the GEANT simulation additionally contains an approximate description of the rear cooling pipes.

Among the first results using HERA II design parameters ('design calculations') was the explanation of the necessity of the additional collimator at $z_{\text{HERA}} = -66$ m to shield the photons coming from the BI magnet at $z_{\text{HERA}} = -92$ m.

The major output information of step 1 is the spatial and energy distribution of the photons at Abs4 (z = -11m, see fig. 4.16). The number of direct photons impinging on the two 'reflecting' surfaces of this absorber is $\sim$ 4.1 10^{17}(5.4 10^{17})γ/s for the positron (electron) orbit. The xy pattern and critical energy distribution of the photons is shown in fig. 4.17a (b). The weighted mean critical energy is E_{crit} = 85 (110) keV respectively.

Additional runs simulating the effect of non-Gaussian beam tails were performed by tracking electron distributions with non-Gaussian tails, as produced by Coulomb scattering, through step 1. The tails started at 7σ of the standard Gaussian beam, based on beam-tail measurements carried out by the HERA machine group (MPY) [72]. The results showed that no major photon contributions to the CTD current from the electron-beam tails were expected. Still, measures to shield against possible contributions from these photons were taken in the redesign of the C5A by including an integrated shield towards the direct photons, see fig. 4.18.

Machine experiments with large transverse beam tilts (up to 1 mrad) and offsets around the

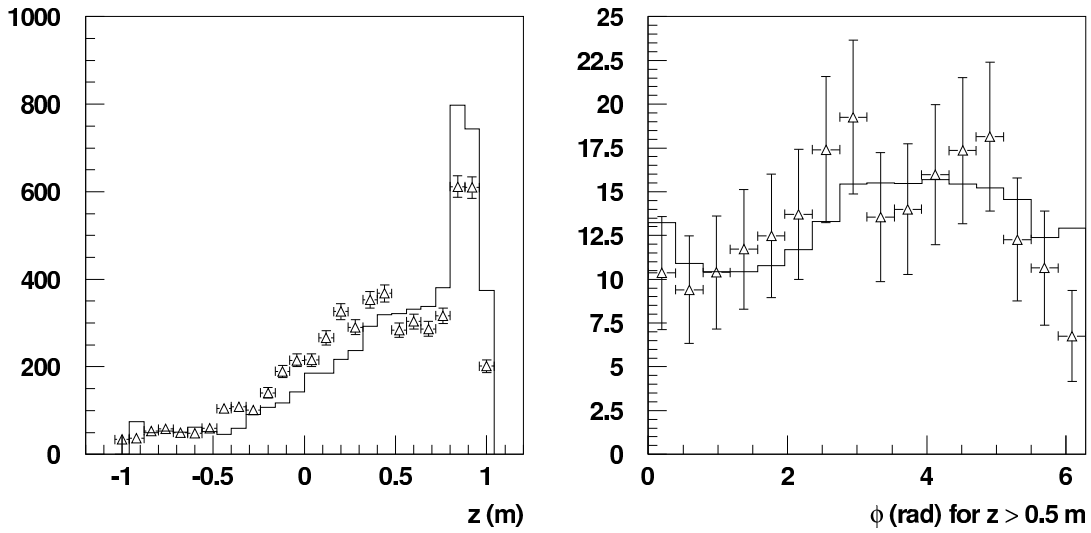

Figure 4.15: A comparison of the ϕ distribution for the rear 50 cm of the CTD super-layer 1 and the z distribution for the whole of super-layer 1 between MOZART and the main simulation. The distributions from MOZART are based on the energy loss in super-layer 1. In the case of ϕ, the distribution from the main simulation is for $z > 50$ cm, while from MOZART it is for the whole CTD.

IPs were performed and reproduced using step 1. Standard operations were found not to lead to additional photon background.

4.2.2.5 Backscattered photons: Spectra (step 2)

The output distributions of step 1 (energy and spacial photon distributions) are used as input to step 2. The main result of step 2 is shown in fig. 4.19. Photons from a spectrum of a given critical energy were sent onto an inclined block of material. A critical energy of 85 keV was chosen for the incoming photons, based on the weighted mean determined from the positron results of step 1. Later, the approach was refined using a spectrum of critical energies. This did not yield sizable changes though. To simulate photons backscattered from the copper absorber 4 (Abs4) at $z = -11$ m, photons were sent onto a plane of copper. The angle between

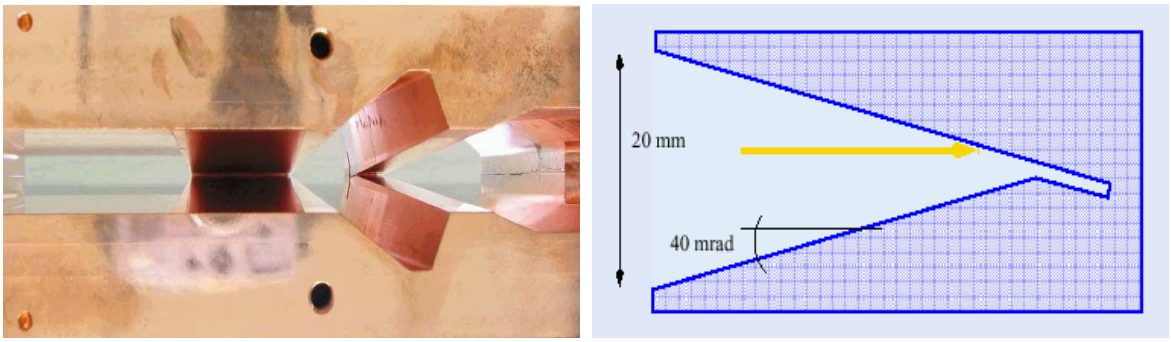

Figure 4.16: A photograph (left) and a cross-sectional side view (right) of the Abs4.

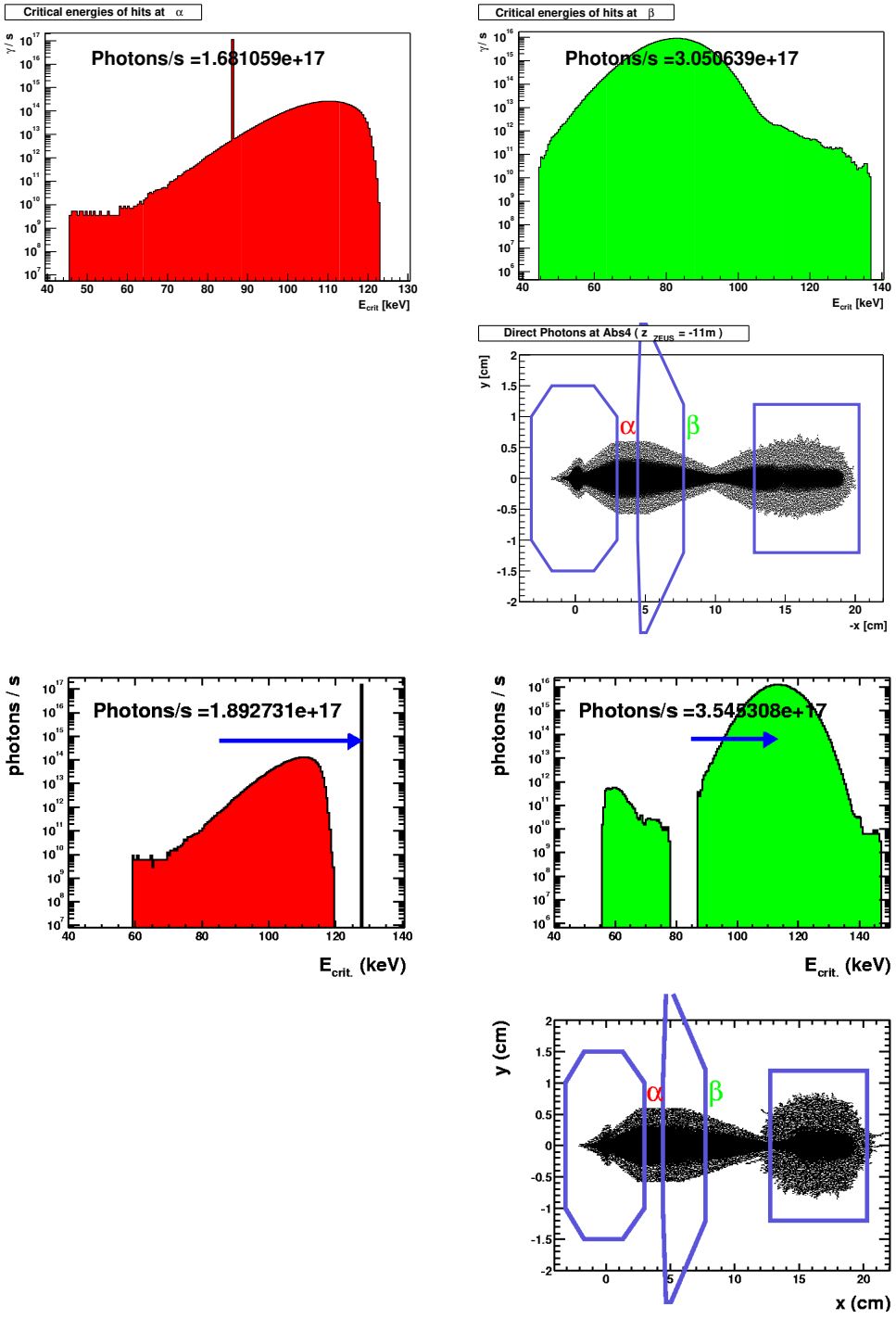

Figure 4.17: Direct photons at Abs4 ($z = -11$ m). Results for the positron configuration are shown in the top three plots, electron results below. On the lower right side of each 3 plots, the xy distribution of the photons are shown (viewed from the proton direction onto the incoming photon beam - note the distorted scale). The blue lines symbolise the inner boundaries of the beam-pipes starting behind this absorber. The leftmost beam-pipe is the electron beam-pipe, the middle one is the proton-pipe and the one on the right is for photons. Copper planes absorb the incoming photons between the electron and the proton (α) as well as between the proton and the photon pipes (β), see fig. 4.16. The critical energy spectrum of photons impinging on the absorber marked with α is shown on the top left side of the plot - that of the photons at β is shown on the top right side. The arrow in the lower 3 plots indicated the shift of the weighted mean of the distributions when changing from positrons to electrons.

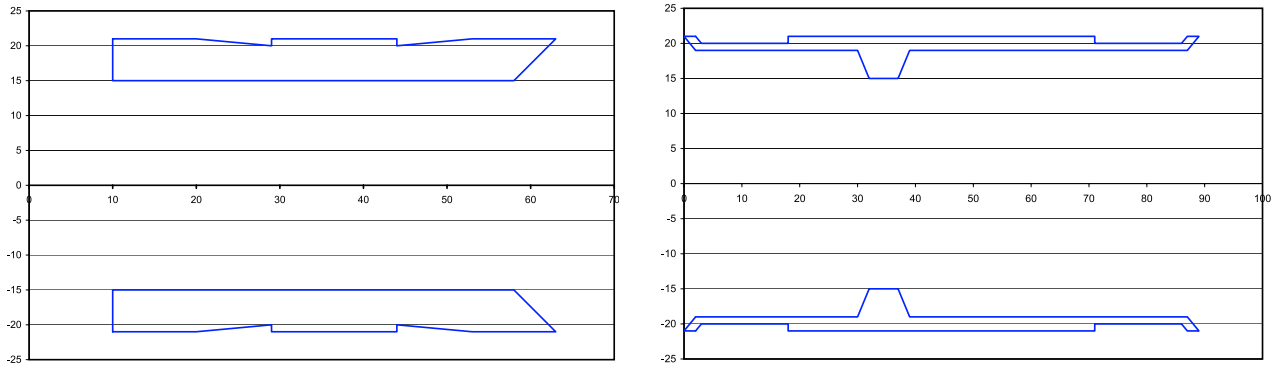

Figure 4.18: A side view of the C5A collimator before and after the improvements (axis units are mm). On the left the old C5A is shown. The large surface on the right side of the old C5A directed backscattered photons into the CTD. On the right side, the improved version of the C5A is shown. The long thin ledges were designed to shield the CTD against photons that are backscattered from the bulk absorber located at $z = -80$ cm. The notches at the outer end of these ledges house metallic RF springs which provide electrical contact to the beam pipe and also contribute to the collimator support. The shallow angles of the surfaces directed towards the beam have been optimised to reduce HOM heating.

the photons and the plane was chosen to be 40 mrad, corresponding to the inclination of the absorbing faces of Abs4.

The spectrum of the reflected photons inside a solid angle with an opening of $\cos(\vartheta) < -0.9$ around the incoming photons, corresponding roughly to the solid angle towards the central C5 collimators, shows a cutoff at half the electron mass introduced by Compton backward scattering. This was especially relevant concerning the minimal thickness of the C5A collimator.

The same simulations were performed in the electron scenario. The same cutoff at half the electron mass was observed. The number of photons was found to be a factor of 1.7 higher than that from positrons. Due to the cutoff introduced by Compton scattering, the spectral shape of backscattered photons is nearly identical for electrons and positrons.

4.2.2.6 Backscattered photons: Tracking (step 3)

The output distributions of step 2 (energy and angular photon distributions) are used as input to step 3. Photons with an energy spectrum as calculated in step 2 (fig. 4.19; solid angle of $\cos(\vartheta) < -0.9$) were tracked and scattered through a version of the ZEUS or H1 beam-line. The most important results of several different scenarios will be shown here. The results shown assume a sources of backscattered photons at $z = -0.8$ m (C5A), $z = -11$ m (Abs4) and $z = -19$ m (beam pipe beyond Abs4). When not mentioned otherwise, the -11 m source was chosen as the standard scenario.

The positron scenario was chosen as the default scenario; electron results are not shown separately. As the input spectra to step 3 in both scenarios are of very similar shape, the positron results are valid also for the electron case. The electron normalisation is obtained by multiplying the positron results by a factor 1.7.

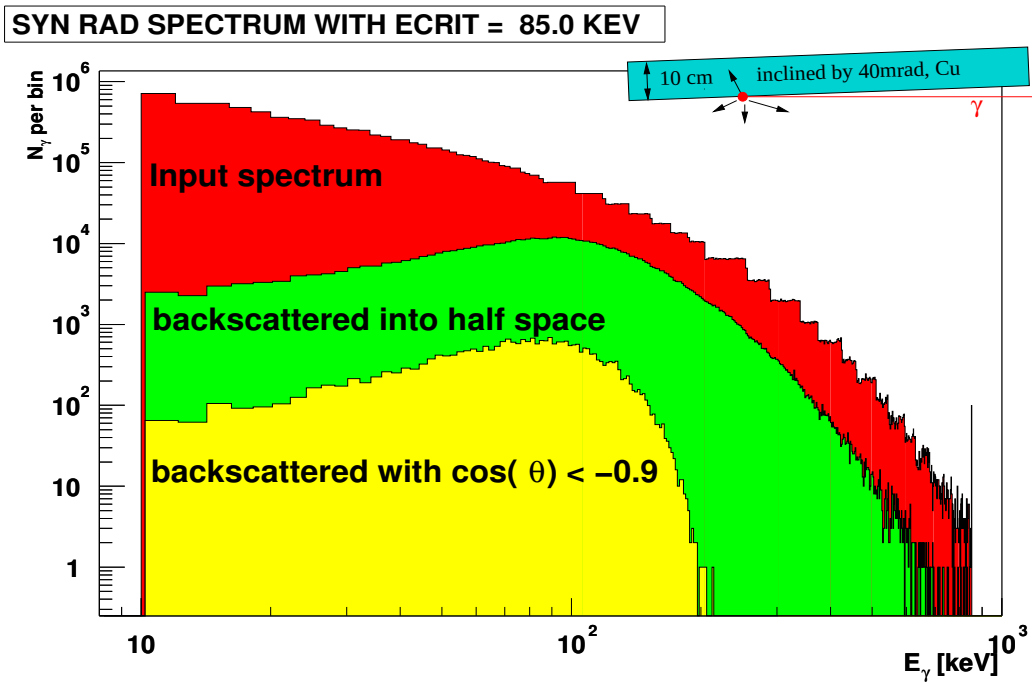

Figure 4.19: Result from backscattering calculations. The input spectrum was generated for $E_{\text{crit}} = 85$ keV. These photons were scattered on a plane of 10 cm thick copper tilted by 40 mrad relative to the incoming photons. The middle spectrum shows the photons being backscattered into the half space where there is no absorbing material. The lowest spectrum shows the photons that come 'back' within a cone given by $\cos(\vartheta) < -0.9$ around the incoming photon. This spectrum has a cutoff at $m_e/2$ given by the angular dependence of Compton scattering.

A hole between C5C/A The collimator C5C at -1.7 m should shield the outer border of the C5A completely. This was the case in the horizontal and vertical plane. However, for photons coming from -11 m, there were two holes at $\phi_{\text{CTD}} \approx (168 \text{ and } 192)°$. These holes are depicted by an example 'sneak-through' ray in fig. 4.20. The 'sneak-through' hits lead to hits all along the central beam-pipe; i.e. for $z \in [-0.8 \text{ m}, 0.5 \text{ m}]$. These photons show up as a broad peak centred around -0.3 m in SL1 of the CTD. The 'sneak' photons made up about 40% to 60% of the total number of photons inside the CTD.

Effect of MVD cables The CTD data showed a strong azimuthal asymmetry for hits in the rear 50 cm, as shown in fig. 4.13. The MVD cables have an asymmetric distribution. An approximation of this cable distribution was implemented in the simulation. The result is shown in fig. 4.21. The blue (upper) histogram in both plots shows the result without the MVD cables. The red (lower) histogram is obtained with the cables. A strong asymmetry results in ϕ (right plot). The agreement of data and MC in ϕ after this implementation is very good (fig. 4.13). This was strong evidence that the ϕ asymmetric backgrounds were produced by photons and that the energy spectra of background photons were similar to those of the simulation photons[4].

[4]The cables were only included in dedicated runs as they slowed the simulation down considerably.

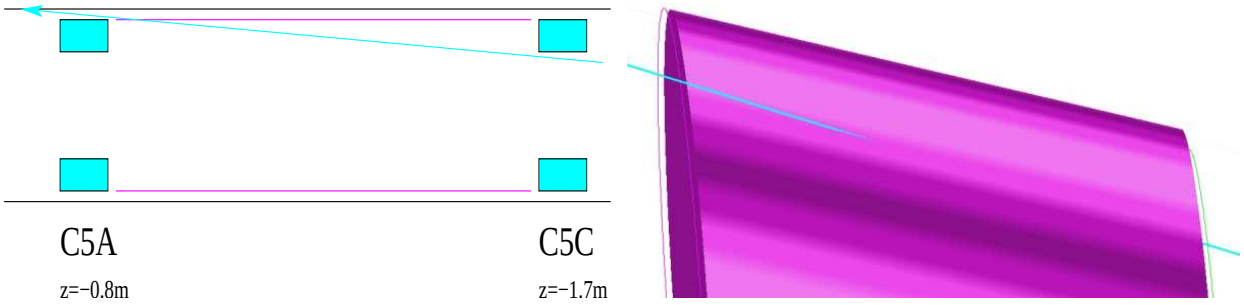

Figure 4.20: Photons coming from Abs4 (at z = -11m) could pass the collimator C5C (at z = -1.7m) on the inner side and pass the collimator C5A on the outer side. This led to hits along the central beam-pipe. Left: Schematic view of the rays passing C5A/C. Right: An example ray from the MC. The magenta elliptical pipe displays the outer boundary of the C5A situated on the left end of the pipe. At the right of the magenta pipe, a slim green line symbolises the inner border of the C5C.

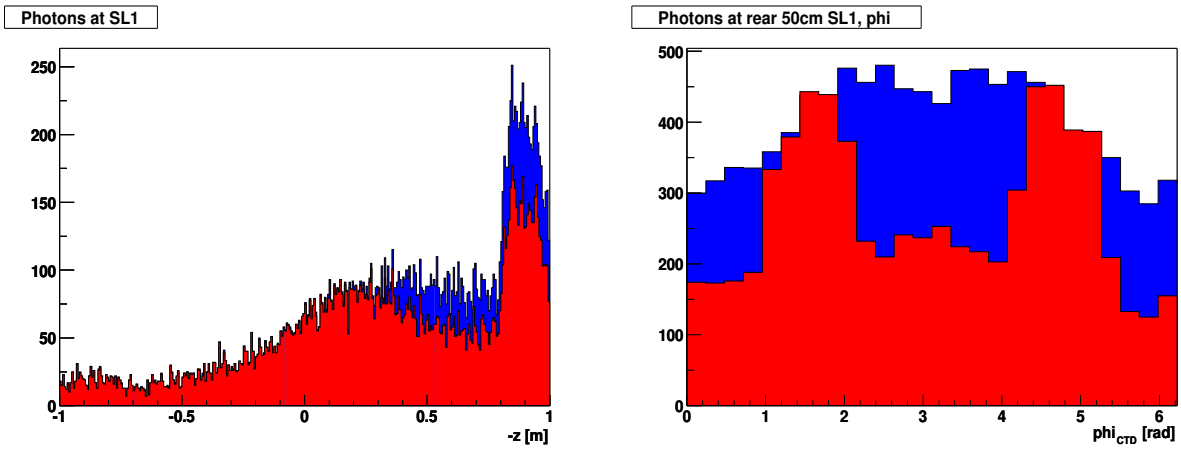

Figure 4.21: The z distribution and the ϕ distribution in the rear 50 cm of photons entering the CTD SL1 are shown. Blue (upper): no MVD cables, red (lower): approximation of MVD cables included.

Comparing H1 and ZEUS In H1 the contribution from backscattered synchrotron radiation was found to be lower than at ZEUS. To understand the reduced influence of synchrotron radiation on H1 compared to ZEUS, the H1 central beam-pipe and C5A/B absorbers have been implemented in the simulation. The result is shown in fig. 4.22.

In the H1 case, about a factor of two less photons arrived at the position of the ZEUS CTD SL1. This difference was mainly due to the reduced flux of photons arriving at the H1 C5A inside the H1 drift chamber, as the photons were strongly collimated by the H1 C5B before they hit the C5A, and the absence of the above-mentioned 'sneak-through' rays.

4.2.2.7 Finalising the C5 collimator system design

The results presented in this section include results from variations in the design of the C5A and B collimators, the influence on photons coming from $z = -11$ m and $z = -19$ m as well as from

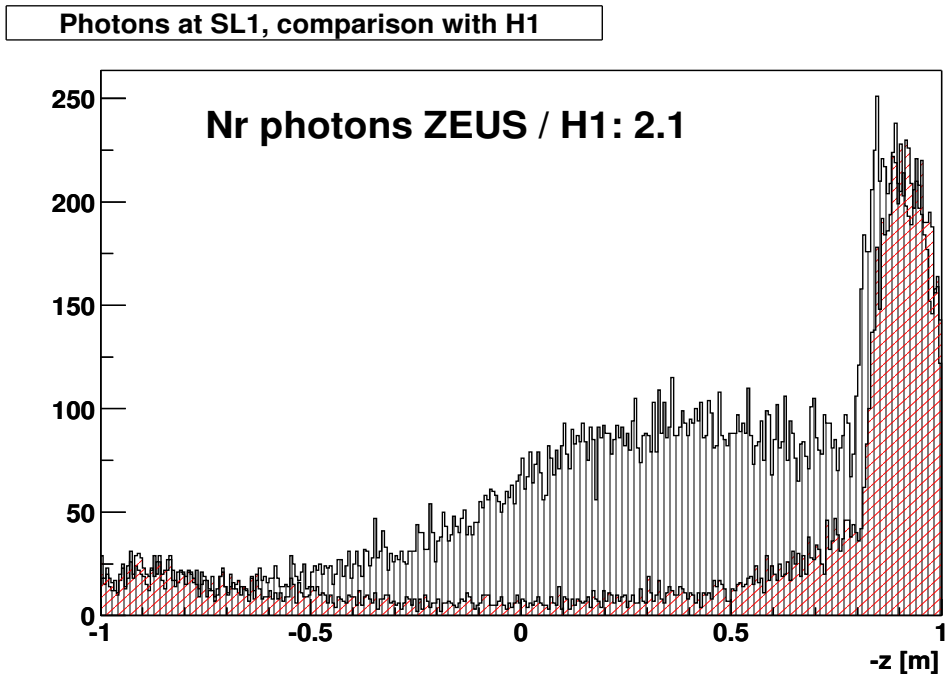

Figure 4.22: The z distribution of photons passing the CTD SL1 for H1 and ZEUS absorber geometry. In black, hatched vertically, the ZEUS standard distribution is shown. In red, hatched slantwise, the distribution is shown when implementing the H1 central beam-pipe and absorbers C5A and C5B.

simulations of direct synchrotron-radiation hits on the C5A from electrons in non-Gaussian transverse beam tails.

Optimising the C5A/B/C shapes To reduce the flux of photons in the CTD having scattered from the C5A surface, an integrated shield as shown in fig. 4.18 was studied. This additional shield reduces the flux of photons in the CTD by a factor 3, as shown in fig. 4.24a.

Thinning of the C5A absorber thickness was studied, with the result that reducing the C5A thickness from about 5 cm to only 0.5 cm enhanced the total photon flux in the CTD by only 6% (by 25% comparing only with photons that have interacted with the C5A, i.e. excluding the contribution from 'sneak-through' photons). The contribution from off momentum positrons showering in the C5A and contributing to the CTD current was estimated to go down by a factor of 1.5 when the C5A thickness was reduced by this amount.

To close the 'sneak-through' hole between the C5A and C5C, the horizontal extension of the C5B could be increased as shown in fig. 4.23. The flux of photons in the CTD can be reduced considerably using the shape labelled *design II*, as is demonstrated in fig. 4.24b.

To reduce the flux of photons impinging on the rear side of the C5A, the C5C was restricted in it's vertical opening. Shortening the vertical major axis of the elliptically shaped collimator by 6 mm led to a sizable reduction of the synchrotron radiation induced CTD current, as is shown in fig. 4.24c.

The inclinations of the C5A/B/C front surfaces were optimised for minimal HOM heating. These optimisation steps are not documented here. In total the local energy loss of the electron beam

due to HOM resonances in the vicinity of the C5 collimators could be reduced by a factor of greater than 2 when the electron beam bunches have a length of 3 mm at injection energy of 12 GeV and by even a factor 8 for the 12 mm long bunches at full energy of 27.5 GeV when comparing to the pre-optimisation collimation configuration.

A further shielding option, that was later abandoned as it led to a large increase of HOM heating, was an additional absorber positioned inside the absorber 1 at $z = -3.6$ m. The effect this absorber would have had was similar to the restriction of the C5C and is shown in fig. 4.24d.

Coating Using tungsten for the C5 collimator system leads to an enhancement of backscattered 74 keV photons from the tungsten K-shell. This can partially be reabsorbed by additional thin layers of coating material on the tungsten bulk. A double coating layer of silver and copper was chosen for the C5A: Cu(135 μm)-Ni-Ag(550 μm)-W(base material) layer. The silver absorbs the 74 keV tungsten K-shell photons and re-emits photons at the lower energy of 47 keV, which are subsequently absorbed by the copper layer. The copper emits at 29 keV, which is not critical anymore, as most of these photons cannot penetrate the beam-pipe. The layer thickness had been optimised using step 2 of the main simulation package.

The energy and flux of photons back-scattered from the copper absorber at $z = -11$ m (Abs4) could also be reduced by an additional coating. A three layer coating of gold, silver and copper would be ideal, resulting in a reduction in the number of backscattered photons of 1.8. It was however a major technical challenge to add additional coating to the existing absorbers.

Comparison of the major shielding improvements The four main shielding options against backscattered photons from e.g. $z_{\mathrm{ZEUS}} = -11$ or -19 m were explained above:

- a modified C5A: integrated tungsten shielding in front of and behind the C5A as well as thinning the central collimator from $\Delta z \approx 5$ cm to $\Delta z \approx 0.5$ cm. Depicted in 4.18,
- a modified C5B: the changes are sketched in fig. 4.23,
- a vertically restricted C5C and
- a vertical absorber at $z_{\mathrm{ZEUS}} = -3.6$ m (abandoned).

Implementing different combinations of these absorbers in the simulation yields a wide range of reduction factors of the photon flux into the CTD going from about 3 up to roughly 18. The results of the implementation of five combinations of the four absorbers is shown in fig. 4.24. The reduction factor for photons from -11 m conservatively using changes of the C5A and B only is ~ 8; with the coating at -11 m it yields a reduction factor of > 12. This factor may be raised by closing the C5B even further. As will be mentioned in the next chapter, a similar reduction can be obtained in this design for photons coming from $\sim$-19 m in the electron pipe.

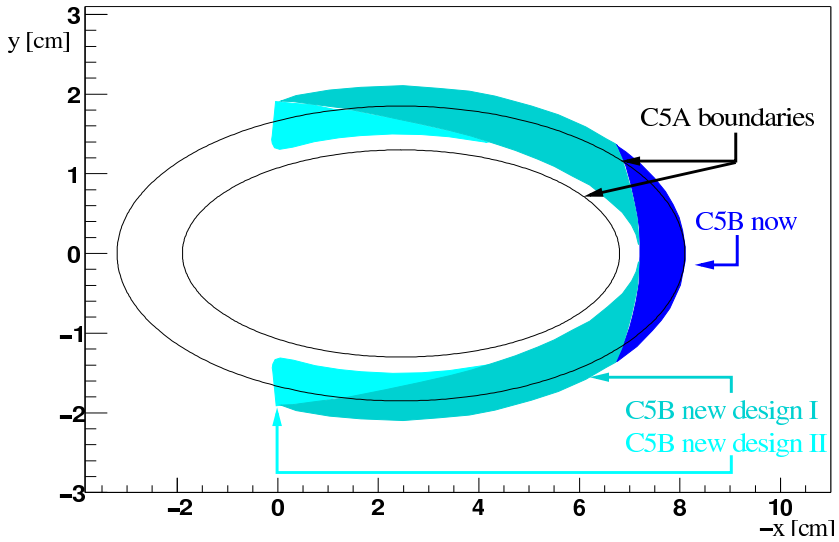

Figure 4.23: The modified C5B. In blue on the right the C5B in its original shape is shown in the *xy*-plane in the HERA electron system. In cyan the extension of the C5B is sketched. This material can stop the 'sneak-through' photons (see section 3.4.3.1 [1]). The black lines are at the position of the outer boundaries of the C5A.

4.2.2.8 Photons from -19m - electron-beam pipe

The beam-pipe and magnet material beyond -11 m was not implemented in the step 3 routines. To be able to predict some number on the reduction of photons coming from -19 m, a solid shield of tungsten at -11 m with an opening size and position of the electron pipe was implemented. In this way, the photons could only propagate directly towards the shield and onwards - a scattering at beam-pipes was not possible, as they were not implemented. The energy and angular spread of these photons however resembles that of photons from -19 m.

The z-distribution and numbers of photons at the super-layer1 of the CTD for the modified C5A/B are shown in fig. 4.25. When using the modified C5A and C5B as exclusive shields, the reduction factor for photons coming from -19 m in the electron beam-pipe is > 20.

4.2.2.9 Scattering of direct-photon hits on the C5A

Measurements of non-Gaussian positron-beam tails by the MPY group triggered a simulation of the photons coming from these tails, as described in [65], section 3.4.1. To gain further understanding of these photons, the results of step 1 were used as input to the backscattering routines (step 3). The energy of the photons was generated from the corresponding critical-energy spectrum. These photons yielded a strong peak in the CTD SL1 at z-position of the C5A and also led to a rather big contribution 'behind' the C5A, as they ranged up to roughly 4 MeV in energy, thus penetrated the collimator. Also a relatively strong phi-asymmetry was observed.

Fig. 4.26 visualises the effect of the integrated shield on the IP side of the C5A collimator. The peak of photons around 0.6 m present in the unimproved situation (high red histogram) is strongly suppressed by the integrated shield (lower green histogram). The high energy photons

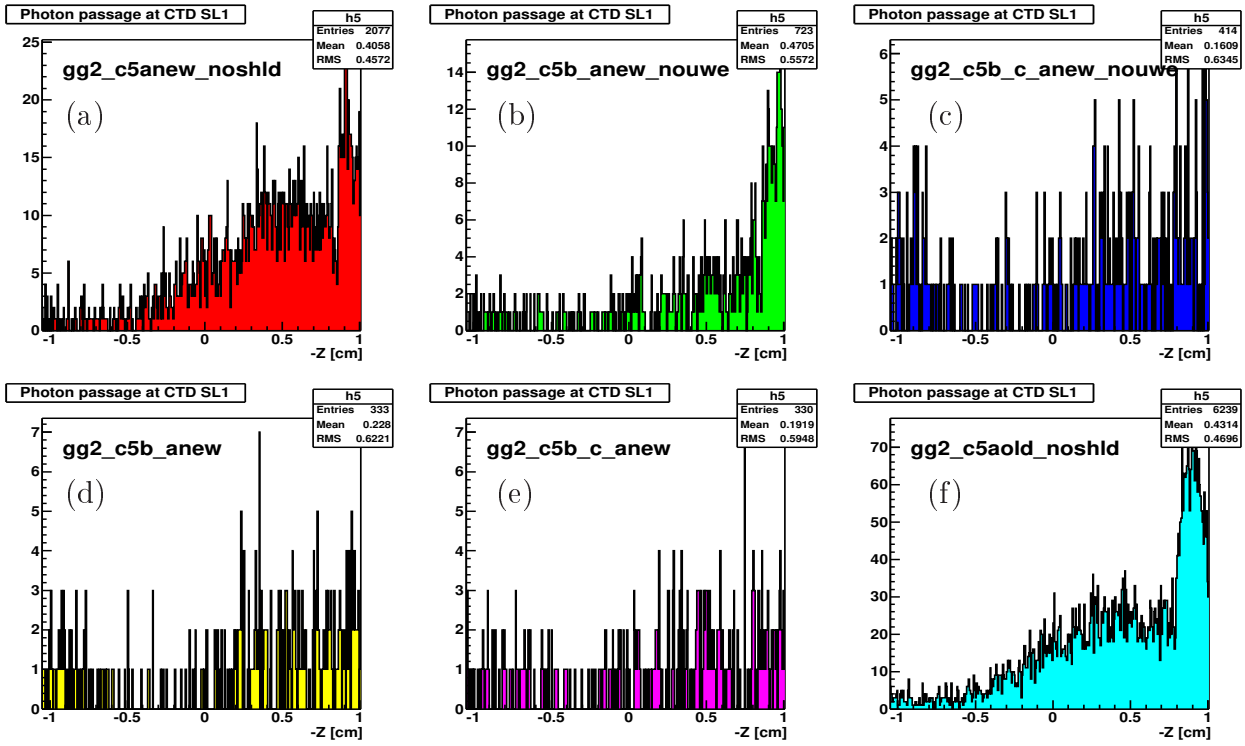

Figure 4.24: Photon-passage distributions for the CTD SL1 for photons coming from $z_{\text{ZEUS}} = -11$ m for a variation of implemented shields. (a) modified C5A with a 2 mm thick integrated tungsten shield (3.5 cm in z-IP direction, 5.7 cm at the other side), no restricted C5C, No abs. at -3.6 m (reduction factor 3.0), (b) like (a) but with the new horizontally extended C5B (reduction factor 8.6), (c) like (b) but with vertically restricted C5C (-6mm in vertical 'diameter') (reduction factor 15), (d) like (c) but without C5C restriction and with an absorber at -3.6 m (vertical opening: $\pm$8.8 mm) (reduction factor 19), (e) like (d) but with a restricted C5C (by 6 mm in the total vertical opening) (reduction factor 19), (f) standard C5A/B/C, like Dec. 2002 in ZEUS, no further shielding (reduction factor 1.0). Note the different vertical scales.

penetrating the tungsten block are reduced only slightly by the other side of the integrated shield.

4.2.2.10 Conclusions

- The modified C5A is superior to the upgrade-design one. The backscattering from its surface is reduced to a very low level. Also the off-momentum-positron rate is reduced.
- The new C5B is very well suited to shield the 'sneak-through' photons.
- The modified C5C can partially fulfil the function of the absorber at -3.6 m, though yielding a reduced reduction factor.
- The reduction factor using the modified C5A and the modified C5B only is $\sim$ 8 for photons from -11 m and larger than 20 for photons from -19 m. The reduction factor

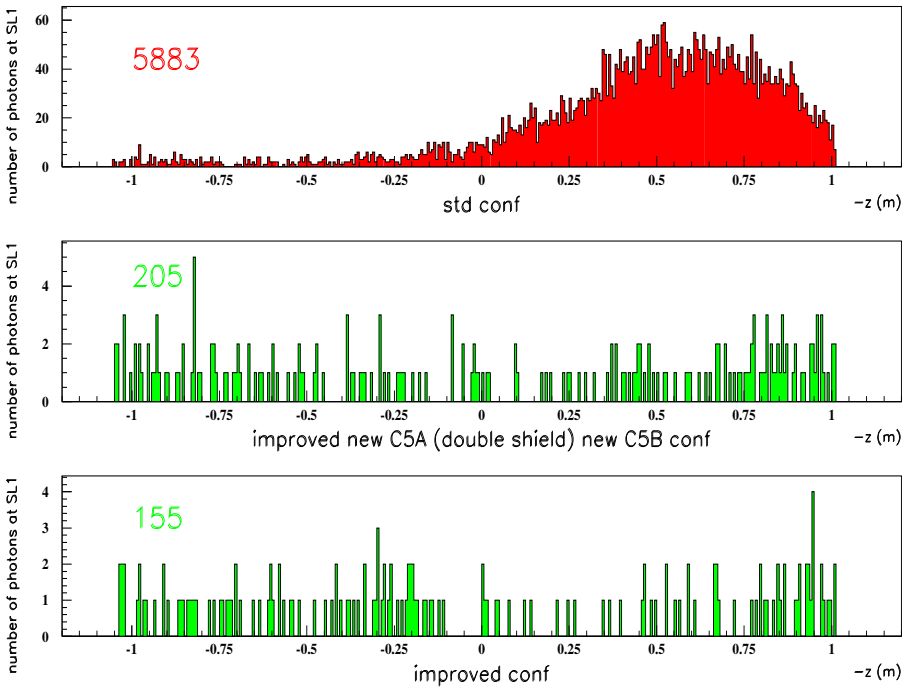

Figure 4.25: Passage of '-19 m photons' along z of the CTD SL1. The upper histogram is the result of the unimproved shielding situation. With the modified C5A and B, a reduction depicted by the middle histogram could be reached, yielding a reduction factor of > 20. The lower plot is obtained using the modified C5A/ B, restricted C5C and the vertical absorber at -3.6 m.

of the -11 m photons scales with the reduction factor gained by coating the Abs4 (i.e. $8 \times 1.6 > 12$).

4.2.3 Electron induced particle backgrounds

The electron particle background was found to be due to beam-gas interactions. Coulomb scattering of the electrons with the residual gas led to off-momentum electrons, which were bent into the conical central beam pipe and the central collimators by the IP magnets and showered there. Vacuum simulations showed, that in a region of $z_{\text{HERA}} = 27-32$ m a rather long un-pumped section led to a roughly factor 6 worse vacuum level compared to the surrounding sections. Simulations predicted, that improvements in this section could yield up to a factor of 1.5 improvement in the electron induced particle background. Accordingly new pumps were installed at this position. This proved to be difficult, as the electron beam pipe passes through the yoke of a proton magnet (GA) in this section. Holes had to be drilled into this magnet, after it had been shown that these would not lead to degeneration of the field quality of the GA. A further reduction in electron backgrounds was obtained by radically reducing the thickness of the C5A collimator (from $\sim \Delta z \approx 5$ cm to ~ 0.5 cm).

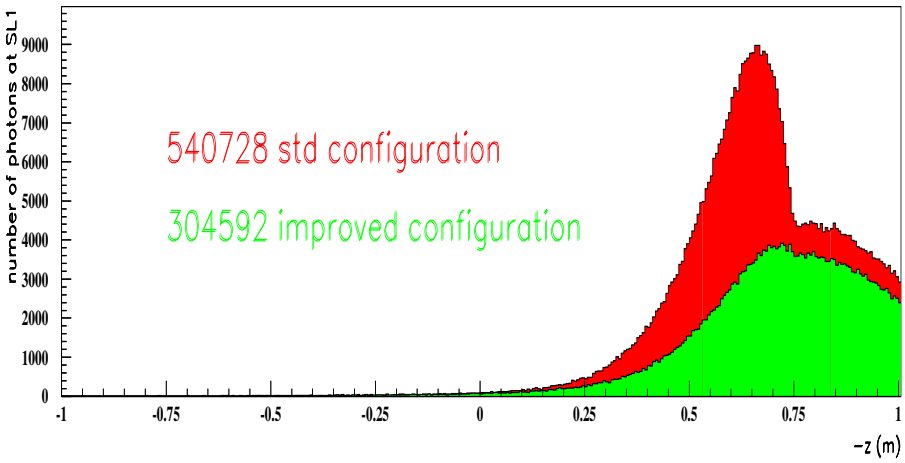

Figure 4.26: CTD SL1 z-distribution of 'direct tail photons' hitting the C5A collimator and scattering into the CTD. The high, red histogram is based on the current C5A geometry. The lower green histogram shows the reduction of scattered photons by the implementation of the integrated IP side shield.

4.2.4 Proton induced particle backgrounds

As for the electron particle background, beam-gas interactions were found be the main cause of the proton-beam induced background in H1 and ZEUS. It was shown, that the tracking chambers are sensitive mainly to interactions close to the detectors, up to about $z = 6$ m. A reduction of this background can be obtained by improving the local vacuum. Stronger pumps and a more refined pumping scheme as well as less frequent and strong disturbances of the vacuum system mainly by the electron beam can be used to obtain this improvement. The pumping scheme was mainly improved by including the cold beam-pipe surfaces inside the GO and GG magnets as effective cryogenic pumps[5]. Additionally some pumps were replaced by more powerful ones and pumping slots were widened up (see also [62, 73]).

As the electron bunches are shorter at lower energy and thus lead to much faster HOM heating, the beam is now accelerated as fast as possible after injection. Only for dedicated "cleaning" purposes (e.g. after a vacuum leak) it is kept a longer time at injection energy followed by a regeneration of the pumps. Additionally all new modifications were optimised to yield minimal higher-oder mode heating.

These improvements could not yield immediate improvements of the vacuum and thus of the proton-induced backgrounds. They did, however, speed up the improvement of the vacuum level. HERA beam currents were thus slowly raised until the experimental backgrounds were not limiting the beam currents any longer[6].

4.2.5 Resulting collimator modifications at ZEUS

To reduce the synchrotron radiation to such a low level, that even at highest HERA II beam currents running the tracking chambers would be possible, modifications to the central synchrotron-

[5]Cryogenic pumps have surfaces at a very low temperature on which residual gas is captured.

[6]Incidents of vacuum leaks close to the detectors ($\sim \pm 30$ m) led to a few short periods where again the beam currents had to be temporarily reduced.

radiation collimation system were applied according to the results of the background simulations and experiments.

At ZEUS, the C5A/B and C collimator masks were redesigned and rebuilt. The new collimators are shown in fig. 4.27 and 4.28. The C5A has been reduced in thickness from $\sim \Delta z = 5$ cm to

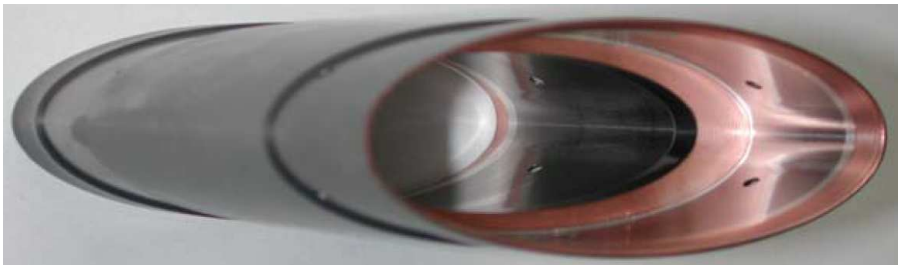

Figure 4.27: The final C5A.

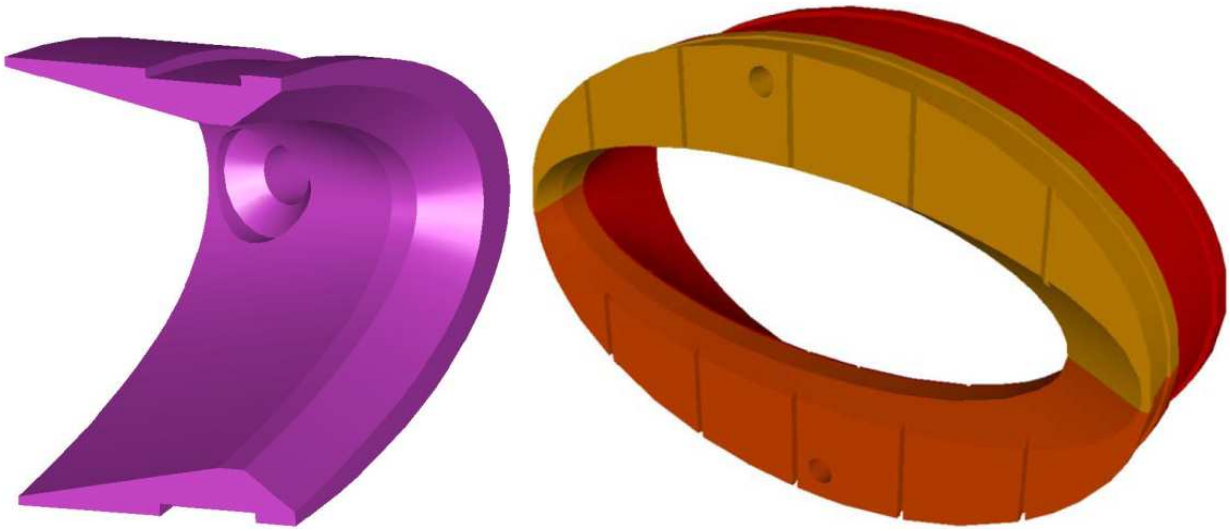

Figure 4.28: The final C5B and C5C.

~ 0.5 cm. An internal shield with a radial extension of 2 mm has been added on both sided of the collimator ellipse with a total length of $\Delta z = 10$ cm, of which about 3.5 cm extend towards the IP and 6 cm towards the rear of ZEUS. A side view of the C5A is shown in fig. 4.18. In the slots at both sides of the collimator RF-springs are connected. These springs establish an electrical connection between the collimator and the beam pipe. This provides only a very bad thermal contact but the collimator is heated by HOM heating of the electron beam. To improve on this, the outer surface of the C5A was coated with a layer of diamond, which improves the emission of low energy photons.

Also according to the simulation results, the C5B and C5C have both been restricted to reduce the flux of photons on the rear C5A side and also close the sneak trough hole. Additionally the longitudinal shape has been optimised for low HOM heating. This has been done by avoiding steps and introducing shallow rises wherever possible, while at the same time minimising the amount of material to reduce particle background showers.

With these modifications the synchrotron radiation background has successfully been reduced to a vanishing level. The further changes in the pumping scheme and the additionally installed and improved pumps have also led to a reduction of the particle induced background. Furthermore the voltage applied to the drift chambers was lowered slightly while in parallel increasing the signal amplifier gain, so that the background induced signal wire currents were decreased at a reasonable loss of signal efficiency. The running of HERA was thus not limited by these backgrounds any longer.

Chapter 5

The ZEUS detector

The ZEUS detector [74] is a general purpose detector designed to study various aspects of lepton proton scattering. The higher energy of the protons relative to the electrons leads to a boost of the centre-of-mass system relative to the laboratory system. To accommodate this boost, the calorimeter has been designed asymmetrically, with more material in the proton direction. Additional forward tacking detectors also support the tracking in the proton direction, shown in the longitudinal cross section in fig. 5.1. The right-handed ZEUS coordinate system, depicted in

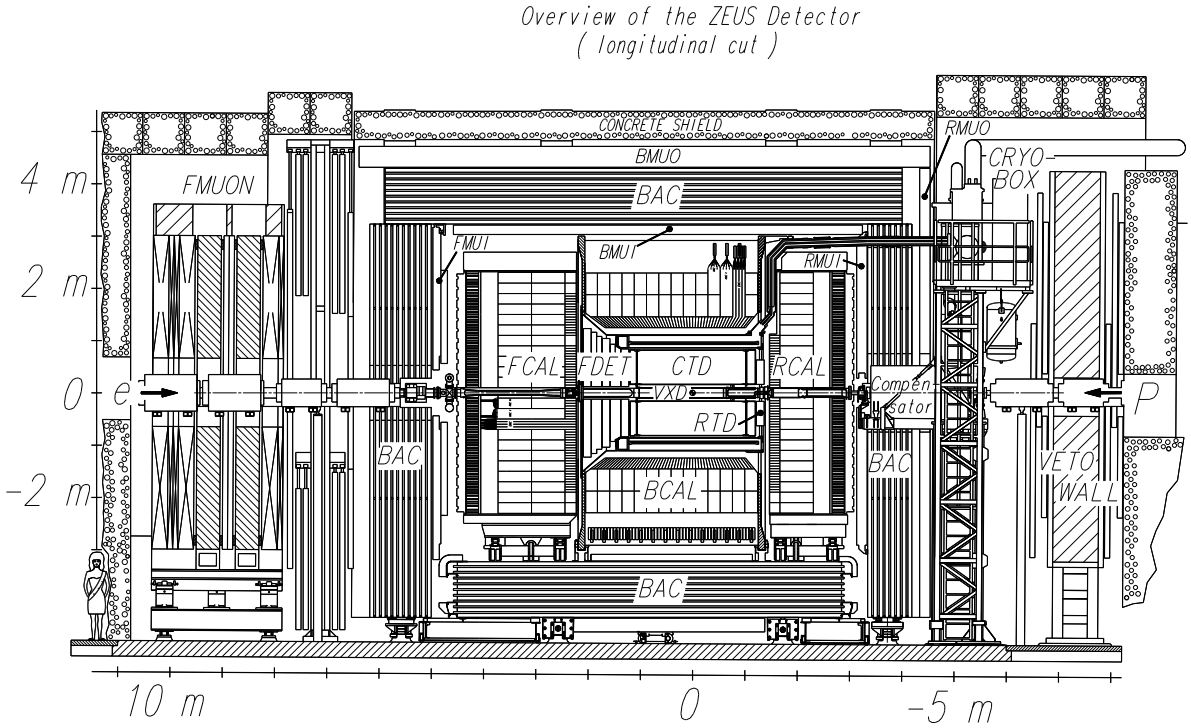

Figure 5.1: Cross section of the ZEUS detector along the beam axis.

fig. A.1 (appendix), is aligned such that its origin is at the nominal interaction point, with the x axis pointing horizontally towards the centre of the HERA ring, the y axis pointing upwards and the z axis pointing in the direction of the outgoing proton beam, also referred to as the

forward direction. The polar angle θ and the azimuth angle ϕ are measured relative to the z and x axis respectively. The detector has been in operation since 1992, however, new detector components have been added intermittently. The main part of the ZEUS detector has a size of 12 m x 10 m x 19 m and a weight of 3600 tons. An overview of the detector in the xy plane is shown in fig. 5.2. In the following short descriptions of the main detector components are

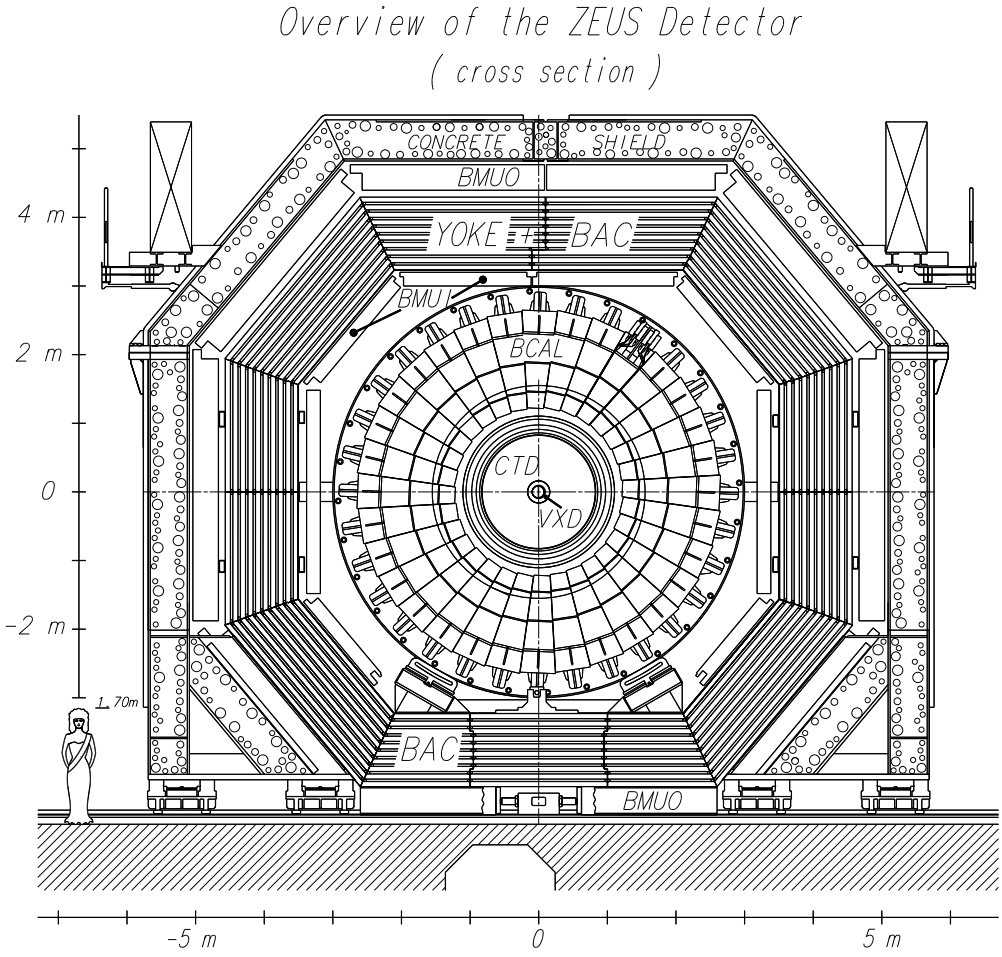

Figure 5.2: Cross section of the ZEUS detector perpendicular to the beam axis.

given. More details on the components most relevant for the beauty analysis are given in later sections.

At the centre of ZEUS a vertex detector (VXD) was situated. It was however removed during the shutdown 1995/1996 as it could not be operated continously due to high beam background levels. During the HERA upgrade in 2001 a silicon micro vertex detector (MVD, see sec. 5.2) was installed at the same place providing high precision tracking measurements. The central tracking detector (CTD, see sec. 5.1), a cylindrical proportional wire drift chamber, encloses the beam pipe in the region of the interaction vertex. It is surrounded by a super-conducting solenoidal magnet providing a field of 1.43 T for the determination of charge and momentum of charged particles in the tracking system. The CTD is supplemented in the forward direction with three sets of planar drift chambers (FTD) with interleaved transition radiation detectors (TRD) (labelled as FDET in fig. 5.1) and, in the rear direction, with one planar drift chamber

consisting of three layers (RTD). The forward TRD was replaced by an additional forward tracking detector called straw tube tracker (STT) in 2001.

A high-resolution compensating uranium-scintillator calorimeter (CAL, see sec. 5.3) surrounds the tracking detectors and the magnet. It is used as the main device for energy measurements and is divided into three parts: the barrel (BCAL), forward (FCAL) and rear calorimeter (RCAL). Scintillator pre-sampler (shower) detectors are mounted on the inner surface of the calorimeter modules. An iron yoke encloses the CAL, providing a return path for the solenoid magnetic field flux. It is instrumented with proportional chambers, which allow a measurement of the energy of particles penetrating the CAL, and therefore called backing calorimeter (BAC, see sec. 5.5). The BAC is also used as a muon detection system. Dedicated muon identification chambers (see sec. 5.4) are mounted on the inner and outer surfaces of the BAC (FMUI, BMUI, RMUI and FMUO, BMUO, RMUO). A detector composed of iron and scintillator, called VETO wall, is located in the rear direction at $z = -7.3\ m$. It is used to reject beam related background. For the same purpose and also to measure the timing of the particle bunches, a shielded scintillator detector called C5 is located close to the beam pipe in the rear direction of ZEUS. Several additional components are installed close to the beam line, outside the main detector, allowing a measurement of particles scattered at low polar angles. The most important of these is the luminosity measurement system, see sec. 5.6. Electromagnetic calorimeters (LUMIE and LUMIG) are placed at $z = -34\ m$ and $z = -107\ m$ to measure ep Bremsstrahlung photons ($ep \to ep\gamma$), a process with well known cross section, for the determination of the luminosity. The ZEUS total integrated luminosity for the years 1993 to 2005 is shown in figure fig. 5.3. In

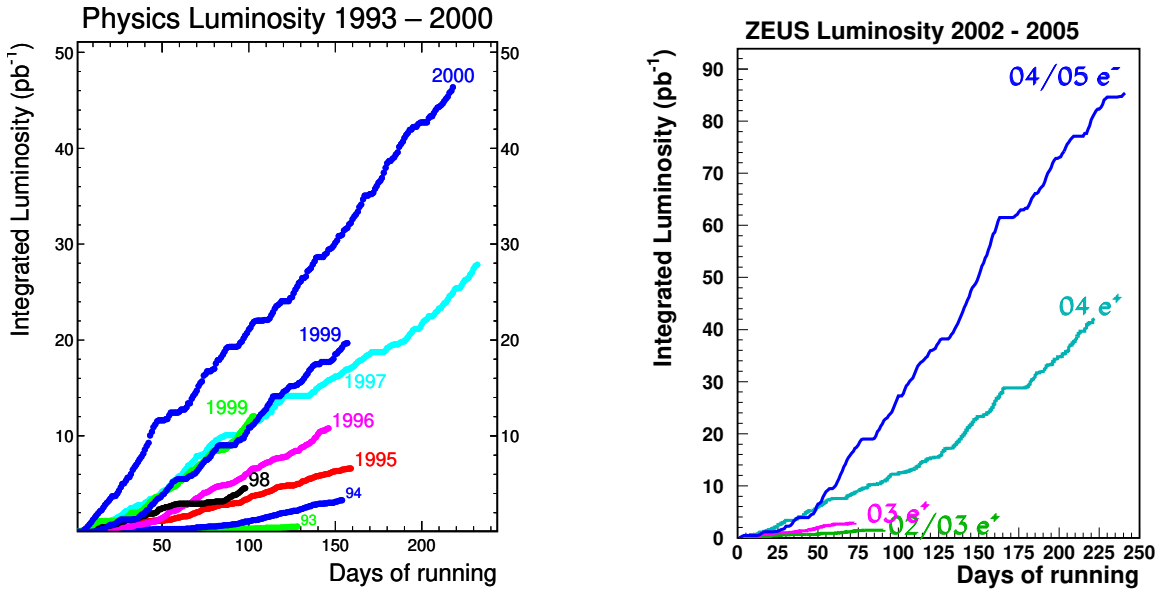

Figure 5.3: Integrated luminosity recorded by ZEUS for the running periods 1993-2000 (left) and 2003-2005 (right).

comparison to fig. 4.3, the values are slightly lower, reflecting the efficiency of the complete ZEUS data taking chain including data quality requirements.

5.1 Central Tracking Detector

The central tracking detector (CTD) [75] is a cylindrical gas-filled wire chamber. It provides measurements of the charge and momentum of charged particles.

The fiducial volume of the CTD extends from $z = -1.01$ m to $z = 1.06$ m. The outer and inner diameter are 159 cm and 35 cm respectively. This results in a polar angle range coverage of $11.3° < \theta < 168.2°$ and a complete azimuthal coverage. 4608 signal wires are mounted in 72 radial layers, organised in 9 super layers (SL) (see fig. 5.4a). Each SL consists of 8 sense wire layers (see fig. 5.4b). SL 1,3,5,7,9 consist of wires oriented parallel to the beam axis, whereas

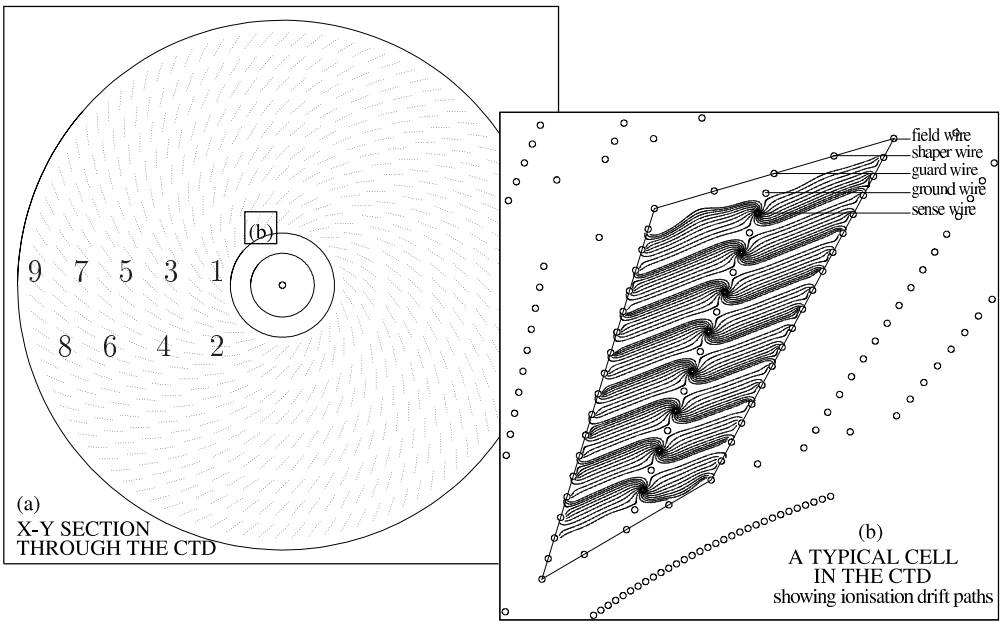

Figure 5.4: (b) XY cross section of the CTD. The numbers of the SLs are given. The even layers provide z information by stereo wires, the odd layers 1, 3 and 5 provide z by timing. (a) a zoomed single cell with field and signal wires as well as the resulting drift field lines (from [76]).

the remaining 4 SLs, called stereo layers, are inclined longitudinally by about $\pm 5°$ to allow a determination of the z position of the hit. The method to determine the z position from the inclination of the wires, called stereo technique, yields a resolution of $\sigma_z = 1.0 - 1.4$ mm. For trigger purposes the layers 1, 3 and 5 are equipped with a system measuring the z hit position using the difference of pulse arrival time at the CTD endplate, called z-by-timing system. It yields a resolution of approximately $\sigma_z = 4 - 6$ cm. The fiducial volume of the CTD is filled with a mixture of argon, CO_2 and ethane.

Traversing charged particles ionise gas molecules along their trajectories. The ionisation electrons drift along the electrical field lines towards the positively charged sense wires with a velocity of approximately 50 μm/ns. Avalanche-like multiplication of the ionisation electrons occurs very close to the sense wires with an amplification factor of approximately 10^4. The positive ions are attracted by the negative field wires.

The relative transverse momentum resolution for full-length tracks, originating from the nominal vertex position with transverse momentum $p_T > 150$ MeV, can be parameterised as

$$\sigma(p_T)/p_T = 0.0058\ p_T \oplus 0.0065 \oplus 0.0014/p_T, \tag{5.1}$$

with p_T in GeV. The first term gives the contribution from the position resolution of the hits, whereas the other two terms reflect the influence of multiple scattering before and inside the CTD, respectively. The typical primary vertex resolution is 4 mm in the beam direction and 1 mm in the transverse direction. It is, however, possible to constrain the transverse coordinates of the vertex by the beam profile, which has width of 330 μm in x- and of 90 μm in y-direction for the ZEUS 1993 to 2000 data.

After 2001 the CTD was complemented by the installation of a silicon vertex detector (Micro-Vertex Detector, MVD, see sec. 5.2). The CTD+MVD combined tracking resolution can, analogous to the CTD-only resolution, be parametrised as [77]

$$\sigma(p_T)/p_T = 0.0026\ p_T \oplus 0.00104 \oplus 0.0019/p_T. \tag{5.2}$$

5.2 The Micro Vertex Detector

The silicon–strip micro vertex detector (MVD), installed in 2001 during the HERA upgrade shutdown, was designed to significantly improve the ZEUS tracking precision and forward acceptance and thus to increase the acceptance e.g. for high Q^2 and heavy flavour events. Measurements of track displacements at the order of 100 μm and precise secondary vertex reconstruction can be used to efficiently tag heavy flavour events [78]. The physics requirements and the restricted available space in the centre of the CTD lead to the following detector design characteristics:

- radial extension smaller than 32.4 cm (inner wall of the CTD);
- polar angular coverage between 10° and 150°;
- measurements of three points per track in two projections each;
- at least 20 μm hit resolution for normal incident tracks;
- two-tracks separation of 200 μm;
- hit efficiency better than 95%;
- noise occupancy better than 10^{-3}.

The MVD is divided into a *barrel region* (BMVD) and a *forward region* (FMVD) [79].

The BMVD length of 64 cm is designed to cover the average longitudinal event vertex distribution given mainly by the average proton bunch length of ~ 20 cm. The BMVD consists of three double layers of silicon strip sensors arranged in concentric cylinders around the interaction point with a polar coverage between 30° and 150°. The inner layer of the BMVD is not complete due to the oval shaped beam pipe which is not centred around the interaction point (fig.

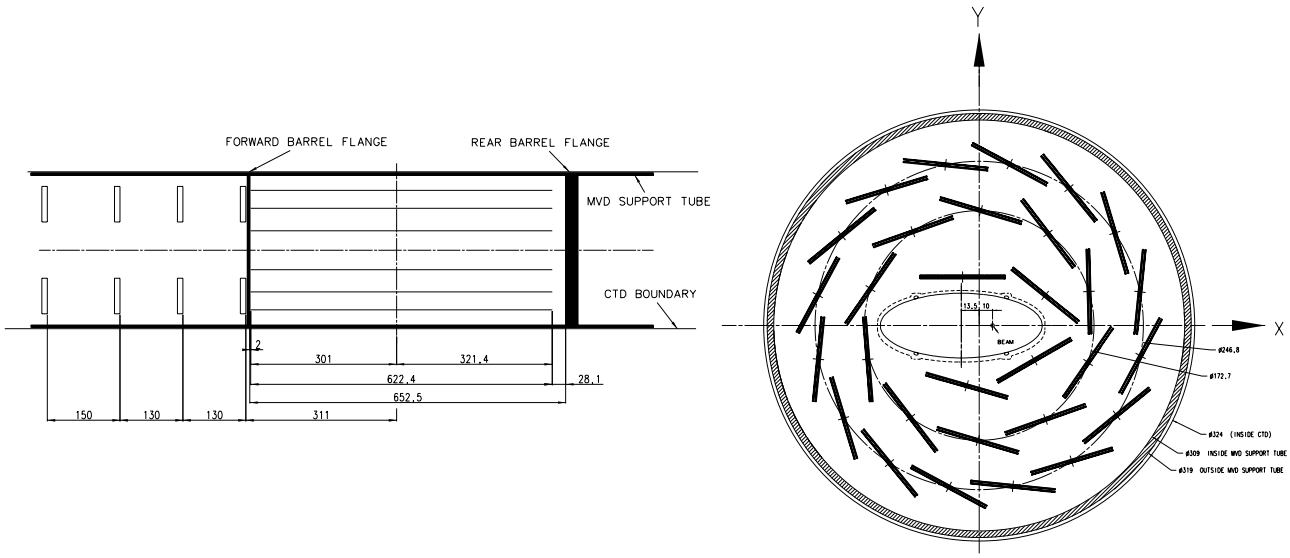

Figure 5.5: Schematic layout of the MVD along the beam direction (*left side*) and in the xy plane (*right side*) only showing the detector layers without support structures.

5.5). The single sided BMVD silicon sensors are square shaped ($64.2 \times 64.2\text{mm}^2$) and 320 μm thick. 3082 silicon strips with a pitch of 20 μm are placed on one side of the sensor. Every sixth strip is read out resulting in 512 readout strips at a readout pitch of 120 μm. Capacitive charge sharing between the strips enhances the position determination. The single hit resolution determined in test beam measurements is 7.5 μm. Two sensors are glued together next to each other with perpendicular readout strips on the same side. They form a *half module* with 512 readout channels by connecting the readout strips of two neighbouring sensors. Two half modules are glued together back to back to form a module providing two coordinates for each particle traversing it. The ambiguity due to the connected sensors per half module is resolved at the reconstruction level.

The FMVD extends the coverage in pseudorapidity to $\eta = 2.6$ and provides additional forward tracking capabilities in a region which was not or only poorly covered before. It consists of four planes (wheels) perpendicular to the beam axis. Each wheel is made of two back to back layers of 14 wedge-shaped silicon sensors of the same type as in the barrel section. The number of readout strips per sensor is 480 for forward sensors tilted by 180°/14 to provide two coordinates for a particle traversing a wheel.

5.3 Uranium-Scintillator Calorimeter

The ZEUS calorimeter (CAL) [80] is a compensating (see below) sampling calorimeter, consisting of alternating layers of absorbing and scintillating material. The absorber layers are made of 3.3 mm thick depleted uranium (98.1%U^{238}, 1.7% Nb, 0.2% U^{235}) plates wrapped in stainless steel foils. Incoming particles interact with the uranium material producing showers of hadronically and electromagnetically interacting particles of lower energy. The energy of the shower particles is measured by recording photons emitted by the scintillating layers in response to

the energy loss of the shower particles. These active layers are made of 2.6 mm thick plastic scintillator (SCSN38) plates.

Uranium was chosen as absorber material, as it provides a high yield of spallation neutrons in hadronic interactions which again loose their energy in the scintillating material. With the additional contribution from photons arising from subsequent neutron capture in the uranium, this essentially compensates the signal loss of hadronic interactions due to losses in binding energy, nuclear fission and decay products escaping detection. These losses are not present in interactions of electrons or photons, as they loose their energy predominantly by interactions with atomic electrons rather than by nuclear interactions. The ratio between signals induced by electrons and those from hadrons of the same energy e/h has been tuned by optimising the relative thickness of scintillating and absorber material. Compensation was achieved with a factor of

$$e/h = 1.00 \pm 0.05. \tag{5.3}$$

The CAL energy resolution for electromagnetic $\frac{\sigma_e}{E}$ and hadronic showers $\frac{\sigma_{\text{had}}}{E}$ has been determined in test-beam measurements to be:

$$\frac{\sigma_e}{E} = \frac{18\%}{\sqrt{E}} \quad \text{and} \quad \frac{\sigma_{\text{had}}}{E} = \frac{35\%}{\sqrt{E}} \ , \tag{5.4}$$

with E in GeV.

The CAL is geometrically segmented in three main parts: The forward calorimeter (FCAL), the barrel calorimeter (BCAL) and the rear calorimeter (RCAL), covering altogether 99.8% of the forward and 99.5% of the backward hemisphere. Given that on average the collision final state particles are boosted to the forward direction, these sections are thicker than in the rear region, ranging in interaction lengths of $\sim 7\lambda$ for the FCAL via $\sim 5\lambda$ for the BCAL down to $\sim 4\lambda$ for the RCAL. Each of these parts is subdivided into single modules. As an example a FCAL module is shown in fig. 5.6. FCAL and RCAL modules are rectangular, whereas the 32 BCAL modules, surrounding the cylindrical CTD are wedge-shaped, see fig. 5.2.

Each module consists of *towers* of 20×20 cm^2, subdivided longitudinally into one electromagnetic section (EMC) and two (only one for RCAL) hadronic sections (HAC1, HAC2). The EMC sections are additionally subdivided into four transverse cells (only two in RCAL). They have a depth in interaction lengths (X^0) of $\sim 26\ X^0$ in the F- and RCAL and of $\sim 22\ X^0$ in the BCAL. The total depth of the towers ensures that at least 90% of the jets, with energies corresponding to the kinematically allowed maximum energy, deposit at least 95% of their energy in the CAL. The efficiency of energy deposition is usually much higher, since most jets have less energy.

The smallest readout unit in the CAL is called a cell. Each of the 5918 cells is read out on two sides via wavelength shifters by photomultiplier tubes (PM). Whereas the sum of the signals of both photomultipliers is independent of the impact point of the impinging particle, the horizontal position can be determined by comparing the two signals. The time resolution of < 1 ns (for energy depositions larger than 4.5 GeV) is used to reject non-ep background with characteristic timing patterns (e.g. particles from the beam halo) already at the trigger level (see sec. 5.7 for a description of the trigger chain).

The CAL is calibrated on a daily basis using the stable signal from the natural radioactivity of the base material uranium. Additional calibrations for both the PMs and the readout electronics can be performed using laser, LED and test pulses.

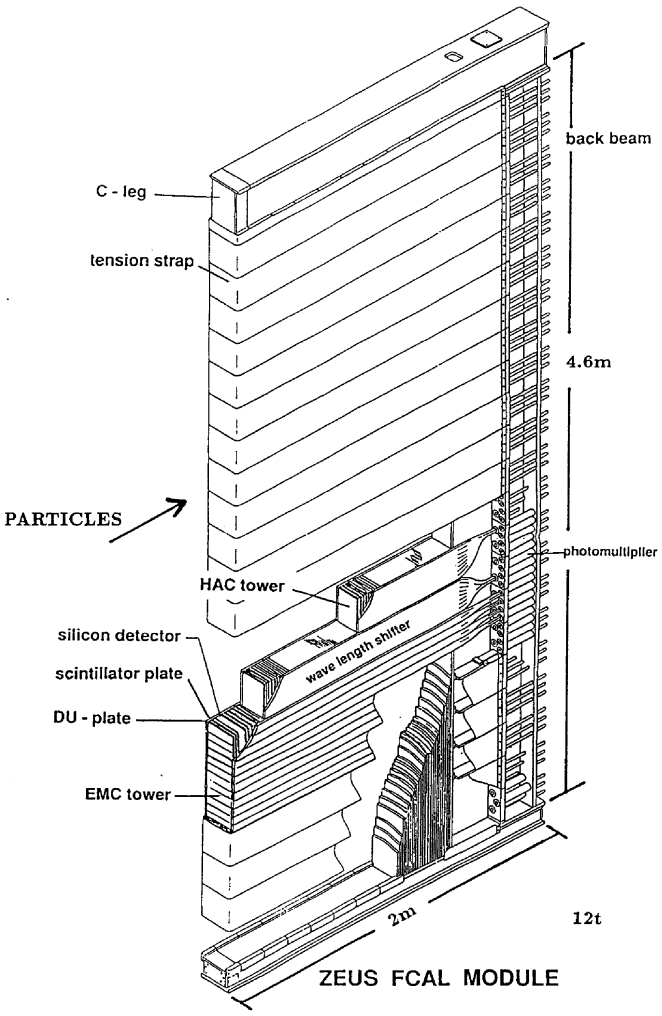

Figure 5.6: View of an FCAL module.

5.4 Muon Chambers

The muon chambers are designed to detect minimally ionising particles, such as muons, coming from the IP and crossing the CAL reaching into or passing the iron yoke. The chambers are split into two sub-detectors, the forward muon detector (FMUON, see sec. 5.4.1) and the barrel and rear muon detector (BMUON and RMUON respectively, see sec. 5.4.2). The instrumented iron yoke (BAC), also used to measure muons and is described in sec. 5.5.

5.4.1 Forward Muon Spectrometer

The forward muon detector [74] is divided longitudinally into two regions (see fig. 5.7). The inner region (FMUI), located between the FCAL and the iron yoke, and the outer region (FMUO) positioned outside the forward iron yoke. The components of the FMUON detector are:

- a system of four planes of limited streamer tubes (LST) [81] trigger planes (LST1 - LST4)

providing digital radial ρ and azimuthal ϕ readout;

- two larger planes of LSTs with digital (ρ, ϕ) *and* analogue (ρ) readout in the so called large polar angle region (LW1, LW2);
- four planes of drift chambers (DC1 - DC4);
- two large toroidal iron magnets providing a magnetic field of 1.7 T used for charge separation and momentum measurement in the angular region $5° < \theta < 16°$.

The first streamer plane (LST1) and drift chambers (DC1) make up the FMUI detector, placed inside the iron yoke while the rest of the system is located on the outside.

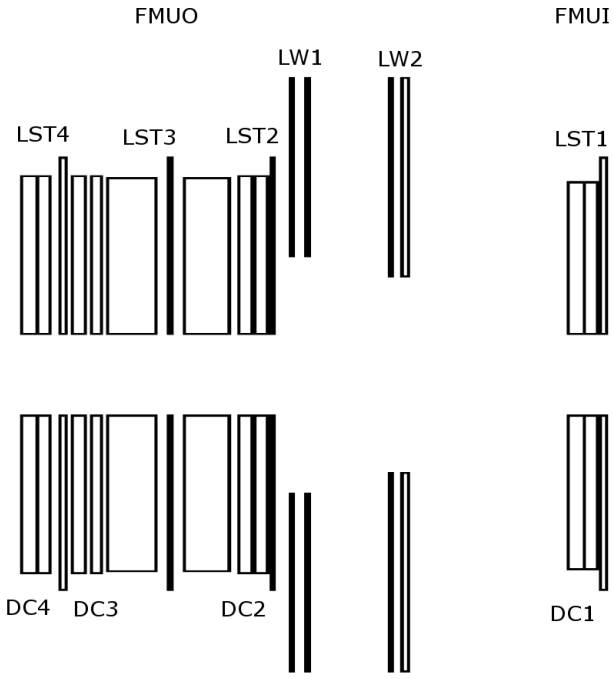

Figure 5.7: Schematic view of the forward muon detector along the beam axis.

The components of the FMUON detector are described in the following.

The limited streamer tube planes: The limited streamer tube planes are used both for triggering on events with muons and to reconstruct the azimuthal and radial position of muon candidates. A trigger plane consists of four LST chambers grouped in two half-planes. A quadrant consists of two layers of LSTs. Copper strips are attached to the outer side in polar geometry. On particle passage, the LSTs induce a signal in the radial and azimuthal copper strips. The number of radial ρ strips is 132 while each strip is 1.9 cm wide. They are divided along the bisector of the quadrant so that the simplest readout unit of the trigger plane is an octant. There are 32 ϕ strips per octant. Each strip covers an interval of 1.4° in the azimuth angle.

The drift chambers: The drift chambers are used for improving the momentum resolution. Each DC plane consists of four chambers grouped two by two in two half planes fixed on a support panel. The basic element of the chamber is a cell made of four sense wires and of the layers generating the electric drift field. Four sense wires measure the radial coordinate.

The large angle coverage planes: The two large angle coverage planes (LW) are used to achieve the desired geometrical acceptance also in the region left uncovered by the toroids ($16^\circ < \theta < 32^\circ$). Each plane consists of eight LST layers. The LST signal is induced on copper strips, radially separated by 0.7° in the ϕ coordinate and by 1.8 cm in the ρ coordinate. There are 64 ϕ strips and 192 ρ strips per octant. Using a centre of gravity algorithm a resolution of ~ 1 mm is achieved for the ρ coordinate.

5.4.2 Barrel and Rear Muon Chambers

The barrel and rear muon detector [82] covers a large area of ~ 2000 m^2, mainly consisting of LST chambers. Inner barrel muon chambers (BMUI) are arranged on the inner barrel part of the BAC. Outer barrel muon chambers (BMUO) are located on the outer barrel part of the BAC. Similar segmentation is found for the rear part with the RMUI and RMUO, see fig. 5.8. While

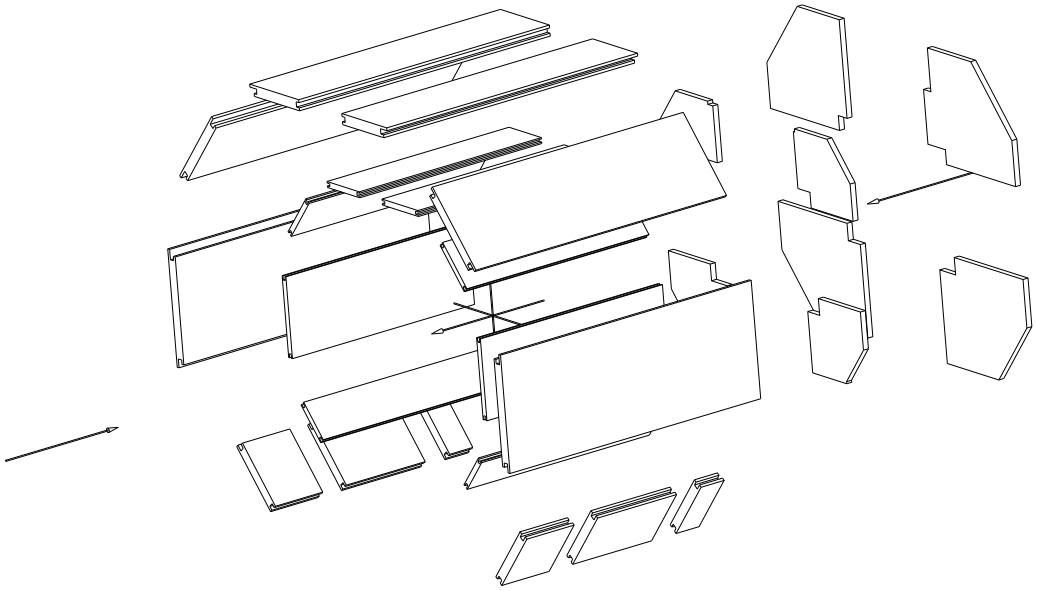

Figure 5.8: Blowup of the layout of the barrel and rear muon detector.

varying in shape and dimension, the different chambers have the same internal structure. An aluminium honeycomb structure with a width of 20 cm in BMUI and 40 cm in BMUO supports a double layer of LST chambers on both sides. Each LST is made of a plastic profile with eight cells. In each cell a copper-beryllium wire of 100 μm diameter is located. The distance between two sense wires is 1 cm.

Each LST plane is equipped on one side with 13 mm wide readout strips with a pitch of 15 mm running orthogonal to the wires. In the BMUI and BMUO chambers the LSTs are directed in parallel to the beam direction while in RMUI and RMUO they are placed parallel to the ZEUS

x direction. The spatial resolution achieved using the analogue strip readout [83] is 200 μm orthogonally to the wires and 700 μm for the coordinate parallel to the wires.

5.5 Backing Calorimeter

The iron return yoke in between the inner and outer muon chambers is interleaved with aluminium proportional tubes. This makes it a tracking calorimeter, called backing calorimeter (BAC) [84]. The BAC is used to handle events with shower leaks of high energy jets penetrating the CAL. Such events can be vetoed or corrected for using the BAC. Additionally, the BAC is used to tag muons, which is specially useful in regions scarcely covered by the muon chambers, e.g. the lower barrel region. This thesis work is one of the first to include the BAC for this purpose. The separation of muon and hadron signatures is also possible, as well as the usage of the BAC in muon triggers.

The BAC modules inserted into the yoke (fig. 5.1) consist of $7-8$ tubes (channels) with a cross section of 11×15 mm^2 each and a longitudinal length of $1.8-7.3$ m. At the centre of the tubes, gold plated tungsten wires with a diameter of 50 μm are placed, supported every ~ 50 cm in the z direction. 50 cm long aluminium cathode pads are located on top of the modules. The wires are read out on one side and provide both analogue and digital signals whereas the pads have analogue read out only.

Energy is measured by summing up the analogue signals from the wires grouped in addition into towers of a width of $25-50$ cm ($2-4$ modules) over the full depth of the BAC. The pads of $2-4$ neighbouring modules are added to pad towers with an area of 50×50 cm^2 (4 modules) similar to the wire towers. They provide a measurement of the location of the energy deposit along the wires (i.e. the z coordinate). The signals from the wires are also used to measure patterns of hit positions in the BAC used to reconstruct muon trajectories.

Details on the dimensions and numbers of the BAC's modules, pads and wires are summarised in tab. 5.1. The BAC spatial resolution perpendicular to the wires is ~ 1 mm, that parallel

	Barrel	Bottom	Forward	Rear
Area [m^2]	1902	296	460	322
Number of layers	9	9	10	7
Gas volume [m^3]	38.0	5.9	9.2	6.4
Number of 8-tube modules	2246	193	840	572
Number of 7-tube modules	658	120	280	112
Module length [m]	4.5 and 5.5	7.3	$1.8 \rightarrow 3.6$	$1.8 \rightarrow 3.6$
Number of wires	22574	2384	7980	5360
Wire towers	100	10	32	36
Pad towers	1100	150	222	230

Table 5.1: Dimensions and numbers of BAC components.

to the wires is defined mainly by the pad size, thus about 50 cm/$\sqrt{12}$. The energy resolution determined by test beam measurements is (with E the particle energy in GeV):

$$\frac{\sigma_E}{E} \sim \frac{1.1}{\sqrt{E}} \tag{5.5}$$

5.6 Luminosity measurement

The time integrated luminosity $\mathcal{L}_{\text{int}}$ is defined as

$$\mathcal{L}_{\text{int}} = \frac{N_{\text{proc}}}{\sigma_{\text{proc}}}, \tag{5.6}$$

where N_{proc} is the number of produced events for a process with cross section σ_{proc}. The determination of the luminosity at ZEUS [85] is based on the measurement of the Bethe-Heitler QED Bremsstrahlung process [86]

$$ep \to ep\gamma. \tag{5.7}$$

This process has a large cross section ($\sigma_{BH} \geq 20$ mb) and can be calculated differentially as a function of the photon energy with an accuracy of 0.5%. Thus a precise measurement of the rate and energy of the Bremsstrahlung photons allows for an accurate determination of the ep luminosity.

A lead/scintillator sampling calorimeter (LUMIG) at $z = -106$ m (fig. 5.9) detects Bremsstrahlung photons emitted at an angle $\theta_\gamma < 0.5$ mrad with respect to the beam axis. These photons leave the beam pipe through a Cu-Be window at $z = -82$ m. A carbon/lead filter shields the detector from synchrotron radiation. An energy resolution of $23\%/\sqrt{E}$ (E measured in GeV) has been achieved in test-beam measurements. The impact position of the photons can be reconstructed with a resolution of 2 mm, making use of embedded layers of scintillator fibres. The Bremsstrahlung event rate is determined counting the number of photons above a fixed energy threshold. The luminosity is then calculated by dividing the measured rate by the Bremsstrahlung cross section corrected for the detector acceptance.

Bremsstrahlung events of electrons with the residual gas lead to a large background with the same experimental signature. This background can be subtracted statistically by measuring the Bremsstrahlung rate of unpaired electron bunches (electron bunches with no corresponding proton bunch) together with a measurement of the current in both paired and unpaired bunches. The recorded Bethe-Heitler rates are sufficiently large, reducing statistical uncertainties to a negligible level. The systematic uncertainty of the luminosity measurement is dominated by the background subtraction, pile-up effects (the measurement of more than one photon per bunch crossing) and energy calibrations as well as linearity and acceptance of the photon calorimeter. The overall systematic uncertainty for the 1994-2000 data taking periods is 1.1 to 2.25%.

5.7 Trigger and data acquisition

The HERA beam bunch structure leads to a beam crossing every 96 ns, corresponding to a rate of potentially interesting events of 10.4 MHz. The rate of ep events ranges from about 0.1 Hz for NC DIS events with $Q^2 > 100$ GeV^2 (Q^2 being the negative four-momentum transfer to the exchanged boson) to 240 Hz for soft photoproduction vector meson production (for an instantaneous luminosity of $2 \cdot 10^{31}$ cm^{-2}s^{-1}) [74]. The rate of background events, on the other hand, exceeds the rate of physics events by several orders of magnitude: interactions of electrons or protons with the residual gas nuclei or elements from the beam line (beam gas events) typically occur at a rate of 10 kHz and an additional background is given by cosmic ray

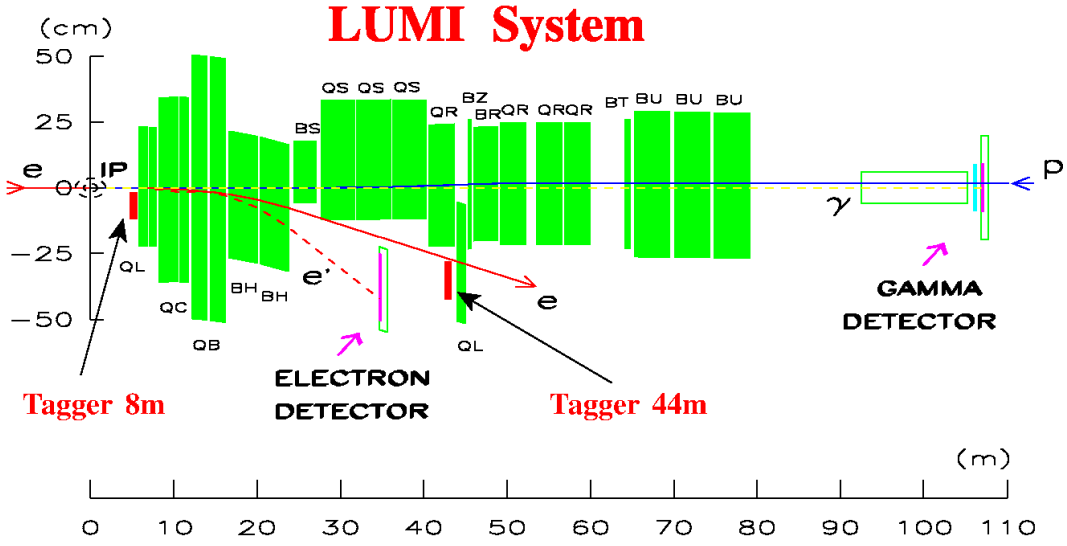

Figure 5.9: The ZEUS luminosity monitoring system. The photon detector (LUMIG) is situated at $z = -106$ m and the electron detector (LUMIE) at $z = -35$ m.

muons passing the CTD. The total data size per event is $\mathcal{O}(10^5)$ byte while the writing speed is limited to $\mathcal{O}(10^6)$ byte/s. Hence a significant reduction of the data rate and size is required.

A three level trigger system [74, 87] is used to select events online, as illustrated in fig. 5.10. The complexity of the trigger decisions rises from level to level, while the data throughput is reduced:

First Level Trigger (FLT) Each detector component is equipped with its own FLT, implemented in hard-wired logic circuits. Each FLT provides a fast trigger decision based on properties as energy sums, thresholds or timing information and passes it on to the global first level trigger (GFLT) while the event data is stored in pipelines. By combining different trigger slots a decision is made by the GFLT after ~ 4.4 μs and the accepted events are passed to the next trigger stage. The trigger processing for all components is pipelined and deadtimeless, accepting data from bunch crossings every 96 ns. The typical GFLT output rate is below 1 kHz.

Second Level Trigger (SLT) The SLT is implemented in a transputer[1] network. The decision of the GFLT is analysed further and the event quantities are recalculated to a higher degree of precision. Beam gas background is rejected on the basis of CAL timing information, which is available at this stage. The decisions of several branches of the SLT are collected by the global second level trigger (GSLT), which provides a decision after 7 ms, reducing the event rate to 50-100 Hz. For GSLT accepted events, the data of all components is combined in a single record of ADAMO [88] database tables by the event builder and passed on to the third level trigger. The GSLT was supplemented by an additional tracking trigger in 2001, called global tracking trigger (GTT).

Third level trigger (TLT) The TLT uses a computer farm for the analysis and classification

[1] A microprocessor optimised for parallel processing by Inmos (UK).

of each event. Based on physical quantities of the fully reconstructed events, such as kinematical variables, output of electron and muon finding algorithms, topologies of hadronic final states etc., a decision is made and the accepted events are classified. Accepted events (with a size of approximately 100 kB) are written to tape at a rate of 5-10 Hz and fully reconstructed offline by the ZEUS software.

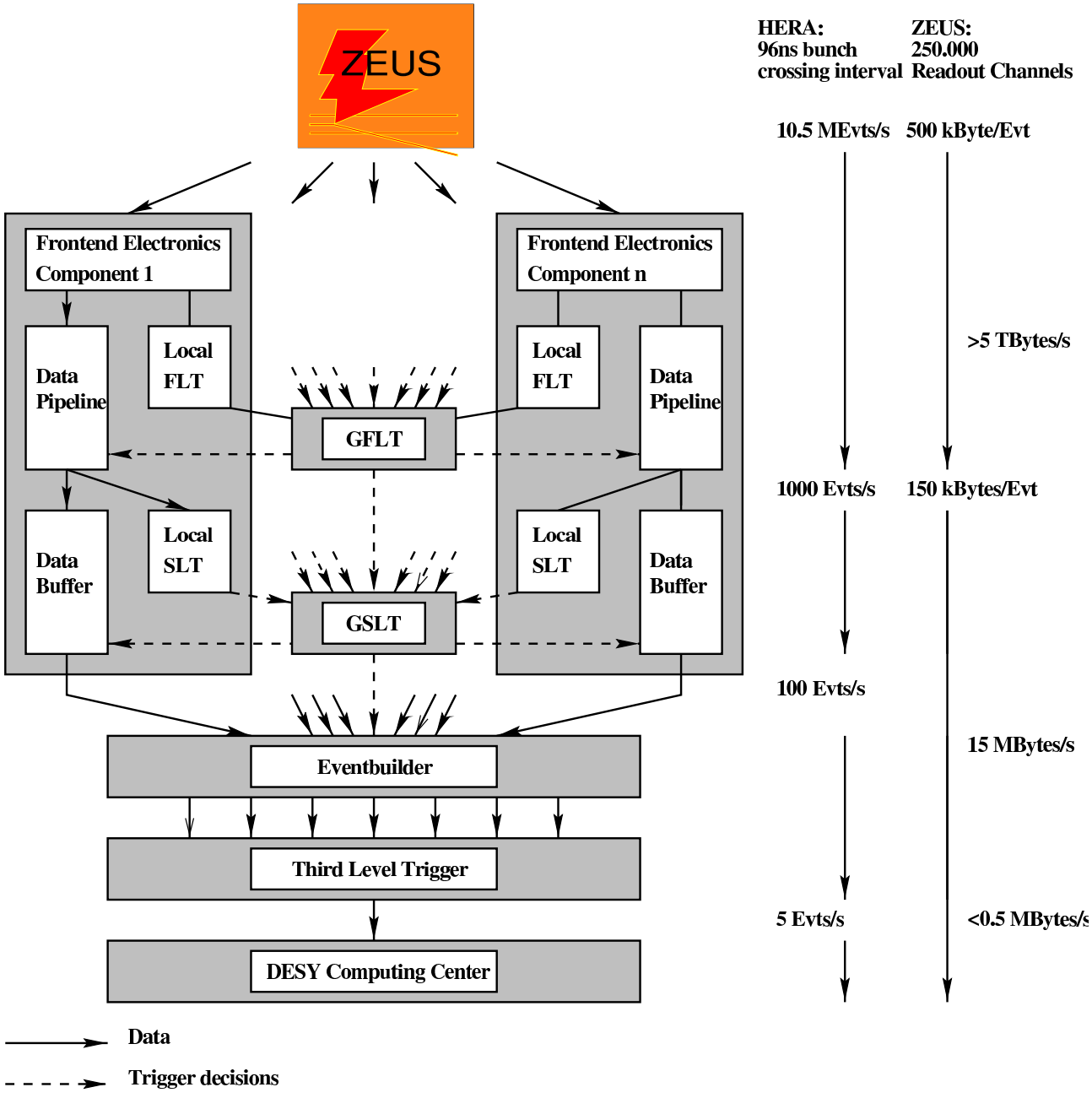

Figure 5.10: The ZEUS trigger and data acquisition system.

Chapter 6

Dataset and event reconstruction

In this section the ZEUS HERA I dataset and MC samples that have been analysed in the scope of this analysis are described. The reconstruction variables and methods applied to these samples in oder to calculate the event characteristics are also described.

Corrections which had to be applied to the reconstructed information are explained later in sec. 7.3. Of special importance here is the correction of the muon detection efficiency, summarised in sec. 7.3.1.

6.1 The ZEUS HERA I data sample

For measuring beauty production from dimuon events, a reliable dataset with well functioning and well understood detector components, especially of the muon chambers, tracking and calorimetry is needed. The largest possible well understood data sample with a consistent set of trigger configurations and stable muon chamber conditions of ZEUS pre-upgrade data has been recorded from 1996 to 2000. During these years both electrons and positrons were brought into collision with protons at centre-of-mass energies of 300 (1996-1997) and 318 (1998-2000) GeV.

The main detector quality based preselection to the data sample are applied using the ZEUS "take" routines. These routines contain veto flags for certain detector subcomponents and runs, which are set if the corresponding components malfunctioned during a given run. The veto flags are the output of data quality monitoring (DQM) jobs performed by component experts. The main ZEUS data quality flag (EVTAKE) corresponds to good data quality of the central components CTD, CAL, trigger chain and luminosity measurement. Additionally to the standard ZEUS data quality veto EVTAKE, a similar run-by-run selection based on the muon chamber quality has been applied based on DQM quality flags called MBTAKE for the barrel and rear muon chambers and FMUTAKE for the forward muon spectrometer. A period of running with a vertex shifted to ± 0.8 m in the year 2000 corresponding to an integrated luminosity of 0.815 pb^{-1} has also been excluded.

The luminosity values collected during the sub running periods are given in tab. 6.1.

running period	**interaction**	$\sqrt{s_{ep}}$ [GeV]	**luminosity** [pb^{-1}] after EVTAKE	**luminosity** [pb^{-1}] EVTAKE +FMU/MBTAKE
1996-1997	e^+p	300	38.62	38.01
1998-1999	e^-p	318	16.68	15.89
1999-2000	e^+p	318	65.88	60.17
			$\sum 121.2 \pm 3.0$	114.0 ± 2.9

Table 6.1: ZEUS data samples collected from 1996 to 2000. The luminosity values are given after EVTAKE only as well as after EVTAKE +FMU/MBTAKE

6.2 Monte Carlo samples

MC samples generated using leading order matrix elements plus additional parton showers have been employed to describe the data samples and are described in this section. Several standard generators have been used and different generator cuts applied, as listed in tab. 6.2.

The PYTHIA samples were originally generated in the context of a ZEUS analysis of beauty production in photoproduction in events with a muon and a jet [49], summarised and compared to other beauty measurements in sec. 3.4. These samples contain several basic processes of beauty and charm production: direct, resolved, excitation from the proton and excitation from the photon. These processes are described in sec. 2.5.1. Examples of corresponding leading-order Feynman diagrams are given in fig. 2.6. The PYTHIA samples have been used only for events with quasi real photons with $Q^2_{\text{generated}} < 1$ GeV^2. The luminosity of these MC samples corresponds to roughly 6 times the data luminosity for both the beauty signal and the charm background sample.

The RAPGAP sample contains direct processes only. At values of $Q^2 > m_b^2$ this is a reasonable approximation, as resolved and excitation processes (hadronic fluctuations) are suppressed by the high virtuality of the incoming photon, or in other words, due to the short timescale of the photon. At low values of Q^2, the absence of non-direct processes in the RAPGAP sample introduces a systematic error - this however is very small as it concerns only a rather small subset of events in the initially small DIS contribution of about 15% to the total sample and has been taken into account when estimating the total systematic error. The RAPGAP samples were produced for a beauty analysis in the deep inelastic scattering regime [50], also summarised and compared to further beauty measurements in sec. 3.4 and have been used for the regime with $Q^2_{\text{generated}} > 1$ GeV^2.

A detailed list of the beauty and charm MC samples with the MC cross sections and the luminosity is given in appendix C.

The J/ψ, ψ' have been produced for a HFL analysis of inelastic J/ψ, ψ' production in photoproduction [89, 90]. They have been produced using the HERWIG generator and had to be reweighted in $p_T^{\mu\mu}$ to describe the data, as explained in sec. 7.3.3.

The Υ sample has been generated in an approximate way by using the PYTHIA J/ψ with a mass corresponding to the Υ and a muonic branching ratio of 100%. This sample had to be reweighted due to a non-physical Q^2 distribution, as described in sec. 7.3.4.

Bethe-Heitler processes have been simulated using the generator LPAIR [37, 38]. Here elastic, quasi-elastic and DIS processes were generated, simulating purely a two photon exchange in the

Process	**Generator**	**Version**	**PDF** p/γ	**Parameters**
ep $\rightarrow$ b$\bar{\text{b}}$ X	PYTHIA	6.203	CTEQ4L / GRV G LO	$Q^2 < 1$ GeV^2, $m_b = 4.75$ GeV, $p_{T\ excitation}^{min} = 4.5$ GeV
ep $\rightarrow$ b$\bar{\text{b}}$ X	RAPGAP	2.0806	CTEQ5M (LO) / dir. only	$1 < Q^2 < 5{\cdot}10^3$ GeV^2 $0.01 < y < 0.85$ $m_b = 5.0$ GeV
ep $\rightarrow$ c$\bar{\text{c}}$ X $\hookrightarrow \mu$ X$'$	PYTHIA	6.203	CTEQ4L / GRV G LO	$Q^2 < 1$ GeV^2, $m_c = 1.35$ GeV, $p_{T\ excitation}^{min} = 3.0$ GeV
ep $\rightarrow$ c$\bar{\text{c}}$ X $\hookrightarrow \mu$ X$'$	RAPGAP	2.0806	CTEQ5M (LO) / dir. only	$Q^2 > 1$ GeV^2, $0.01 < y < 0.85$ $m_c = 1.5$ GeV $p_{\text{T}}^{\text{parton}} > 3$ GeV
ep $\rightarrow$ J/$\psi(\psi')$ X $\hookrightarrow \mu\mu$ X$'$	HERWIG	6.1	CTEQ4 LO	$Q^2 < 10$ GeV^2 reweighted in $p_{\text{T}}^{\mu\mu}$
ep $\rightarrow \Upsilon$ X $\hookrightarrow \mu\mu$ X$'$	PYTHIA	6.203	CTEQ4L LO	reweighted in Q^2
ep $\rightarrow \mu\mu$ X	LPAIR	-	-$^{(*)}$	one μ with: $p_{\text{T}}^{\mu} > 3$ GeV $5^\circ < \eta^{\mu} < 170^\circ$

Table 6.2: The used MC samples and the most important parameters. Some background samples were reweighted to describe the background enriched data samples as listed in 'Parameters'. (*): Here several "proton structures" were used, depending on the process.

t-channel, see left diagram in fig. 2.19.

Backgrounds from fake muons, i.e. originating from $K \to \mu$ or $\pi \to \mu$ decays, or misidentified hadrons were not simulated. They were estimated from the data, as described in sec. 8.

6.3 Event reconstruction

In this section, the reconstruction of final-state quantities used for the selection of beauty event candidates is described. Corrections applied to the reconstructed information are also described.

Tracks of charged particles were found using the CTD and the standard ZEUS track reconstruction software, explained in sec. 6.3.1.

Particle energies were reconstructed from signals in the CAL cells as summarised in sec. 6.3.2. Energy islands (2d energy clusters) and cone islands (3d energy clusters) were formed from the CAL cells and combined with tracking information to form *energy flow objects* (EFOs). This is described in sec. 6.3.3. From the EFOs, collimated bundles of particles, called *jets*, were found using clustering algorithms, as described in sec. 6.3.4.

Muons were reconstructed using all available muon detection systems of the ZEUS detector, i.e. EFOs (CTD + CAL), muon track segments in the inner and outer barrel and rear muon chambers (BRMUON), in the instrumented iron yoke (BAC) as well as in the additional forward muon system (FMUON). All available muon reconstruction algorithms have been combined into one general ZEUS muon finder, called $\mathcal{G}$MUON [91]. The muon reconstruction, is described in sec. 6.3.7.

Based on the muon track and EFO information a muon and dimuon isolation criterion was calculated, as described in sec. 6.3.8. A new quantity called *pseudo thrust* was introduced and its calculation and possible use is explained in sec. 6.3.5

6.3.1 CTD track reconstruction

Here the ZEUS tracking methods are summarised. More detail can be found in [92], furthermore a nice overview of modern track reconstruction methods can be found in [93]. Tracks were reconstructed based on CTD hit information and are found in several passes. The first pass is called pattern recognition. It consists of two separate 2d fits: a circle fit in the XY plane and a fit in the sZ plane, being a line fit for the path length s on the circle in XY. XY hit position ambiguities introduced by only measuring the distance of the ionisation along the field lines, not on which side of the signal wire the ionisation occurred, are removed by assigning CTD segments consisting of up to 8 hits in one CTD cell to proto tracks. The pattern recognition in sZ uses Z information from the CTD Z-by-timing system, which has a resolution of roughly 6 cm as well as information from the stereo super layers using the segments from the XY plane fit. Varying curvature of the track is accounted for even in the first fast pass.

The second pass is a full 3d helix parameter fit with 5 parameters of the previously determined pattern recognition tracks to the hits. Here several corrections are applied to the hits and resulting tracks. These include corrections due to the non-uniform magnetic field, time of flight

corrections, kinks of the track when passing detector boundaries and energy-loss corrections as well as corrections applied to the hits, e.g. drift velocity or pulse-hight corrections.

In a third step a main event vertex as well as secondary vertices are found from the fitted tracks. The association of the tracks to vertices is used as an additional input to refit the tracks.

As an additional step, the tracks and the error matrices are extrapolated to the CAL inner surface. Thus the positions and directions of the tracks at the CAL can be used to match CAL energy deposits to tracks.

6.3.2 CAL energy reconstruction

The CAL (see sec. 5.3) photomultiplier (PM) signals are converted into particle energy measurements during the event reconstruction. Calibration factors determined in test-beam measurements are used to translate the PM readings into values of energy. The resulting values have still to be corrected for detector effects and noise.

The main sources of noise are sparks in the PMs and so called hot cells, e.g. cells read out by temporarily badly behaving PMs or electronics. Hot cells are determined by offline CAL DQM jobs. The produced calibration lists are used to reject these bad channels. Noise signals due to small sparks are suppressed by setting cell energy thresholds for isolated cells. Cells are rejected if there is no signal in neighbouring cells and the cell itself has a signal amplitude corresponding to less than 80 MeV in the electromagnetic part of the CAL and less than 140 MeV in the hadronic part. Bigger sparks are suppressed using the redundant CAL cell readout by two independent PMs.

Persisting differences can be corrected by multiplying energy values in data by a correction factor, as described in [94]. The data-correction factors for the electromagnetic and hadronic parts of the forward, barrel and rear CAL are summarised in tab. 6.3. Additional corrections

CAL section	cell type	energy corr. 1996-1997	energy corr. 1998-2000
FCAL	electromagnetic	+4.0%	+2.4%
	hadronic	-5.0%	-5.9%
BCAL	electromagnetic	+4.0%	+5.3%
	hadronic	+8.2%	+9.6%
RCAL	electromagnetic	+2.2%	+2.2%
	hadronic	+2.2%	+2.2%

Table 6.3: Energy-correction factors for the electromagnetic and hadronic parts of the FCAL, BCAL and RCAL for the running period 1996-1997 and the running periods 1998-2000.

are needed for parts of dead material that are modelled incompletely as well as for shifts in the modelling of energy losses of minimally ionising particles (MIPs) such as muons. These corrections are applied to EFOs, as described in sec. 6.3.3.[1]

[1] A standard correction in analyses with parton-model-like events, called Back-splash correction (the subtraction of isolated clusters with energy up to 3 GeV originating e.g. from backscattered photons from the inner CAL surface) has not been applied as the correction strategy was not considered appropriate for heavy flavour events.

From the corrected CAL information, the total transverse energy $E_{\mathrm{T}}^{\mathrm{cal}}$ is calculated from all cells by the scalar sum of the transverse energy of each individual cell:

$$E_{\mathrm{T}}^{\mathrm{cal}} = \sum_{i=1}^{N_{\mathrm{cells}}} E_i \cdot \sin(\theta_i) \tag{6.1}$$

6.3.3 CAL island and energy flow object reconstruction

The basic CAL information is the energy content of a cell. From this basic measurement, higher level variables are constructed. Cells in the 3 separate layers of the CAL (EMC, HAC1 and HAC2) are clustered separately in each layer to form so called islands. To form islands, all neighbouring cells with an energy content bigger than the noise are grouped starting from the cell with the largest signal. By clustering single cells the complete energy deposits of separate particles can be determined. This method can be improved by building so called cone islands, combining islands in cones in θ and ϕ, oriented towards the interaction point. Here one starts at the outermost CAL layers (HAC2) and combines cell islands across layers guided by single pion MC probabilities [95]. The spacial centre of the CAL cone island is determined by the logarithmically weighted centre of gravity. At low momentum however the cone island method has a low resolution and some low energy particles are not measured at all.

A possible method to compensate for the low resolution at low momenta is the combination of CAL clusters with tracking information to form EFOs. The p_{T} dependence of the separate energy resolutions for CAL entries and CTD tracks are shown in fig. 6.1. Here primary vertex

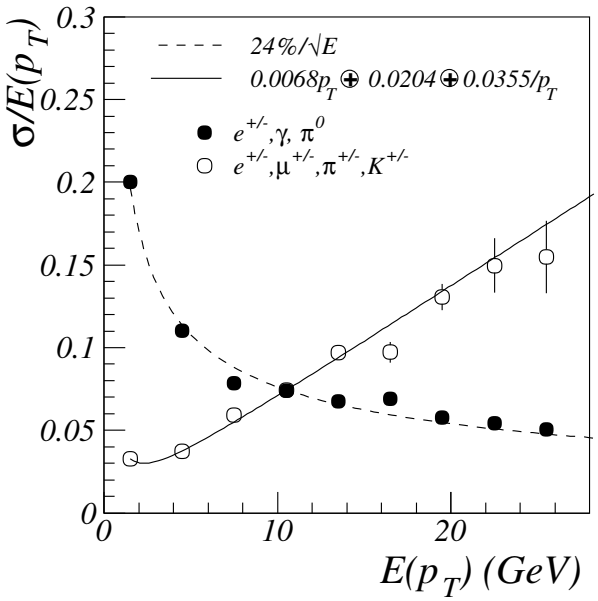

Figure 6.1: The tracking and CAL energy-resolution dependence on the transverse momentum of the corresponding particle is shown. It has been determined from single particle MC simulations [95]. The track transverse momentum resolution of CTD tracks is shown in open circles, that of the CAL in full dots.

tracks having crossed more than 4 CTD super layers are matched to the energy weighted

centre of gravity of the CAL clusters. A match is found if the track has a momentum of $|\vec{p}^{\,\text{track}}| \in [0.1, 20^{(4\ \text{SL tracks})}\ \textit{or}\ 25^{(>7\ \text{SL tracks})}]$ GeV and is either less than 20 cm away from the centre of gravity measured in a plane perpendicular to the cluster vertex connection line at the CAL inner surface or is less far from the centre than the island radius. The EFO momentum is then taken from either the CAL cluster or the matched track, depending on the resolution of the track momentum as well as the CAL cluster energy resolution. Pion masses are assumed for the matched tracks. There can be unmatched CAL clusters ($m = 0$ is assumed) as well as unmatched tracks ($m = m_\pi$ is assumed) in the final EFO sample, as depicted in fig. 6.2.

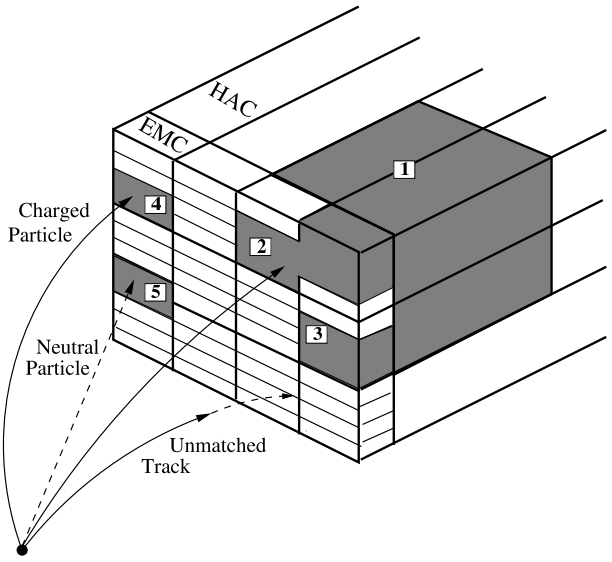

Figure 6.2: Examples of track island matches in EFOs. Four EMC and one HAC1 2d islands are shown. The islands 1, 2 and 3 are matched to from a 3d cone island. The island 4 and the cone island (1, 2 and 3) are matched with tracks. Island 5 is not matched to a track (neutral particle) and the lower right track has also not been matched (low momentum particle).

6.3.3.1 EFO and cone island energy corrections

Energy corrections are applied to the cone islands and the EFOs. The cone island corrections are:

- Correction for energy loss in dead material in front of the inner CAL surface. A detailed map of the dead material distribution is given in fig. 6.3.
- Corrections for slight inadequacies in the MC description of cracks between CAL cells.
- Corrections for energy overestimations for low momentum hadrons. At low energy the energy loss by ionisation starts to dominate over hadronic losses reducing the uranium self compensation effect ($e/h \sim 0.6$). This causes an overestimation of the particle energy which is corrected for.

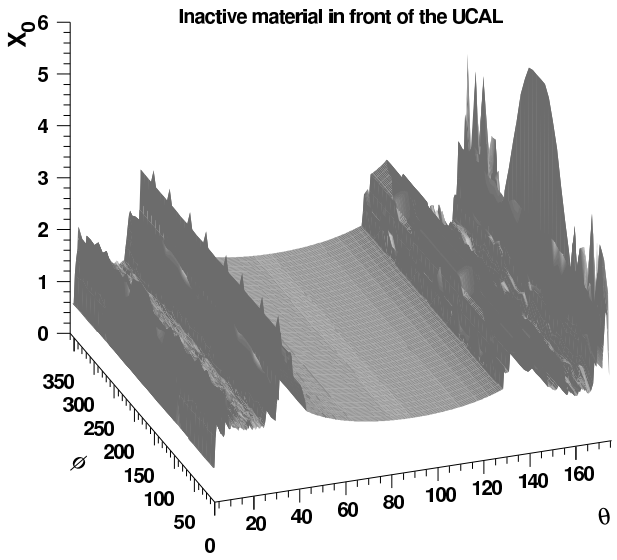

Figure 6.3: A map in η and ϕ of the dead material in units of hadronic interaction lengths of the material in front of the CAL inner surface.

Furthermore corrections are applied to correct for the presence of identified muons (see sec. 6.3.7). As they, being MIPs, do not deposit their full amount of energy in the CAL, the corresponding energy entries are corrected to the full energy of the particle using the corresponding track momentum. The EFOs corresponding to reconstructed muons are marked during the correction for the presence of a muon using the relation $\mu \rightarrow \text{EFO} \rightarrow jet$. Here two classes of muons are corrected. Isolated muons (that is, muons with a separated CAL MIP cluster and a track) are corrected by using the track information rather than the CAL MIP cluster.

Nonisolated muons can be contained in an EFO also containing hadronic activity. The EFO is then corrected by subtracting the typical muon energy loss and adding the actual muon momentum. The typical energy release of a muon in the CAL is parametrised as a function of the polar angle θ using single muon MC simulations, shown in fig. 6.4.

The following classes of EFOs are corrected per muon:

- If the EFO uses the track information for the energy determination, the EFO four–vector is already determined from the reconstructed muon properties and no correction is needed.
- If the EFO uses the CAL measurement for the four–vector determination and the energy of the EFO is less than 150% of the typical energy loss of a muon $E_{\text{Efo}} \leq 1.5 E_{\text{MIP}}$, the EFO four–vector is determined from the reconstructed muon momentum.
- If the EFO uses the CAL measurement for the four–vector determination and the energy of the EFO is larger than 150% of the typical energy loss of a muon $E_{\text{Efo}} > 1.5 E_{\text{MIP}}$, a new EFO corresponding to the reconstructed muon is added and a MIP is subtracted from the initial EFO. This residual EFO is interpreted as hadronic activity accompanying the muon.

As last correction applied herein the transverse energy of identified DIS electrons is subtracted from the total calorimetric transverse energy.

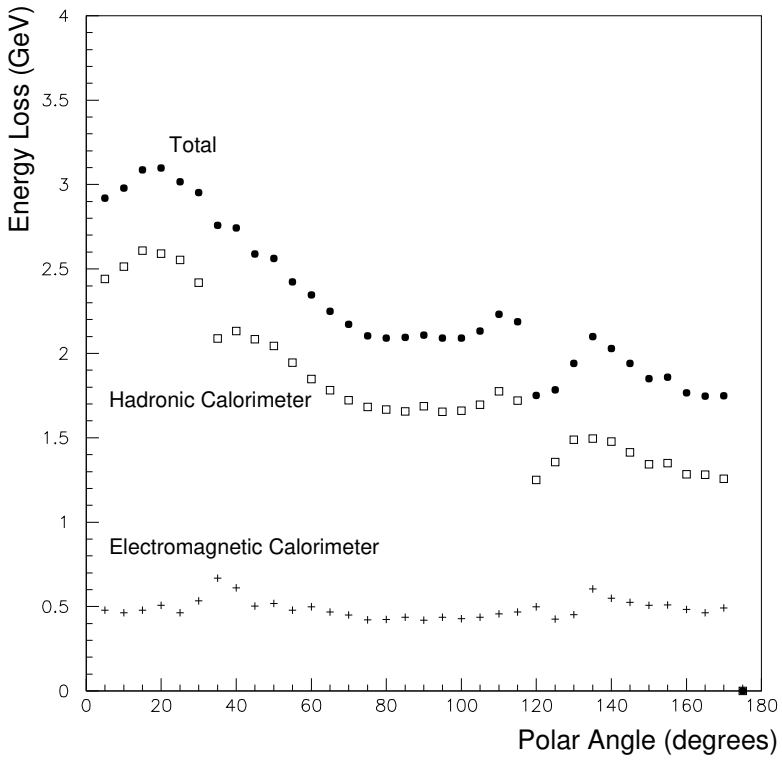

Figure 6.4: Typical muon energy loss in the CAL as a function of the polar angle θ (full circles) and the energy fractions in the electromagnetic (crosses) and hadronic (open squares) calorimeter sections. [96]

6.3.4 Jet reconstruction

Here the definition of jets is given. Jets were reconstructed when possible, but not required to be present in the events.

Jets were reconstructed using a $k_\perp$*-type clustering algorithm* [97] based on EFOs (see sec. 6.3.3). The jet reconstruction definition using this algorithm has the main advantages of being invariant against longitudinal boosts, being insensitive to the emission of very low energy particles (infrared safety) and final state collinear particle splitting (collinear safety). Additionally the forward particle spray from the proton final-state colour connection (often referred to as proton remnant) and the rear spray of particles from a potential resolved photon can be removed in a controlled way.

The formation of jets by the $k_\perp$ algorithm is implemented by the definition of:

- a test variable (energy-angle resolution) d_{kl} to test if two hadrons (each EFO is taken as one hadron) h_k and h_l belong to the same cluster;
- a recombination procedure defining the iterative formation of jets from single particle entries in the EFO list;
- a hard scattering scale $d_{\mathtt{cut}}$ to separate hard and soft processes.

The used *KTCLUS* algorithm clusters the EFOs into jets using the following scheme:

1. the resolution variables d_{kl} and d_k, d_l are calculated for all pairs of EFOs e_k and e_l:

$$d_k = (p_T^k)^2 \tag{6.2}$$
$$d_{kl} = \min((p_T^k)^2, (p_T^l)^2)\Delta \mathrm{R}_{kl}^2 \tag{6.3}$$

   where $\Delta \mathrm{R}_{kl}^2 = (\eta_k - \eta_l)^2 + (\phi_k - \phi_l)^2$

2. The smallest value from the list of resolution variables $\{d_k, d_{kl}\}$ is determined:

   - If d_{ij} is the smallest resolution variable, the two EFOs e_i and e_j are combined into a single *pseudo particle* using the so called *E recombination scheme*. Here the hadrons are treated as massive particles and their four–momenta are added as: $p_{(ij)} = p_i + p_j$. The resulting new resolution variables are given by:

$$d_{(ij)} = (\vec{p}_{T,i} + \vec{p}_{T,j})^2 \tag{6.4}$$
$$d_{(ij)k} = \min((\vec{p}_{T,i} + \vec{p}_{T,j})^2, (\vec{p}_{T,k})^2)\Delta \mathrm{R}_{(ij)k}^2 \tag{6.5}$$

     where $\Delta \mathrm{R}_{(ij)k}^2 = (\eta_{(ij)} - \eta_k)^2 + \Delta\phi_{(ij)k}^2$ to guarantee the longitudinal boost invariance.
   - If d_k is the smallest resolution variable, the EFO e_k is removed from the EFO list and is included in a soft so called *remnant jet*.

3. This procedure continues until all particles and pseudo particles not included in remnant jets have resolution variables larger than the hard scale $d_{\mathtt{cut}}$ where $\Lambda^2 \ll d_{\mathtt{cut}} \ll s$ with Λ the QCD scale and $\sqrt{s}$ the centre-of-mass energy. For this analysis, the hard cutoff scale was chosen as $d_{\mathtt{cut}} = 1$ GeV.

This procedure results in *hard final-state jets* and remnant jets. The use of the E recombination scheme in HFL studies is advantageous compared with other recombination schemes [97] as the massive approach yields a good agreement of measurements and theoretical predictions of jets from beauty quarks [28].

In this analysis, only jet candidates with

$$E_{\mathrm{T}}{}^{\mathrm{jet}} > 4.0 \text{ GeV} \quad \text{and} \quad |\eta^{\mathrm{jet}}| < 2.5 \tag{6.6}$$

are counted as jets. The lower E_{T} cut is introduced to ensure the correspondence of a jet to a initial quark, while the η cut removes remnant jets and effects due to CAL cell sizes.

6.3.5 Pseudo thrust

Beauty quarks produced close to the kinematic threshold have very low transverse momenta p_{T}^b thus not giving rise to collimated bundles of hadrons (jet) but rather a broad spray of particles in the detector. It should be possible to separate events produced near threshold from those giving rise to collimated two-jet systems (e.g. charm events) by cutting on a variable sensitive

to the event shape. Such a variable shall be defined here. Let us call it *pseudo thrust* (T_{pseudo}). The definition is given by:

$$T_{pseudo} = \frac{\sum_{i=1}^{n\text{EFO}} \vec{p}_i \cdot \vec{T}_1 + \sum_{i=1}^{n\text{EFO}} \vec{p}_i \cdot \vec{T}_2}{\sum_{i=1}^{n\text{EFO}} \vec{p}_i} \tag{6.7}$$

The sums run over all reconstructed EFOs, where the $\vec{p}_i$ are the momenta of the EFOs and the unit vectors $\vec{T}_{1(2)}$ are iterated until the scalar T_{pseudo} is maximised:

- First T_{pseudo} is maximised in ϕ for $\theta = \pi/2$.
- The plane perpendicular to the now determined axis in ϕ (fig. 6.5 left) divides the detector into two hemispheres.
- In these two hemispheres, $\vec{T}_1$ and $\vec{T}_2$ are iterated separately in θ while keeping the previously found ϕ fixed (thus allowing a kink in the zx plane, see fig. 6.5 right).

As an example a dimuon event with the measured pseudo thrust axis is shown in fig. 6.5. This new method, that is, allowing the additional kink in the axis in θ, allows to compensate

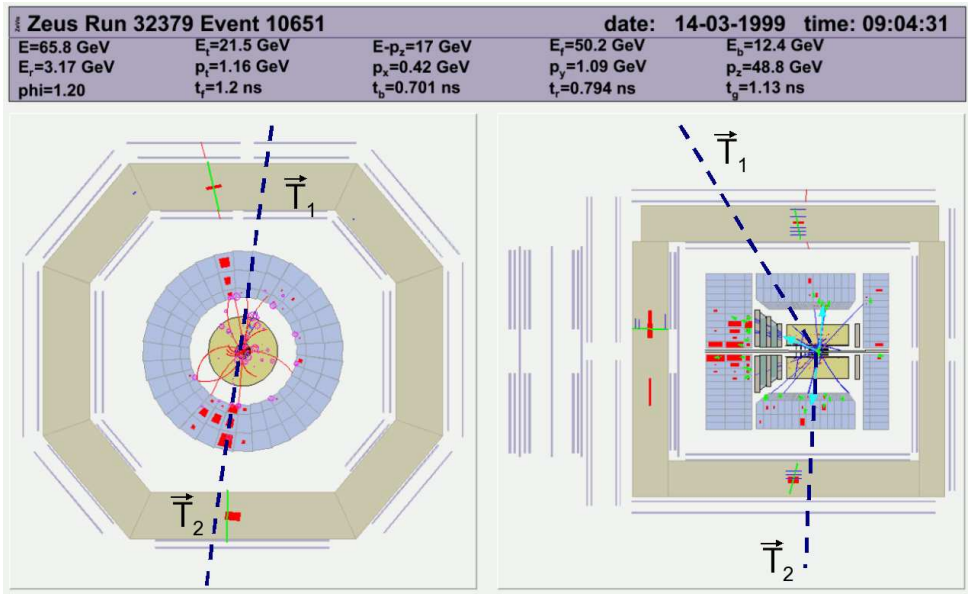

Figure 6.5: A dimuon event in ZEUS. The lines give the measured pseudo thrust axes. Notice the kink in θ compensating the longitudinal boost.

for the unknown longitudinal boost of the initial $b\bar{b}$ system. T_{pseudo} is inspired by the thrust initially used in ee collisions to select two-jet like events. It has a value close to 1 for a perfectly back-to-back events with a very small spread and approaches 0.5 for isotropic events. The pseudo-thrust distributions for nonisolated dimuon events in charm and beauty MC (PYTHIA direct process only) are shown in fig. 6.6. Beauty events, being produced with lower tansverse momentum than charm events, have on average a lower pseudo thrust.

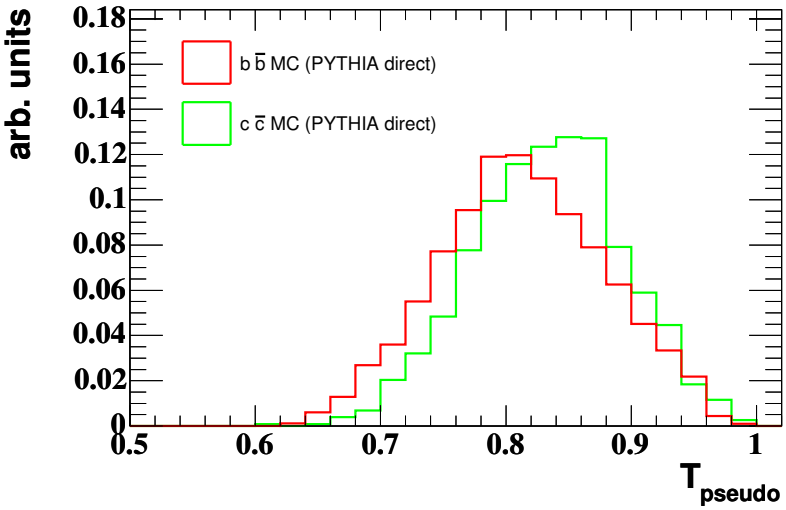

Figure 6.6: Peusdo thrust distributions for nonisolated dimuon events in charm and beauty MC (PYTHIA direct process only).

The pseudo thrust could be combined with measurements other tags to separate beauty events from other processes, e.g. with the muon momentum relative to the closest jet, $p_{\mathrm{T}}^{\mathrm{rel}}$ and impact-parameter tags. Events with low p_{T}^{b} should be broad and have no jets but lead to low values of the pseudo thrust, whereas high p_{T}^{b} events should have jets and thus allow for a $p_{\mathrm{T}}^{\mathrm{rel}}$ measurement. Most beauty events should contain tracks with large impact parameters.

6.3.6 Electron reconstruction

Scattered electrons were tagged to be subtracted from the total $E_{\mathrm{T}}^{\mathrm{cal}}$. The SINISTRA finder was used [98]. This finder uses a neural network based approach. The input variables are purely CAL based. From the lateral and longitudinal shape of the cluster in the CAL an output value is determined which is then combined with tracking information to find the most probable electron candidate. The cuts applied to the electron candidate and the finder output are given in tab. 6.4. These cuts are standard ZEUS electron selection cuts, see e.g. [50]:

- a well reconstructed electron was required with the cuts on E_e, Q^2, y and p_{si},
- the rear box cut assured that the electron was inside the acceptance of the CAL,
- and backgrounds are reduced using the $E - p_z$ cut.

The SINISTRA finder is optimised for tagging scattered electrons. The tagging efficiency for semileptonic decay electrons is rather low and other finders are used for that purpose, while for electrons within $\theta_e \geq 2.2$, $E'_e \leq 30$ GeV and $Q^2 \leq 100$ GeV^2 (the dominant part of the scattered electrons lie within these boundaries) it is as high as 85% at 10 GeV rising to full efficiency at 17 GeV [99].

Property	cut value
electron momentum transfer	$Q^2 > 2$ GeV^2
inelasticity	$y \in [0.05,\ 0.7]$
finder probability (Sinistra)	$p_{\mathrm{si}} > 0.9$
energy of electron (sum of cells of electron island)	$E_{\mathrm{ele}} > 10$ GeV
rear box cut around beam pipe	$\lvert x_{\mathrm{ele}}\rvert > 12$ cm or $\lvert y_{\mathrm{ele}}\rvert > 6$ cm
experimental DIS selection criterion	$E - p_z \in [40,\ 60]$ GeV

Table 6.4: The cuts applied to the reconstructed electron candidate are given here. The electron candidate (if any) with the highest probability was chosen as the scattered electron in the event.

6.3.7 Muon reconstruction

For efficiently tagging dimuon events, a highly efficient single-muon reconstruction with a good signal-to-background ratio is required. This has been achieved by using the high level of muon-signature redundancy supplied by the ZEUS detector. First the main features of muon signatures in the ZEUS detector and also the corresponding backgrounds with similar signatures are described. Then different muon finder algorithms are described. How they were combined by the general muon finding package $\mathcal{G}$MUON [91] is also described.

6.3.7.1 Muon signature

Four main features are used to tag the signature of muons from beauty decays with the ZEUS detector.

1. The charge of the muons leads to a track that can be reconstructed using the tracking detectors. From this track the muon momentum and direction can be determined.
2. Muons from beauty decays are produced very close to the primary ep collision point and thus are associated to the primary vertex within the resolution of the CTD (prompt muons)[2]. Requiring the muon track to be associated to the primary vertex can reduce muons from Kaon and pion decays, considered as background here.
3. The muon energy loss due to ionisation in matter is very low (for muons with $p_{\mathrm{T}}^{\mu} > 0.3$ GeV as e.g. from beauty decays). The muons are therefore classified as MIPs. Whereas all other particles (e.g. Kaons, pions, electrons) are stopped in the CAL, depositing the total amount of their energy, the muons have a high penetration power and typically lose only about 1 GeV/m in uranium, thus reaching the muon chambers.
4. Muons from heavy flavour decays are accompanied by hadrons thus nonisolated.

To use all features and to arrive at a large geometrical coverage and high detector efficiency, measurements from the tracking detectors were matched with those from the CAL, the inner, outer and forward muon chambers as well as from the BAC. This combination of measurements is performed within the general muon reconstruction package $\mathcal{G}$MUON.

[2] With the MVD it becomes possible to use even the very short decay distance of B mesons to identify events.

6.3.7.2 Muon backgrounds

There are several sources of backgrounds to the prompt muon signature [91].

- Muonic Kaon and pion decays in flight. Charged Kaons and pions have long lifetimes, but still have a finite probability to decay within the CTD volume before they reach the calorimeter or inside the calorimeter before they interact ($c\tau$ of 3.7 and 7.8 m, respectively). This probability varies from several % for 1-2 GeV Kaons to $\sim 10^{-3}$ for 10 GeV pions. Fortunately not all these decay muons are misidentified as prompt muons.
  - The decay muons have lower momenta than the original hadrons, so they often do not reach the muon detectors.
  - If the decay occurs late in the CTD or in the CAL, the measured momentum will be the one of the original hadron. The decay muon, if at all, will reach the muon chambers with much lower momentum than expected, and exhibit much larger multiple scattering. This often results in a bad matching χ^2, which can be used to reduce this background.
  - If the decay occurs early in the CTD, the measured momentum will be approximately the one of the decay muon. However, due to the decay kink, the track will tend not to be associated to the primary vertex, and will often be rejected by a vertex association requirement. This is particularly valid for Kaon decays, which produce a bigger decay kink.
  - Sometimes the decay kink is resolved by the CTD, and reconstructed as a secondary vertex. This can again be used to reject the muon candidate. However, if the kink is not resolved, and the track is still associated to the primary vertex, the "muon" momentum can be mismeasured since the kink is misinterpreted as an additional contribution to the track curvature. In particular, it can reduce the curvature. Low momentum K and π decays can thus sometimes result in high momentum muon candidates. Sometimes these candidates also survive the matching cuts. This is one of the dominant backgrounds to nonisolated muons at very high momenta.
- Leakage of hadronic showers. Hadronic interactions produce showers of varying depth, which logarithmically increases with hadron energy. In particular for high energy jets, there is a small but finite probability that one of the shower particles "leaks" out of the back of the calorimeter, and is detected in the inner muon chambers or in the BAC. The high energy hadron which produced the shower will approximately point to this place, and can be mistaken for a muon if it survives the matching cuts. This is one of the dominating backgrounds for muons in high E_T jets. Since the BAC normally completely absorbs such shower leaks, this background becomes negligible if the muon is required to reach the outer muon chambers.
- Sail through of hadrons. There is a very small, but finite probability that a hadron will not interact at all before it stops or leaves the detector. In this case the hadron appears as a minimum ionising particle, and is indistinguishable from a muon. This is called "sail through" or "punch through"[3]. Fortunately, this irreducible background decreases

[3]the term "punch trough" is sometimes also used for shower leaks, and is thus slightly ambiguous.

exponentially with penetration depth (number of interaction lengths crossed) and is thus usually small.

- Cosmic ray muons. A single cosmic ray muon crossing the detector close to the vertex region can be misreconstructed as two oppositely charged muons originating from the same vertex. Since both the event timing and the "vertex" distribution are random for such events, most of them can be rejected using vertex and timing cuts. The remaining ones can be removed by requiring that the two muons are not completely back-to-back in ϕ and θ. Occasionally, a cosmic ray muon accidentally overlaps with a good *ep* event. This background can again be removed by vertex cuts and timing cuts on the muon MIP.
- Matching ambiguities. Non-muon tracks from the central tracking system can be accidentally associated to muon system hits or tracks produced by either a true muon or a background "muon" from one of the other background categories above. The momentum of this misassociated track will then be assigned to the muon candidate. Through the same mechanism, alternative reconstruction solutions can exist for the same muon candidate, at most one of which is the true muon. This is called matching ambiguity background.

Hadron-related backgrounds, including matching ambiguities, are the dominant background source for semileptonic muons from heavy flavours, while cosmic rays dominate the background for elastic dimuon candidates.

6.3.7.3 Combined muon finding in $\mathcal{G}$MUON

The muon signature can best be reconstructed when optimally combining all available sub signatures found in the separate detector components into one muon object. An approach to this aim is explained here. The general muon finder package ($\mathcal{G}$MUON [91]) is built as a combination of a large set of ZEUS muon finder algorithms. The algorithms can be grouped into finders using the CAL (MUONFIND, MV), the barrel and rear muon chambers (GLOMU, BREMAT), the BAC (MUBAC) and the forward muon spectrometer (MCTS, MPMATCH, MUFO).

The general methods of the different algorithms are summarised below, followed by the methods of combining the results of these algorithms.

MUONFIND The MUONFIND [91] algorithm performs a simple matching of CTD tracks with CAL cone islands compatible with a MIP signature. It is used only for high momentum ($p_{\mathrm{T}}^{\mu} >$ 2 GeV) CTD tracks.

MV This muon finding algorithm finds and classifies CAL energy clusters by their shape and orientation using a neural network like approach, called phase space probability function [100]. The function outputs a probability for the examined cluster to have been induced by a minimally ionising particle, such as a muon, coming from the event vertex. It also matches CTD tracks with the MIP CAL cone islands.

The track cluster match is performed at the CAL surface using simple distance of approach cuts using the CTD track extrapolation to the CAL. For low momentum muons and in the case

of hadronically nonisolated muons the MV algorithm alone does not provide a high signal to background ratio (S/N).

GLOMU The GLOMU algorithm [101] provides simple matches (based on distance and angle cuts) between CTD tracks and inner, outer, or inner+outer BRMUON track segments. It also provides matches to MIP clusters, though less sophisticated than MV. Several versions of this algorithm exist, both for the trigger at TLT level, and in the standard ZEUS reconstruction.

BREMAT The BREMAT algorithm [102] reconstructs muons by matching track segments measured in the inner and/or outer muon chambers with CTD tracks. The following CTD track preselection is applied within BREMAT:

- momentum $p > 1$ GeV
- polar angle $\theta > 20°$
- track starting from CTD super-layer 1 and extending at least to super-layer 3
- distance of closest approach (DCA) of the muon track helix to the origin of the coordinate system in which the CTD track helices are defined (reference point) $|D_H| < 10$ cm
- z position of the DCA to the reference point $|Z_H| < 75$ cm
- χ^2 per number of degrees of freedom ($d.o.f.$) of the track fit $\chi^2_{\text{d.o.f.}} < 5$
- distance Δ between a central point on a barrel/rear muon segment and the crossing point of a straight line obtained by continuing the track to the muon chambers $\Delta \leq 150$ cm

To match the CTD to the muon-chamber tracks, the CTD track is extrapolated to the inner muon chamber plane. The possible scattering processes of the muon passing the considerable amount of material on the way to the muon chambers (e.g. the magnet, CAL) as well as the variation of the magnetic field along the trajectory are simulated using the GEANE [103] package and also included in the error matrix of the extrapolated CTD track. The material in front of the inner muon chambers leads to an effective momentum threshold for BREMAT muons of about $|\vec{p}^{\,\mu}| \approx 1$ GeV.

For matching with an inner muon chamber track, the extrapolated CTD track is then matched in position and angle in two projections (4 d.o.f. match). If the muon chamber track segment spans the inner and outer muon chambers, one can derive an additional muon momentum estimate from the two muon chamber tracks alone (as the yoke magnet field bends the muon track). In this case, the momenta of the extrapolated CTD track and the muon chamber track are matched too, yielding an additional degree of freedom and a higher quality match (5 d.o.f match). The matching yields a χ^2 value, which is used to calculate a matching probability.

MUBAC The MUBAC algorithm [104] reconstructs muon segments from the BAC strip and pad information (see sec. 5.5). Rather precise position information of the order of 1 cm is gained from the strip information ($r\phi$ plane in the barrel BAC and zr plane in the forward and rear BAC). The other position is only loosely constrained with a resolution of 0.15 to 2 m, depending on the position in the BAC and whether the position information is derived from analogue wires only (z resolution of $0.9 - 2$ m given by the wire length) or also from the pad readout (z resolution ~ 0.15 m). A simple closest approach (DCA) method is used to match CTD tracks to the reconstructed BAC muon segments. CTD tracks are extrapolated in a straight line from the vertex towards the inner face of the BAC. The track is required to differ less than DCA < 50 cm or DCA < 120 cm, depending on whether additional supporting muon signature measurements from the CAL or the outer muon chambers exist.

MCTS MCTS segments [91] are obtained by combining a simplified curved spline fit in the FMUON system with a straight line fit through the CAL and the CTD towards the primary vertex, including an estimation of the muon energy loss. They thus provide a rudimentary momentum estimate at the vertex based on FMUON information only.

MPMATCH The MPMATCH algorithm [105, 106] matches FMUON segments with CTD primary vertex tracks using a KALMAN filter technique [107, 93]. As in BREMAT, the CTD tracks are extrapolated using GEANE. The muon momentum is determined from the combined track measurement. Requirements on CTD track quality are minimal, in particular, there is no minimum super-layer cut. CAL or BAC information is not used within MPMATCH.

As for BREMAT a matching probability is calculated from the matching χ^2, where for the forward muon detector the maximum number of degrees of freedom is 11. The innermost chamber which is included in the fit is given and can be used to estimate the muon candidate quality.

MUFO MUFO [91] is an algorithm very similar to MPMATCH which has been developed in parallel. It has two main sub streams.

- Match (KALMAN filter fit) between an FMUON segment, a CTD track, and the primary vertex. This is essentially identical to MPMATCH and yields almost the same muon candidates.
- Match between an FMUON segment and the primary vertex, without a CTD track. This is interesting in particular for the very forward region in which a CTD track might not be reconstructed.

$\mathcal{G}$MUON This algorithm combines all finders above. Whereas each separate finder might be limited to reconstruct only a certain type of muon candidates (e.g. isolated muons, high or low p_{T} muons, forward muons, etc.) and may partially have limited geometrical coverage, the combination of all finders drastically reduces these limitations. The higher level of redundancy can be used to increase the S/N or, at the same S/N, increase the number of muon candidates. The number of muon candidates is increased both by being able to lower the muon momentum

cut due to the increased redundancy and by reduced geometric inefficiency due to the logical OR of finders.

Minimally, $\mathcal{G}$MUON can be used as a simple front end to the separate finders. Additionally, as the main output, it provides a qualification of the muon candidates ranging on a scale from 0 (worst S/N) to 6 (best S/N), the so called "muon quality". The S/N dependence on the muon quality has been estimated using a beauty and light flavour MC sample. For each step in muon quality, the S/N is typically raised by roughly a factor of two. The determination of the muon quality is based on the number of the above finders that found the candidate and the quality of the respective matches. The complete list of finder combinations and major cuts applied to the matching probabilities is given in appendix D. Good MPMATCH or BREMAT candidates as well as good MUBAC matches are assigned a quality of four or greater. Also weaker candidates, e.g. a MUBAC candidate with loose matching are given this quality if an additional MIP signature is found by MV or MUONFIND. Only muons found separately or by combinations of the finders BREMAT, MUBAC, MV, MUONFIND, MPMATCH or MUFO were used in this analysis.

Forward muon correction: A correction for the muon quality is applied for forward muons. The definition is given in tab. 6.5. The quality is reduced if less than four (out of 8) forward muon chamber planes were included in the track fit and if the muon track does not start at the innermost plane. Additionally the quality is lowered for forward MUBAC muons if there is no supportive measurement from MPMATCH. The quality is reduced less if the muon has also been found by MV or MUBAC. The resulting new quality is used only if it is lower than the original value.

Found by	Property	value	quality change
MPMATCH or MUFO	Nr. d.o.f.	3	-2
MPMATCH or MUFO	Nr. d.o.f.	1	-3
MPMATCH or MUFO	Starting at innermost plane	no	-1
MPMATCH or MUFO	MUBAC match	yes	+1
MPMATCH or MUFO	MV match	yes	+2
MUBAC	not (MPMATCH or MUFO) and $\eta^\mu > 1.2$	-	-1

Table 6.5: Definition of the forward muon quality correction.

Muon EFO association: Muons are associated to EFOs. The following selection is applied to these muons:

- quality of the muon ≥ 4
- muon track is a vertex fitted track
- $p^\mu > 1$GeV

The corresponding EFO is found by requiring the muon to have the same track as the EFO.

6.3.8 Muon and dimuon isolation

Dimuons from semileptonic beauty decays are accompanied by hadronic activity. Dimuons from background events like the muonic quarkonia decays or Bethe-Heitler like events usually lead to very isolated dimuons in the detector. To differentiate between these two event classes, a dimuon isolation was defined. First the single muon isolation I^{μ} was calculated from which then the dimuon isolation $I^{\mu\mu}$ was determined.

The single muon isolation is defined as the total sum of the transverse momenta of all EFOs with an angular distance of

$$\Delta R = \sqrt{\Delta\varphi^2 + \Delta\eta^2} < 1$$

between the EFO and the muon, excluding those EFOs that have been associated to the muon, i.e. are part of the muon signature. The single muon isolation is then calculated according to:

$$I^{\mu_j} = \sum_{i=1}^{n\text{EFO}} p_{\text{T}}^{\text{EFO}_i}{}_{|\text{EFO}_i \neq muon_j} \qquad \Delta R < 1 \tag{6.8}$$

An EFO is associated to a muon and thus not included in this sum, if:

- the muon track is identical to the EFO track or
- the muon and the EFO are separated by $\Delta R < 0.02$ (only for EFOs containing one track and one island) or
- it is the closest EFO to the muon inside a cone of $\Delta R < 0.4$ with a $p_{\text{T}}^{\text{EFO}} < 3.0$ GeV.

The dimuon isolation is the root mean square of the single muon isolations:

$$I^{\mu\mu} = \sqrt{I_{\mu_1}^2 + I_{\mu_2}^2} \tag{6.9}$$

The dimuon isolation distribution for J/ψ and beauty events is shown in fig. 6.7. The J/ψ events are peaked at low values of $I^{\mu\mu}$.

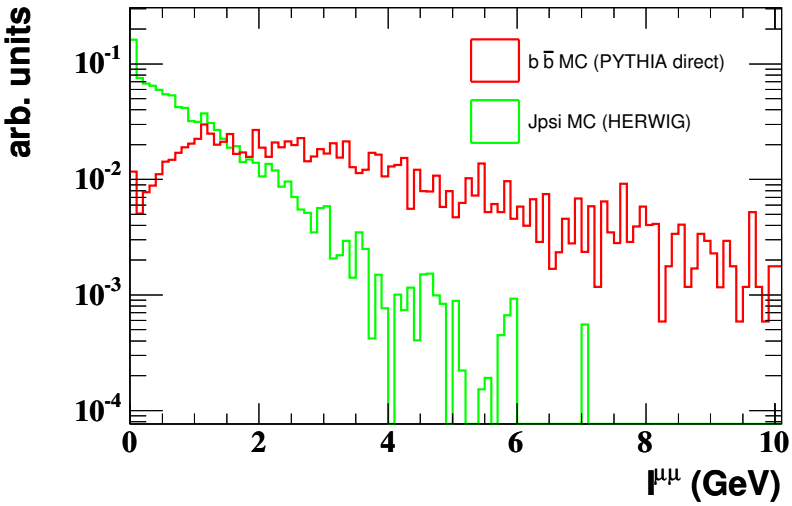

Figure 6.7: Dimuon isolation distributions for J/ψ (HERWIG) and beauty MC (PYTHIA direct process only).

Chapter 7

Event selection and MC corrections

Beauty event candidates were selected from the dataset described in sec. 6 requiring the presence of two well reconstructed muons as well as a total transverse energy deposit of the order of twice the beauty quark mass in the calorimeter. Additional data cleaning and cosmic cuts were used to suppress experimental backgrounds.

Trigger requirements were used on both data and simulated events to control the bias of the ZEUS online data selection.

Corrections were applied to the muon MC information and to several background MC samples. They are summarised at the end of this chapter, following a summary of the principle of the beauty measurement and the explanation of the selection criteria.

7.1 Principle of the measurement

A summary of the ideas behind the dimuon beauty measurement is given here. The selection criteria are based largely on these principles.

Two main event classes contribute to the beauty signal to be measured. First, events in which the two muons originate from the same parent B hadron, e.g. through the sequential decay chain $b \to c\mu X \to s\mu\mu X'$. These yield unlike-sign muon pairs produced in the same event hemisphere and are constrained to dimuon invariant masses of $m_{\text{inv}}^{\mu\mu} < 4$ GeV (i.e. a partially reconstructed B-meson mass). Secondly, events in which the two muons originate from different beauty quarks of a $b\bar{b}$ pair. These can yield both like- and unlike-sign dimuon combinations, depending on whether the muon originates from the decay of the primary beauty quark, or from a secondary charm quark, and whether $B^0\overline{B^0}$ mixing has occurred. Such muons will predominantly be produced in different hemispheres, and tend to have a large dimuon mass.

An important background contribution arises from charm-pair production, where both charm quarks decay into a muon. This yields unlike-sign muon pairs only, and the two muons will be produced predominantly in opposite hemispheres.

Since the charm background is too small to be measured directly from the dimuon data, it was normalised to the charm contribution to the $D^* + \mu$ sample [55] explained in sec. 3.4.3, which has a very similar event topology.

Other backgrounds yielding unlike-sign muon pairs include heavy quarkonium decays and Bethe-Heitler processes. In contrast to muons from semileptonic decays, muons from these sources are not directly accompanied by hadronic activity, thus giving an isolated muon signature.

Beauty production is the only source of genuine like-sign muon pairs. Background contributions to both like- and unlike-sign combinations include events in which either one or both muons are fake, i.e. originate from $K \to \mu$ or $\pi \to \mu$ decays, or misidentified hadrons. This background is referred to as *light-flavour background*. Dedicated studies, summarised in sec. 8.1.3.1, have shown that the charge of the two fake muons is almost uncorrelated, i.e. the contributions to the like- and unlike-sign dimuon distributions are almost equal. The *difference* between the unlike- and like-sign distributions is thus essentially free from fake-muon background, without the need to simulate this background with Monte Carlo (MC) methods. Once the other background contributions are known, the difference can therefore be used to measure the beauty contribution. This in turn can be used to *measure* the fake muon background by subtracting the beauty contribution from the total like-sign sample, and mirroring it onto the unlike-sign sample.

In this analysis, the beauty signal was hence extracted from the *difference* between the like and unlike-sign samples, while the like-sign sample was used to determine the contribution from fake-muon background to the unlike-sign sample.

7.2 Event selection

The beauty event selection is based on the dataset described in sec. 6, corresponding to a total integrated luminosity of 114 ± 2.9 pb^{-1}.

To arrive at a high trigger selection efficiency, a rather inclusive set of triggers was chosen for the event selection.

The selection cuts were chosen such that average beauty contributions of $\gtrsim 50\%$ in several control distributions were achieved. The cuts are explained in the following sections. They are summarised in tab. 7.1.

7.2.1 Trigger selection

For MC events, the ZEUS online trigger decisions are simulated within the ZEUS reconstruction program ZEPHYR. To control the online selection bias, thus making the MC events comparable to the ZEUS data, an offline trigger selection was imposed on both the data and the MC sample. All triggers were chosen on the third level of the ZEUS trigger chain (see sec. 5.7).

The selected trigger slots include triggers on charm events, dijet events, generic deep inelastic scattering events, muon triggers as well as combinations of the given trigger types. A summary is found in tab. 7.2. The detailed trigger slot definitions are summarised in appendix F. Corrections were applied to events triggered solely by muon triggers, as described in sec. 7.3.2.

Calorimetry cuts:	
$E_{\mathrm{T}}^{\mathrm{cal,\ corr.}}$ (corrected)	$E_{\mathrm{T}}^{\mathrm{cal,\ corr.}} \geq 8$ GeV
$\hat{=}$ partially reconstructed $b\bar{b}$ mass	
muon E_{T} fraction	$(p_{\mathrm{T}}^{\mu_1} + p_{\mathrm{T}}^{\mu_2})/E_{\mathrm{T}}^{\mathrm{cal,\ corr.}} > 0.1$ and
$\rightarrow$ reject events with very high	$(p_{\mathrm{T}}^{\mu_1} + p_{\mathrm{T}}^{\mu_2})/E_{\mathrm{T}}^{\mathrm{cal,\ corr.}} \leq 0.7$ for $m^{\mu\mu} > 4$ GeV
or low hadronic activity, $m^{\mu\mu}$ dependent	$(p_{\mathrm{T}}^{\mu_1} + p_{\mathrm{T}}^{\mu_2})/E_{\mathrm{T}}^{\mathrm{cal,\ corr.}} \leq 0.5$ for $m^{\mu\mu} \leq 4$ GeV
Dimuon cuts:	
number of muons	$N_\mu > 1$
transverse momentum,	$p_{\mathrm{T}}^{\mu} > 0.75$ GeV high qual (≥ 5),
quality dependent (see sec. 6.3.7 and tab. D.2)	$p_{\mathrm{T}}^{\mu} > 1.5$ GeV low qual ($= 4$)
isolation, mass dependent. Peak:	$I^{\mu\mu} > 0.25$ GeV outside $J/\psi,\ \psi'$ peak
$m_{J/\psi}^{\mu\mu} \in [2.9,\ 3.25]$ GeV, $m_{\psi'}^{\mu\mu} \in [3.6,\ 3.75]$ GeV	$I^{\mu\mu} > 2.0$ GeV inside the peak
Difference in pseudorapidity (reject BH)	$\lvert\eta^{\mu_1} - \eta^{\mu_2}\rvert < 3.0$
Background cuts:	
reject cosmic muon events	$(\lvert\lvert\phi^{\mu_1} - \phi^{\mu_2}\rvert - \pi\rvert < \pi/200$ or
- muons not back to back	$\lvert\vartheta^{\mu_1} - (\pi - \vartheta^{\mu_2})\rvert < \pi/200)$ and
- events well timed	CAL timing < 10 ns
reject cosmic showers	BAC energy < 100 GeV or BAC $N_\mu < 15$
require well reconstructed vertex	$\lvert z_{\mathrm{vtx}}\rvert < 50$ cm,
	$x_{\mathrm{vtx}} \neq$ default, $y_{\mathrm{vtx}} \neq$ default
	$\sqrt{x_{\mathrm{vtx}}^2 + y_{\mathrm{vtx}}^2} < 3$ cm
reject combinatorial and light-flavour bg.	$m^{\mu\mu} > 1.5$ GeV
reject lfl bg by the dimuon p_{T} asymmetry	$(\lvert p_{\mathrm{T}}^{\mu_1} - p_{\mathrm{T}}^{\mu_2}\rvert)/(p_{\mathrm{T}}^{\mu_1} + p_{\mathrm{T}}^{\mu_2}) \leq 0.7$

Table 7.1: The complete set of cuts applied to the reconstructed information to select beauty event candidates.

Trigger property	Trigger name	Main cuts
hadronic triggers:		
Dijet + muon	HFL1	$\eta^\mu < 1.3$, 2 jets with $E_{\mathrm{T}}^{\mathrm{jet}} > 3.5$ GeV, $\lvert\eta^{\mathrm{jet}}\rvert < 2.5$
Dijet	HPP14	2 jets with $E_{\mathrm{T}}^{\mathrm{jet}} > 4(4.5)$ GeV, $\lvert\eta^{\mathrm{jet}}\rvert < 2.5$
Generic charm	HFL10/11	D^* in $K\pi\pi$ channel, $p_{\mathrm{T}}(D^*) > 1.8$ GeV
DIS triggers:		
DIS	DIS3	$E^{\mathrm{electron}} > 4$ GeV, $30 < E - p_z < 100$ GeV
DIS + muon	DIS27	$E^{\mathrm{electron}} > 7$ GeV, $\eta^\mu < 1.3$
pure muon triggers:		
Forward muon	MUO1/2/4	$\eta^\mu > 1.3$
Barrel/Rear muon	MUO3	$\eta^\mu < 1.3$
outer BRMuon	EXO11/12	outer BRMUON by GLOMU, cosmic μ rejection

Table 7.2: The TLT trigger selection applied to the reconstructed information. The detailed TLT trigger definitions can be found in appendix F.

7.2.2 Calorimeter based selection

Among the main selection criteria was the restriction of the sample to events with at least

$$E_{\mathrm{T}}^{\text{cal, corr.}} \geq 8 \text{ GeV} \tag{7.1}$$

with

$$E_{\mathrm{T}}^{\text{cal, corr.}} = \begin{cases} E_{\mathrm{T}}^{\text{cal}} - E_{\mathrm{T}}^{\text{cal}}{}_{|\text{in } 10^\circ \text{ forward cone}} & \text{for } \gamma\text{p events} \\ E_{\mathrm{T}}^{\text{cal}} - E_{\mathrm{T}}^{\text{cal}}{}_{|\text{in } 10^\circ \text{ forward cone}} - E_{\mathrm{T}}{}^{electron} & \text{if a DIS electron was found.} \end{cases} \tag{7.2}$$

where $E_{\mathrm{T}}^{\text{cal}}$ is the transverse energy reconstructed in the CAL. This is intended as a cut on the partially reconstructed mass of the two beauty quarks (as neutrinos escape detection). The transverse energy was corrected by subtracting the transverse energy in a cone of 10° around the forward beam pipe (to subtract the particles coming from the proton remnant↔final state colour connection) as well as subtracting the transverse energy of the scattered DIS electron if measured in ZEUS. The standard DIS cuts applied to select these electrons are summarised in tab. 6.4.

An additional cut with a similar influence was applied on the fraction of the total transverse energy carried by the muon pair:

$$0.1 < (E_{\mathrm{T}}{}^{\mu_1} + E_{\mathrm{T}}{}^{\mu_2})/E_{\mathrm{T}}^{\text{cal, corr.}} < \begin{cases} 0.5 & \text{for } m^{\mu\mu} < 4 \text{ GeV} \\ 0.7 & \text{for } m^{\mu\mu} \geq 4 \text{ GeV} \end{cases} \tag{7.3}$$

This E_{T}-fraction cut removes events with very high or low hadronic activity. It effectively introduces a lower bound of about 4 GeV on $E_{\mathrm{T}}^{\text{cal, corr.}}$.

The corrected $E_{\mathrm{T}}^{\text{cal, corr.}}$ distribution before both the E_{T} and the muon-E_{T} fraction is shown in fig. 7.1a. Fig. 7.1b shows the distribution after having applied the dimuon-E_{T} fraction cut. In the region removed by this cut combination, few beauty events are found. Also the used MC samples do not describe the data here. The poor MC description at low values of $E_{\mathrm{T}}^{\text{cal, corr.}}$ is due to cuts that were applied at generator level to the charm, BH and quarkonia MC samples. The region above the cut of 8 GeV is well described.

7.2.3 Dimuon Selection

Dimuon momentum based cuts: Dimuon events were selected by requiring two muons with transverse momenta of

$$p_{\mathrm{T}}^{\mu} \geq \begin{cases} 1.5 \text{ GeV} & \text{for muons with a quality } = 4 \\ 0.75 \text{ GeV} & \text{for muons with a quality } \geq 5, \end{cases} \tag{7.4}$$

depending on the muon reconstruction redundancy/quality defined in sec. 6.3.7. Roughly, the two quality levels 4 and 5 separate muons that were found by one finder/detector only (quality 4) from those which were found more redundantly by more than one finder (quality ≥ 5).

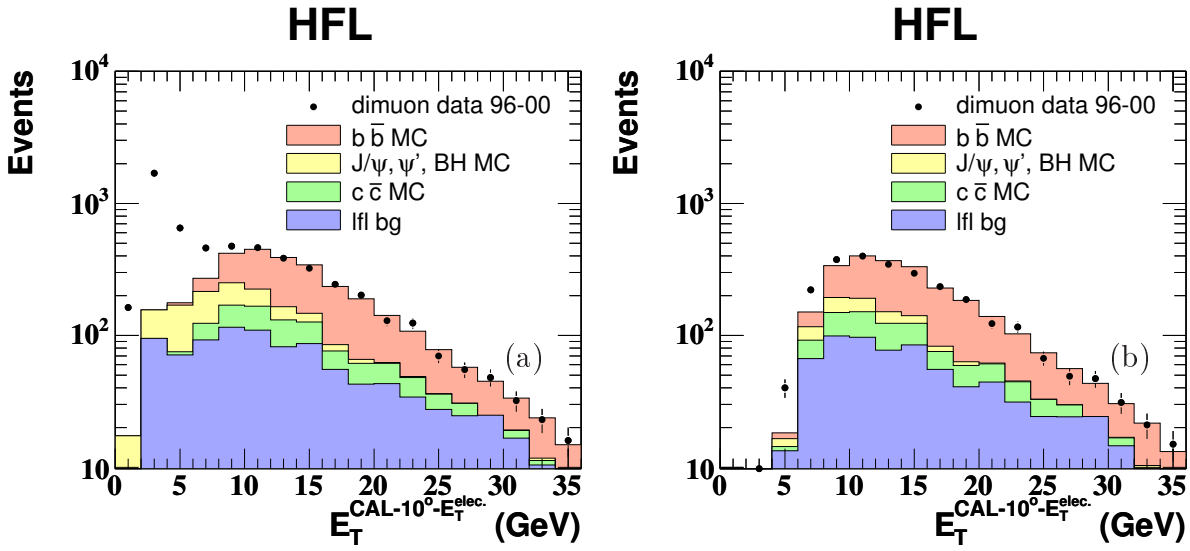

Figure 7.1: The corrected total calorimetric transverse energy for isolated high and low mass dimuon events. In (a) both the cut on the dimuon E_T fraction and the corrected CAL energy have not been applied. In (b) the dimuon-E_T fraction cut has been applied. The breakdown into the expected contributions from different processes is also shown.

Dimuon mass and charge separation: To additionally differentiate between muon pairs from the cascade decay of *the same* b quark and those from *different* b quarks, the distributions were separated depending on the dimuon invariant mass. Events were separated in a sub-sample of low-mass dimuons with

$$m^{\mu\mu} < 4 \text{ GeV}, \tag{7.5}$$

a sample enriched in muons from the same b quark and of high-mass dimuons with

$$m^{\mu\mu} \geq 4 \text{ GeV}, \tag{7.6}$$

containing dimuons originating from the decay of different b quarks.

Additionally events were separated by the muon charges into like- and unlike-sign dimuon events.

The mass distributions for dimuons in the high and low mass range, as well as for like and unlike-sign muon pairs are shown in fig. 7.2. The dominating signal and background contributions to the 4 subsamples are summarised in tab. 7.3.

Dimuon isolation cuts: Muons from semileptonic beauty decays can, as mentioned before, be separated from background processes (J/ψ, ψ', Υ and BH) by a muon isolation requirement. Based on the dimuon isolation, events were separated into an isolated (background) and a nonisolated (signal) sample. The definition of the isolation variable $I^{\mu\mu}$ is given in sec. 6.3.8 and corresponds roughly to the root mean square of the energy in cones with an opening angle of $\Delta R < 1$ around each of the two muons. The isolation separation was applied depending on the dimuon mass. If a dimuon fulfilled the following relation:

$$I^{\mu\mu} \geq \begin{cases} 2.0 \text{ GeV} & \text{for } m^{\mu\mu}_{J/\psi} \in [2.9,\ 3.25] \text{ or } m^{\mu\mu}_{\psi'} \in [3.6,\ 3.75] \\ 0.25 \text{ GeV} & \text{else.} \end{cases} \tag{7.7}$$

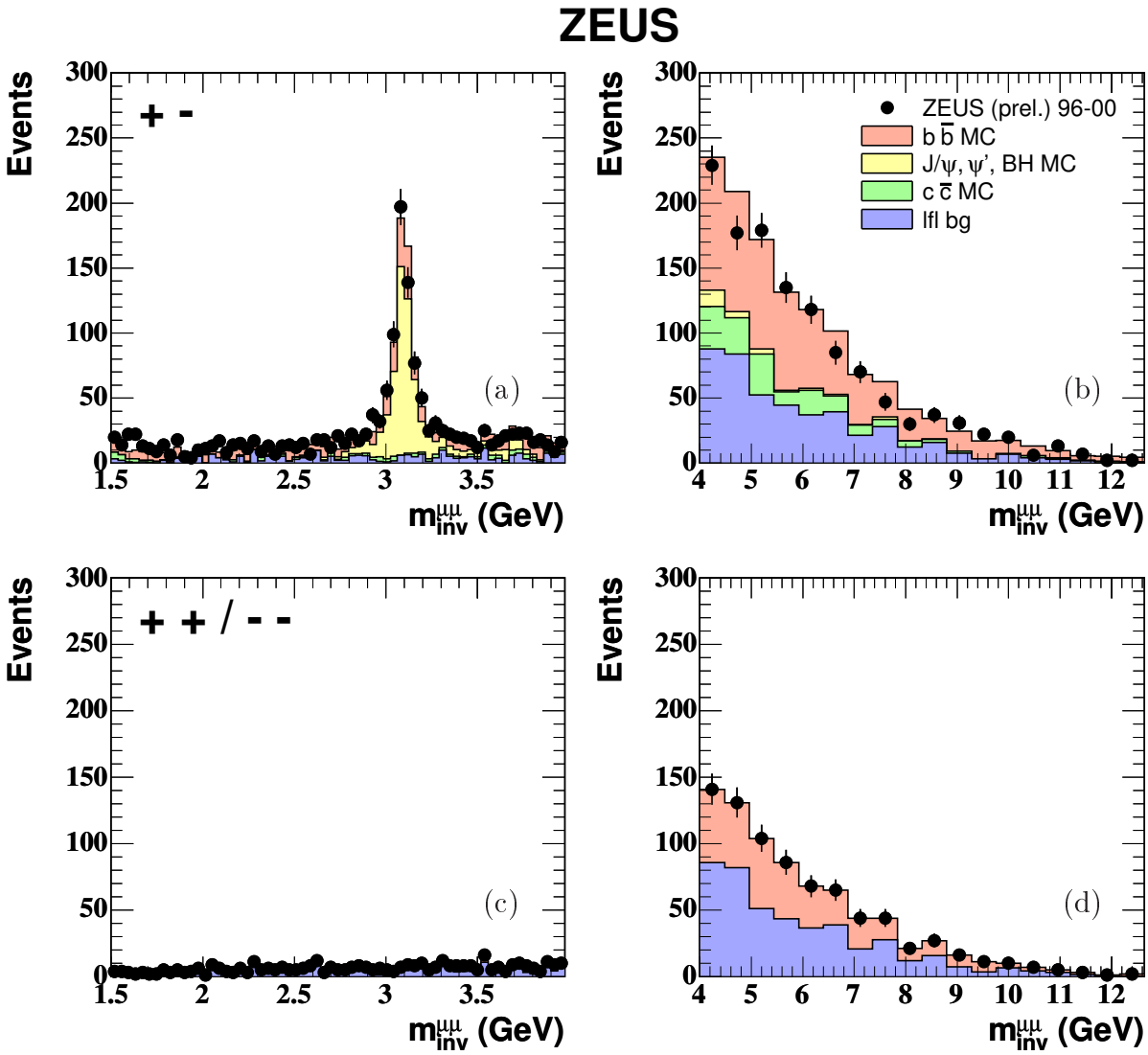

Figure 7.2: Dimuon mass distributions of unlike-sign muon pairs in the (a) low mass and (b) high mass subsamples, as well as like-sign muon pairs in (c) the low and (d) high mass subsamples. The breakdown into the expected contributions from different processes is also shown.

	low inv. mass ($m_{\mu\mu} < 4$ GeV)	high inv. mass ($m_{\mu\mu} \geq 4$ GeV)
unlike-sign $\pm/\mp$	**muons from same b**, J/ψ, ψ' + light-flavour bg	**muons from diff. b** or c, Υ, Bethe Heitler + light-flavour bg
like-sign $++/--$	**light-flavour bg**, + few muons from diff. b	**muons from diff. b** + light-flavour bg

Table 7.3: Grouping of events using dimuon mass and charge correlations. The main contributions of types of events are given.

it is referred to as nonisolated. All other dimuon events are part of the isolated subsample.

The resulting separation into isolated and nonisolated events is shown in fig. 7.3. The isolated dimuon mass distributions for unlike-sign low- (fig. 7.3a) and high-mass (fig. 7.3b) muon pairs are dominated by the background processes from quarkonia and BH events. These backgrounds are suppressed in the nonisolated signal region distributions of the low- (fig. 7.3c) and high-mass range (fig. 7.3d).

A small remaining BH component in the nonisolated sample and some light-flavour background was removed by a cut on the difference in pseudorapidity of the dimuon of:

$$|\eta^{\mu_1} - \eta^{\mu_2}| < 3.0. \tag{7.8}$$

Furthermore BH events are suppressed also by the dimuon E_{T}-fraction cut.

Dimuon selection control distribution: A rather involved control distribution for the dimuon selection can be found in fig. 7.4. Here the data are compared to the MC description for different combinations of muon finders (MC corrections were applied as described in sec. 7.3). The definitions of the bins of this plot are given in table 7.4. In the region $x \in [4, 7[$, single muon properties of each muon in the muon pair are shown. The bins 4 to 5 include muons found by a single muon finder yielding a muon quality of 4. The calorimeter muon finder (MV) is used supplementally only and thus is not counted as a full separate finder. The bins 5 to 7 include muons found by more than one finder classified as quality 5 or 6. The second region $x \in [7, 8[$ contains rates concerning dimuon rather than single muon properties. While the first bin in this region contains all dimuons, the bins 7.2 - 7.6 contain muons with a sum of the quality equal to 8 - 12. The last two bins give the dimuon events that have been found by the muon chamber finders (last but one bin) or by the BAC finders (last bin). Very good agreement is found for every single muon finder combination. The separate efficiencies are thus well understood.

In rare cases, events contain more than one muon pair that fulfils the selection cuts. For these events, the first selected muon pair was chosen as the default and cuts were based on its properties; other muon pairs were discarded. It was checked, that alternatively using all rather than just the first dimuon yields consistent results.

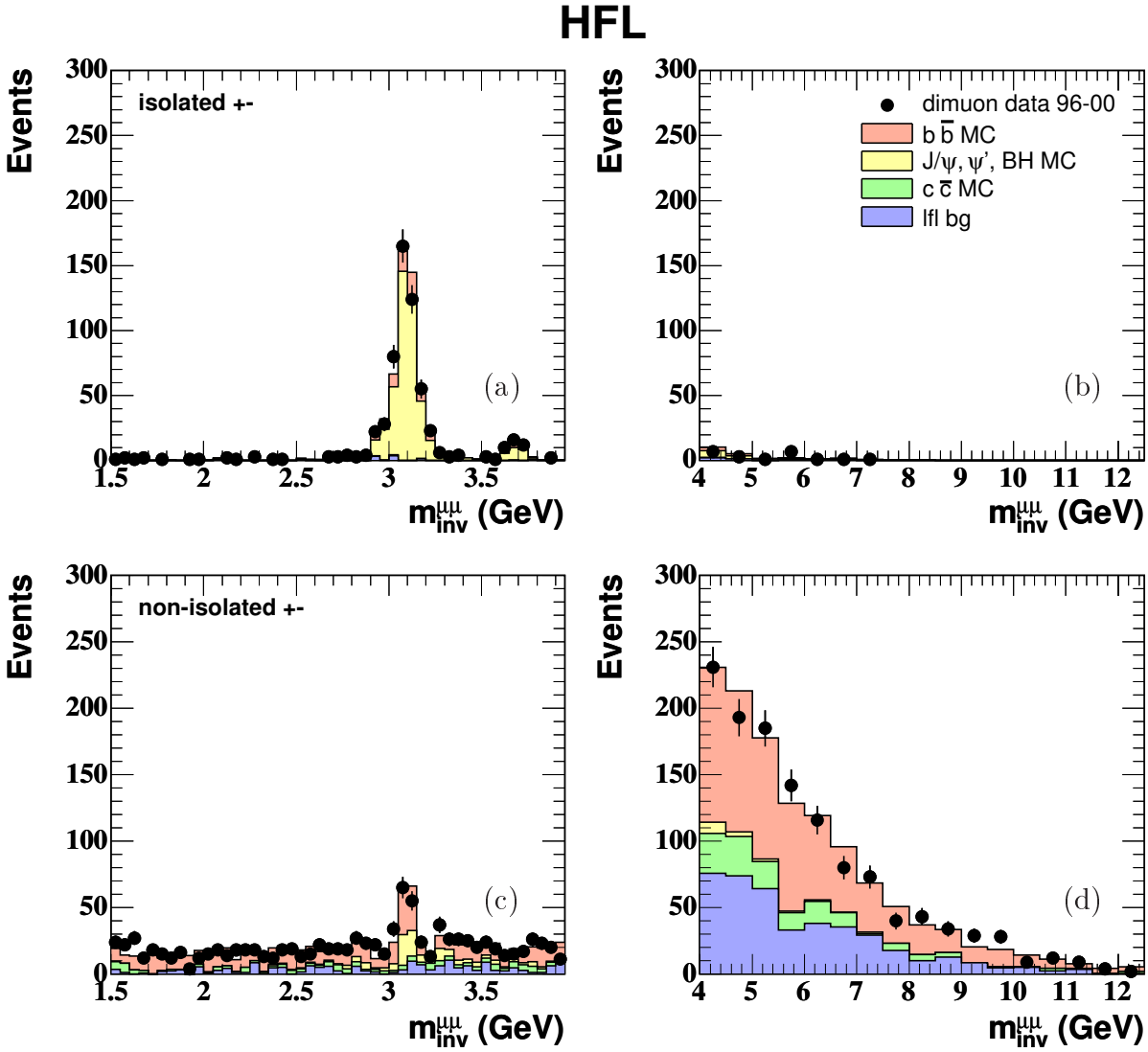

Figure 7.3: Dimuon mass distributions of unlike-sign muon pairs in the isolated (a) low mass and (b) high mass subsamples, as well as nonisolated unlike sign muon pairs in the (c) low and (d) high mass subsamples. The breakdown into the expected contributions from different processes is also shown.

	Bin	Finder	Comment
4 =	quality 4		
	4.2	BREMAT	inner chambers
	4.4	BAC	
	4.5	BAC/BREMAT + MV	low qual. or not vtx associated
	4.6	MPMATCH or MUFO	low probability, with track match
	4.7	MUFO	no track
5 =	quality 5		
	5.1	BREMAT + MV	BREMAT: outer chambers low prob.
	5.2	BREMAT + MV	BREMAT: inner chambers, MV: $\|\eta^\mu\| > 0.6$
	5.4	BAC + MV	$\|\eta^\mu\| > 0.6$
	5.5	BREMAT + BAC + MV	BREMAT: inner chambers, MV: $\|\eta^\mu\| < 0.6$
	5.6	MPMATCH/MUFO	lower quality forward muon
6 =	quality 6		
	6.1	BREMAT	outer chambers
	6.6	MPMATCH or MUFO	with track
	6.8	MPMATCH/MUFO + MV	MPMATCH/MUFO: lower prob.
7 =	all dimuons		
	7.2	quality 4 + 4	
	7.3	5 + 4	
	7.4	6 + 4, 5 + 5	
	7.5	6 + 5	
	7.6	6 + 6	
	7.8	muon chambers only	MPMATCH, MUFO or BREMAT (inner or outer)
	7.9	BAC only	

Table 7.4: Definition of the bin contents of fig. 7.4. The muon finders are explained in sec. 6.3.7.3.

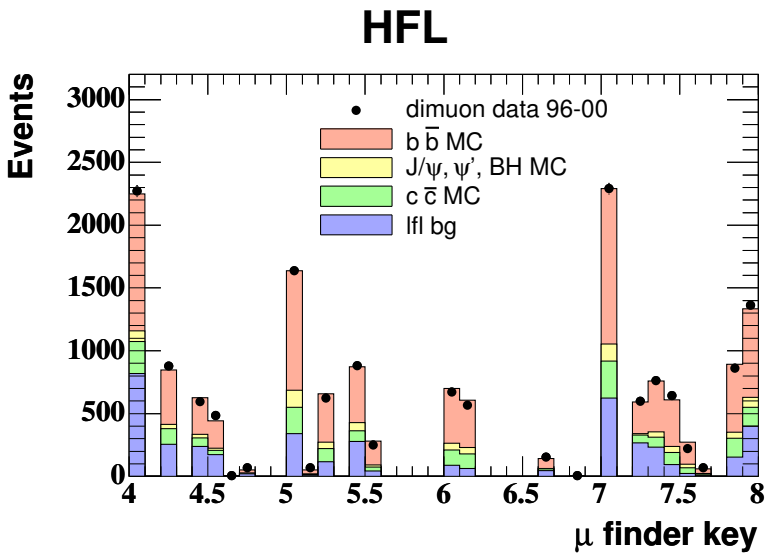

Figure 7.4: The breakdown of dimuon events depending on the combinations of finders reconstructing the muons. The key to the bin entries is given in tab. 7.4. The contributing processes are also shown.

7.2.4 Background and cleaning cuts

To suppress events with ambiguous matches between the tracks and the muon chamber segments as well as light-flavour background (e.g. light quarkonia) from this sample of muons, a lower invariant mass cut of

$$m^{\mu\mu} > 1.5 \text{ GeV} \tag{7.9}$$

was applied.

Badly matched muons and light-flavour backgrounds were removed using the imbalance between the transverse momenta of the muon pair:

$$(|p_{\mathrm{T}}^{\mu_1} - p_{\mathrm{T}}^{\mu_2}|)/(p_{\mathrm{T}}^{\mu_1} + p_{\mathrm{T}}^{\mu_2}) \leq 0.7. \tag{7.10}$$

Cosmic ray muons were suppressed by discarding events with back to back muons and events in which the average calorimeter timing differs more than 10 ns from the nominal collision time. Large cosmic showers were suppressed using the BAC total energy and number of BAC muon segments.

Finally cleaning cuts are imposed at the tracking level, requiring a well defined event vertex.

7.3 Muon corrections applied to MC samples

Corrections to the muon MC description of the reconstruction and matching efficiency and the muon trigger efficiency are summarised here. Also corrections to the dimuon $p_{\mathrm{T}}^{\mu\mu}$ spectrum of the J/ψ and ψ' as well as corrections to the Υ Q^2 spectrum are described.

7.3.1 Muon MC efficiency correction

The MC implementation of the muon-detector components is not fully complete. Especially the muon hit- and segment-reconstruction efficiencies are generally overestimated in the MC description. A method of determining and applying a MC efficiency correction is therefore necessary and described in this section.

The efficiency-correction *determination* is described in detail in [108]. Here only the principle of this determination will be summarised. The *application* of the efficiency correction factors in the special case of the dimuon selection is described in more detail.

Muon-efficiency determination: The MC description of the tracking and energy reconstruction has been tested and fine tuned in high precision measurements at ZEUS, e.g. measurements of the proton structure function F_2. The determination of the muon-efficiency correction is thus based on the assumption that both the tracking and calorimeter efficiencies are described correctly in the MC. With this assumption, efficiencies were measured for both data and MC relative to the muons found by the tracking and CAL system, i.e. by MV.

A specially selected sample of isolated dimuons from the muonic decay of J/ψ and ψ' as well as Bethe-Heitler events were used in both data and MC as the base sample for the muon-efficiency determination.

The efficiency was determined for the inner and outer muon chambers (BREMAT finder), for the BAC (MUBAC finder) and FMUON (MPMATCH finder) and also includes the respective segment track matching efficiency. The influence of muon triggers was folded out. Additionally, the finder efficiencies were determined for *loose* and *tight* muon track matches, where tight and loose was defined as:

- **MUBAC:** tight requires a distance of closest approach of the matched track to the muon segment on the BAC surface of DCA < 0.5 m, loose for all other matches,
- **BREMAT:** tight requires a track segment matching probability of $P > 0.01$, loose for all other matches,
- **MPMATCH:** tight requires a track segment matching probability of $P > 0.05$, loose for all other matches with a minimal matching probability of $P > 0.01$.

Muon-efficiency application: The efficiency correction factor to be applied to a muon found by the finder "finderX", in the tight or loose configuration depends on the muon η^μ and p_{T}^μ and is given by the ratio of the measured efficiencies in data and MC:

$$f_{\text{corr, finderX, tight/loose}}(\eta^\mu, p_{\mathrm{T}}^\mu) = \frac{\varepsilon_{\text{Muon, } \mathbf{data}\text{, finderX, tight/loose}}(\eta^\mu, p_{\mathrm{T}}^\mu)}{\varepsilon_{\text{Muon, } \mathbf{MC}\text{ finderX, tight/loose}}(\eta^\mu, p_{\mathrm{T}}^\mu)} \tag{7.11}$$

The criteria for the application of the tight or loose matching correction depend on the presence of supportive measurements from the CAL or the outer muon chambers and are defined in in detail in appendix E.

These efficiencies were applied in a random number based scheme: A flat distribution of random numbers x_{rand} was used. If

$$x_{\text{rand}} < f_{\text{corr, finderX, tight/loose}} \tag{7.12}$$

the finderX information for the corresponding muon was reset, simulating that the muon finder did not tag this muon. Based on the new finder information, the muon quality was recalculated.

The muon was discarded if the recalculated muon quality dropped below 4 by removing the finderX tag. A higher p_{T}^{μ} cut was applied if it was only reduced from e.g. 6 to 4.

Good agreement of the MC with the data for all kinds of finder combinations was achieved using the described method. The rates of muons in dimuon events separated in different finder combinations are shown in fig. 7.5. In fig. 7.5a the muon-efficiency correction has not been applied. Figure 7.5b shows the much better finder by finder MC description achieved by applying the correction.

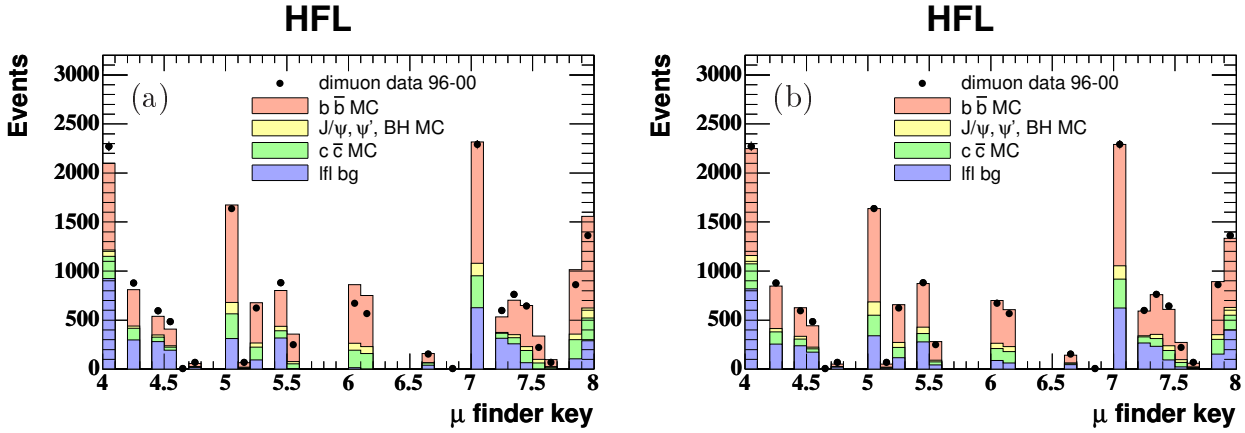

Figure 7.5: The breakdown of dimuon events depending on the combinations of finders reconstructing the muons (a) without and (b) with applying the muon efficiency correction. An estimation of the contributing processes is also shown. The key to the bin entries is given in tab. 7.4.

7.3.2 Muon trigger correction

The barrel and rear muon trigger efficiency is overestimated in the MC description [109]. The data trigger efficency $\varepsilon_{\text{Trigger, data}}$ is only 88% of the MC efficiency $\varepsilon_{\text{Trigger, MC}}$:

$$\varepsilon_{\text{Trigger, data}} = 0.88 \cdot \varepsilon_{\text{Trigger, MC}}, \tag{7.13}$$

independent of the muon transverse momentum.

To correct the trigger efficiency for one specific muon, one needs to determine whether the muon actually triggered the event. From the recorded FLT trigger information one can derive that *a muon* has triggered, but not *which muon*. The BREMAT and GLOMU finders were used to determine which muon actually triggered the event. Very similar algorithms to GLOMU (though partially without MIP matches) are applied on the ZEUS online trigger chain making

this method reliable. GLOMU was used as estimator for isolated, BREMAT for nonisolated muon triggers. Muons with a GLOMU or BREMAT tag were assumed to have fired the trigger.

The trigger efficiency correction was applied only to events which have exclusively been triggered by muon triggers. If a hadronic or DIS trigger fired (see tab. 7.2), no trigger corrections were applied.

The following scheme was used to determine correction factors to be applied via event weights:

- if both muons were tagged by GLOMU or BREMAT apply $weight = 1 - (1 - 0.88)^2$
- if only one muon was tagged by GLOMU or BREMAT apply $weight = 0.88$
- if no muon was tagged by GLOMU or BREMAT apply $weight = 0$

7.3.3 J/ψ and ψ' MC reweighting in $p_{\mathrm{T}}^{\mu\mu}$

The J/ψ production and decay is not well described in the PYTHIA charm MC sample that has been used. ψ' production was not included in the sample in the first place.

Thus, J/ψ events were rejected in the PYTHIA $c\bar{c}$ MC sample and J/ψ and ψ' events were simulated using a more reliable MC sample (HERWIG). This sample was used for an earlier analysis of inelastic J/ψ and ψ' production at HERA [89, 90].

Still, the HERWIG generator is known to generate a too soft p_{T} spectrum for J/ψs. For this analysis the HERWIG MC was thus reweighted to describe the dimuon p_{T} distribution in the low mass ($m^{\mu\mu} < 4$ GeV) isolated range. A mass window of $2.8 < m^{\mu\mu} < 3.4$ was set around the J/ψ. The resulting mass distribution of isolated muons and the corresponding unreweighted dimuon p_{T} spectrum are shown in fig. 7.6a and c. By fitting the data over MC ratio of the dimuon p_{T} distribution, a reweighting function was determined:

$$weight(p_{\mathrm{T}}^{\mu\mu}) = 0.385 \cdot \min(e^{0.425 \cdot p_{\mathrm{T}}^{\mu\mu}}, 24.1) \tag{7.14}$$

This fit to the data/MC ratio is shown in fig. 7.6b. The low mass isolated p_{T} spectrum after reweighting (no mass cut) is shown in fig. 7.6d. Good agreement was achieved.

7.3.4 Υ MC reweighting in Q^2

The Υ MC Q^2 distribution does not follow the shape of the data Q^2 distribution. A rough estimate was performed similar to the method described above, yielding a correction weight function as given below:

$$weight(Q^2_{\mathrm{MC}}) = \begin{cases} Q^2_{\mathrm{MC}} \cdot 1/2.5 & \text{for } \log_{10}(Q^2_{\mathrm{MC}}) \leq 2.5 \\ Q^2_{\mathrm{MC}} \cdot 1/(2.5 + (\log_{10}(Q^2_{\mathrm{MC}}) - 2.5) \cdot 100) & \text{for } \log_{10}(Q^2_{\mathrm{MC}}) > 2.5. \end{cases} \tag{7.15}$$

In an early state of the analysis the Υ background was not negligible, as shown in fig. 7.7. The weight was applied to the Υ MC event by event, yielding a reasonable description of the data. After the final event selection the Υ contribution turned out to be essentially negligible. Therefore the MC sample was not included in the final analysis presented here.

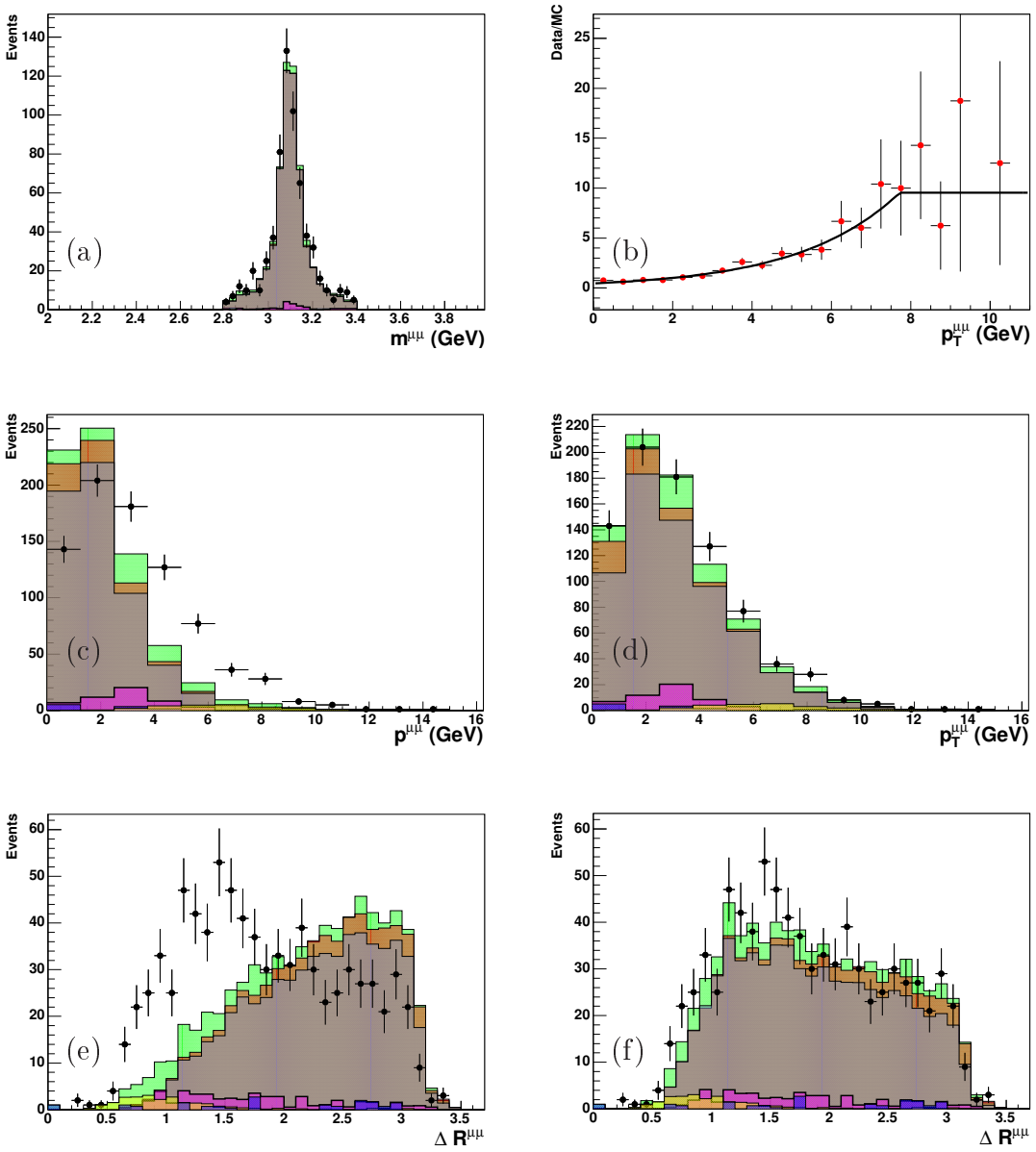

Figure 7.6: Reweighting the J/ψ $p_{\mathrm{T}}^{\mu\mu}$ spectra. In (a) the event selection as the input for the determination of the weighting function is shown. The dimuon mass is restricted to the J/ψ-peak region. (b) shows the fit to the data over MC ratio. In (c) the low mass dimuon p_{T} spectrum before the J/ψ and ψ' reweighting and (d) after the reweighting is shown (No mass restriction here). The same for the dimuon ΔR is shown in (e) and (f).

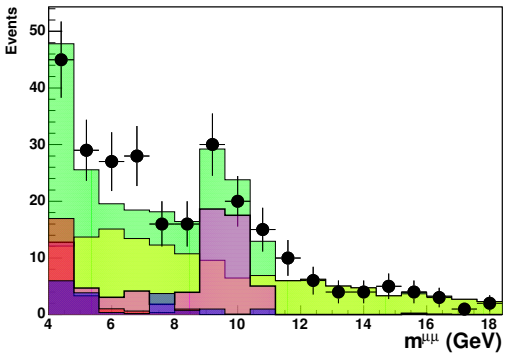

Figure 7.7: The Υ peak in isolated dimuon events in an early state of the analysis. The E_{T}-fraction cut had not been implemented.

Chapter 8

Signal determination

The determination of the normalisation for the beauty signal MC is described here. As a necessary condition, first the backgrounds need to be determined. Thus the methods of determining and normalising the backgrounds in the final selected dataset in the signal sample are also described here.

8.1 Normalisation of backgrounds

The backgrounds to be normalised are muonic decays of quarkonia (J/ψ and ψ'[1]), BH events as well as charm and light-flavour backgrounds.

The distributions from all MC samples were normalised to the data luminosity before any further normalisations were applied.

8.1.1 Normalisation of quarkonium and BH backgrounds

The quarkonium and BH background is highly enriched in the sample of isolated dimuon events shown in fig. 7.3a and b, while the beauty contribution is strongly suppressed. Thus the corresponding MC samples were normalised to describe these distributions. The J/ψ and ψ' MC was normalised to describe the peaks in the low mass range (fig. 7.3a) and the BH to fit the isolated high mass distribution (fig. 7.3b).

This normalisation factor was then used for the nonisolated sample where these backgrounds are however contributing very little.

8.1.2 Normalisation of the charm background

Due to the small charm contribution in the selected sample, the charm MC was normalised using the MC scaling factor determined in the topologically very closely related $D^* + \mu$ analysis [55],

[1] Υ decay is another background process, that was however neglected, as it was strongly suppressed.

introduced in sec. 3.4.3. The charm scale factor $s^c_{\rm MC}$ applied to the luminosity normalised charm MC samples (sum of PYTHIA and RAPGAP) is [110]:

$$s^c_{\rm MC} = 1.3. \tag{8.1}$$

The systematic error arising from differences between the $D^* + \mu$ and the dimuon analyses is evaluated in sec. 9.2.1.

8.1.3 Determination of the light-flavour background

The last background to be determined is made up from events coming from the decay of light mesons (e.g. K, π, etc) and falsely reconstructed muons, referred to as light-flavour background.

The generation of an inclusive MC background sample was not feasible as the loose data selection cuts would have required to produce enormously large inclusive samples. Therefore the light-flavour background was determined from the data.

Since there is no standard-model process with significant cross section that produces like-sign muon pairs originating from the primary vertex within the selected phase space other than beauty decay, the like-sign dimuon distributions are made up from beauty decays and false muons only. The fake muon distributions could thus be obtained by subtracting the like-sign beauty MC distribution from the like-sign data. The resulting distribution should be valid in both shape and normalisation for like and unlike-sign distributions, as no charge correlations are expected for falsely reconstructed muons. The prerequisite for this background estimation are two central assumptions:

1. there is no other process that produces like-sign muon pairs apart from beauty decay,

2. light-flavour background "muons" are not charge correlated, thus symmetric in like and unlike-sign dimuons.

With these assumptions (Tests are described in the next section) the charge symmetry of the light-flavour background can be used to measure the light-flavour background distributions from the data. Relying on assumption 1., we can extract the like-sign background distribution ($bg^l_{\rm lfl}$) from the like-sign data (d^l) by subtracting the like-sign beauty contribution (b^l):

$$bg^l_{\rm lfl} = d^l - b^l. \tag{8.2}$$

With assumption 2., we can use $bg^l_{\rm lfl}$ in both shape and normalisation also for the *unlike-sign* background distribution ($bg^u_{\rm lfl}$):

$$bg^u_{\rm lfl} = bg^l_{\rm lfl}. \tag{8.3}$$

All light-flavour backgrounds shown in the unlike-sign distributions in the figures 7.1 to 7.5 were obtained using this method. As a further example, the η^μ and $p^\mu_{\rm T}$ distributions are shown in fig. 8.1.

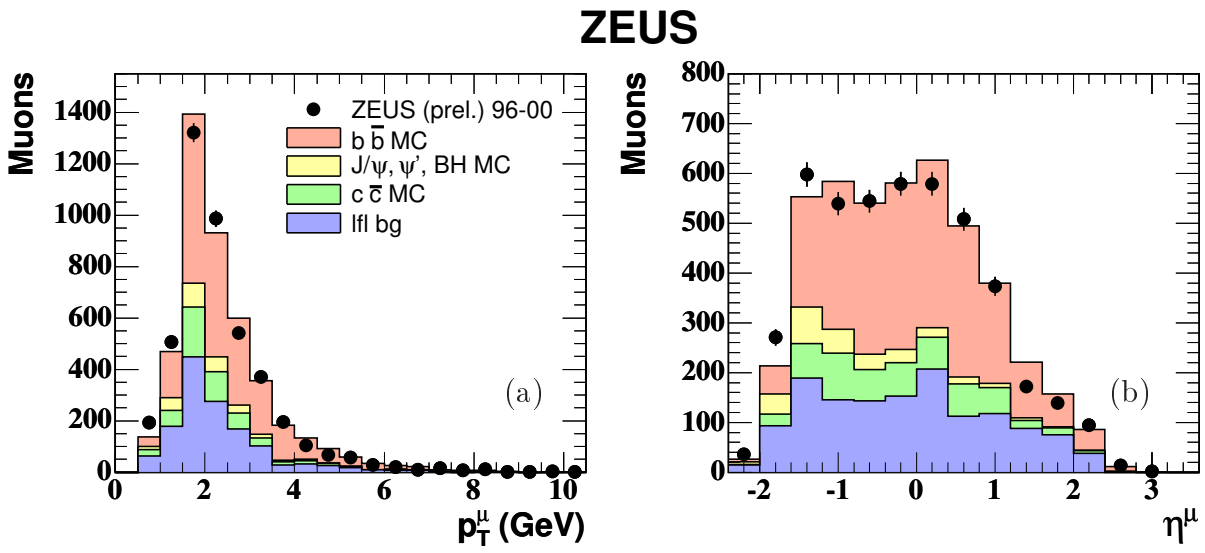

Figure 8.1: (a) Muon transverse momentum and (b) pseudo-rapidity distribution from both high and low mass muon pairs in the nonisolated unlike-sign sample. Two muons were entered for each event. The breakdown into the expected contributions from different processes is also shown.

8.1.3.1 Testing the light-flavour background assumptions

The first of the two light-flavour assumptions was based on the standard model and is thus not tested further. The second assumption was tested directly. If it was correct, distributions filled predominantly from unlike-sign fake dimuons must have the same shape and normalisation as those from fake muons of like sign. Thus a sample highly enriched in light-flavour background was selected. The muon pair selection had been tuned to yield a good signal to background ratio. If the cuts on the muon reconstruction quality are loosened, the signal to background ratio is reduced and mainly fake muons are reconstructed. Using this feature, namely reducing the requirement of the $\mathcal{G}$MUON quality (see sec. 6.3.7) from four or five (depending on the muon transverse momentum) to be only greater than zero, a sample highly enriched in fake dimuon events was produced.

In fig. 8.2a-d control distributions from the fake muon sample are shown. Very good agreement of the unlike-sign dimuon data with the like-sign distribution was found. Assumption 2. was therefore confirmed.

Still, small differences between bg^u_{lfl} and bg^l_{lfl} are seen. They amount to $\sim 2\%$ in the high mass range. In the low mass range, processes producing unlike-sign fake-muon candidates are slightly more pronounced, giving rise to differences of about 6%. These differences have been corrected for when determining the cross sections. This correction is described in sec. 9.1.1.

8.2 Signal normalisation

In the preceding paragraphs the backgrounds in the selected data sample and the normalisations of the corresponding background MC samples were described. The normalisation of the beauty

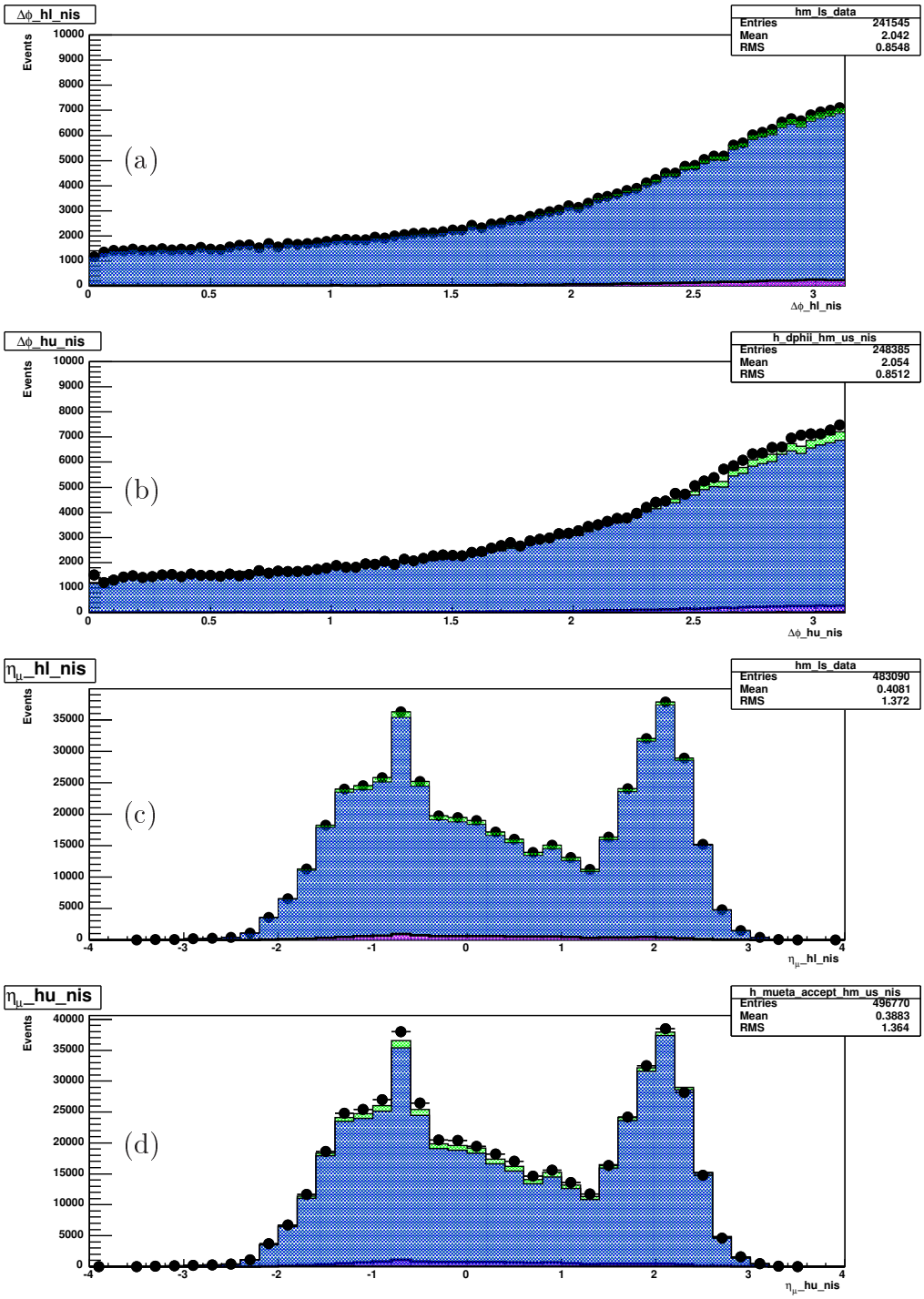

Figure 8.2: (a) and (b): Azimuthal distance $\Delta\phi^{\mu\mu}$ between the two muons in a dimuon and (c) and (d): muon pseudorapidity η^{μ} in the high mass range ($m^{\mu\mu} > 4$ GeV). Like-sign events are shown in (a/c). In (b/d) the light-flavour background derived from (a/c) was applied to the data shown in the blue dominating contribution. The sum of the remaining contributions from beauty, charm and BH is shown in the green band above the background. For this very loose muon selection, nearly no contribution other than light-flavour background was found, as intended.

signal was performed after having fixed the quarkonium, BH and the charm background.

The unlike-sign data (d^u) was assumed to be the sum of the unlike-sign components of beauty (b^u), charm (c^u), J/ψ (J/ψ^u), ψ' (ψ'^u), BH (BH^u) and the light-flavour background (bg^u_{lfl}):

$$d^u = b^u + bg^u_{\mathrm{lfl}} + c^u + J/\psi^u + \psi'^u + \mathrm{BH}^u. \tag{8.4}$$

The beauty normalisation factor (s^b_{MC}) was defined as

$$b^{u/l} = s^b_{\mathrm{MC}} \cdot b^{u/l}_{\mathrm{MC}}. \tag{8.5}$$

and was applied to the luminosity weighted beauty MC distributions $b^{u/l}_{\mathrm{MC}}$.

Using equations 8.2 and 8.3 to substitute bg^u_{lfl} in eq. 8.4 and resolving for s^b_{MC}, we obtain:

$$s^b_{\mathrm{MC}} = \frac{d^u - d^l - bg^l_{\mathrm{lfl}}}{b^u_{\mathrm{MC}} - b^l_{\mathrm{MC}}}. \tag{8.6}$$

This scaling factor to the luminosity normalised beauty MC was determined to be:

$$s^b_{\mathrm{MC}} = 2.06 \pm 0.23(stat.). \tag{8.7}$$

This factor applies to the sum of PYTHIA and RAPGAP samples that were used for the signal simulation for values of $Q^2 < 1$ GeV and $Q^2 > 1$ GeV respectively, as described in sec. 6.2.

By eq. 8.2 the light-flavour normalisation is fixed once the beauty normalisation has been determined.

8.2.1 Control distributions

The normalisation of the beauty contribution was checked on an independent subsample of events containing jets with transverse energies ${E_{\mathrm{T}}}^{\mathrm{jet}} > 4$ GeV within the pseudorapidity region of $|\eta^{\mathrm{jet}}| < 2.5$ (about 40% of all selected events contain jets). For these events the transverse momentum of the muons relative to the closest jet ($p^{\mathrm{rel}}_{\mathrm{T}}$) was calculated. The mass of the b quark leads to a higher value of the $p^{\mathrm{rel}}_{\mathrm{T}}$ for muons from beauty decays than from charm or light-flavour events. Using the beauty (and background) normalisations obtained on the full sample, very good agreement of the subset data with the MC is found, as shown in fig. 8.3a. Events with $p^{\mathrm{rel}}_{\mathrm{T}} > 1.5$ GeV have a very high beauty purity.

For events from the complementing subsample of events without jets the pseudo thrust (sec. 6.3.5) distribution was calculated and is shown in fig. 8.3b. Also in this subsample good agreement is found. A combination of these two variables could thus be used in principle to get an independent determination of the beauty fraction.

A control plot for the unlike-sign dimuon isolation $I^{\mu\mu}$ is shown in fig. 8.4. Both isolated and nonisolated events for both the high and low dimuon mass sample are entered in this plot. The quarkonium and BH background clearly peaks at low values of $I^{\mu\mu}$, whereas the charm and beauty events as well as most of the fake/light-flavour muons have higher values of $I^{\mu\mu}$. Again the data are described well by the MC supporting eq. 8.4.

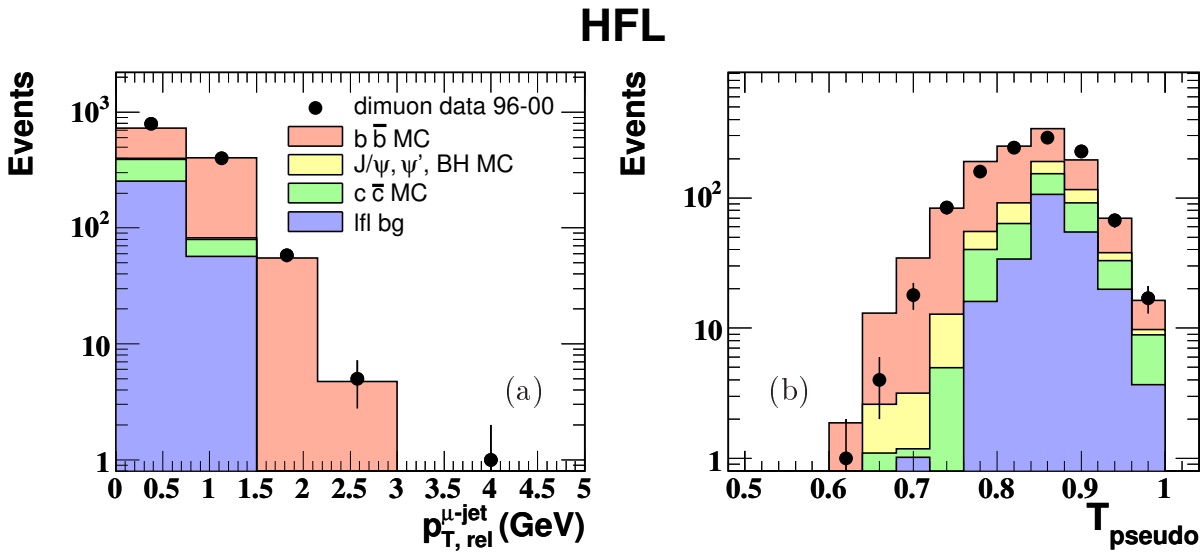

Figure 8.3: The transverse momentum of muons relative to the closest jet ($p_{\mathrm{T}}^{\mathrm{rel}}$) for events in which jets could be found is shown in (a). For those events where no jet could be found, the pseudo thrust (defined in sec. 6.3.5) is shown in (b). The breakdown into the expected contributions from different processes is also shown.

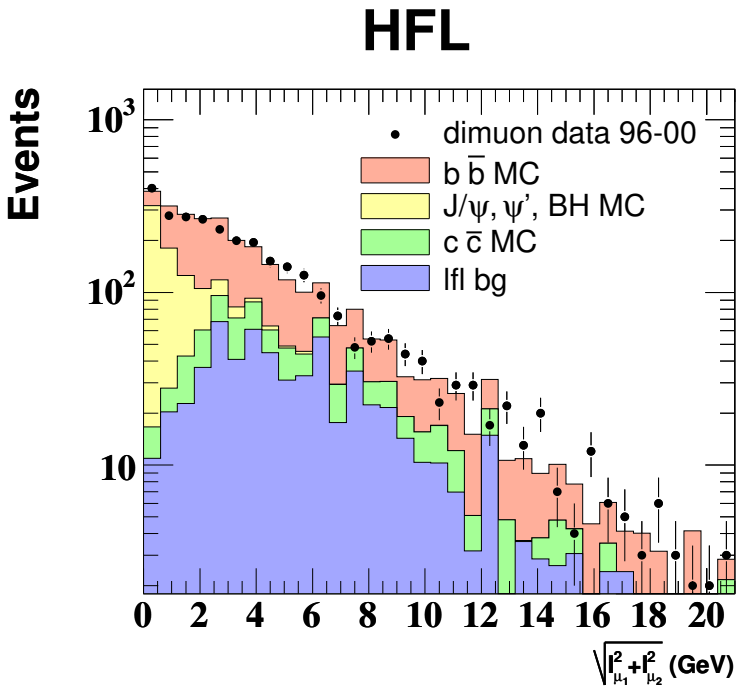

Figure 8.4: Dimuon isolation $I^{\mu\mu}$ for the sum of the low and high mass unlike-sign dimuon events.

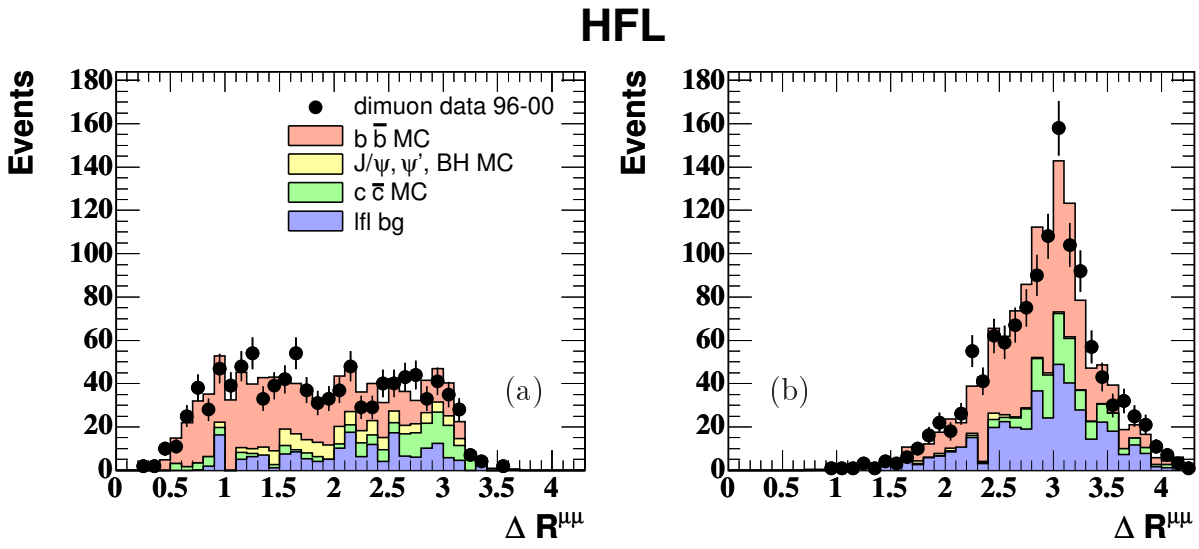

Figure 8.5: Angular correlations in ΔR of the two muons in dimuon events. In (a) the low mass and in (b) the high mass nonisolated unlike-sign subsample is shown.

As a control for the event topology and muon/$b\bar{b}$ correlations, angular correlations between the muons from dimuon events are presented by ΔR distributions in fig. 8.5. Fig. 8.5a is taken from the low mass, fig. 8.5b from the high mass dimuon sample. The MC samples also provide a very good description of the angular correlations.

The normalisation of the γp contribution relative to the DIS part (about 15% of the total sample) was checked using the Q^2 distribution, shown in fig 8.6a. The distribution of $E - p_z$ is also well described as shown in fig. 8.6b. As (for γp) $E - p_z$ is related to the photon-proton centre-of-mass energy W this indicates a good description of the ep kinematics.

Other control distributions have already been shown in the preceeding sections:

- To control the description of the reconstructed energy, the corrected CAL transverse energy before the cut on this quantity as well as before dimuon-E_T fraction cut is shown in fig. 7.1.
- To check the finder dependent muon MC efficiency description, the breakdown of the event sample separated depending on which muon finder was used to tag the muons is shown (after corrections) in fig. 7.4.
- To check the charm normalisation, the D^* mass distributions used to fix the charm normalisation are shown in in fig. 3.10.
- As a control for the normalisation of the isolated and nonisolated samples, the unlike-sign muon mass distributions are shown separately for the isolated and nonisolated subsample in the high and low mass range in fig. 7.3,
- The total normalisation is checked by the sum of the isolated and nonisolated muon mass ranges in like-sign and unlike-sign events as shown in fig. 7.2.

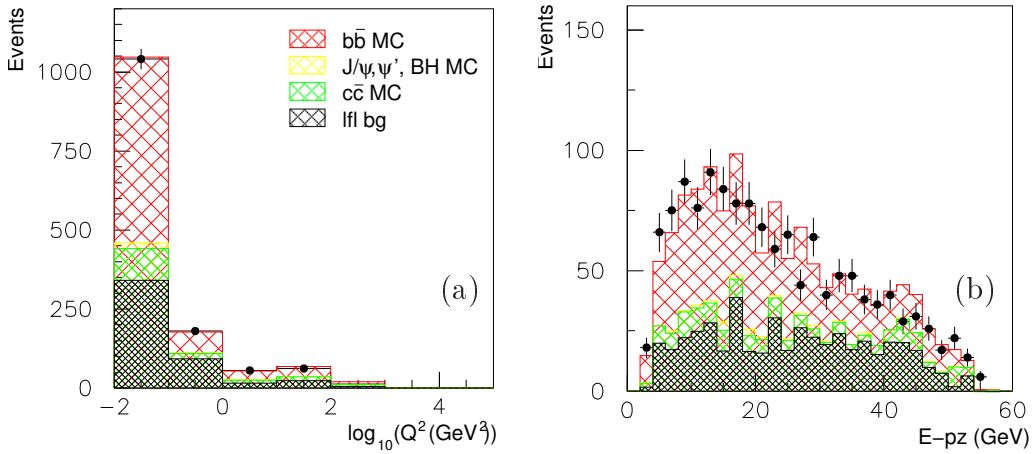

Figure 8.6: (a) Q^2 and (b) $E-p_z$ distributions for high-mass nonisolated dimuon events. In the Q^2 distribution, the lower two bins are filled for non-DIS events: The first bin contains events with $E-p_z < 34$ GeV and the second bin contains events with $E-p_z > 34$ GeV that did however not fulfil the DIS electron selection.

- Muon spectra are controlled in distributions of the muon pseudorapidity and transverse momentum for the sum of high and low mass unlike-sign dimuons, shown in fig. 8.1.
- A further control of muon angular correlations is given by the azimuthal difference $\Delta\phi^{\mu\mu}$ for muons predominantly from different b-quark decays in fig. 9.9.

Similar checks were performed on distributions of e.g. the transverse momentum of the muon pair, the p_T asymmetry of the muon pair, the muon E_T fraction, the distance in pseudorapidity between the two muons and the azimuthal distribution of single muons and dimuons. In all distributions good agreement of the MC description with the data was found.

The agreement of the of the MC QCD description with the data found in all relevant kinematic distributions is an impressive success of the LO+PS models.

Chapter 9

Cross sections

Based on the measured normalisation of the beauty MC, described in the previous chapter, the number of events from beauty in the selected event sample was determined. From these events $b\bar{b}$ production cross sections were extracted and compared to LO+PS and NLO predictions.

9.1 Signal extraction

The beauty contribution to the total event sample in both like- and unlike-sign dimuon events can be determined by exploiting the symmetry in charge of the light-flavour backgrounds. As there is an equal contribution of this background in the like- and unlike-sign dimuon sample,

$$N^{\mathrm{u}}_{\mathrm{bg}} = N^{\mathrm{l}}_{\mathrm{bg}}, \tag{9.1}$$

the difference of these samples is essentially free from light-flavour background. From this difference sample we also subtract the remaining backgrounds (charm, J/ψ, ψ' and BH) using the normalised background-MC samples. The remainder is the beauty contribution to the difference of unlike- and like-sign dimuon events. The extrapolation to the sum of like- and unlike-sign dimuon events is done using the beauty MC:

$$N_{b\bar{b}\to\mu\mu} = \left(N^{\mathrm{u}}_{\mathrm{data}} - N^{\mathrm{l}}_{\mathrm{data}} - \left(N_{\mathrm{charm}} + N_{J/\psi} + N_{\mathrm{BH}} + ...\right)\right) \times \left(\frac{N^{\mathrm{u}}_{b\bar{b}} + N^{\mathrm{l}}_{b\bar{b}}}{N^{\mathrm{u}}_{b\bar{b}} - N^{\mathrm{l}}_{b\bar{b}}}\right)^{\mathrm{MC}} \tag{9.2}$$

Events from unlike-sign backgrounds that have falsely been reconstructed as like-sign dimuon events are included both in the light-flavour background estimation and in the MC samples. To avoid double counting, this (very small) contribution is subtracted from the MC samples. Falsely reconstructed beauty MC muons are considered as signal (if they lead to an excess of unlike sign events).

9.1.1 Corrections for background charge correlations

In the context of the background study described in sec. 8.1.3.1, a small residual excess of the unlike-sign background over the like-sign background was found. This excess amounted to 2%

difference in the high mass and to 6% difference in the low-mass dimuon sample, thus:

$$N_{\mathrm{bg}}^{\mathrm{u}} = \alpha_{\mathrm{corr}} \cdot N_{\mathrm{bg}}^{\mathrm{l}} \tag{9.3}$$

where the correction factor α_{corr} is:

$$\alpha_{\mathrm{corr}} = \begin{cases} 1.02 & \text{for the high mass } (m^{\mu\mu} \geq 4 \text{ GeV}) \text{ signal sample} \\ 1.06 & \text{for the low mass } (m^{\mu\mu} < 4 \text{ GeV}) \text{ signal sample.} \end{cases} \tag{9.4}$$

To account for this background charge asymmetry, the beauty fraction was determined using a corrected version of eq. 9.2:

$$N_{b\bar{b}\to\mu\mu} = \left(N_{\mathrm{data}}^{\mathrm{u}} - \alpha_{\mathrm{corr}} \cdot N_{\mathrm{data}}^{\mathrm{l}} - \left(N_{\mathrm{charm}} + N_{J/\psi} + N_{\mathrm{BH}} + ...\right)\right) \times \left(\frac{N_{b\bar{b}}^{\mathrm{u}} + N_{b\bar{b}}^{\mathrm{l}}}{N_{b\bar{b}}^{\mathrm{u}} - \alpha_{\mathrm{corr}} \cdot N_{b\bar{b}}^{\mathrm{l}}}\right)^{\mathrm{MC}} \tag{9.5}$$

9.2 Visible and total beauty cross section

Based on the total number of beauty events determined using eq. 9.5 and relying on the good description of the data by the MC simulation as shown in sec. 8.2, a visible and a total cross section for $b\bar{b}$ production in ep collisions at HERA were measured according to:

$$\sigma_X = \frac{N_X}{\mathcal{L} \cdot acc} \tag{9.6}$$

where σ_X is the cross section for a process X, N_X the number of events determined for the process X, $\mathcal{L}$ the luminosity of the corresponding data sample and acc the acceptance:

$$acc = \frac{N_{\mathrm{rec}}^{\mathrm{MC}}}{N_{\mathrm{true,\ X}}^{\mathrm{MC}}} \tag{9.7}$$

the ratio of the number $N_{\mathrm{rec}}^{\mathrm{MC}}$ of MC events that were reconstructed in the MC sample to the number $N_{\mathrm{true,\ X}}^{\mathrm{MC}}$ of events of the process X that were in fact contained in that MC sample.

In order to present results from the combined data sets, the measurements from the 1996-97 running period at $\sqrt{s} = 300$ GeV have been corrected to correspond to the higher centre-of-mass energy using the predicted change of the cross section from FMNR. This correction changes the cross section by only 2%. The visible and total cross sections are therefore quoted for $\sqrt{s} = 318$ GeV.

The visible cross section was determined for the process $ep \to b\bar{b}X \to \mu\mu X'$ in a region of phase space with high single muon-detection efficiency ($\gtrsim 30\%$). This region was defined as:

- for both muons: $-2.2 < \eta < 2.5$
- and for one of the two muons: $p_{\mathrm{T}} > 1.5$ GeV
- and for the other muon: $p_{\mathrm{T}} > 0.75$ GeV and [$p^{\mu} > 1.8$ GeV for $\eta^{\mu} < 0.6$ or ($p^{\mu} > 2.5$ GeV or $p_{\mathrm{T}}^{\mu} > 1.5$ GeV) for $\eta^{\mu} > 0.6$]

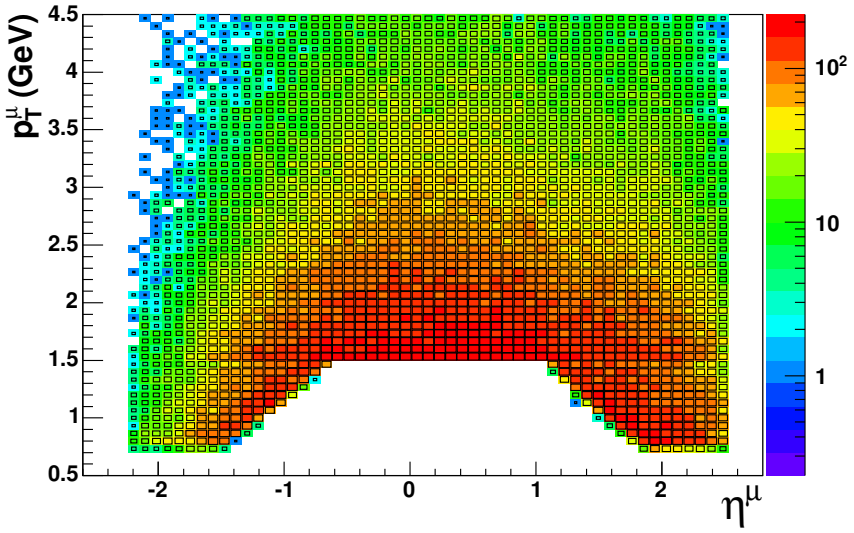

Figure 9.1: Muons from beauty decays in the visible range.

High mass $N^{\mathrm{u}}_{b\bar{b}} - \alpha_{\mathrm{corr}} \cdot N^{\mathrm{l}}_{b\bar{b}}$	Low mass $N^{\mathrm{u}}_{b\bar{b}} - \alpha_{\mathrm{corr}} \cdot N^{\mathrm{l}}_{b\bar{b}}$	Total range $N_{b\bar{b}\to\mu\mu}$
262	359	1910

Table 9.1: The number of beauty events from dimuon events in the HERA I data sample. The difference of unlike- and like-sign beauty events is given in the high- and low-mass dimuon range, as well as the extrapolated sum of unlike- plus like-sign events in the total range.

The muons from beauty decays in the visible range are shown in fig. 9.1. The measurement has not been restricted to the γp or DIS regime. The cross section is thus valid for the total phase space in W and Q^2 limited only by the b-quark mass (and the given visible muon range). The number of beauty events measured in the high- and low-mass range are given in tab. 9.1. The visible cross section for dimuon production from beauty decays in this phase space was measured to:

$$\sigma_{\mathrm{vis}}(ep \to b\bar{b}X \to \mu\mu X') = 63 \pm 7(stat.)^{+20}_{-18}(syst.)\ \mathrm{pb}. \tag{9.8}$$

The statistical error arises from the determination of the beauty fraction using the difference of like- and unlike-sign events, as described in sec. 9.1. The determination of the systematic error is summarised in sec. 9.2.1. The cross section includes muons from direct beauty decays as well as indirect muonic decays, e.g. $b \to c \to \mu$ cascade decays, $b \to J/\psi \to \mu\mu$ decays or muons from intermediate tau leptons. Decay muons from light hadrons are not included. Events with more than two valid muons enter only once.

Figure 9.2 shows the the transverse-momentum distribution for tagged b quarks in the PYTHIA direct sample. It demonstrates that the low muon transverse-momentum cuts yield a significant acceptance also for b quarks with $p^b_{\mathrm{T}} \approx 0$. This allows to extract a total $b\bar{b}$ production cross

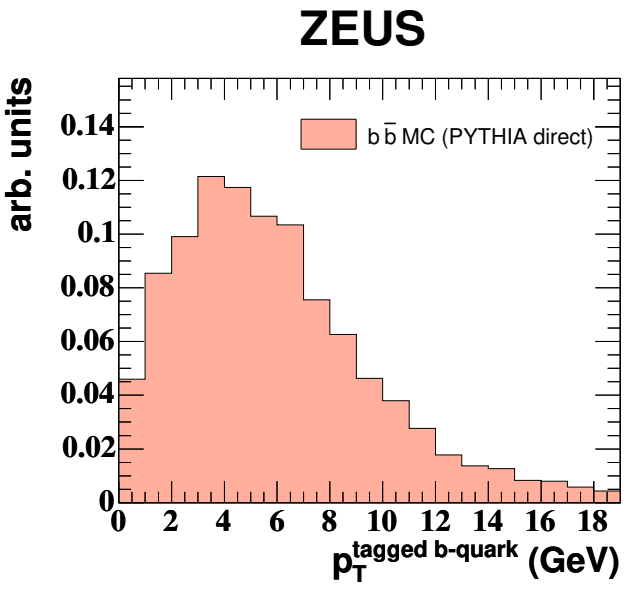

Figure 9.2: Example of b quark transverse-momentum distribution for quarks tagged by reconstructed muons in dimuon events, from PYTHIA direct processes. The tagging method is sensitive to b quarks with vanishing transverse momentum.

section for ep collisions at 318 GeV without restrictions in Q^2, W or any other kinematic variable. The total $b\bar{b}$ cross section was determined by scaling the PYTHIA+RAPGAP MC cross section with the beauty-MC scaling factor $s^b_{\mathrm{MC}} = 2.06$ (see sec. 8.2 and eq. 8.7). Using this approach, the total cross section for beauty production in ep collisions at $\sqrt{s} = 318$ GeV has been determined as:

$$\sigma_{\mathrm{tot}}(ep \to b\bar{b}X) = 16.1 \pm 1.8(\mathrm{stat.})^{+5.3}_{-4.8}(\mathrm{syst.})\ \mathrm{nb}. \tag{9.9}$$

The sources of the systematic uncertainty are summarised in sec. 9.2.1. The total cross section is compared to a NLO prediction in sec. 9.4.1.

Extrapolation from the visible to the total cross section The total cross section can also be obtained by dividing the visible cross section in eq. 9.8 by the probability $P^{b\bar{b}\to\mu\mu}_{\mathrm{vis}}$ of a $b\bar{b}$ pair to decay into two muons in the given visible range. This yields the same cross section by definition.

This probability $P^{b\bar{b}\to\mu\mu}_{\mathrm{vis}}$, with an average value of

$$P^{b\bar{b}\to\mu\mu}_{\mathrm{vis}} \sim 0.38\%, \tag{9.10}$$

is quite small [111]. However, it is almost entirely dominated by quantities measured with good precision at e^+e^- colliders. The effective branching fraction of a $b\bar{b}$ pair into at least two muons is 6.3% [25, 1]. Both the b-fragmentation functions and the $B \to \mu X$ decay spectra are well measured [1] and yield an average $b\bar{b}$ acceptance for the visible range of 6%. This includes the cases where:

- both muons come from the b quark or
- both muons come from the $\bar{b}$ quark or
- one muon comes from the b quark and the other from the $\bar{b}$ quark.

The errors on these parameters are included into the systematic error. Furthermore, the value of this acceptance varies by only a factor 3 (about 3 to 9%) in 90% of the $b\bar{b}$ phase space, delimited by

$$0 < p_{\mathrm{T}}^{b\ \mathrm{max}} < 10\ \mathrm{GeV} \quad \text{or} \quad |y^{b\ \mathrm{rap}}|^{\mathrm{min}} < 2,$$

as shown in fig 9.3. As the "worst case scenario", the $b\bar{b}$ acceptance is shown versus the transverse

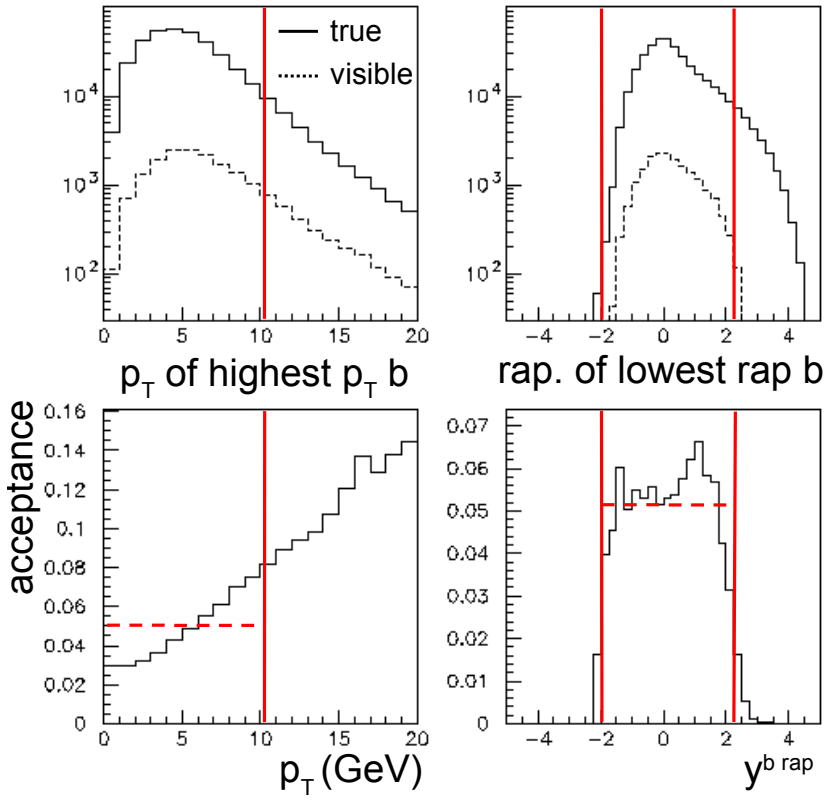

Figure 9.3: Acceptance for $b\bar{b}$ events versus the transverse momentum of the highest p_{T} b quark (*left*) and the rapidity of the lowest y^{rap} b quark (*right*). If a minimum acceptance of 3% is required, an extrapolation of the total cross section is only necessary outside the range bordered by the vertical lines. The dashed horizontal lines show the average acceptance.

momentum of the highest p_{T}^b b quark ($p_{\mathrm{T}}^{b\ \mathrm{max}}$) and the rapidity of the lowest $|y^b|$ b quark, ($|y^{b\ \mathrm{rap}}|^{\mathrm{min}}$). Showing the $b\bar{b}$ acceptance for the alternative case versus p_{T} of the lowest p_{T}^b b quark would result in seemingly higher acceptance at low p_{T}^b as the second b quark would have a larger p_{T} and thus contribute with higher acceptance. Similar reasoning is valid for y^b.

At larger p_{T}^b the acceptance rises, but the fraction of events is small. Requiring the acceptance to be greater than $\sim 1/2$ of the average (greater than 3%), a full acceptance coverage in p_{T}^b is

obtained. In y^b only 10% of the total beauty contribution in the region $y^{b\ \mathrm{rap,\ min}} > 2$ remains unmeasured.

This uniformity of acceptance means that the dependence on details of the simulation of the $b\bar{b}$ topology is rather weak, and that the extrapolation to unmeasured regions is small.

9.2.1 Systematic error of the visible and total beauty cross section

It was checked that the b-quark spectra from PYTHIA and RAPGAP agree well with the corresponding spectra from the NLO predictions described below [109]. Nevertheless, the systematic uncertainty associated to this source was estimated from drastic changes such as using the PYTHIA direct contribution only, or doubling the resolved contributions for the acceptance calculation. This is possible due to the small sensitivity to the corresponding changes in topology discussed in the previous section.

The detailed list of performed systematic checks and the resulting systematic error is given in tab. 9.2. The largest systematic uncertainty arises from the muon-efficiency correction. This contribution was estimated from the cross sections shown in fig. 9.4. Here the cross sections

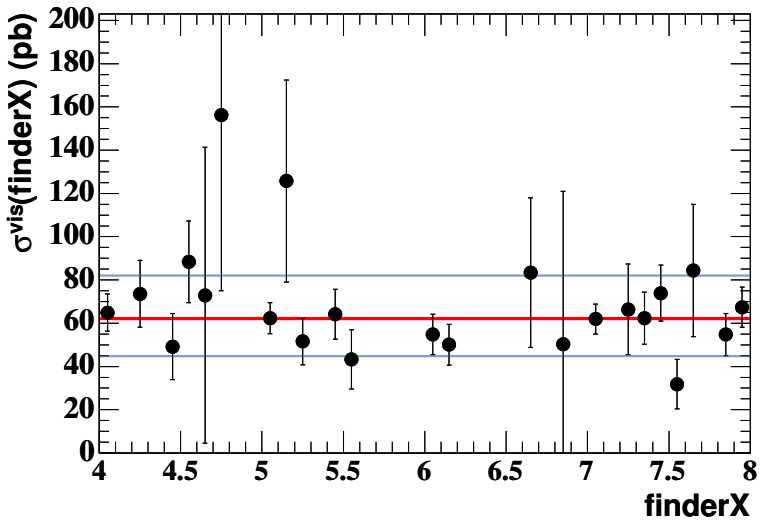

Figure 9.4: Measured visible cross sections (statistical errors only) for the breakdown of dimuon events depending on the combinations of finders reconstructing the muons. The key to the bin entries is given in tab. 7.4. The finder dependence of the cross section was used as an estimate for the systematic uncertainty of the muon-efficiency correction. The visible cross section with the total systematic uncertainty is given by the horizontal lines.

measured for different subsets of finder combinations (as explained in tab. 7.4) are shown. Differences are assumed to be due to partially incomplete corrections of the corresponding muon efficiency. The variation (root mean square) of the cross sections is 15%. An additional muon-efficiency error of 17% is quoted. This was estimated from the difference between two different muon-efficiency correction methods.

The dependence on extrapolations when using the normalisation obtained in the $c\bar{c} \to D^* + \mu X$ channel for the $c\bar{c} \to \mu\mu X$ channel was estimated by varying the charm fraction by $\pm 21\%$ and

Source of syst. error		relative error
Errors on scale factor $s^b_{\rm MC}$		
variation of charm fraction by 21% (see comment in text):		±12%
Branching ratio $c \to \mu$	$\sim 10\%$	
$D^{*+/-}$ fraction	$\sim 6\%$	
Branching ratio $D^* \to K\pi\pi_s$	$\sim 3\%$	
μ spectr.+fragmentation	$\sim 10\%$	
$D^*\mu$ stat.	$\sim 10\%$	
all finders vs. BREMAT only	$\sim 10\%$	
use of a different c MC		- 5%
$B^0\overline{B^0}$-oscillation parameter, varied by 8%		±4%
generic additional error assumed for PYTHIA c and b model		±10%
BH, J/ψ, ψ' variation by 50%		±10%
b spectral shape uncertainty: use $b\bar{b}$ MC direct only		-12%
use non-direct twice		+ 4%
muon eff. + muon eff. corr. (from fig. 9.4)		±15%
muon eff. correction (difference between two analyses)		+17%
trigger efficiency (±5%)		±8%
background like-unlike ratio (change by 3%)		±3%
variation of isolation cuts by 500 MeV		±2%
variation of $E_{\rm T}$ cuts by 3% (energy scale)		±2%
variation of $p_{\rm T}$ cut (B field scale) by 0.3%		<1%
Errors on $\mu \to$total extrapolation		
direct only / double exc., res (*)		±5%
variation of $b \to \mu$ branching ratio by 3%		±6%
PYTHIA model vs. FMNR/HVQDIS		(**)
luminosity		±2%
total systematic error - total cross section		+33 - 30%
- visible cross section (excl. extrapolation err.)		+32 - 28%
statistical error		11%

Table 9.2: Estimations of the systematic error for the visible and the total cross section. The statistical error is given also. Remarks: (*) In addition to acceptance for the visible cross section. (**) Assumed to be covered by direct/excitation variation.

resulted in a systematic variation of ±12%. The 21% is the quadratic sum of the the list of uncertainties given in tab. 9.2 below "variation of the charm fraction".

The dependence on the details of the b-quark spectra was estimated by using the direct $b\bar{b}$ MC only or the non-direct MC contribution twice. The influence of these drastic changes, +12% and −4%, was found to be small.

Other uncertainties include the variation of branching ratios, the $B^0\overline{B^0}$-mixing parameter, and an adequate variation of the charm, J/ψ, and Bethe-Heitler backgrounds.

Uncertainties due to calorimetry, tracking, and luminosity measurement were found to be essentially negligible.

9.3 Differential muon cross sections

To have a more detailed look at correlations in the $\mu\mu/b\bar{b}$ system as well as at single muon/b-quark properties, differential cross section in p_{T}^{μ}, η^{μ} and $\Delta\phi^{\mu\mu}$ are compared to simulations. As for the visible cross section, all differential cross sections include muons from direct beauty decays as well as indirect muonic decays, e.g. $b \to c \to \mu$ cascade decays, $b \to J/\psi \to \mu\mu$ decays or muons from intermediate tau leptons.

9.3.1 Differential muon cross section in p_{T}^{μ} and η^{μ}

The method used to derive the visible and total cross section was also applied to extract differential cross sections, except that the cross section was determined bin by bin. A higher p_{T}^{μ} cut enriches muons from the direct decay of b quarks (rather than cascade decays) and thus yields a better correlation between the quark and the muon. Thus the differential cross sections for the process $ep \to b\bar{b}X \to \mu\mu X'$ were defined for a simpler phase space than the one chosen for the visible cross section. Both muons were required to lie in the range:

$$p_{\mathrm{T}}^{\mu\ (1,2)} > 1.5 \text{ GeV} \tag{9.11}$$

$$-2.2 < \eta^{\mu\ (1,2)} < 2.5. \tag{9.12}$$

For the differential cross sections, the muon selection was simplified to

$$p_{\mathrm{T}}^{\mu\ (1,2)} > 1.5 \text{ GeV}. \tag{9.13}$$

The harder cuts still retained about 2/3 of the originally selected sample. The data distributions for this selection in p_{T}^{μ} and η^{μ} are shown in fig. 9.5. The beauty normalisation did essentially not change compared to the wider dimuon selection:

$$s^{b}_{\mathrm{MC}\ (p_{\mathrm{T}}^{\mu\ (1,2)} > 1.5\ \mathrm{GeV})} = 1.95 \pm 0.23(stat.) \tag{9.14}$$

As compared to previous HERA analyses, the phase space coverage in p_{T}^{μ} and η^{μ} could be enlarged. The larger muon detection efficiency, lower p_{T}^{μ} cuts and the effectively lower transverse energy restriction (due to the "jet-less" selection) allowed for finer segmented differential cross sections.

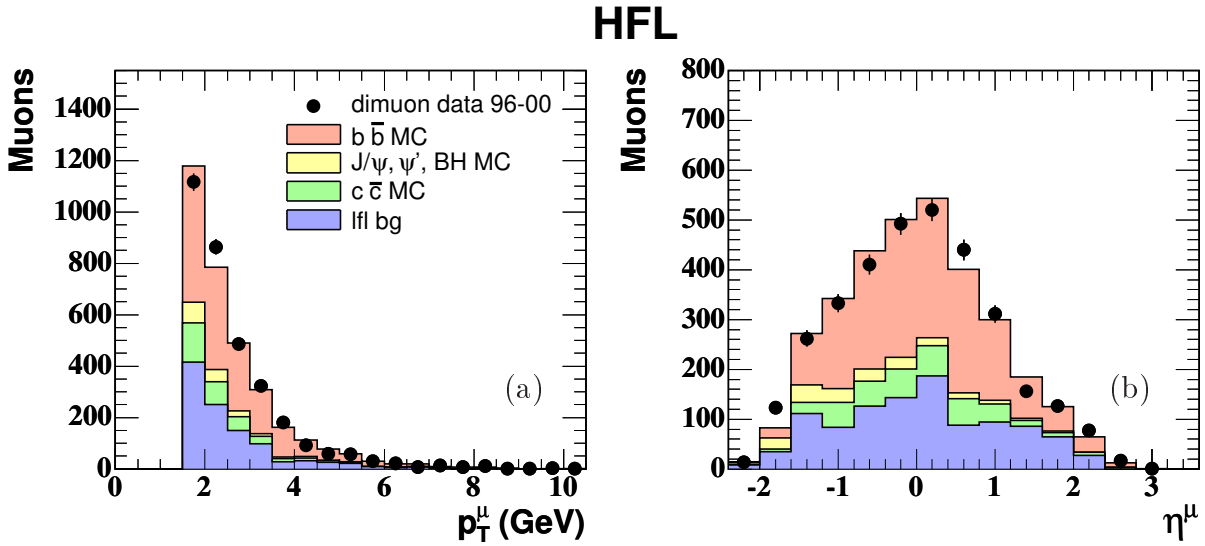

Figure 9.5: (a) Muon transverse-momentum and (b) pseudo-rapidity distribution from both high and low mass muon pairs in the nonisolated unlike-sign sample. Two muons with the higher p_T^μ cut were entered for each event. The breakdown into the expected contributions from different processes is also shown.

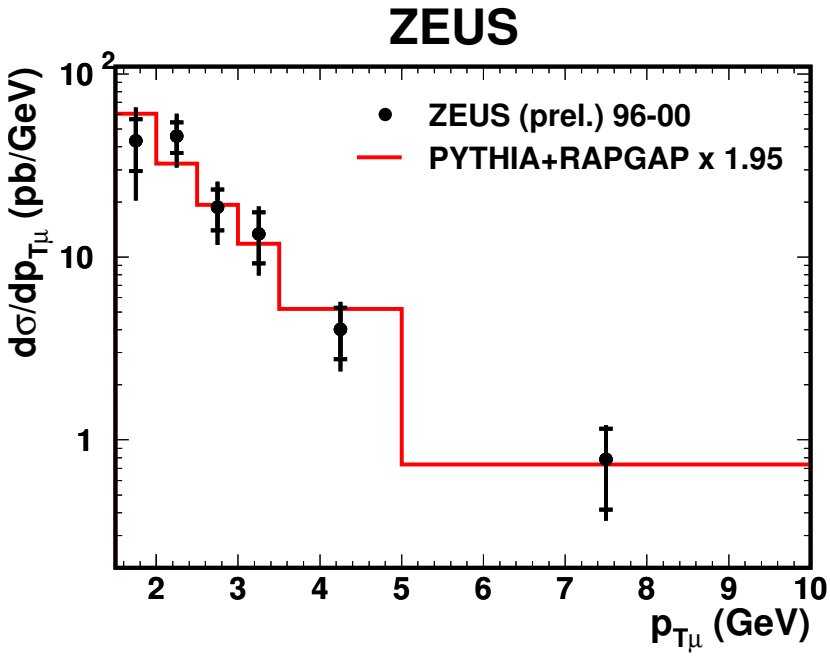

Figure 9.6: Differential cross section $d\sigma/dp_T^\mu$ for muons from b decays in dimuon events with $p_T^\mu > 1.5$ GeV and $-2.2 < \eta^\mu < 2.5$ for both muons. Two muons contribute for each event. The data (solid dots) are compared to the scaled sum of the predictions by the LO+PS generators PYTHIA and RAPGAP (histogram).

bin in p_T^μ [GeV]	differential cross section [pb/GeV]
$1.5 \leq p_T^\mu < 2.0$	43.1 ± 13.7
$2.0 \leq p_T^\mu < 2.5$	45.8 ± 8.7
$2.5 \leq p_T^\mu < 3.0$	18.7 ± 4.8
$3.0 \leq p_T^\mu < 3.5$	13.4 ± 4.1
$3.5 \leq p_T^\mu < 5.0$	4.0 ± 1.3
$5.0 \leq p_T^\mu \leq 10.0$	0.78 ± 0.37

Table 9.3: Differential cross section $d\sigma/dp_T^\mu$ for muons from b decays. Errors are statistical only.

The differential cross section in bins of p_T^μ is shown in fig. 9.6. The bin ranges and corresponding cross section values (with statistical errors) are summarised in tab. 9.3. Bin-dependent systematic uncertainties were calculated wherever possible, see sec. 9.3.3. The PYTHIA+RAPGAP MC scaled by the beauty normalisation factor 1.95 (eq. 9.14) is in very good agreement with the measured cross sections in p_T^μ.

The differential cross section in bins of η^μ is shown in fig. 9.7. The bin ranges and corresponding cross section values (with statistical errors) are summarised in tab. 9.4. Very good agreement

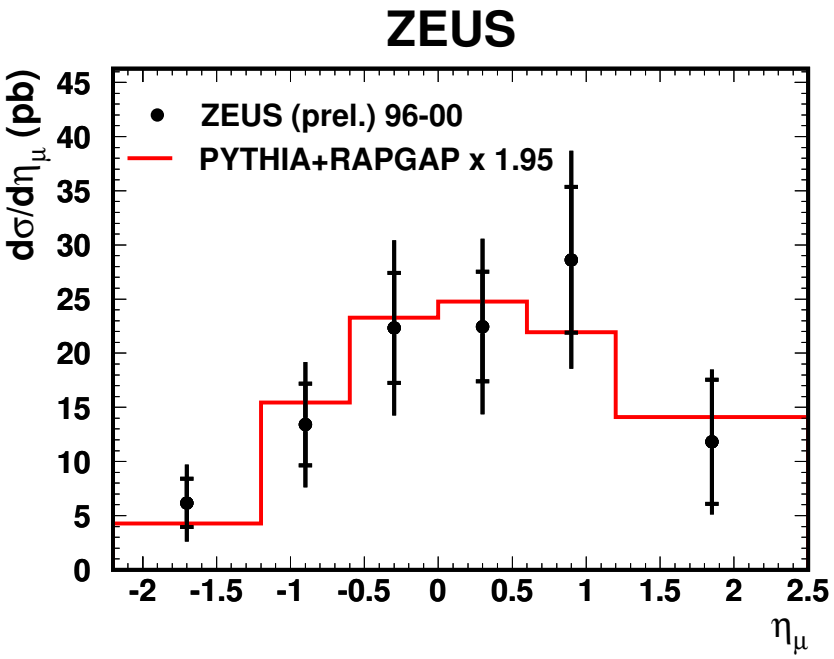

Figure 9.7: Differential cross section $d\sigma/d\eta^\mu$ for muons from b decays in dimuon events with $p_T^\mu > 1.5$ GeV and $-2.2 < \eta^\mu < 2.5$ for both muons. Two muons contribute for each event. The data (solid dots) are compared to the scaled sum of the predictions by the LO+PS generators PYTHIA and RAPGAP (histogram).

of the PYTHIA+RAPGAP MC is found also in case of the η^μ cross section.

Apart from the normalisation, the QCD description using the LO+PS approach implemented in the event generators PYTHIA and HERWIG (sec. 2.5.1) thus yields a good description of beauty production in ep collisions from dimuon events within the entire accessible phase space, especially at low values of p_T^μ.

bin in η^μ	differential cross section [pb]
$-2.2 \leq \eta^\mu < -1.2$	6.2 ± 2.2
$-1.2 \leq \eta^\mu < -0.6$	13.4 ± 3.8
$-0.6 \leq \eta^\mu < 0.0$	22.3 ± 5.1
$0.0 \leq \eta^\mu < 0.6$	22.5 ± 5.1
$0.6 \leq \eta^\mu < 1.2$	28.6 ± 6.7
$1.2 \leq \eta^\mu \leq 2.5$	11.8 ± 5.7

Table 9.4: Differential cross section $d\sigma/d\eta^\mu$ for muons from b decays. Errors are statistical only.

9.3.2 Angular muon-correlation cross section

For the purpose of measuring correlations in the $b\bar{b}$ system, the event selection was optimised for retaining the largest possible amount of muon pairs coming from different beauty quarks. The fraction of dimuon events from the same or from different quarks can be separated by the invariant dimuon mass, as the b-quark mass sets an upper limit on the invariant dimuon mass for muons from the same b quark. In fig. 9.8 the dimuon mass distributions are shown. The

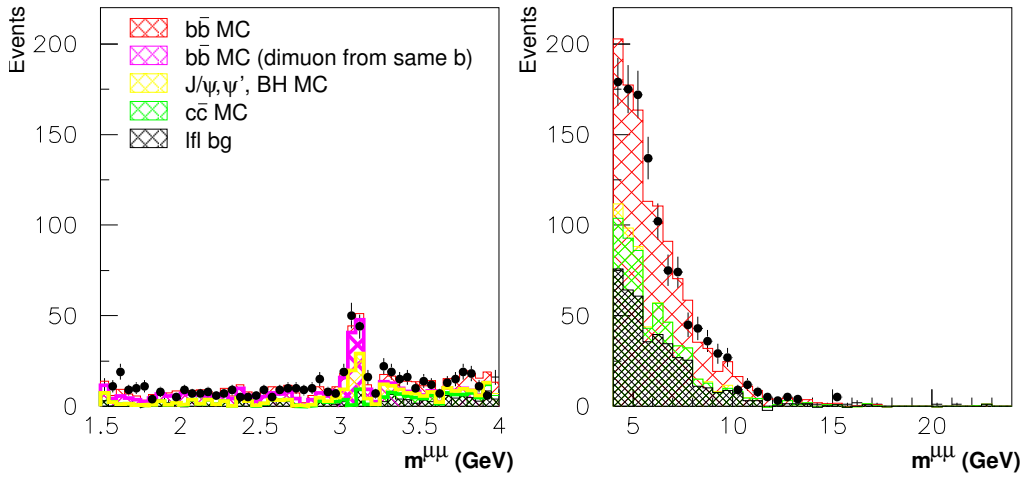

Figure 9.8: Dimuon-mass distributions for the signal region. To eliminate contribution from dimuons from the same b quark, a dimuon-mass cut at $m^{\mu\mu}_{\text{inv}} > 3.25$ GeV was introduced for determining the $\Delta\phi$ cross section.

fraction of muons from the same b quark becomes small at about 3 GeV. Thus a mass cut for these dimuons was set to

$$m^{\mu\mu}_{\text{inv}} > 3.25 \text{ GeV}. \tag{9.15}$$

This also excludes most J/ψ candidates. As above, to further enrich muons from the direct decay of the b quark (rather than cascade decays) and thus improve the angular correlation of the muon with the b quark, the muon transverse-momentum cut was raised to

$$p^\mu_{\text{T}} > 1.5 \text{ GeV} \tag{9.16}$$

for both muons.

The difference in azimuth angle between the two muons from this selection is shown in fig. 9.9. Consequently, for the MC simulation, muons were now additionally required to originate from different b quarks. This definition results in the differential cross section shown in Fig. 9.10.

As before, the statistical errors arise from the method of the signal determination from the difference of like- and unlike-sign dimuon events. In some bins this difference is quite small, leading to the partially large statistical errors. For the systematic errors, see sec. 9.3.3.

The distribution is again well described by the LO+PS MC within the large errors resulting from the subtraction method.

The average azimuthal distance in $\Delta\phi$ between the muon and the corresponding b quark is about 36°. Thus the direction of the muon is correlated with that of the b quark. The good agreement of cross section in $\Delta\phi$ and also the good description found in control distributions for angular correlations e.g. in $\Delta R^{\mu\mu}$ and $\Delta\phi^{\mu\mu}$, indicates that the correlations in the $b\bar{b}$ system are described adequately by the LO+PS MC.

9.3.3 Systematic errors of the differential muon cross sections

Essentially the same method to determine the systematic errors as for the visible and total cross sections was applied bin by bin for the differential cross sections. The typical relative errors are given in tab. 9.5. No excessive bin by bin variations were found and the errors correspond closely to those of the visible and total cross section.

9.4 Comparison with NLO calculations and other measurements

9.4.1 NLO prediction for the total cross section

The total cross section predicted by NLO QCD calculations was obtained [112] in the massive approach by adding the predictions from FMNR and HVQDIS for $Q^2 < 1$ GeV^2 and $Q^2 > 1$ GeV^2, respectively. The renormalisation and factorisation scales of these calculations (see sec. 2.5.2, eq. 2.24 and 2.25) are varied by a factor 2, and the b-quark mass was varied between 4.5 and 5 GeV. The CTEQ5M/CTEQ5F4 structure functions were used. The resulting cross section for $\sqrt{s} = 318$ GeV

$$\sigma_{\mathrm{tot}}^{\mathrm{NLO}}(ep \to b\bar{b}X) = 5.8_{|Q^2<1\ \mathrm{GeV}^2} + 1.0_{|Q^2>1\ \mathrm{GeV}^2} = 6.8^{+3.0}_{-1.7}\ \mathrm{nb} \tag{9.17}$$

is a factor 2.4 lower than the measured value, although still compatible within the large uncertainties (about two standard deviations). As the cross section is dominated by the low p_{T} region ($p_{\mathrm{T}}^{\mu} \lesssim 3$ GeV), the main part of the data/NLO offset can be located in this region.

9.4.2 Comparison with the $D^* + \mu$ results

Figure 9.11 shows a comparison of the total cross section to the slightly less inclusive cross

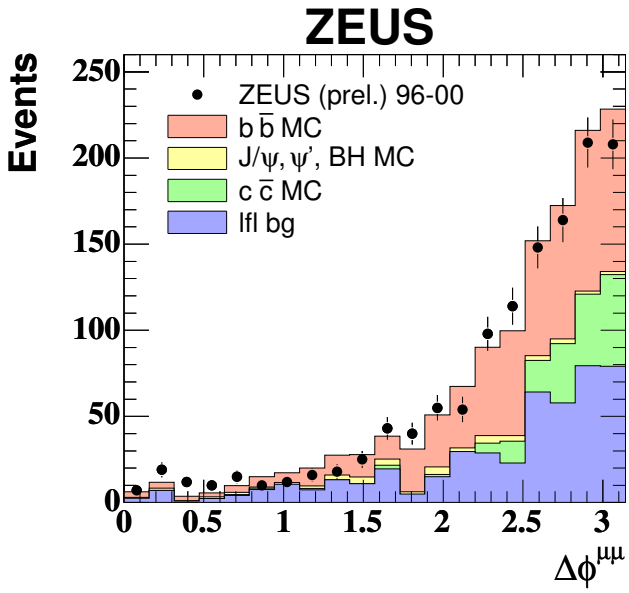

Figure 9.9: Distribution of the azimuthal distance $\Delta\phi$ between the two muons in dimuon events with $p_{\mathrm{T}}^{\mu} > 1.5$ GeV for both muons, and $m^{\mu\mu} > 3.25$ GeV. The breakdown into the expected contributions from different processes is also shown.

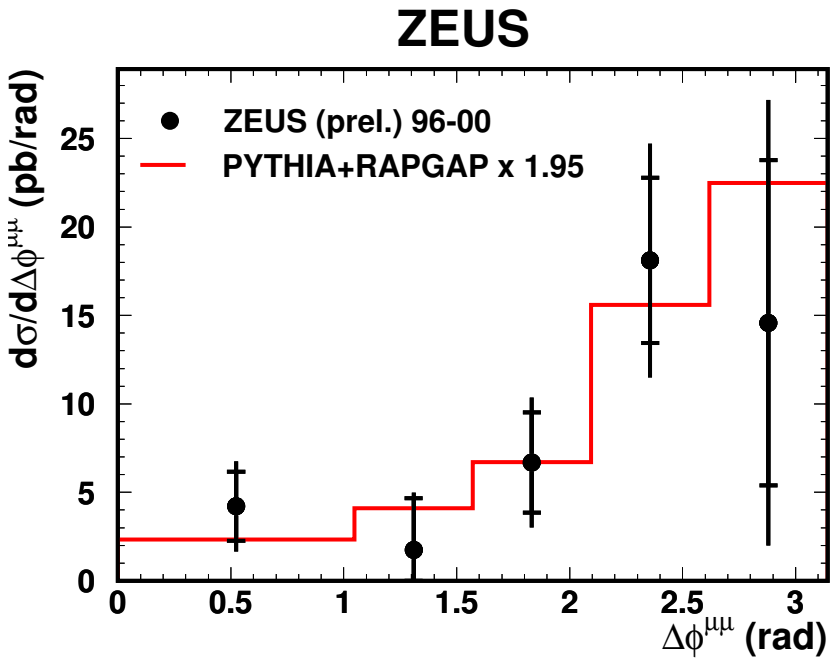

Figure 9.10: Differential cross section $d\sigma/d\Delta\phi^{\mu\mu}$ for dimuon events from $b\bar{b}$ decays in which each muon originates from a different $b(\bar{b})$ quark, with $p_{\mathrm{T}}^{\mu} > 1.5$ GeV and $-2.2 < \eta^{\mu} < 2.5$ for both muons. The data (solid dots) are compared to the scaled sum of the predictions by the LO+PS generators PYTHIA and RAPGAP (histogram)

Source of syst. error		typical bin-by-bin error
Errors on scale factor s^b_{MC}		
variation of charm fraction by 21%:		±12%
Branching ratio $c \to \mu$	$\sim 10\%$	
$D^{*+/-}$ fraction	$\sim 6\%$	
Branching ratio $D^* \to K\pi\pi_s$	$\sim 3\%$	
μ spectr.+fragmentation	$\sim 10\%$	
$D^*\mu$ stat.	$\sim 10\%$	
all finders vs. BREMAT only	$\sim 10\%$	
c spectral shape uncertainty: $0\times$ /$2\times$ non-direct contribution		±5%
$B^0\overline{B^0}$-oscillation error, varied by 8%		±4%
generic additional error assumed for PYTHIA c and b model		±10%
BH, J/ψ, ψ' variation by 50%		±10%
b spectral shape uncertainty: use direct $b\bar{b}$ MC only		-10%
use non-direct twice		+10%
muon eff. + muon eff. corr. (from fig. 9.4)		±15%
trigger efficiency (±5%)		±8%
background like-unlike ratio (change by 3%)		±3%
variation of isolation cuts by 500 MeV		±2%
variation of E_{T} cuts by 3% (energy scale)		±2%
variation of p_{T} cut (B field scale) by 0.3%		<1%
luminosity		±2%
total typical systematic error		$\sim \pm$ 30%

Table 9.5: Estimations of the systematic error for the differential cross sections.

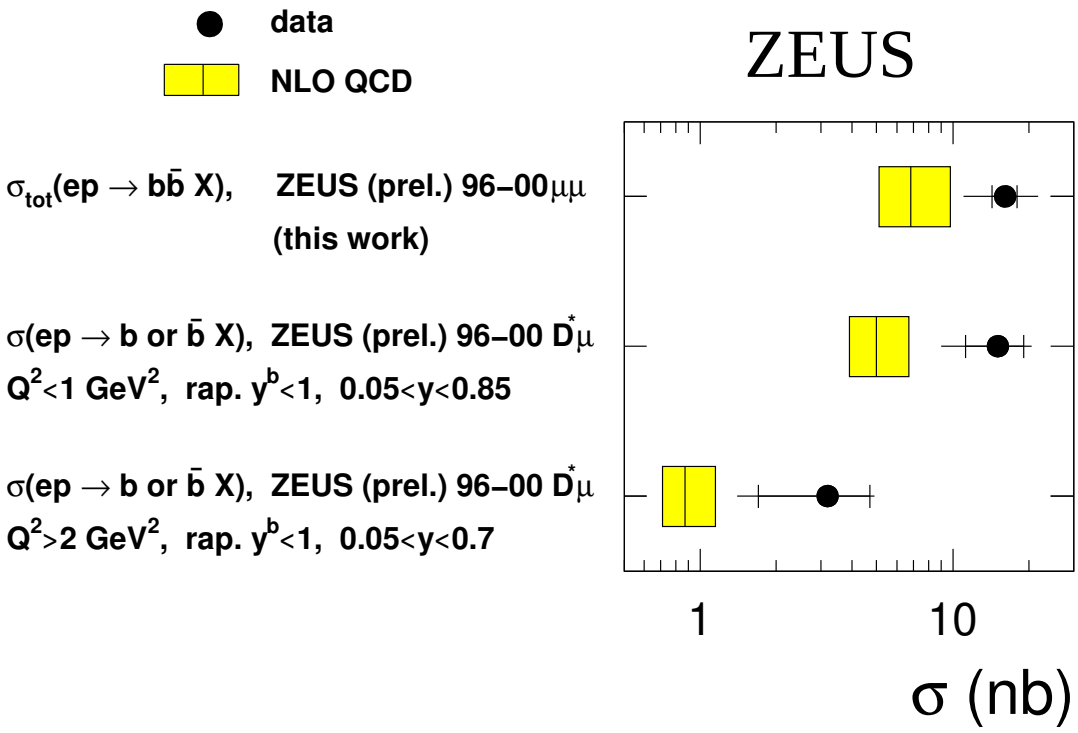

Figure 9.11: Comparison of measured cross sections to NLO predictions. The $b\bar{b}$ cross section from this analysis is shown at the top. For comparison, related b or $\bar{b}$ cross sections obtained in the ZEUS $D^*\mu$ analysis for the photoproduction regime (middle line) and DIS (lower line), are also shown.

sections from the $D^* + \mu$ final state obtained by ZEUS in earlier measurements [55], explained in sec. 3.4.3. These measurements, as well as similar measurements by H1 [56] show the same trend to be larger than the corresponding QCD predictions.

9.4.3 NLO prediction for the differential cross sections

Differential cross sections were obtained in p_{T}^{μ}, η^{μ} and in $\Delta\phi^{\mu\mu}$. Due to technical reasons a NLO prediction could not be calculated for the p_{T}^{μ} and η^{μ} cross sections. These cross sections were calculated for muons from different or from the same b quark. The available NLO prediction allows to produce one muon from each b quark but not two from the same. Thus the prediction was not applicable for the measured cross sections in p_{T}^{μ} and η^{μ}.

The prediction for the differential cross section in $\Delta\phi^{\mu\mu}$ was calculated [113] in the massive approach using FMNR. The DIS part was approximated here using the Weizsäcker-Williams approximation [114], rather than adding the result from HVQDIS. In this approach, the cross section is calculated up to an upper cut in $Q^2_{\mathrm{max}} = m_b^2$. The resulting cross section is valid for the total Q^2 range. It was shown that this approach yielded the same result for the total cross section as the sum of FMNR and HVQDIS. As before, the renormalisation and factorisation scale was varied by a factor 2, and the b-quark mass was varied between 4.5 and 5 GeV. The CTEQ5M proton and the GRV-G HO photon structure functions were used.

The muons from different b quarks were generated according to the following scheme:

- Collinearly fragment b quarks to B hadrons
- decay B hadron into muons isotropically in B hadron rest frame using parametrised inclusive muon-momentum spectra as extracted from PYTHIA.

The resulting differential cross section in bins of $\Delta\phi^{\mu\mu}$ for $\sqrt{s} = 318$ GeV is compared to the measured cross section in fig. 9.12. Reasonable agreement is found within the large errors. Also

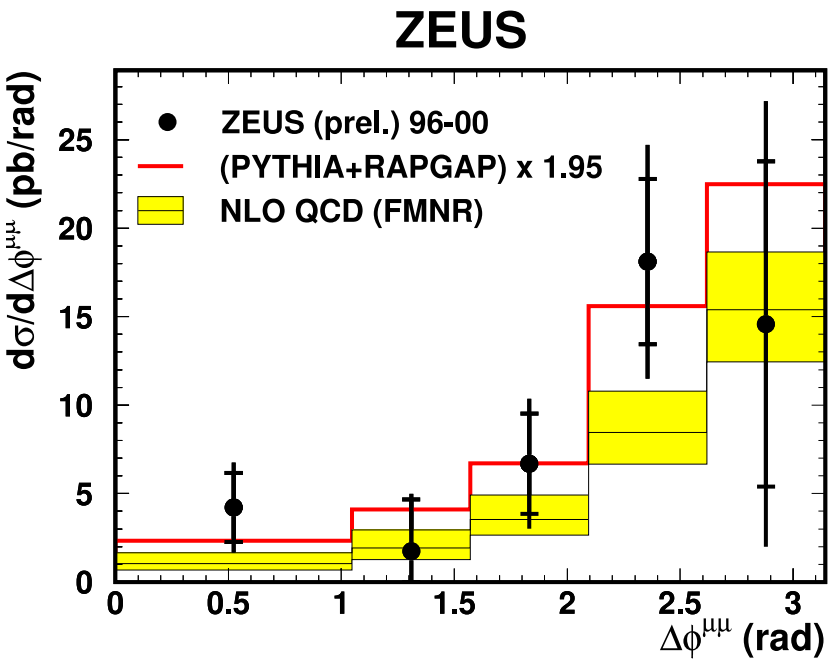

Figure 9.12: Differential cross section $d\sigma/d\Delta\phi^{\mu\mu}$ for dimuon events from $b\bar{b}$ decays in which each muon originates from a different $b(\bar{b})$ quark, with $p_{\mathrm{T}}^{\mu} > 1.5$ GeV and $-2.2 < \eta^{\mu} < 2.5$ for both muons. The data (solid dots) are compared to the scaled sum of the predictions by the LO+PS generators PYTHIA and RAPGAP (histogram) and the prediction by FMNR (shaded band).

here the NLO prediction tends to slightly undershoot the measured cross section.

Events with higher-order topology, e.g. with several radiated gluons, could lead to a low value of $\Delta\phi^{\mu\mu}$ for muons from different b quarks. The measurement of $\Delta\phi^{\mu\mu}$ is thus in principle sensitive to the contribution of such processes.

In the current state of the analysis the large errors do not allow a conclusive statement concerning these contributions. The errors of the measurements could be reduced by increasing the number of selected events (e.g. by increasing the data sample using data from the HERA II running period) and also by reducing the systematic uncertainty by a further reduction of the backgrounds. The backgrounds could be reduced by e.g. using a combined $p_{\mathrm{T}}^{\mathrm{rel}}$, pseudo thrust and impact-parameter method (making use of the MVD). This should improve especially the $\Delta\phi^{\mu\mu}$ measurement close to $\Delta\phi^{\mu\mu} \approx \pi$ which is dominated by errors introduced by the locally large charm background.

The errors could also be reduced by the use of a different method to determine the light-flavour background. In this analysis, the beauty contribution was obtained from the difference of like-

and unlike-sign dimuons. Finding an alternative method to determine the absolute shape and normalisation of the dimuon light-flavour backgrounds would allow to use the sum rather than the difference of like- and unlike-sign events and thus increase the useful statistics. A possible method would be to determine a parametrisation of the probability to misidentify a hadron as a muon. Applying this parametrisation to an inclusive hadron sample would yield a description of the background [115]. The estimation of the systematic uncertainty of such alternative methods might however prove to be challenging.

Chapter 10

Conclusion and Outlook

Measurements of open beauty production in dimuon events have been presented using data from the ZEUS detector corresponding to an integrated luminosity of 114 ± 2.9 pb^{-1} at a centre-of-mass energy of $\sqrt{s} = 318$ and 300 GeV.

In previous analyses the ZEUS muon detection system was used via muon reconstruction algorithms, that were limited to subcomponents of the system. This thesis was among the first to make use of the full redundancy in the muon detection system by the combination of several standalone muon algorithms yielding a highly efficient, low-background method to reconstruct muons. This included also the use of some so far unused muon detector components and allowed to expand the kinematical muon region to lower transverse momenta and greater pseudorapidities. A "jet-less" selection, with only a cut on the transverse energy together with the loose muon cuts, resulted in a coverage of the beauty-quark phase space down to zero transverse momentum (p_{T}). Special emphasis was put on the low p_{T} and high pseudorapidity (η) region. This is interesting as in several earlier analyses the next-to-leading order (NLO) quantum chromo dynamics (QCD) description did not match the data well in this region of phase space.

Charge correlations of the dimuon beauty signal and corresponding backgrounds were exploited to measure the beauty fraction in the selected data sample. It was established that light-flavour background muons are essentially uncorrelated in charge. Thus the difference of the like- and unlike-sign dimuon distributions is free from light-flavour background and was used to measure the beauty signal. The dimuon charm background was normalised using an external constraint from a ZEUS $D^* + \mu$ measurement. The remaining backgrounds from quarkonia ($(J/\psi$, ψ' and $\Upsilon) \to \mu\mu$) and Bethe Heitler-like events were normalised on a complementary sample of isolated dimuon events.

The achieved beauty purity of about 50% is relatively high and reduces the dependence on the description of the backgrounds.

The dimuon double tag yields sensitivity to $b\bar{b}$ correlations. These correlations can e.g. be observed in distributions of the azimuthal distance between two muons. The good agreement of the Monte Carlo simulation (MC) with the measured cross section in $\Delta\phi^{\mu\mu}$ and also the good description found in control distributions for angular correlations e.g. in $\Delta R^{\mu\mu}$ and $\Delta\phi^{\mu\mu}$, indicates that the original $b\bar{b}$ correlations are described adequately by the leading-order plus parton-shower MC.

Restricting the muons to an η and p_T region with high acceptance (defined in sec. 9.2), a visible cross section for the process $ep \to b\bar{b}X \to \mu\mu X'$ at a centre-of-mass energy of $\sqrt{s} = 318$ GeV was obtained:

$$\sigma_{\text{vis}}(ep \to b\bar{b}X \to \mu\mu X') = 63 \pm 7(stat.)^{+20}_{-18}(syst.) \text{ pb.} \tag{10.1}$$

From this measurement, the first measurement of the total cross section for beauty production in HERA *ep* collisions was possible with only small extrapolations into unmeasured regions of beauty-quark phase space. The result is:

$$\sigma_{\text{tot}}(ep \to b\bar{b}X) = 16.1 \pm 1.8(\text{stat.})^{+5.3}_{-4.8}(\text{syst.}) \text{ nb} \tag{10.2}$$

which is a factor of 2.4 higher than the corresponding NLO prediction (obtained by the two NLO QCD programs FMNR and HVQDIS for the regions of $Q^2 < 1$ GeV^2 and $Q^2 > 1$ GeV^2 respectively) of

$$\sigma^{\text{NLO}}_{\text{tot}}(ep \to b\bar{b}X) = 6.8^{+3.0}_{-1.7} \text{ nb.} \tag{10.3}$$

The significance of this 'excess' is, however, only about two standard deviations. As a general trend, the measurements of beauty production at HERA by the H1 and ZEUS collaborations (in the $D^* + \mu$ and jet+μ channels in γp and DIS) found that at lower transverse momenta of muons or beauty quarks the data are less well described by NLO QCD calculations. In this analysis, the range in p^μ_T was extended from typically $p^\mu_T \sim 2.5$ GeV in previous analyses down to $p^\mu_T > 0.75$ GeV. As the total cross section measured in the dimuon analysis is dominated by the contribution from the low p_T region, the measurements presented here support the previous observations at low values of p^μ_T.

Differential cross sections in the pseudorapidity, η^μ, and transverse momentum, p^μ_T, of the muons, as well as $b\bar{b}$ correlations in the azimuthal distance $\Delta\phi^{\mu\mu}$ of the dimuon system were also measured. While the leading-order plus parton-shower approach used in the Monte Carlo models fails to describe the normalisation of the differential cross sections, the measured shape is reproduced well. This approach thus provides a good description of the corresponding physics processes involved in the entire accessible phase space. This refers especially to the description of $b\bar{b}$ correlations, as mentioned above. The cross section in $\Delta\phi^{\mu\mu}$ was constrained to muons from different b quarks, allowing for a calculation of differential NLO predictions. While it is also smaller than the measured cross section, the NLO prediction agrees in shape. Stronger conclusions, as e.g. the possible need for calculations of processes at higher order can not be claimed with the currently large errors of the measurement.

The HERA upgrade in 2000/2001 led to the aimed for higher luminosity. The startup of HERA II was, however, accompanied by high background levels which prevented an efficient running of the detectors. A detailed simulation environment was successfully set up and used to determine the origin of the sizable synchrotron radiation part of the backgrounds. Based on these results, the collimation system has been improved reducing the synchrotron-radiation backgrounds by more than a factor of 10. Together with other measures to reduce also the remaining electron and proton particle backgrounds, these measures enabled successful data taking at the upgraded HERA accelerator.

Possible future improvements to the analysis presented in this thesis include the measurement of further differential distributions, the exploitation of the large anticipated HERA II dataset, as well as further work on the NLO predictions:

- Cross section were obtained for muons from b quarks. The next logical step to follow is the extrapolation to *beauty quark* differential cross sections. This would allow a comparison with beauty production from other final states.

- The influence of the systematic uncertainty arising from backgrounds to beauty production (especially from the charm background) could be reduced by selecting even higher purity beauty samples, allowing for measurements with higher precision. The corresponding loss in statistics can be balanced by the large data samples that are being recorded during the HERA II phase. The increased beauty purity could be gained by the combination of the dimuon tag with additional beauty tags, like the transverse momentum of the muon relative to the closest jet, $p_{\mathrm{T}}^{\mathrm{rel}}$, and pseudo thrust (see sec. 6.3.5), and, on the HERA II data, also the use of the decay length of B mesons making use of the high precision provided by the ZEUS Micro-Vertex detector.

- Beauty measurements from LEP, sensitive to the gluon contribution in the photons, showed an offset of 3-4 over NLO predictions. As photons are also contributing to beauty production at HERA, it would be interesting to study in more detail the influence of the photon structure on beauty production at HERA. A well understood photon structure will also be important for measurements at the planned e^+e^- collider ILC.

Complementing previous measurements of beauty production at HERA, the measurements presented in this thesis provided further insight into QCD processes involving beauty quarks. They show that, e.g. making use of the improvements discussed above, the study of beauty at HERA (II) will provide further exciting and accurate results in the near future.

Appendix A

Coordinate systems

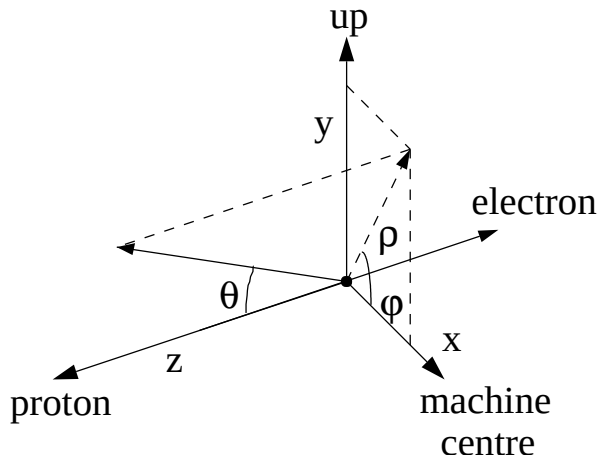

Figure A.1: The ZEUS coordinate system. The z axis points along the positive proton direction. The point of origin is located at the nominal interaction point. The angles θ (angle to z axis), φ (angle in xy plane) and the distance $\rho = \sqrt{x^2 + y^2}$ shown are standard polar coordinates.
In the HERA coordinate system, the z and x axes are inverted relative to the ZEUS coordinate system. Thus the x_{HERA} axis points away from the HERA centre and the z_{HERA} axis along the electron direction.

Appendix B

Design changes from positrons to electrons

Magnet	$\sim$ **z**	$\sim \Delta$**x**	$\sim \Delta 1/\rho$ **(m^{-1})**	$\sim \Delta$**k (m^{-2})**
GJ08	9 m	+ 3.0 mm	-	-
GI07	7 m	- 4.0 mm	-	-
GI06	4 m	- 6.5 mm	-	-
GGO1	2 m	-	$+9.0 \cdot 10^{-3}$	-
GO	-2 m	-	$+1.65 \cdot 10^{-1}$	$-1.0 \cdot 10^{-2}$
GI7	-7 m	-	-	$-1.0 \cdot 10^{-3}$
GJ9	-9 m	-	-	$+1.0 \cdot 10^{-3}$
BO09	-11 m	-	$+4.4 \cdot 10^{-4}$	-
QL14	-43 m	-	-	$-6.2 \cdot 10^{-3}$
QL15	-55 m	-	-	$+1.9 \cdot 10^{-2}$

Table B.1: The modifications of the magnet parameters for the switch from the positron to the electron simulation. The columns show the name and Z position of the magnets (HERA coordinate system, in which the electron beam is the positive Z direction), shift in the position of the magnets, change in the dipole strength and change in the quadrupole strength.

Appendix C

MC samples - detailed list

Detector configuration →		1996-1997		1998-1999		1999-2000	
process		σ(pb)	$\mathcal{L}$(pb^{-1})	σ(pb)	$\mathcal{L}$(pb^{-1})	σ(pb)	$\mathcal{L}$(pb^{-1})
b direct	γp	3673	249.88	3954	75.10	3955	368.49
b resolved	γp	819	256.34	912	98.67	914	360.99
b excitation in photon	γp	1499	240.11	1657	72.40	1657	361.96
b excitation in proton	γp	308	286.47	347	84.99	350	421.32
b direct	DIS	-	-	-	-	749	6281.03
c direct	γp	48952	257.90	52508	100.71	52492	286.74
c resolved	γp	2761	292.20	3061	132.21	3064	262.01
c excitation in photon	γp	87851	247.64	95302	103.83	95321	290.27
c excitation in proton	γp	15063	269.96	16553	121.41	16560	284.68
c direct	DIS	-	-	-	-	79289	529.34

Table C.1: Generator cross section predictions and integrated luminosities of the used PYTHIA (marked "γp") and RAPGAP (marked "DIS") MC samples for signal (beauty quarks) and charm background. (The luminosity values of the PYTHIA γp sample in this table have been corrected relative to the originally generated MC samples to account for the Q^2 cut that was applied during the analysis but not during the generation. The following correction factors were applied: dir: 0.9, res and excitation from photon: 1.0 and excitation from proton: 0.98.)

Appendix D

Definition of the std. $\mathcal{G}$MUON quality

quality	finder combination	CTD match?	match prob/ DCA cut	vtx ass.	mip prob	mom. or rap.
6	BREMAT 5dof	yes	> 0.01	yes	-	-
	MPMATCH or MUFO	yes	> 0.05	-	-	-
	MPMATCH/MUFO + MV	yes	$> 0.01, < 0.05$	-	> 0.6	p>1
5	BREMAT 4dof + MV	yes	> 0.01	yes	> 0.6	$\|\eta\| > 0.6$
	MUBAC + MV	yes	-	yes	> 0.6	$\|\eta\| > 0.6$
	MUBAC+BREMAT4dof+MV	yes	> 0.01	yes	> 0.6	$\|\eta\| < 0.6$
	MUBAC+BREMAT5dof+MV	yes	> 0.01	no	> 0.6	-
	MPMATCH or MUFO	yes	$> 0.01, < 0.05$	-	-	-
	MUFO good vtx	no	–	yes	-	-
4	BREMAT 4dof	yes	> 0.01	yes	-	-
	MUBAC	yes	< 50 cm	yes	-	-
	MUBAC + MV	yes	< 120 cm	yes	> 0.6	$\|\eta\| < 0.6$
	MUBAC + MIP	yes	< 120 cm	-	impl.	pt>2
	MUFO other vtx	no	-	yes	-	-
	MCTS + MV	no	-	no	> 0.6	-

Table D.1: Default muon quality assignments (accepted muon candidates).

quality	finder combination	CTD match?	match prob/ DCA cut	vtx ass.	mip prob	mom. or rap.
3	MV	yes	-	yes	> 0.95	p>1
	BREMAT 5dof	yes	> 0.01	no	-	-
	GLOMU + MV	yes	implicit	-	> 0.6	-
	MUBAC + MV	yes	< 120 cm	-	> 0.4	p>1
	MUBAC + GLOMU	yes	implicit	-	-	-
	MAMMA+CTD	yes	-	-	impl.	-
	MAMMA+vtx	no	-	yes	impl.	-
	MAMMA	no	-	-	impl.	-
2	MV	yes	-	yes	> 0.8	p>1
	MCTS	no	-	no	-	-
	BAC	yes	< 120 cm	yes	-	-
	BREMAT 4dof	yes	> 0.01	no	-	-
	GLOMU	yes	implicit	-	-	-
1	MV	yes	-	yes	> 0.6	p>1
0	MV	-	-	-	> 0.4	p>1
	MIP	yes	-	-	impl.	pt>2
-1	BREMAT 5dof	yes	< 0.01	-	-	-
-2	BREMAT 4dof	yes	< 0.01	-	-	-
	MCTS rec. problem	no	-	no	-	-
-3	any finder, same VC track	yes	-	-	-	-
-999	sim. μ, not rec.	-	-	-	-	p>1,pt> .5
-1000	sim. π/K decay, not rec.	-	-	-	-	p>1,pt> .5

Table D.2: Default muon quality assignments (rejected muon candidates).

Appendix E

Tight and *loose* matching for the efficiency correction application

The efficiency correction value determined for the tight or loose matching is applied to a muon tagged by the given finder as follows:

- **MUBAC:** loose requires the presence of an MV tag ($P_{\mathrm{MV}} > 0.6$), tight is applied for all other muons,
- **MPMATCH:** same as above.
- **BREMAT:** loose requires the presence of an MV tag ($P_{\mathrm{MV}} > 0.6$) *and* a MUBAC tag, tight is applied for all other muons.

In the case of BREMAT the underlying logic is the following: A DCA cut of 50 cm is applied to MUBAC muon candidates that do not have a supporting MIP tag (see tab. D.2) thus corresponding to the the *tight* determination criterion. The DCA cut is widened up to 120 cm if the MIP tag is present and thus correspond to the *loose* determination criterion.

The muon finder efficiency was determined relative to muons found by the MV algorithm. It still has to be applied to muons that have not been found by MV. Thus the application is based on the assumption that the BREMAT, MPMATCH and MUBAC muon efficiencies do not depend on the MV response (thus roughly on the muon isolation).

Appendix F

Trigger definition

F.1 Muon plus Dijets for Running Periods 1999-2000: TLT HFL 1

- only for running periods 1999-2000
- good muon found by barrel/rear muon chambers
- two jets with $E_T > 3.5$ GeV and $|\eta| < 2.5$
- CAL: $p_z/E < 1.0$ GeV
- CAL: $E - p_z < 100$ GeV
- logical OR of second level trigger slots: SLT HPP 1, 2, 3
- included logical OR of first level trigger slots: FLT 40, 41, 42, 43 required by SLT slots above

F.2 Generic Charm: TLT HFL 10/11

- Tags D^* in K, π, π decay channel
- -50 cm $< z_{\text{vtx}} < 50$ cm and $2 <$ Nr of tracks < 100
- $p_{\text{T}\pi_s} > 0.1$ GeV and $p_{\text{T}D^*} > 1.8$ GeV and $p_{\text{T}D^0} > 0.35(0.4)$ GeV and $1.4 < m(D^0) < 2.2$ GeV and $\delta m(D^* - D^0) < 0.17$ GeV OR
- $p_{\text{T}}(D^*) > 1.35$ GeV and DIS electron with $E_e > 4$ GeV and $30 < E - p_z < 100$ GeV and ($x_e > 6$ cm or $y_e > 12$ cm).

F.3 Low E_{T} Dijet: TLT HPP 14

- 2 or more jets with $E_T \geq 4$ GeV and $|\eta| < 2.5$ for the running periods 96-99 or 2 or more jets with $E_T \geq 4.5$ GeV and $|\eta| < 2.5$ for the running periods 99-00
- logical OR of second level trigger slots SLT HPP 1, 2, 3
- included logical OR of first level trigger slots: FLT 40, 41, 42, 43 required by SLT slots above

F.4 Medium Q^2 DIS Electron: TLT DIS 3

- good electron with
- $E_e > 4$ GeV and $30 < E - p_z < 100$ GeV
- box cut around beam pipe with $\sqrt{x_e^2 + y_e^2} > 35$ cm

F.5 DIS Electron plus Muon: TLT DIS 27

- good electron with
- $E_e > 7$ GeV and
- a good BRMUON muon segment match with a CTD tack with a track selection of:
  - $p > 1$ GeV
  - track crossed > 3 CTD superlayers
  - DCA (beamline-track) < 10 cm
  - DCA-vertex < 10 cm
- the muon segment is matched to the track using a straight line extrapolation to the inner muon chamber surface and a DCA < 200 cm cut.

F.6 Barrel/Rear Muon Trigger: TLT EXO 11/12

- one outer barrel/rear muon reconstructed by the GLOMU muon finder (see sec. 6.3.7.3)
- cosmics rejection if:
  - $n_{\texttt{tracks-CTD}} \leq 3$ and
  - $E_{\texttt{FCAL}} < 1.0$ GeV and
  - the two tracks with highest p_{T} have $p_{\mathrm{T}} > 0.5$ and $cos(\theta_{\texttt{tracks}}) < -0.9998$
- CAL timing cut compatible with physics event
- logical OR of first level trigger slots: FLT 14 (barrel muon), FLT 15 (rear muon)

F.7 Semi-Isolated Muon with the Barrel/Rear Muon Chambers: TLT MUO 3

- good inner barrel/rear muon found on the second trigger level
- hit in barrel or rear inner muon chambers
- muon-like CAL-island
- $n_{\texttt{tracks}-\texttt{CTD}} \geq 1$
- track going into barrel or rear CAL with $p_{\mathrm{T}} > 1$ GeV
- second level trigger slot: SLT MUO 1
- included logical OR of first level trigger slots FLT 8, 9, 10, 11 required by SLT slots above

F.8 Forward Muon Trigger: TLT MUO 1, 2, 4

- MUO 1 : Isolated muon in FMU
- MUO 2 : high p_{T} muon in FMU
  - barrel/rear muon MUO SLT slots
  - B/RMuon hit with matching CTD track (GLOMU, loose cuts)
  - match to mip island
- MUO 4 : elastic J/ψ in FMU

List of Figures

2.1 Scale dependence of α_s . . . 5
2.2 Basic quark and gluon loops . . . 6
2.3 *ep* scattering at HERA . . . 7
2.4 Differential CC and NC DIS cross sections . . . 10
2.5 Parton density functions from ZEUS and H1 . . . 11
2.6 Diagrams for direct and resolved components of *ep* photoproduction . . . 13
2.7 String fragmentation . . . 14
2.8 NLO gluon radiation . . . 16
2.9 NLO virtual corrections . . . 16
2.10 LO, NLO and PS in $b\bar{b}$ production . . . 16
2.11 Comparison of shape: Peterson $f(z)$ for charm and beauty . . . 17
2.12 Spectator model of hadron decay . . . 18
2.13 Cascade decay of beauty quarks . . . 18
2.14 Methods of *ep* event generators . . . 19
2.15 B-hadron momentum spectra . . . 20
2.16 Muons from beauty decay . . . 22
2.17 $B^0_d\overline{B^0_d}$ mixing . . . 23
2.18 Muon pairs from quarkonium decays . . . 24
2.19 Bethe-Heitler and Drell-Yan like muon pair production . . . 25

3.1 UA1 dimuon $\Delta\phi$ . . . 28
3.2 Inclusive single beauty quark cross section from UA1 . . . 29
3.3 Beauty quark correlation cross sections in $\Delta R_{b\bar{b}}$ and $\Delta\phi^{b\bar{b}}$ from UA1 . . . 29
3.4 Beauty and charm quark cross sections from L3 . . . 30
3.5 Beauty quark cross section from the Tevatron . . . 31
3.6 Beauty from J/ψ at CDF: Cross section . . . 32

3.7 Differential cross sections in p_T^μ and η^μ at HERA 33
3.8 η^μ cross section of muons from beauty events in DIS at HERA 34
3.9 Beauty contribution to the proton structure function F_2 at HERA 35
3.10 D^* mass distributions 37

4.1 Aerial photo of the DESY laboratory 39
4.2 The electron proton storage ring HERA 40
4.3 HERA delivered luminosity for 1993-2000 and 2002-2005 41
4.4 Cross section of the HERA II mirror plate quadrupole 42
4.5 The HERA II interaction zone magnet lattice 43
4.6 Central synchrotron-radiation collimation system after the HERA upgrade . . . 44
4.7 CTD hits during an electron beam energy scan 47
4.8 Estimating direct and delayed components from the CTD timing information . . 48
4.9 CTD background: Beam current dependence 49
4.10 The horizontal plane of the synchrotron radiation simulation environment . . . 51
4.11 3D simulated energy loss of photons in ZEUS 52
4.12 Photons at the collimator C15 53
4.13 Comparison of the synchrotron radiation simulation to CTD data 54
4.14 Comparison of step 3 to a GEANT simulation 55
4.15 ϕ distribution for the rear 50 cm of the CTD super-layer 1 56
4.16 Absorber 4 56
4.17 Direct photons at Absorber 4 57
4.18 C5A cross section 58
4.19 Result from backscattering calculations 59
4.20 'Sneak-through' photons (between C5A and C5C) 60
4.21 Effect of the MVD cables 60
4.22 Backscattered photons in H1 and ZEUS 61
4.23 The modified C5B 63
4.24 Variations of shielding options 64
4.25 Photons from $z = -19$ m 65
4.26 Reduction of direct photon hits from beam-tail photons 66
4.27 Final C5A collimator 67
4.28 Final C5B and C5C collimators 67

5.1 Cross section of the ZEUS detector along the beam axis . . . 69
5.2 Cross section of the ZEUS detector perpendicular to the beam axis . . . 70
5.3 ZEUS recorded luminosity for 1993-2000 and 2003-2005 . . . 71
5.4 XY cross section of the CTD . . . 72
5.5 Schematic layout of the MVD . . . 74
5.6 View of an FCAL module . . . 76
5.7 Schematic view of the forward muon detector along the beam axis . . . 77
5.8 Blowup of the layout of the barrel and rear muon detector . . . 78
5.9 The ZEUS luminosity monitoring system . . . 81
5.10 The ZEUS trigger and data acquisition system . . . 83

6.1 Resolution of CAL and CTD momentum information . . . 90
6.2 Examples of EFO track cluster matches . . . 91
6.3 Dead material map used to correct the CAL cone islands . . . 92
6.4 Muonic energy in the CAL as a function of θ . . . 93
6.5 Determination of the pseudo thrust . . . 95
6.6 Pseudo thrust distributions for charm and beauty MC . . . 96
6.7 Dimuon isolation distributions for J/ψ and beauty MC . . . 104

7.1 Calorimeter energy cut . . . 109
7.2 Dimuon mass distributions . . . 110
7.3 Dimuon mass distributions, nonisolated and isolated high and low mass . . . 112
7.4 Muon finders . . . 114
7.5 Muon finders - without and with muon-efficiency correction . . . 116
7.6 Reweighting the $J/\psi p_{\mathrm{T}}^{\mu\mu}$ spectra . . . 118
7.7 Υ peak in isolated dimuon events . . . 119

8.1 Muon transverse momentum and pseudo-rapidity distributions . . . 123
8.2 Fake muon control distribution: high mass dimuon $\Delta\phi^{\mu\mu}$ and η^{μ} . . . 124
8.3 $p_{\mathrm{T}}^{\mathrm{rel}}$ and pseudo-Thrust distributions . . . 126
8.4 Dimuon isolation $I_{\mu\mu}$ . . . 126
8.5 ΔR distributions, separate for high and low mass dimuon events . . . 127
8.6 Q^2 and $E - p_z$ distribution for dimuon events . . . 128

9.1 Muons from beauty decays in the visible range . . . 131

9.2 Tagged b quark transverse-momentum distribution 132
9.3 Extrapolation from visible to total cross section 133
9.4 Visible cross section using different combinations of muon finders 134
9.5 Muon p_{T}^{μ} and η^{μ} distributions with high p_{T} cuts 137
9.6 Differential cross section $d\sigma/dp_{\mathrm{T}}^{\mu}$ for muons from b decays 137
9.7 Differential cross section $d\sigma/d\eta^{\mu}$ for muons from b decays 138
9.8 Dimuon-mass cut for $\Delta\phi$ cross section 139
9.9 Azimuthal distance $\Delta\phi$ between the two muons in dimuon events 141
9.10 Differential cross section $d\sigma/d\Delta\phi^{\mu\mu}$ for dimuon events from $b\bar{b}$ decays 141
9.11 Comparison of measured cross sections to NLO predictions 143
9.12 Differential cross section $d\sigma/d\Delta\phi^{\mu\mu}$ for dimuon events from $b\bar{b}$ decays, NLO comparison 144

A.1 ZEUS coordinate system 151

List of Tables

2.1 SM fermions . . . 3
2.2 Known forces in nature . . . 4
2.3 Heavy hadrons . . . 17
2.4 Parameters used for the NLO predictions . . . 21

4.1 HERA design parameters . . . 42

5.1 BAC components: Dimensions and numbers . . . 79

6.1 ZEUS data samples 1996 - 2000 . . . 86
6.2 MC samples . . . 87
6.3 CAL energy-correction factors . . . 89
6.4 Cuts defining the scattered electron . . . 97
6.5 Definition of the forward muon quality correction. . . . 102

7.1 Cuts on reconstruction level . . . 107
7.2 Trigger selection . . . 107
7.3 Dimuon mass and charge correlations . . . 111
7.4 Key for figures 7.4, 7.5 and 9.4 . . . 113

9.1 Number of beauty events in the high and low mass signal range . . . 131
9.2 Systematic error estimation for the visible and the total cross section . . . 135
9.3 Differential cross section $d\sigma/dp_T^\mu$ for muons from b decays . . . 138
9.4 Differential cross section $d\sigma/d\eta^\mu$ for muons from b decays . . . 139
9.5 Systematic error estimation for the differential cross sections . . . 142

B.1 Orbit and optics changes: from positrons to electrons . . . 153

C.1 Generator cross sections and luminosities of the available PYTHIA and RAPGAP MC samples . . . 155

D.1 Default muon quality assignments (accepted muon candidates). 157
D.2 Default muon quality assignments (rejected muon candidates). 158

Bibliography

[1] Particle Data Group, Eidelman, S. et al., *Review of particle physics*, Phys. Lett. **B592**, 1 (2004).

[2] Halzen, F., Martin, A.D., *Quarks and Leptons: An Introduction Course in Modern Particle Physics*. John Wiley & Sons, 1984.

[3] Sterman, G., Smith, J., Collins, J. C., Whitmore, J., Brock, R., Huston, J., Pumplin, J., Tung, W.-K., Weerts, H., Yuan, C.-P., Kuhlmann, S., Mishra, S., Morfín, J. G., Olness, F., Owens, J., Qiu, J., Soper, D. E., *Handbook of perturbative QCD*, Reviews of Modern Physics **67**, 157 (1995).

[4] Collins, John C., *The problem of scales: Renormalization and all that* (1995), hep-ph/9510276.

[5] Bardeen, William A., Buras, A. J., Duke, D. W., Muta, T., *Deep inelastic scattering beyond the leading order in asymptotically free gauge theories*, Phys. Rev. **D18**, 3998 (1978).

[6] F. Jacquet, A. Blondel. Proc. of the Study of an ep facility for Europe, ed U Amaldi, DESY 79/48, p391, 1979.

[7] Feynman, Richard P., *Very high-energy collisions of hadrons*, Phys. Rev. Lett. **23**, 1415 (1969).

[8] Bjorken, J. D., *Asymptotic sum rules at infinite momentum*, Phys. Rev. **179**, 1547 (1969).

[9] Callan, Curtis G. , Jr., Gross, David J., *High-energy electroproduction and the constitution of the electric current*, Phys. Rev. Lett. **22**, 156 (1969).

[10] Cooper-Sarkar, Amanda M., Devenish, R. C. E., De Roeck, A., *Structure functions of the nucleon and their interpretation*, Int. J. Mod. Phys. **A13**, 3385 (1998), hep-ph/9712301.

[11] ZEUS and H1 Coll., Gabareen Mokhtar, Arafat, Preprint hep-ex/0406036, 2004.

[12] Collins, John C., Soper, Davison E., *The theorems of perturbative QCD*, Ann. Rev. Nucl. Part. Sci. **37**, 383 (1987).

[13] Altarelli, Guido, Parisi, G., *Asymptotic freedom in parton language*, Nucl. Phys. **B126**, 298 (1977).

[14] Ciafaloni, Marcello, *Coherence Effects in Initial Jets at Small Q**2 / s*, Nucl. Phys. **B296**, 49 (1988);
Catani, S. and Fiorani, F. and Marchesini, G., *QCD Coherence in Initial State Radiation*, Phys. Lett. **B234**, 339 (1990);
Catani, S. and Fiorani, F. and Marchesini, G., *Small x Behavior of Initial State Radiation in Perturbative QCD*, Nucl. Phys. **B336**, 18 (1990);
Marchesini, Giuseppe, *QCD coherence in the structure function and associated distributions at small x*, Nucl. Phys. **B445**, 49 (1995), hep-ph/9412327.

[15] Kuraev, E. A. and Lipatov, L. N. and Fadin, Victor S., *Multi - Reggeon Processes in the Yang-Mills Theory*, Sov. Phys. JETP **44**, 443 (1976);
Kuraev, E. A. and Lipatov, L. N. and Fadin, Victor S., *The Pomeranchuk Singularity in Nonabelian Gauge Theories*, Sov. Phys. JETP **45**, 199 (1977);
Balitsky, I. I. and Lipatov, L. N., *The Pomeranchuk Singularity in Quantum Chromodynamics*, Sov. J. Nucl. Phys. **28**, 822 (1978).

[16] ZEUS Structure Functions and Electroweak Physics working group, *Combined H1 and ZEUS proton PDF's* (unpublished). 2004.

[17] Von Weizsaecker, C. F., *Radiation emitted in collisions of very fast electrons*, Z. Phys. **88**, 612 (1934);
Williams, E. J., *Nature of the high-energy particles of penetrating radiation and status of ionization and radiation formulae*, Phys. Rev. **45**, 729 (1934).

[18] Kroseberg, J., *A Measurement of Beauty Production in High-Energy Positron-Proton Scattering*. Ph.D. thesis, University of Zurich (2002).

[19] Peterson, C., Schlatter, D., Schmitt, I., Zerwas, Peter M., *Scaling violations in inclusive e+ e- annihilation spectra*, Phys. Rev. **D27**, 105 (1983).

[20] ALEPH Coll., Buskulic, D. et al., *Measurement of the effective b quark fragmentation function at the Z resonance*, Phys. Lett. **B357**, 699 (1995).

[21] Jones, L. M., Wyld, H. W., *Charmed particle production by photon gluon fusion*, Phys. Rev. **D17**, 759 (1978).

[22] UA1 Coll., Albajar, C. et al., *Measurement of b anti-b correlations at the CERN p anti-p collider*, Z. Phys. **C61**, 41 (1994).

[23] Nason, Paolo and Oleari, Carlo, *A phenomenological study of heavy-quark fragmentation functions in e+ e- annihilation*, Nucl. Phys. **B565**, 245 (2000), hep-ph/9903541.

[24] Blobel, V., Lohrmann, E., *Statistische und numerische Methoden der Datenanalyse*. Teubner Studienbücher, 1998.

[25] Sjostrand, Torbjorn et al., *High-energy-physics event generation with PYTHIA 6.1*, Comput. Phys. Commun. **135**, 238 (2001), hep-ph/0010017;
Sjostrand, Torbjorn and Lonnblad, Leif and Mrenna, Stephen, *PYTHIA 6.2: Physics and manual* (2001), hep-ph/0108264.

[26] Jung, Hannes, *Hard diffractive scattering in high-energy e p collisions and the Monte Carlo generation RAPGAP*, Comp. Phys. Commun. **86**, 147 (1995).

[27] Belle Coll., Abe, K. et al., *Measurement of the inclusive semileptonic branching fraction of B mesons and /V(cb)/. ((B))*, Phys. Lett. **B547**, 181 (2002), hep-ex/0208033;
BABAR Coll., Aubert, B. et al., *Measurement of the branching fraction for inclusive semileptonic B meson decays*, Phys. Rev. **D67**, 031101 (2003), hep-ex/0208018.

[28] M. Corradi, M. Turcato, *Beauty production in dijet events* (unpublished). ZEUS-Note 04-005, 2004.

[29] Brun, R., Bruyant, F., Maire, M., McPherson, A. C. , Zanarini, P., *GEANT3.* CERN-DD/EE/84-1.

[30] Frixione, Stefano, Mangano, Michelangelo L., Nason, Paolo, Ridolfi, Giovanni, *Heavy quark correlations in photon - hadron collisions*, Nucl. Phys. **B412**, 225 (1994), hep-ph/9306337.

[31] Harris, B. W., Smith, J., *Heavy quark correlations in deep inelastic electroproduction*, Nucl. Phys. **B452**, 109 (1995), hep-ph/9503484;
Harris, B. W., Smith, J., *Invariant mass distributions for heavy quark - anti-quark pairs in deep inelastic electroproduction*, Phys. Lett. **B353**, 535 (1995), hep-ph/9502312.

[32] Harris, B. W., Smith, J., *Charm quark and D*+- cross sections in deeply inelastic scattering at HERA*, Phys. Rev. **D57**, 2806 (1998), hep-ph/9706334.

[33] Olness, Fredrick I. and Tung, Wu-Ki, *When is a Heavy Quark Not a Parton? Charged Higgs Production And Heavy Quark Mass Effects in the QCD Based Parton Model*, Nucl. Phys. **B308**, 813 (1988);
Buza, M. and Matiounine, Y. and Smith, J. and van Neerven, W. L., *Comparison between the various descriptions for charm electroproduction and the HERA-data*, Phys. Lett. **B411**, 211 (1997), hep-ph/9707263.

[34] Marchesini, G. et al., *HERWIG: A Monte Carlo event generator for simulating hadron emission reactions with interfering gluons. Version 5.1 - April 1991*, Comput. Phys. Commun. **67**, 465 (1992).

[35] ZEUS Coll., Breitweg, J. et al., *Measurement of elastic Upsilon photoproduction at HERA*, Phys. Lett. **B437**, 432 (1998), hep-ex/9807020.

[36] H1 Coll., Adloff, C. et al., *Elastic photoproduction of J/psi and Upsilon mesons at HERA*, Phys. Lett. **B483**, 23 (2000), hep-ex/0003020.

[37] S. P. Baranov et al., LPAIR- *A Generator for Lepton Pair Production.*

[38] Vermaseren, J. A. M., *Two photon processes at very high-energies*, Nucl. Phys. **B229**, 347 (1983).

[39] Herb, S. W. et al., *Observation of a dimuon resonance at 9.5-gev in 400-*GeV *proton - nucleus collisions*, Phys. Rev. Lett. **39**, 252 (1977).

[40] Geiser, A., *Beauty production at the CERN proton anti-proton collider: A Test of QCD.* PITHA-92-31.

[41] Nason, P., Dawson, S., Ellis, R. K., *The total cross-section for the production of heavy quarks in hadronic collisions*, Nucl. Phys. **B303**, 607 (1988);
Nason, P., Dawson, S., Ellis, R. K., *The one particle inclusive differential cross-section for heavy quark production in hadronic collisions*, Nucl. Phys. **B327**, 49 (1989).

[42] Achard, P. et al., *Measurement of the cross section for open-beauty production in photon photon collisions at LEP*, Phys. Lett. **B619**, 71 (2005), hep-ex/0507041.

[43] D0 Coll., Abbott, B. et al., *The b anti-b production cross section and angular correlations in p anti-p collisions at s**(1/2) = 1.8- TeV*, Phys. Lett. **B487**, 264 (2000), hep-ex/9905024.

[44] CDF Coll., D'Onofrio, Monica, *Beauty production cross section measurements at E(cm) = 1.96-TeV* (2005), hep-ex/0505036.

[45] Frixione, Stefano, Mangano, Michelangelo L., *Heavy-quark jets in hadronic collisions*, Nucl. Phys. **B483**, 321 (1997), hep-ph/9605270.

[46] CDF Coll., Acosta, D. et al., *Measurement of the J/psi meson and b-hadron production cross sections in p anti-p collisions at s**(1/2) = 1960- GeV*, Phys. Rev. **D71**, 032001 (2005), hep-ex/0412071.

[47] H1 Coll., Aktas, A. et al., *Measurement of beauty production at HERA using events with muons and jets*, Eur. Phys. J. **C41**, 453 (2005), hep-ex/0502010.

[48] Coppola, Nicola, *The Study of Open Beauty in Photoproduction at HERA* (unpublished). DESY-THESIS-2000-034;
Turcato, Monica, *Measurement of beauty photoproduction at HERA* (unpublished). DESY-THESIS-2003-039.

[49] Chekanov, S. and others, *Beauty photoproduction measured using decays into muons in dijet events in e p collisions at s**(1/2) = 318-GeV* (2003), hep-ex/0312057.

[50] ZEUS Coll., Chekanov, S. et al., *Measurement of beauty production in deep inelastic scattering at HERA*, Phys. Lett. **B599**, 173 (2004), hep-ex/0405069.

[51] H1 Coll., Aktas, A. et al., *Measurement of F2(c anti-c) and F2(b anti-b) at high Q**2 using the H1 vertex detector at HERA*, Eur. Phys. J. **C40**, 349 (2005), hep-ex/0411046.

[52] H1 Coll., Adloff, C. et al., *Measurement and QCD analysis of neutral and charged current cross sections at HERA*, Eur. Phys. J. **C30**, 1 (2003), hep-ex/0304003.

[53] Martin, A. D., Roberts, R. G., Stirling, W. J. and Thorne, R. S., *Uncertainties of predictions from parton distributions. II: Theoretical errors*, Eur. Phys. J. **C35**, 325 (2004), hep-ph/0308087.

[54] Aktas, A. et al., *Measurement of F2(c anti-c) and F2(b anti-b) at low Q**2 and x using the H1 vertex detector at HERA* (2005), hep-ex/0507081.

[55] ZEUS Coll., Chekanov, S. et al.. Abstract 5-0342, 11-0343, International Conference on High Energy Physics, Beijing, China, August 16-22, 2004;
ZEUS Coll., Chekanov, S. et al.. Abstract 784, International Conference on High Energy Physics, Amsterdam, The Netherlands, July 24-31, 2002.

[56] H1 Coll., Aktas, A. et al., *Measurement of charm and beauty photoproduction at HERA using D* mu correlations*, Phys. Lett. **B621**, 56 (2005), hep-ex/0503038.

[57] *HERA - A proposal for a large electron proton colliding beam facility at DESY.* Hamburg Desy - DESY-HERA-81-10 (81,REC.AUG.) 292p.

[58] Seidel, M., *The upgraded interaction regions of HERA.* DESY-HERA-00-01.

[59] Schneekloth, U. , (ed.), *The HERA luminosity upgrade.* DESY-HERA-98-05.

[60] Schneekloth, U., *Recent HERA results and future prospects* (1998), hep-ex/9806010.

[61] B. Holzer, private communication, 2002.

[62] M. Seidel, *Report on HERA Vacuum Status and Modifications in Preparation for the Shutdown 2003* (unpublished). 2002.

[63] V. Andreev et al., *Technical Report on the Beam Induced Backgrounds in the H1 Detector* (unpublished). H1-Note H1-10/02-606, 2002.

[64] V. Andreev et al., *Further Report on the Beam Induced Backgrounds in the H1 Detector* (unpublished). H1-Note H1-01/03-607, 2003.

[65] D. Bailey et al., *Study of beam-induced backgrounds in the ZEUS detector from 2002 HERA running* (unpublished). ZEUS-Note 02-018, 2002.

[66] D. Bailey et al., *Study of beam-induced backgrounds in the ZEUS detector from 2002 HERA running (Addendum 1)* (unpublished). ZEUS-Note 02-020, 2002.

[67] D. Bailey et al., *Study of beam-induced backgrounds in the ZEUS detector from 2002 HERA running (Addendum 2)* (unpublished). ZEUS-Note 02-027, 2003.

[68] Pitzl, D., *Abschirmung der HERA-Detektoren gegen Synchrotronstrahlung.* Diploma Thesis at the University of Hamburg, 1987 (in German).

[69] Wille, K., *Physik der Teilchenbescheuniger und Synchrotronstrahlungsquellen.* Teubner Studienbücher, 1996.

[70] R. Carlin, private communication, 2005.

[71] Meseck, A., *The electron distribution in HERA and the consequences for the H1 detector after the luminosity upgrade.* DESY-THESIS-2000-042.

[72] W. Decking, private communication, 2002.

[73] Seidel, M., Kouptsidis, J., Nawrath, G., Schneekloth, U., Zapfe, K., *The vacuum system for the upgraded HERA interaction regions*, Vacuum **60**, 267 (2001).

[74] ZEUS Coll., U. Holm (ed.), *The ZEUS Detector*. Status Report (unpublished), DESY (1993), available on `http://www-zeus.desy.de/bluebook/bluebook.html`.

[75] Harnew, N. et al., *Vertex triggering using time difference measurements in the ZEUS central tracking detector*, Nucl. Instrum. Meth. **A279**, 290 (1989);
Foster, B. et al., *The Performance of the Zeus central tracking detector z-by- timing electronics in a transputer based data acquisition system*, Nucl. Phys. Proc. Suppl. **32**, 181 (1993);
ZEUS Coll., Foster, B. et al., *The Design and construction of the ZEUS central tracking detector*, Nucl. Instrum. Meth. **A338**, 254 (1994).

[76] Catterall, C., *Measurement of Charged Particles from the Hadronic Final State of Electron-Proton Deep Inelastic Scattering at a Centre of Mass Energy of 296 GeV* (1995). PhD Thesis at the University College of London.

[77] Maddox, Erik, *Study of heavy quark production at HERA using the ZEUS microvertex detector* (unpublished). Thesis, 2004.

[78] The ZEUS Collaboration, *A Microvertex Detector for ZEUS* (unpublished). Tech. Report DESY-PRC 97/01, 1997.

[79] Chiochia, V., *The ZEUS micro vertex detector*, Nucl. Instrum. Meth. **A501**, 60 (2003), hep-ex/0111061;
ZEUS Coll., Koffeman, E. N., *The construction of the ZEUS micro vertex detector*, Nucl. Instrum. Meth. **A473**, 26 (2001);
Petrucci, M. C., *The ZEUS microvertex detector*, Int. J. Mod. Phys. **A16S1C**, 1078 (2001);
Koetz, U., *Test of silicon strip detectors for the ZEUS microvertex detector*, Nucl. Instrum. Meth. **A461**, 210 (2001);
Koffeman, E. N., *A silicon micro vertex detector for the ZEUS experiment*, Nucl. Instrum. Meth. **A453**, 89 (2000);
Coldewey, C., *Test of silicon strip detectors for the ZEUS microvertex detector*, Nucl. Instrum. Meth. **A453**, 149 (2000);
Coldewey, C., *The ZEUS microvertex detector*, Nucl. Instrum. Meth. **A447**, 44 (2000);
Klanner, R., *The ZEUS microvertex detector*. Prepared for International Europhysics Conference on High- Energy Physics (EPS-HEP 99), Tampere, Finland, 15-21 Jul 1999;
Garfagnini, A., *The ZEUS microvertex detector*, Nucl. Instrum. Meth. **A435**, 34 (1999);
Dannheim, D. et al., *Design and tests of the silicon sensors for the ZEUS micro vertex detector*, Nucl. Instrum. Meth. **A505**, 663 (2003), hep-ex/0212026.

[80] Derrick, M. et al., *Design and construction of the ZEUS barrel calorimeter*, Nucl. Instrum. Meth. **A309**, 77 (1991);
Andresen, A. et al., *Construction and beam test of the ZEUS forward and rear calorimeter*, Nucl. Instrum. Meth. **A309**, 101 (1991);
Caldwell, A. et al., *Design and implementation of a high precision readout system for the ZEUS calorimeter*, Nucl. Instrum. Meth. **A321**, 356 (1992);
Bernstein, A. et al., *Beam tests of the ZEUS barrel calorimeter*, Nucl. Instrum. Meth. **A336**, 23 (1993).

[81] Battistoni, G. et al., *Electrodeless plastic streamer tubes*, Nucl. Instr. Meth. **217**, 429 (1983).

[82] Abbiendi, G. et al., *The ZEUS barrel and rear muon detector*, Nucl. Instrum. Meth. **A333**, 342 (1993).

[83] De Giorgi, M. et al., *The LST analog readout system of the ZEUS muon detector*, Nucl. Instrum. Meth. **A378**, 472 (1996).

[84] Tomasz Jezynski et al., Proc. SPIE **5484**, 180 (2004);
Krzysztof T. Pozniak et al., Proc. SPIE **5484**, 186 (2004).

[85] Andruszkow, J. et al., *Luminosity measurement in the ZEUS experiment*, Acta Phys. Polon. **B32**, 2025 (2001).

[86] H. Bethe, W. Heitler, *On the Stopping of fast particles and on the creation of positive electrons*, Proc. Roy. Soc. Lond. **A146**, 83 (1934).

[87] W. H. Smith, K. Tokushuku, L. W. Wiggers. *Proc. Computing in High-Energy Physics (CHEP), Annecy, France, 1992*, C. Verkerk and W. Wojcik (eds.), p.222. CERN, Geneva, Switzerland (1992). Also in pre print DESY-92-150B.

[88] S.M. Fisher, P. Palazzi, *ADAMO Reference Manual for Version 3.3*. CERN ECP, available on `http://adamo.web.cern.ch/Adamo/refmanual/Document.html`.

[89] H1 and ZEUS Coll., Brugnera, R., *Inelastic J/psi production at HERA*, Eur. Phys. J. **C33**, s494 (2004).

[90] A. Bertolin et al., *Inelastic ψ' and J/ψ photoproduction at HERA* (unpublished). ZEUS-Note 03-004, 2003.

[91] A. Geiser et al., *GMuon - A general ZEUS muon finder* (unpublished). ZEUS-Note *in preparation*, 2005.

[92] G.F. Hartner, *VCTRACK briefing: Program and Math* (unpublished). ZEUS-Note 98-058, 1998.

[93] Mankel, Rainer, *Pattern recognition and event reconstruction in particle physics experiments*, Rept. Prog. Phys. **67**, 553 (2004), physics/0402039.

[94] Repond, J., *Jet Energy Corrections* (1996). ZEUS-Note 96-133.

[95] Briskin, Gennady M., *Diffractive dissociation in e p deep inelastic scattering.* DESY-THESIS-1998-036;
Tuning, N., *ZUFOs: Hadronic final state reconstruction with calorimeter, tracking and backsplash correction* (unpublished). ZEUS-Note 01-021, 2001.

[96] Longhin, A., *Misura delle sezioni d'urto di fotoproduzione di Open Beauty ad HERA. (In Italian)* (unpublished). Master's thesis, University of Padua, 2000.

[97] Catani, S., Dokshitzer, Yuri L., Webber, B. R., *The K-perpendicular clustering algorithm for jets in deep inelastic scattering and hadron collisions*, Phys. Lett. **B285**, 291 (1992); Catani, S., Dokshitzer, Yuri L., Seymour, M. H., Webber, B. R., *Longitudinally invariant K(t) clustering algorithms for hadron hadron collisions*, Nucl. Phys. **B406**, 187 (1993).

[98] Abramowicz, Halina, Caldwell, Allen, Sinkus, Ralph, *Neural network based electron identification in the ZEUS calorimeter*, Nucl. Instrum. Meth. **A365**, 508 (1995), hep-ex/9505004;
Sinkus, R., Voss, T., *Particle identification with neural networks using a rotational invariant moment representation*, Nucl. Instrum. Meth. **A391**, 360 (1997).

[99] A. López-Durán Viani, S. Schlenstedt, *Electron finder efficiencies and impurities. A comparison between SINISTRA95, EM and EMNET* (unpublished). ZEUS-Note 99-077, 2000.

[100] Kuzmin, V. A., *Identification of leptons by ZEUS calorimeter*, Nucl. Instrum. Meth. **A453**, 336 (2000).

[101] G. Abbiendi et al., *Observation of* $J/\psi \to \mu^+\mu^-$ *in the first* 273 nb^{-1} *of 1993 run* (unpublished). ZEUS-Note 93-120, 1993.

[102] G. Abbiendi, *Global tracking of muons in the Barrel and Rear region* (unpublished). ZEUS-Note 99-063, 1999.

[103] Innocente, V., Maire, M., Nagy, E., *GEANE: Average tracking and error propagation package.* In *Amsterdam 1991, Proceedings, MC91: Detector and event simulation in high energy physics* 58-78. (see High energy physics index 30 (1992) No. 3237).

[104] R. Ciesielski, private communication, 2004.

[105] M. Corradi, private communication, 2004.

[106] L. Bellagamba, *MVMATCH: A package to match FMUON tracks with Central Detectors* (unpublished). ZEUS-Note 96-051, 1996.

[107] Kalman, Rudolph, Emil, *A New Approach to Linear Filtering and Prediction Problems*, Transactions of the ASME–Journal of Basic Engineering **82**, 35 (1960), Series D.

[108] Gutsche, Oliver, *Measurement of beauty quark cross sections in photoproduction with the ZEUS experiment at the electron proton collider HERA.* DESY-THESIS-2005-010.

[109] Longhin, Andrea, *Measurement of beauty production at HERA with a D* + mu tag.* DESY-THESIS-2004-050.

[110] A. Geiser, private communication, 2005.

[111] ZEUS Coll., S. Chekanov et al., *Measurement of beauty production from dimuon events at HERA.* Abstract 269, submitted to the XXII International Symposium on Lepton-Photon Interactions at High Energy, LP05, Uppsala, Sweden, June 30 2004, 2005.

[112] E. Nuncio-Quiroz, private communication, 2005;
R. Hall-Wilton, private communication, 2005.

[113] M. Corradi, private communication, 2005.

[114] Frixione, Stefano and Mangano, Michelangelo L. and Nason, Paolo and Ridolfi, Giovanni, *Improving the Weizsacker-Williams approximation in electron - proton collisions*, Phys. Lett. **B319**, 339 (1993), hep-ph/9310350;
Frixione, Stafano, Mangano, Michelangelo L., Nason, Paolo, Ridolfi, Giovanni, *Total cross.sections for heavy flavour production at HERA*, Phys. Lett. **B348**, 633 (1995), hep-ph/9412348.

[115] Samson, Ursula. Ph.D. thesis in preparation.

Acknowledgements

I would like to express my gratitude for a very fruitful, challenging, instructive, interesting... time with all the people who worked with me at DESY. I cannot possibly do any justice to the insights, guidance, inspirations, friendship and support, that I was allowed to experience during this time in a few words. Still, I would like express my special gratitude to:

Robert Klanner for making this thesis possible and his very helpful comments on this thesis.

My mentor Achim Geiser for his delightfully unceasing and invaluable stream of exciting new ideas and suggestions. I am very grateful for his enthusiasm and curiosity about physics and our many, long and enjoyable discussions.

As I enjoy working in a team, I am especially grateful for the close teamwork in the "beauty team" with Ursula Samson, Benjamin Kahle, Oliver Gutsche and Achim Geiser. The hunt for bugs, complicate extensions of the muon reconstruction and analysis code were much more fun to conquer together.

For the same reason I would like to thank Nicola Coppola. Without his friendship, calmness and dedication the synchrotron-radiation simulations would have been an insurmountable task. I am grateful to have worked with Uwe Schneekloth who set the simulation boundary conditions, came up with very creative designs and also finally proof-read the HERA chapter. Thanks also for the help from Stefan Schlenstedt and the other people in the synchrotron-radiation working group: Daniel Pitzl for providing the base code for the simulation and detailed, dedicated help in extending it, Stathes Paganis, Chi-Nhan Nguyen, Erich Lohrmann, Victor Lendermann, Ulrich Koetz, Katarzyna Klimek-Wiechmann and Jo Cole. The HERA team I owe special thanks for many patient explanations and for providing all the necessary input for the detailed simulations.

Specially I would like to thank the good soul of the DESY/ZEUS group Uli Koetz for always being ready to most patiently explain many complicate issues. I am also grateful for the care and commitment of Wolfram Zeuner.

The physics working environment in the ZEUS group and specially the careful advise from members of the HFL group has certainly played an immense part during the progress of this thesis, for which I am very grateful. Specially for calculating the NLO predictions used in this thesis I'd like to thank Richard Hall-Wilton, Massimo Corradi and Liz Nuncio-Quiroz.

A great thanks goes to my fellow Ph.D. students and friends - to Dominik Dannheim specially for among many other things, at the end, patiently reading and commenting the whole thesis, his friendship and tons of insightful advice.

A huge 'thank you' also to my friends ("outside DESY") for ceaselessly proving that indeed a life "outside of Physics" exists and enriching my life with music, discussions and very much fun and friendship.

Last but certainly not least, I would like to express my deep gratitude to my family, especially my dear parents Karin and Horst and my sister Anja. Their support, patience and good examples to live up to made it possible for me to accomplish this task.